ADVANCES IN DESIGN OPTIMIZATION AND GROWTH TECHNOLOGY FOR HIGH-EFFICIENCY INDIUM GALLIUM NITRIDE PHOTOVOLTAICS

A Dissertation
Presented to
The Academic Faculty

By

Chloé Fabien

In Partial Fulfillment
of the Requirements for the Degree
Doctor of Philosophy in the
School of Electrical and Computer Engineering

Georgia Institute of Technology

May 2016

ADVANCES IN DESIGN OPTIMIZATION AND GROWTH TECHNOLOGY FOR HIGH-EFFICIENCY INDIUM GALLIUM NITRIDE PHOTOVOLTAICS

Approved by:

Dr. William A. Doolittle, Advisor
School of Electrical and Computer Engineering
Georgia Institute of Technology

Dr. Ajeet Rohatgi
School of Electrical and Computer Engineering
Georgia Institute of Technology

Dr. Albert B Frazier
School of Electrical and Computer Engineering
Georgia Institute of Technology

Dr. Phillip First
School of Physics
Georgia Institute of Technology

Dr. Shyh-Chiang Shen
School of Electrical and Computer Engineering
Georgia Institute of Technology

Date Approved: December 7th, 2015

– ET LE SOLEIL ? QUI C'EST QUI LE RÉVEILLE ?

– WHAT ABOUT THE SUN? WHO IS SUPPOSED TO WAKE HIM UP?

Philippe Geluck - Le Fils Du Chat: Le Soleil

ACKNOWLEDGMENTS

First and foremost, it has been a real privilege to work under the supervision of Dr. W. Alan Doolittle. As a passionate professor, he has instilled in me his enthusiasm, and as a caring advisor, he has afforded me invaluable support. I am especially grateful for all the opportunities that he provided me.

I had the great pleasure to collaborate with talented labmates, who have always been keen on sharing their scientific knowledge as much as their American culture. Brendan Gunning, Joe Merola, Evan Clinton, Jordan Greenlee, Brooks Tellekamp, Joshua Shank, and Michael Moseley, thanks y'all!

I also wish to thank Dr. Bruno Frazier, Dr. Shyh-Chiang Shen, Dr. Ajeet Rohatgi, and Dr. Phillip First for being part of my dissertation committee, as well as the NSF, DOE, ARPA-E, and AVSE for supporting my research. Moreover, the Institute for Electronics and Nanotechnology staff, especially Gary Spinner, Dr. Mikkel Thomas, Walter Henderson, and Devin Brown, have been extremely helpful throughout my research. Many thanks to Ajay Upadhyaya for all the shared coffee and insightful discussions. I cannot leave Georgia Tech without mentioning Dr. Thomas Gaylord, who has made me feel part of the GT Optics Laboratory.

I am very grateful to the Quantum Energy and Sustainable Solar Technologies (QESST) community, particularly Aymeric Maros, Sebastian Husein, Dr. Fernando Ponce and his group, Dr. Jenefer Husman, Dr. Alex Freundlich, and Dr. Christiana Honsberg. Being part of the QESST Engineering Research Center has been a truly gratifying experience both scientifically and personally. I would also like to extend my

deepest gratitude to Soo Chin who has been a very supportive mentor. Her helpful advice and unwavering guidance were key motivations for my professional and personal development.

I also found the strength to go through these last five years thanks to my friends on both sides of the Atlantic. Special thanks to the GT international-student team, particularly Spyros Pavlidis and Stef Alexopoulos, and the A300 crew.

I have been extremely fortunate to be able to count on the unconditional support and love of my family, Marco, Florence, Victor, and Alice F2L, who have always kept up with my ups and downs, even over the miles. Finally, I cannot begin to express my thanks to Matthieu, to whom I owe this thesis. He has been an amazingly supportive ally and cheerful accomplice for many years and, hopefully, many more.

REMERCIEMENTS

Tout d'abord, cela a été pour moi un véritable privilège de travailler sous la supervision de Dr. W. Alan Doolittle. En tant que professeur passionné, il m'a insufflé son enthousiasme et, en tant que conseiller bienveillant, il m'a apporté un soutien inestimable. Je suis particulièrement reconnaissant pour toutes les opportunités qu'il m'a accordées.

J'ai eu le grand plaisir de collaborer avec des collègues talentueux, qui ont toujours été désireux de partager aussi bien leurs connaissances scientifiques que leur culture américaine. Brendan Gunning, Joe Merola, Evan Clinton, Jordan Greenlee, Brooks Tellekamp, Joshua Shank, et Michael Moseley, thanks y'all !

Je tiens également à remercier Dr. Bruno Frazier, Dr. Shyh-Chiang Shen, Dr. Ajeet Rohatgi, et Dr. Phillip First de faire partie de mon comité de thèse, ainsi que NSF, DOE, ARPA-E, et AVSE d'avoir soutenu financièrement ma recherche. De plus, le personnel de l'IEN, en particulier Gary Spinner, Dr. Mikkel Thomas, Walter Henderson, et Devin Brown, a été extrêmement serviable tout au long de mon doctorat. Un grand merci à Ajay Upadhyaya pour tous les cafés partagés et toutes les discussions enrichissantes. Je ne peux pas quitter Georgia Tech sans mentionner Dr Thomas Gaylord, qui m'a en quelque sorte accueillie au GT Optics Laboratory.

Je suis très reconnaissante envers la communauté QESST, en particulier Aymeric Maros, Sebastian Husein, Dr. Fernando Ponce et son groupe, Dr. Jenefer Husman, Dr. Alex Freundlich, et Dr. Christiana Honsberg. Faire partie de QESST a été une expérience gratifiante à la fois scientifiquement et humainement. Je tiens également à

exprimer ma plus profonde gratitude à Soo Chin qui a été une mentore formidable. Ses conseils utiles et son solide encadrement ont été précieux pour mon développement professionnel et personnel.

J'ai aussi trouvé la force de traverser ces cinq dernières années grâce à mes amis des deux côtés de l'Atlantique. Un merci spécial à la GT international-student team, en particulier Spyros Pavlidis et Stef Alexopoulos et l'A300 crew.

J'ai été extrêmement chanceuse de pouvoir compter sur le soutien et l'amour inconditionnels de ma famille, Marco, Florence, Victor, et Alice F2L, qui m'ont toujours supportée, dans les hauts comme dans les bas, malgré la distance. Enfin, les mots me manquent pour exprimer mes remerciements à Matthieu, à qui je dois cette thèse. Il a été un soutien indéfectible et un compagnon complice depuis de nombreuses années, et je l'espère, pour de nombreuses autres à venir.

.

TABLE OF CONTENTS

LIST OF TABLES

LIST OF FIGURES

LIST OF NOMENCLATURE

°C	Degree Celsius
η	Conversion efficiency
θ	Surface coverage
μm	Micron
μs	Microsecond
ρ_c	Specific contact resistivity
ρ_f	Metal resistivity
Ω	Ohm
A	Ampere
AFM	Atomic force microscopy
Al	Aluminum
ARC	Antireflection coating
a-Si	Amorphous silicon
Au	Gold
b	Bowing parameter
BEP	Beam equivalent pressure
BOE	Buffered oxide etch
C	Coulomb
CdTe	Cadmium Telluride
CIGS	Copper indium gallium selenide
CL	Cathodoluminescence
cm	Centimeter
c-Si	Crystalline silicon
CTLM	Circular transmission line model
d	Finger thickness
DHJ	Double heterojunction
DI	Deionized

e^-	Electron
EBL	Electron beam lithography
E_g	Band gap energy
EHP	Electron-hole pairs
eV	Electron volt
FF	Fill factor
FWHM	Full width at half maximum
Ga	Gallium
GaAs	Gallium arsenide
GaN	Gallium nitride
h^+	Hole
H_2O_2	Hydrogen peroxide
H_2SO_4	Sulfuric acid
HBT	Heterojunction bipolar transistor
HCl	Hydrochloric acid
HNO_3	Nitric acid
I	Current
IB	Intermediate band
ICP	Inductively coupled plasma
In	Indium
InGaN	Indium gallium nitride
InN	Indium nitride
J	Current density
J	Joule
J_0	Reverse saturation current density
J_L	Photogenerated current density
J_{mp}	Current density at maximum power density
J_{sc}	Short-circuit current density
k	Boltzmann constant
K	Kelvin

L	Finger length
LED	Light-emitting diode
LN_2	Liquid nitrogen
L_t	Transfer length
MBE	Molecular beam epitaxy
Mg	Magnesium
Mg_3N_2	Magnesium nitride
min	Minute
ML	Monolayer
mm	Millimeter
MME	Metal-modulated epitaxy
MOCVD	Metalorganic chemical vapor deposition
MQW	Multi-quantum well
M-rich	Metal-rich
n	Diode ideality factor
N	Nitrogen
N_2	Molecular nitrogen
NH_3	Ammonia
Ni	Nickel
nm	Nanometer
N-rich	Nitrogen-rich
ns	Nanosecond
P	Power density
P_c	Resistive power losses due to contact
P_e	Resistive power losses in the emitter
P_f	Resistive power losses in the fingers
P_{inc}	Incident optical power density
PL	Photoluminescence
P_{max}	Maximum power density
P_{pz}	Piezoelectric polarization

PR	Photoresist
P_s	Optical power losses due to shading
P_{sp}	Spontaneous polarization
P_{tot}	Total power losses
PV	Photovoltaic
q	Elementary charge
QD	Quantum dot
QW	Quantum well
r	Radius of inner region
R	Radius of outer region
RC	Rocking curve
RF	Radio frequency
RGA	Residual-gas analysis
RHEED	Reflection high-energy electron diffraction
RIE	Reactive-ion etching
RLP	Reciprocal lattice point
RMS	Root mean square
rpm	Revolutions per minute
r_s	Specific series resistance
R_{sh}	Sheet resistance
r_{sh}	Specific shunt resistance
RSM	Reciprocal space map
s	Second
sccm	Standard cubic centimeters per minute
SEM	Scanning electron microscopy
Si	Silicon
Si	Silicon
SL	Superlattice
T	Temperature
Ta	Tantalum
TCE	Trichloroethylene

TEM	Transmission electron microscopy
Ti	Titanium
UID	Unintentionally doped
USD	United States dollar
V	Volt
V	Voltage
V_{mp}	Voltage at maximum power density
V_{oc}	Open-circuit voltage
w	Finger width
W	Watt
XRD	X-ray diffraction

SUMMARY

Photovoltaic energy has proven to be a sustainable, abundant, and cost-effective alternative energy source. III-nitride semiconductors, particularly indium gallium nitride (InGaN) alloys, are a promising candidate for high-efficiency solar applications because of their highly-attractive inherent properties and the widely-available manufacturing infrastructure for the growth and fabrication of nitride-based devices. However, the full potential of InGaN for photovoltaic applications requires significant progress in the areas of device design, material growth, and device fabrication.

The goal of this work is to evaluate the viability of InGaN alloys for high-efficiency solar cell applications. Numerical simulations are employed to provide guidelines for the design of high-efficiency InGaN-based solar cells and to identify present and future material limitations. The growth of $In_xGa_{1-x}N$ alloys over the entire composition range by molecular beam epitaxy (MBE) is then investigated with the goal of eliminating phase separation and improving the crystal and optical quality. The electrical and structural properties of doped III-nitride films, required to create the collecting *p-n* junction, are studied. Several fabrication aspects, including plasma etching, metal contacts, and metal grid patterns that are necessary for the fabrication of InGaN-based solar cells, are developed. These advances in material growth and device fabrication are implemented to demonstrate functioning InGaN/GaN double-heterojunction solar cells. The performance of the devices is inherently limited by the heterostructures as evidenced by simulation and experimental results. These restrictions can be eliminated by employing InGaN homojunction devices that are

currently challenging to fabricate due to the need for thick, high-quality InGaN layers. To address this issue, a hybrid MBE growth technique is presented. Finally, the fabrication and integration of InGaN quantum dots for intermediate-band solar-cell applications is investigated.

These advances in the understanding of III-nitride solar cells lay the foundations for future high-efficiency InGaN photovoltaics.

CHAPTER 1

INTRODUCTION

1.1 Solar Cells

As the global energy consumption will dramatically increase over the next 20 years [1], meeting growing demand for a secure, affordable, and sustainable energy source is a major challenge. Currently, fossil fuels, which have detrimental effects on the environment, represent more than 80% of the world's energy consumption [2]. To reduce fossil fuel dependency, an economically viable, environmentally sustainable, and abundant energy source is required. Photovoltaic (PV) energy – the conversion of light into electricity – is one of the most promising alternative energy sources that can enhance global energy security while limiting the emission of carbon dioxide and other greenhouse gases.

1.1.1 Solar Cell Operation

The PV effect was first observed in 1839 by a French physicist, Alexandre-Edmond Becquerel, who noted a light-dependent voltage from electrodes immersed in an electrolyte [3]. In 1954, Bell Laboratories announced the first silicon-based *p*-*n* junction PV cell (also referred to as solar cell) with a conversion efficiency of ~6% [4]. Since then, a variety of semiconductor materials and cell structures have been studied. The conversion of light into electricity in a solar cell involves two mechanisms: (i) photogeneration of carriers in a light-absorbing material and (ii) collection of the light-generated carriers. The two processes are depicted in Figure 1.1. Incident photons with

energy greater than the band gap of the material can be absorbed and create electron-hole pairs (EHPs). Charge carrier separation can occur by two mechanisms: drift of carriers due to an electric field and diffusion of carriers due to a density gradient. The EHPs generated in the depletion region are swept across the *p*-*n* junction by the built-in electric field. To contribute to the photocurrent, EHPs must be generated within a diffusion length of the junction to be able to diffuse to the junction before recombining. Recombination, which leads to current and voltage losses, can occur at the surface, at the heterointerfaces, and in the bulk of the solar cell. Three types of recombination in the bulk exist: (i) radiative recombination, which happens when an electron and hole recombine and emit a photon, (ii) Auger recombination, which involves three carriers, and (iii) Shockley-Read-Hall recombination, which is related to traps created by defects in the material [5].

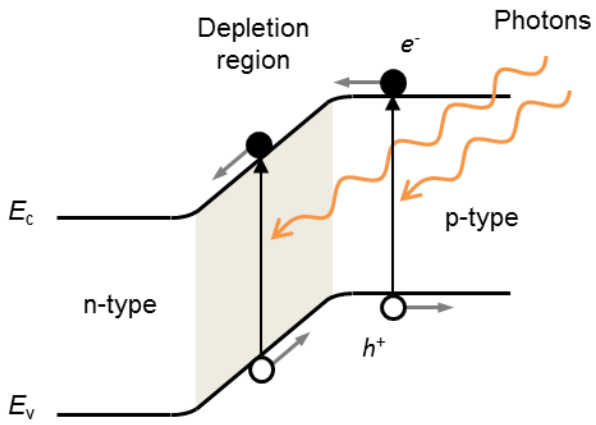

Figure 1.1: Band diagram of an illuminated solar cell showing photogeneration and separation of carriers by diffusion and drift.

A solar cell can be electrically modeled by a diode equivalent circuit as shown in Figure 1.2(a). The characteristic equation of a solar cell that relates the current density (J) and the voltage (V) is given by

$$J = J_L - J_0\left(e^{\frac{q(V+Jr_s)}{nkT}} - 1\right) - \frac{V + Jr_s}{r_{sh}}, \tag{1.1}$$

where J_L is the photogenerated current density (A/cm^2), J_0 is the reverse saturation current density (A/cm^2), r_s is the specific series resistance ($\Omega\cdot$cm^2), r_{sh} is the specific shunt resistance ($\Omega\cdot$cm^2), q is the elementary charge (C), n is the diode ideality factor, k is the Boltzmann constant (J/K^1), and T is the temperature (K). The series resistance includes the bulk resistance of the semiconductor, sheet resistance, and the resistance of the metal contacts. The shunt resistance is due to defects in the depletion region and leakage current around the edges of the device.

The performance of a solar cell may be defined by its *J*-*V* characteristics in dark and illuminated conditions. Figure 1.2(b) shows a typical *J*-*V* characteristic of a solar cell under illumination and the power density (P), defined as the product of J and V, as a function of applied voltage. The conversion efficiency (η) of a solar cell is characterized by three parameters derived from the *J*-*V* characteristics under illumination: the short-circuit current density (J_{sc}), the open-circuit voltage (V_{oc}), and the fill factor (FF). The conversion efficiency of a solar cell is determined as the fraction of incident power that is converted to electricity and is defined as

$$\eta = \frac{J_{sc} \times V_{oc} \times FF}{P_{inc}} = \frac{J_{mp} \times V_{mp}}{P_{inc}}, \tag{1.2}$$

where P_{inc} is the incident optical power density. V_{oc} and J_{sc} represent the maximum voltage and maximum current density extractable from the solar cell under illumination, respectively.

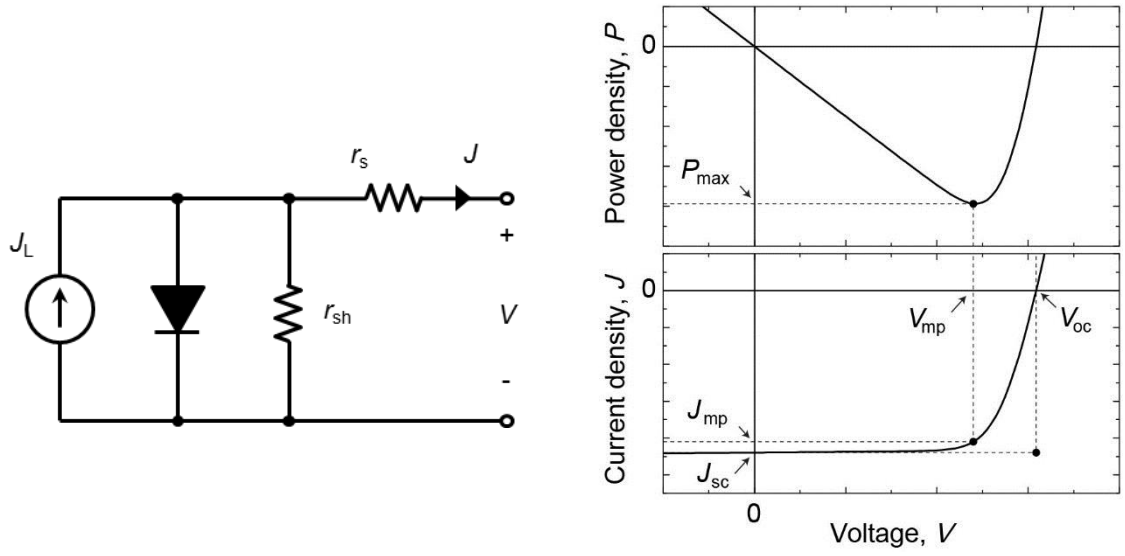

(a) (b)

Figure 1.2: (a) Equivalent electrical circuit of a solar cell and (b) *P*-*V* and *J*-*V* characteristics of a solar cell under illumination.

J_{sc} is related to the generation rate and the collection probability of charge carriers and V_{oc} is the voltage required to cause the light-generated current and the forward bias diffusion current to balance, leading to a zero net current. The power density reaches its maximum absolute value, P_{max}, at a point defined by the voltage value V_{mp} and the corresponding current density J_{mp}. The *FF* is defined as the ratio between P_{max} and the product of V_{oc} and J_{sc}:

$$FF = \frac{J_{mp} \times V_{mp}}{J_{sc} \times V_{oc}} \tag{1.3}$$

1.1.2 Photovoltaic Technologies

Another key metric to compare PV technologies is the price per watt as the ultimate goal of PV technologies is maximum power at minimum cost. PV technologies are generally classified depending on the light-absorbing material. Figure 1.3 depicts the cell efficiencies for a range of photovoltaic technologies. Crystalline silicon (*c*-Si) is the most widely used technology because of its high conversion efficiency and reliable yield. However, bulk Si solar cells require thick absorbing layers that account for a significant part of the total cell cost. Various thin-film technologies based on amorphous silicon (*a*-Si), cadmium telluride (CdTe), and copper indium gallium selenide (CIGS) have lower fabrication costs but are typically less efficient than conventional *c*-Si technology. Currently, the most efficient PV technology is based on III-V semiconductors such as gallium arsenide (GaAs) with multi-junction structures and light concentration. Each subcell of a multi-junction solar cell harvests a different portion of the solar spectrum, thus improving the total conversion efficiency of the cell. Despite their high efficiency, III-V solar cells are predominantly used for space applications because of their very high costs.

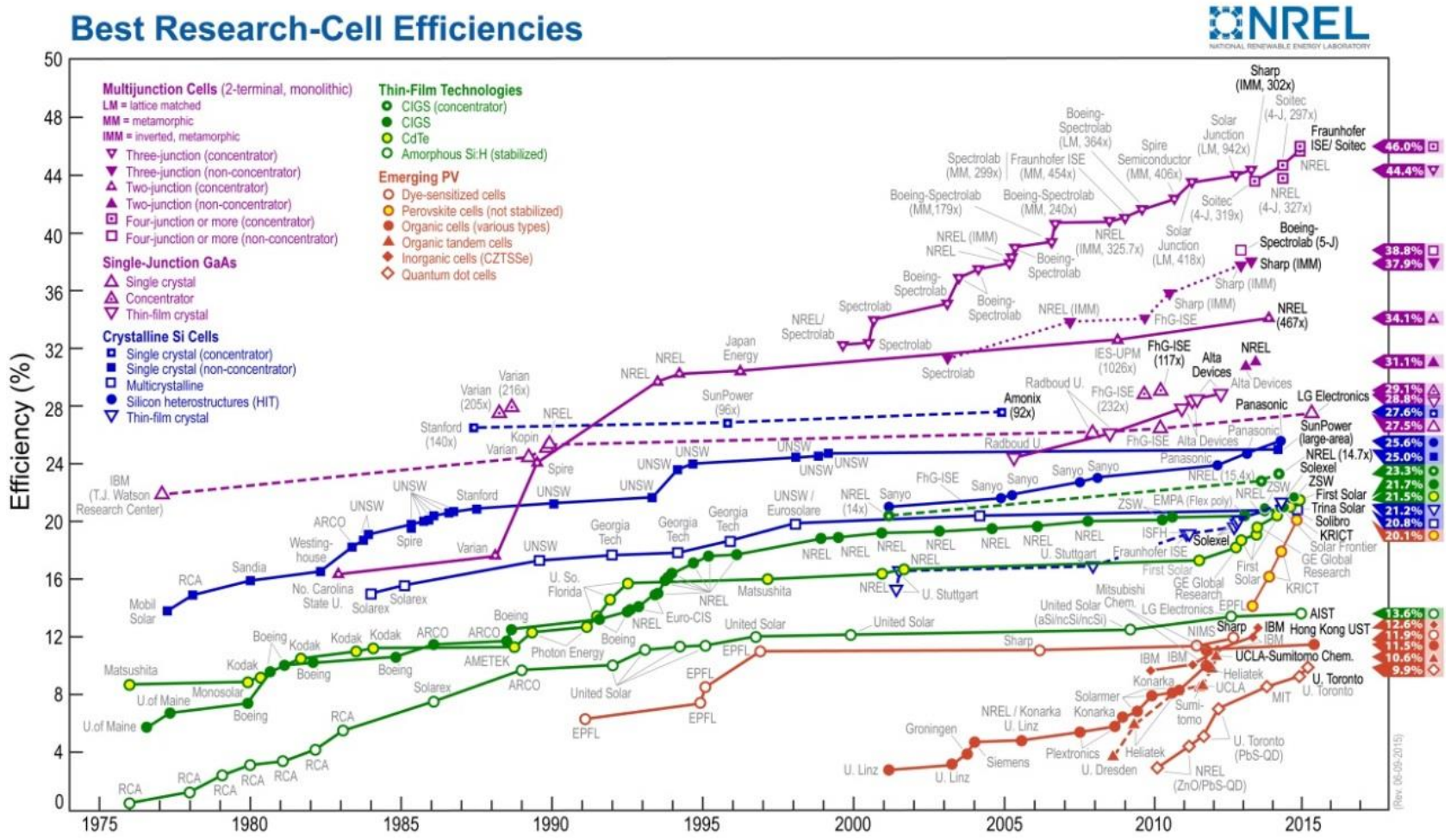

Figure 1.3: Record cell efficiencies from 1976 to the present for a range of photovoltaic technologies. This plot is courtesy of the National Renewable Energy Laboratory, Golden, CO [6].

1.2 InGaN Alloys for Photovoltaic Applications

1.2.1 Advantages of InGaN Alloys for Photovoltaic Applications

As *c*-Si solar cells are now approaching their theoretical maximum efficiency, alternative materials for high-efficiency photovoltaics need to be investigated. A promising candidate for high-efficiency solar cells is InGaN semiconductors [7, 8], which display a strong industrial manufacturing capability as well as highly-attractive inherent properties.

1.2.1.1 Strong Industrial Capabilities

Contrary to many emerging PV technologies, III-nitride solar cells are based on mature semiconductor technologies that are commercially used today. According to a recent report [9], the GaN semiconductor devices market was valued at ~US$380 million in 2012 and is expected to reach US$2 billion by 2019 as illustrated in Figure 1.4. The major GaN semiconductor products are the power semiconductors and optoelectronic semiconductors with various applications in the military, defense, aerospace, and consumer electronics sector. The development of GaN power devices such as Schottky diodes, field-effect transistors, and high-electron-mobility transistors is driven by the growing demand for high-speed, high-temperature, and power-handling capabilities. On the other hand, the development of nitride optoelectronic devices such as light-emitting diodes (LEDs) and lasers is expected to expand due to the growing market for solid state lighting. Thus, III-nitride solar cells benefit from the already-existing technological infrastructure for the growth and fabrication of nitride-based devices.

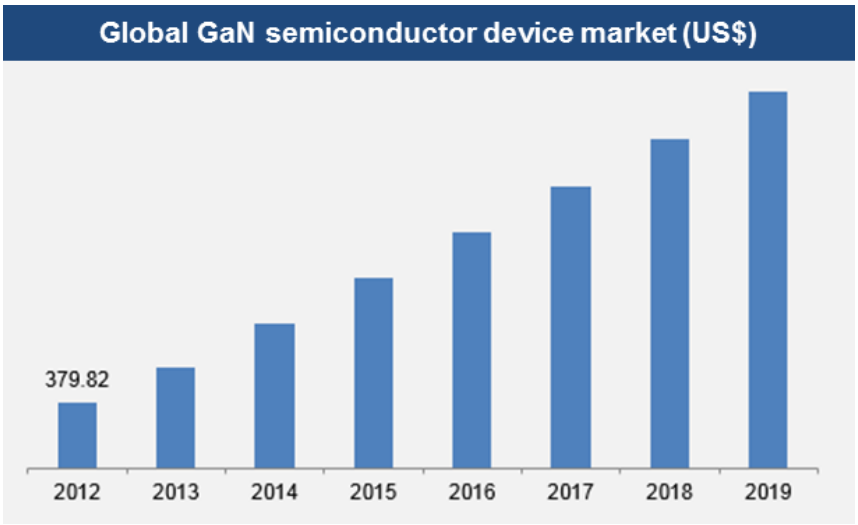

Figure 1.4: Global GaN semiconductor device market size and forecast, 2012-2019 [9].

1.2.1.2 Suitable Material Properties

In addition to the widely-available industrial manufacturing capability for III-nitride devices, InGaN alloys show unique inherent properties suitable for PV applications. The major advantage of the InGaN material system is its tunable band gap over the alloy composition ranging from 0.65 to 3.42 eV [10] and thus, covering the entire visible solar spectrum as shown in Figure 1.5. Because of this wide range of band gaps, InGaN alloys show considerable promise for high-efficiency multi-junction solar cells. Several InGaN subcells with adjusted In content can be stacked to form a full-spectrum-response solar cell based on a single-material system [11]. Another multi-junction design consists of an InGaN/Si tandem solar cell, which would benefit from the mature and low-cost silicon technology. Hsu *et al.* [12] proposed a two-junction solar cell comprised of an $In_{0.46}Ga_{0.54}N$ subcell (1.8 eV) on top of an Si subcell (1.1 eV). These band gaps are close to the most efficient combination predicted for two-junction solar cells [13]. In addition,

the conduction band of $In_{0.46}Ga_{0.54}N$ is aligned with the valence band of Si so that the *p*-Si/*n*-$In_{0.46}Ga_{0.54}N$ interface forms a low-resistance contact for the series connection of the two subcells [12]. An additional adequate property of InGaN alloys for PV applications is their high absorption coefficients (~10^5 cm^{-1}) [14, 15]. Thus, only a few hundred nanometers of InGaN material are required to absorb most of the incident light, thereby relieving the cost constraint due to moderately expensive indium. In contrast, several hundred microns of silicon are needed to absorb a large fraction of incident light [16]. Other suitable PV properties include a direct band gap over the entire alloy composition range, high carrier mobility [17], high drift velocity, and superior radiation resistance for space-based PV applications [18].

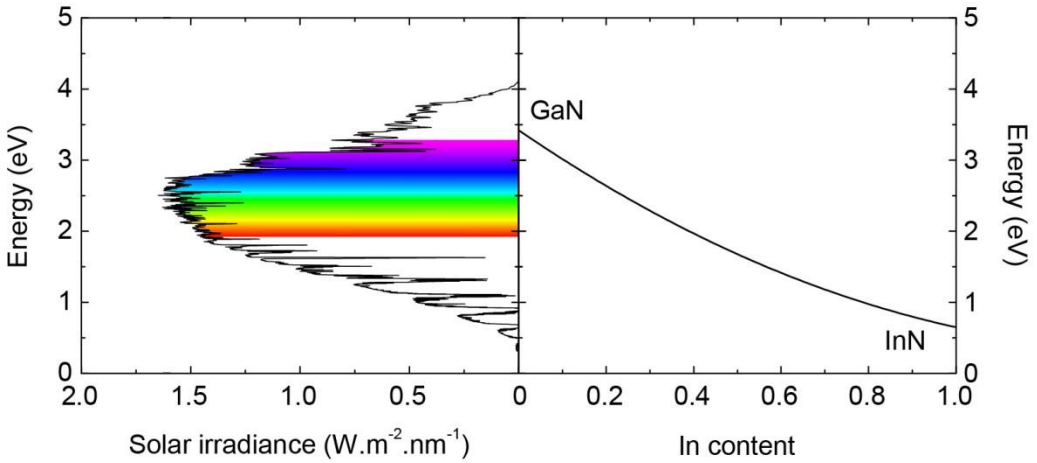

Figure 1.5: Solar irradiance (left) and the corresponding In content (right) as a function of energy. The band gap of InGaN ternary alloys spans the entire visible spectrum [10].

1.2.2 Challenges of InGaN Photovoltaics

Despite these suitable inherent properties for high-efficiency photovoltaics, InGaN alloys exhibit several challenges to such a goal. Recent experimental studies on InGaN-based solar cells have demonstrated conversion efficiency of less than 4% for both InGaN/GaN heterostructures [19-21] and *p*-*i*-*n* homojunction devices [22, 23]. The conversion efficiency of InGaN-based solar cells is limited by material issues including *p*-type doping, polarization effects, and crystal quality.

1.2.2.1 *P*-type Doping

A major issue is *p*-type doping in nitride alloys. Typical hole concentrations for *p*-type GaN and low-In-content InGaN are in the mid-10^{18} cm^{-3} range [24, 25]. The growth of highly *p*-type layers remains challenging as a result of limited solubility of acceptors, large activation energy of acceptors, and compensation by native defects. The solubility of magnesium (Mg), commonly used as a *p*-type dopant in III-nitrides, is limited by the formation of Mg_3N_2 [26] as illustrated in Figure 1.6. The competition between the formation of this precipitate and the incorporation of Mg on a Ga/In substitutional site moderates the *p*-doping efficiency. Recent efforts have partially overcome these thermodynamic limits by controlling the kinetics of Mg incorporation using a low substrate temperature and a specific growth procedure [27, 28]. These experimental studies have resulted in highly *p*-type III-nitride films with hole concentrations exceeding 7×10^{19} cm^{-3} [29], offering promise for future subcells and tunnel junctions.

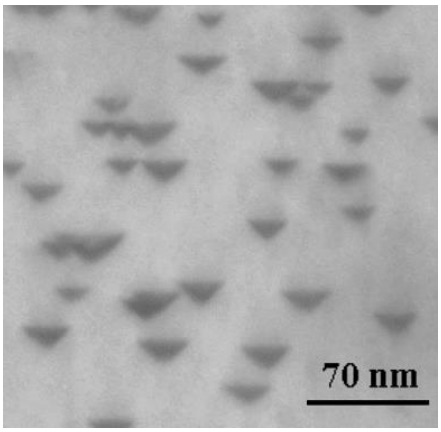

Figure 1.6: Cross-section TEM image showing pyramidal defects due to Mg precipitates [30].

P-type doping in III-nitrides is also hindered by the high thermal activation energy of the Mg-acceptor. Larger activation energy lowers the ionization efficiency of dopants, which leads to lower free carrier concentration. Previous studies have reported Mg activation energy of 140-220 meV in GaN, which yields poor ionization efficiency of 1-5% [31, 32]. The Mg-acceptor activation energy in *p*-InGaN is lower than that in *p*-GaN and decreases with increasing In composition [33, 34]. Another limitation to the development of reliable *p*-type layers arises from the formation of compensating native defects [26]. Such defects, commonly attributed to nitrogen vacancies associated with dislocations [35] or oxygen, hydrogen, and silicon impurities [36], act as donors that compensate acceptors. As a result, undoped GaN and InGaN films usually display a high background donor concentration. As the InN mole fraction increases, the residual electron concentration increases from 10^{16} cm^{-3} (GaN) to 10^{19} cm^{-3} (InN) [37]. This high concentration of background donors decreases the *p*-doping efficiency.

1.2.2.2 Polarization Effects

Other unique properties of III-nitrides that influence device performance are strong spontaneous and piezoelectric polarization effects [38]. Due to the non-centrosymmetry of their wurtzite structures and a large degree of ionicity between metal and nitrogen atoms, nitride semiconductors exhibit spontaneous polarization [39]. In addition, strained III-nitride materials display piezoelectric polarization. Figure 1.7 depicts the wurtzite crystal structure, spontaneous polarization field (P_{sp}), and piezoelectric polarization field (P_{pz}) in a III-polar InGaN layer. At an abrupt heterojunction interface, the discontinuity in spontaneous and piezoelectric polarization generates interface charges that produce strong band bending. In III-polar InGaN/GaN heterojunction solar cells, the polarization-induced electric field hinders carrier collection [40, 41].

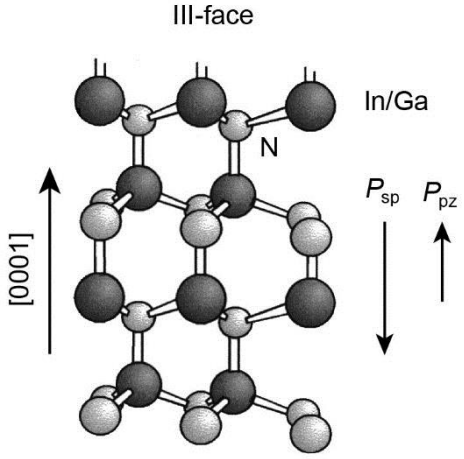

Figure 1.7: Wurtzite crystal structure, spontaneous polarization field (P_{sp}), and piezoelectric polarization field (P_{pz}) for InGaN coherently strained to GaN (0001) [42].

1.2.2.3 Crystal Quality

Another challenge to high-efficiency InGaN solar cells is the growth of thick, high-quality InGaN layers with high In content needed to absorb lower-energy photons. As a result of the miscibility gap between InN and GaN, In-rich InGaN films commonly display compositional fluctuation or complete phase separation as illustrated in Figure 1.8 [43]. However, advances in growth technology using control of surface kinetics have demonstrated the growth of high-In-content InGaN throughout the miscibility gap without phase separation [44, 45].

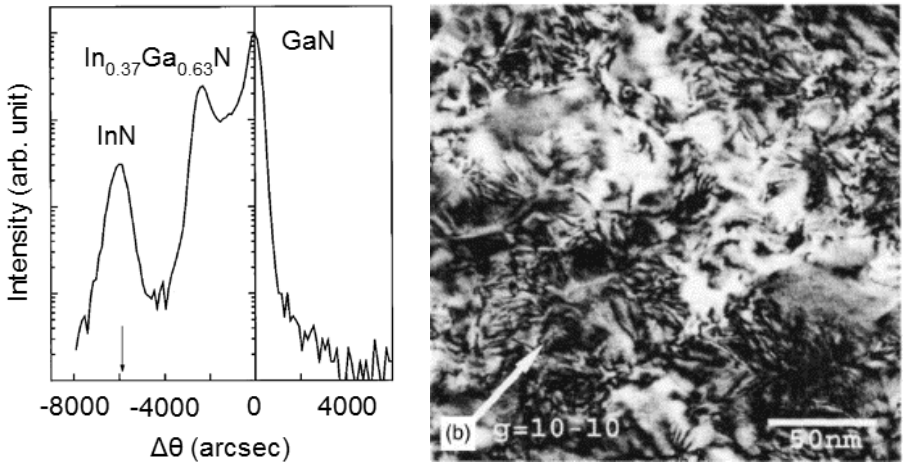

(a) (b)

Figure 1.8: (a) X-ray diffraction (XRD) data for $In_{0.37}Ga_{0.63}N$ showing phase-separated InN [15] and (b) dark-field plan view transmission electron microscopy (TEM) image of $In_{0.22}Ga_{0.78}N$ showing strong contrast variations indicative of a phase-separated microstructure [46].

A critical issue to the development of high-quality III-nitride films is the lack of a native substrate because of the wurtzite crystal structure of nitride semiconductors. The most widely used substrate for the growth of III-nitrides is sapphire. Because of the large

thermal and lattice mismatch between sapphire and nitride semiconductors, epitaxial films grown on sapphire usually result in a high density of threading dislocations, V-shaped defects, and stacking faults as illustrated in Figure 1.9. These crystalline defects can act as shunt pathways [47] that increase leakage current and non-radiative recombination centers [48] that degrade minority carrier lifetime. The high dislocation density can be moderated by growing a thick GaN buffer that will eliminate many defects [49]. This method allows for the growth of thin, low-In-content InGaN layers that are completely strained to the thick GaN buffer. However, the growth of InGaN films on GaN beyond a critical thickness will result in strain relaxation, creating more recombination centers. The critical thickness becomes smaller as the In composition increases due to larger lattice mismatch between GaN and InGaN. According to the energy balance model, the calculated critical thickness for In content higher than 30% is less than 2 nm [50], significantly limiting the absorption of light and thus, the performance of heterojunction solar cells. However, as the In fraction exceeds ~60%, InGaN films exhibit a significant improvement in the crystalline quality and optical properties due to uniform full lattice-mismatch strain relaxation through misfit dislocations [51].

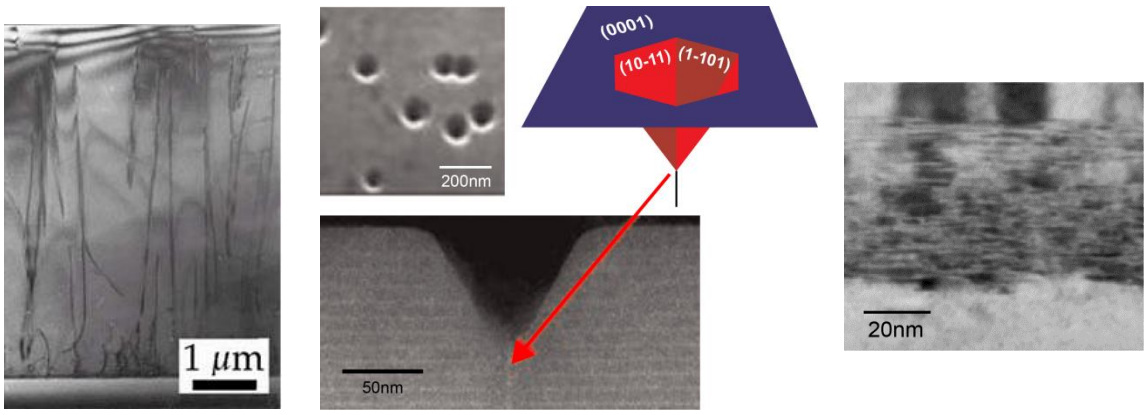

(a) (b) (c)

Figure 1.9: (a) Cross-section TEM image of GaN film grown on sapphire displaying threading dislocations [52], (b) planar scanning electron microscopy (SEM) view, cross-section TEM image, and schematic structure of a V-defect [53], and (c) cross-section TEM image of $In_{0.22}Ga_{0.78}N$ in which stacking faults appear as horizontal lines [51].

The high density of recombination centers in InGaN drastically reduces the carrier diffusion length, which is a critical parameter for solar-cell performance. Indeed, only the electron-hole pairs generated within a diffusion length from the depletion region are collected. The carriers generated in greater distances from the junction will recombine, causing the collection efficiency to drop. While the diffusion length of GaAs is within the range 10-50 μm [54], that of III-nitrides is typically 0.2-0.3 μm [55, 56]. Unlike conventional solar cells that rely on the diffusion process for the collection of minority carriers, InGaN solar cells must rely on a drift process by means of built-in fields to efficiently separate minority carriers. Such drift fields can be extended by inserting an intrinsic InGaN layer between the *n*- and *p*-type layers, forming a *p*-*i*-*n* junction [57]. The intrinsic layer sandwiched between the *n*- and *p*-doped layers serves as an absorbing layer. The photogenerated EHPs are separated and collected by the drift process enabled

by the built-in field across the intrinsic layer. The collection of photogenerated carriers greatly depends on the profile and the intensity of the internal electric field. Therefore, the thickness of the intrinsic layer is a critical parameter. The optimal thickness must account for the tradeoff between light absorption, which is higher in thicker layers, and carrier collection, which is higher in thinner layers. While intrinsic InGaN layers are essential for drift devices, the growth of such films is difficult since undoped-InGaN films commonly exhibits *n*-type conductivity resulting from a high residual donor concentration. This high concentration of background donors negatively affects the width of the depletion region.

Due to these challenges, the full potential of InGaN alloys for solar cell applications requires significant progress in the areas of crystal structure, impurity doping, formation of defects, heteroepitaxial growth, and the formation of homojunction and heterojunction structures.

1.3 Molecular Beam Epitaxy of InGaN Alloys

1.3.1 Molecular Beam Epitaxy

Growth of high-quality III-nitrides epitaxial layers has been achieved by a variety of methods. The most widely used techniques are metalorganic chemical vapor deposition (MOCVD) and molecular beam epitaxy (MBE). MOCVD uses metalorganic gases (*e.g.*, tri-methyl Ga, In, and Al) as group-III precursors and ammonia (NH_3) to supply active N. The constituent chemicals dissociate and chemically react at the substrate surface to grow the epitaxial film. The pyrolysis of these reactants requires an extremely high substrate temperature (900-1,100°C for GaN and 550-650°C for InN).

Unlike MOCVD that uses chemical reaction for crystal growth, MBE uses physical deposition to form an epitaxial film. In MBE, thermal beams of atoms or molecules collide on the surface of a crystalline substrate under ultra-high vacuum conditions (typically $<10^{-9}$ torr). Figure 1.10 depicts a typical MBE system. Each group-III metal source and dopant material is introduced through an effusion cell where solid material is placed in a crucible surrounded by a heating filament and heated until the material sublimates. Two nitrogen sources can be employed: NH_3, which is decomposed on the substrate surface by pyrolysis and molecular nitrogen (N_2), which is activated by radio-frequency (RF) plasma. MBE allows for the growth of epitaxial film with high purity and excellent crystal quality at relatively low temperatures (typically 600-750°C for GaN and 350-550°C for InN). Shutters placed in front of the sources permit a precise control of the epitaxial growth surface enabling abrupt interfaces required for multi-quantum well (MQW) and superlattice structures.

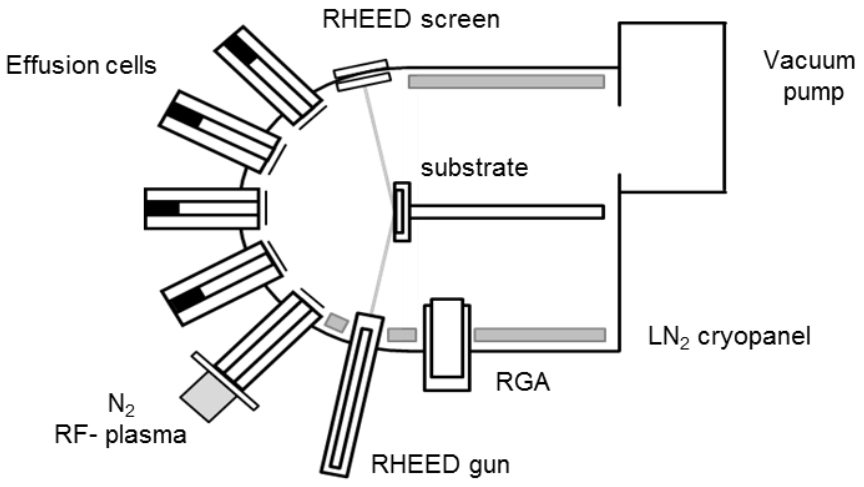

Figure 1.10: Schematic of an MBE system [58].

The extremely-low pressure used in MBE enables the real-time study of the surface, interface, and bulk properties using *in-situ* characterization techniques such as residual-gas analysis (RGA) and reflection high-energy electron diffraction (RHEED). RGA is a mass spectrometer typically used for vacuum leak check, contamination monitoring, and desorption mass spectroscopy to study surface kinetics. RHEED consists of a collimated electron beam produced by a RHEED gun and directed at a glancing angle towards the substrate surface, which diffracts the electrons. The resulting diffraction pattern, which depends on the crystalline structure of the surface, is formed on a fluorescent screen. RHEED is suited for real-time monitoring of thin-film deposition since none of the equipment intrudes into the experimental growth region. Because of electron scattering by matter, the electron-beam penetration depth is limited to a few atomic layers making RHEED a surface sensitive technique [59, 60]. RHEED is usually used to study thermal desorption of oxides prior to growth, to control the initial stages of epitaxial growth, to study surface reconstruction, and to examine surface topography.

The RHEED pattern observed on the screen can be derived from the reciprocal lattice structure in the approximation of limited penetration [59]. The RHEED pattern from a smooth single-crystalline surface is expected to display long streaks running perpendicular to the surface of the crystal, which is consistent with a two-dimensional (2D) diffraction. On the other hand, the RHEED pattern from a rough surface is expected to be spotty, since the penetration of electrons through surface asperities results in a three-dimensional diffraction (3D) [60]. RHEED is also used to study reconstruction of surface to different configurations in order to lower its free energy. Since surface

reconstruction leads to a lower symmetry than that of the bulk crystal, extra diffraction lines are observed in the RHEED pattern.

In addition to qualitative analyses of the surface via the diffraction patterns, RHEED can also provide quantitative measures such as surface composition and growth rate. Figure 1.11 illustrates the correlation between surface coverage and RHEED intensity in the two-dimensional growth of thin films. The time dependence of the diffraction-pattern intensity can be used to extract the growth rate in real time. Oscillations of the RHEED intensity (RHEED transients) are associated with constructive and destructive interference by electrons scattered from adjacent terraces on the surface of the growing film [61, 62].

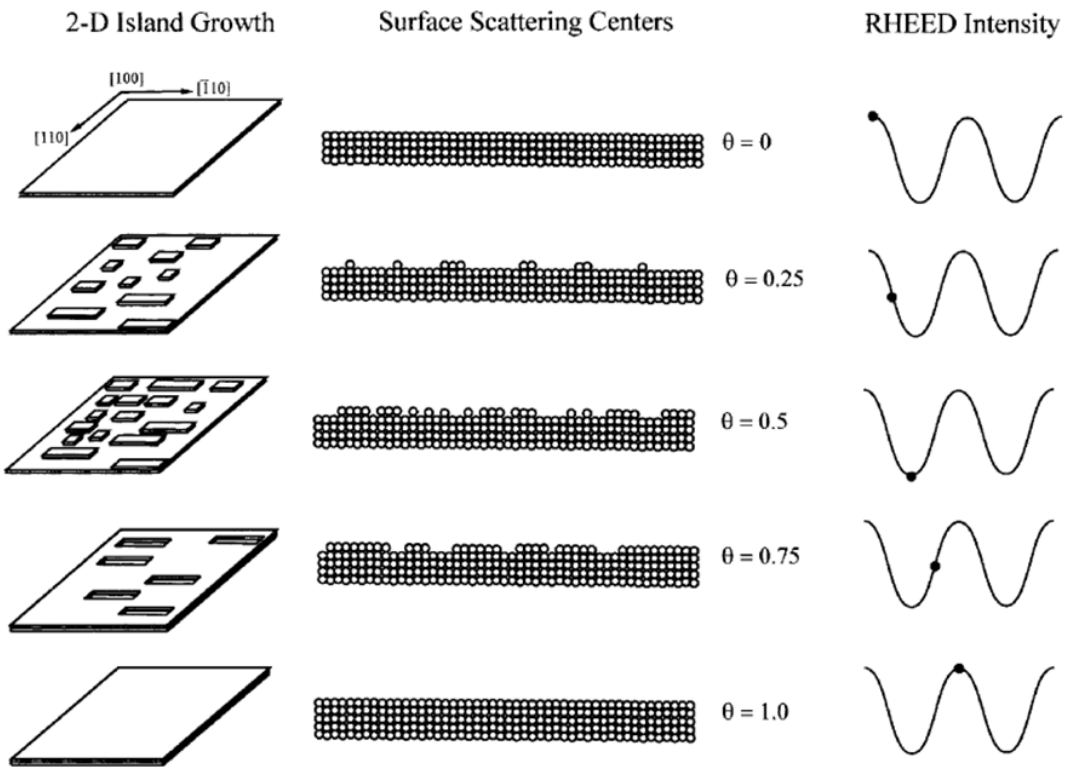

Figure 1.11: Schematic diagram of the correlation of surface coverage and RHEED oscillations in 2D growth [63].

1.3.2 MBE Growth Regimes of InGaN Alloys

The epitaxial growth of InGaN over the entire composition range faces many challenges such as (i) the lack of appropriate substrates, which leads to dislocation formation [64], (ii) the control of In incorporation, which depends on the growth chemistry and temperature [65], and (iii) the miscibility gap between InN and GaN, which results in phase separation [15]. Since InN has a low dissociation temperature, the preferred growth technique for InN and In-rich InGaN growth is MBE. For the growth of InGaN epilayers by MBE, a precise control and optimization of the III/N ratio and the growth temperature is required to obtain single-phase, high-quality InGaN films. The growth of InGaN by MBE follows the growth diagram depicted in Figure 1.12. The diagram reveals three growth regimes: nitrogen-rich (N-rich), metal-rich (M-rich), and intermediate M-rich [66-68]. The growth modes depend on the growth temperature and the impinging metal flux. The boundaries between the growth regimes are defined by In desorption and InN decomposition.

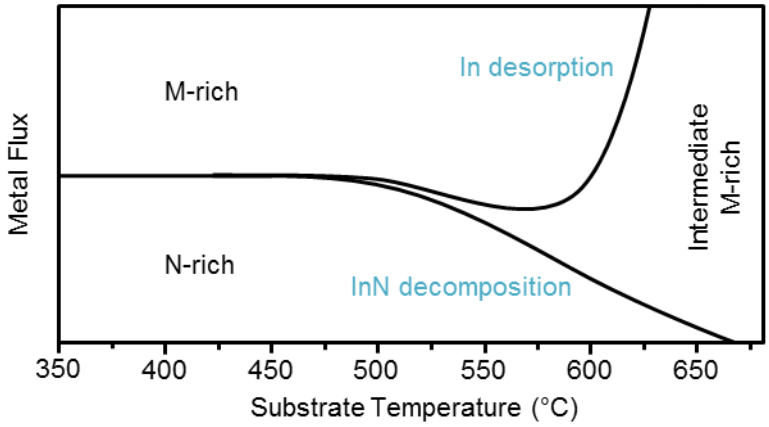

Figure 1.12: InGaN MBE growth diagram revealing three growth regimes as a function of growth temperature and impinging metal flux [66].

The growth of single-phase InGaN by MBE has been previously reported using various approaches [66, 69-71]. M-rich growth favors a 2D growth mode, which promotes smoother surfaces as depicted in Figure 1.13(a) but results in compositional alloy fluctuations and metal droplets as illustrated in Figure 1.14(a) and (b), respectively [69, 70]. On the other hand, N-rich growth leads to more uniform InGaN alloys (Figure 1.14(a)) but reduces surface adatom mobility, resulting in 3D growth mode and grain-like morphology as shown in Figure 1.13(b) [66, 70, 71]. Intermediate M-rich growth typically results in high density of surface pits due to an incomplete metal adlayer formation as demonstrated in Figure 1.13(c) [66, 67, 72]. The structural and optical properties of InGaN films also strongly depend on growth temperature [73]. An optimized growth temperature must account for a tradeoff between enhanced compositional homogeneity and In incorporation at low temperatures and improved surface morphology and threading dislocation density at high temperatures.

In order to take advantage of both M-rich and N-rich conditions, several modulated growth methods have been studied [74, 75]. Metal-modulated epitaxy (MME) is a modified form of MBE in which the metal shutters are modulated with a fixed duty cycle while a constant nitrogen flux is maintained. MME alternates between N-rich and M-rich growth regimes by employing a M-rich group-III flux, but periodically opening and closing the metal shutters. A metal adlayer builds up while the metal shutters are open and is consumed into the film while the metal shutters are closed. This modulated technique has enabled the growth of single-phase InGaN epilayers throughout the miscibility gap [44, 45] with an improvement in the structural and optical quality for In

content higher than 60% [51]. However, the moderate-In-content films (22-46% InGaN) display a high density of defects that annihilate the optical properties of the films.

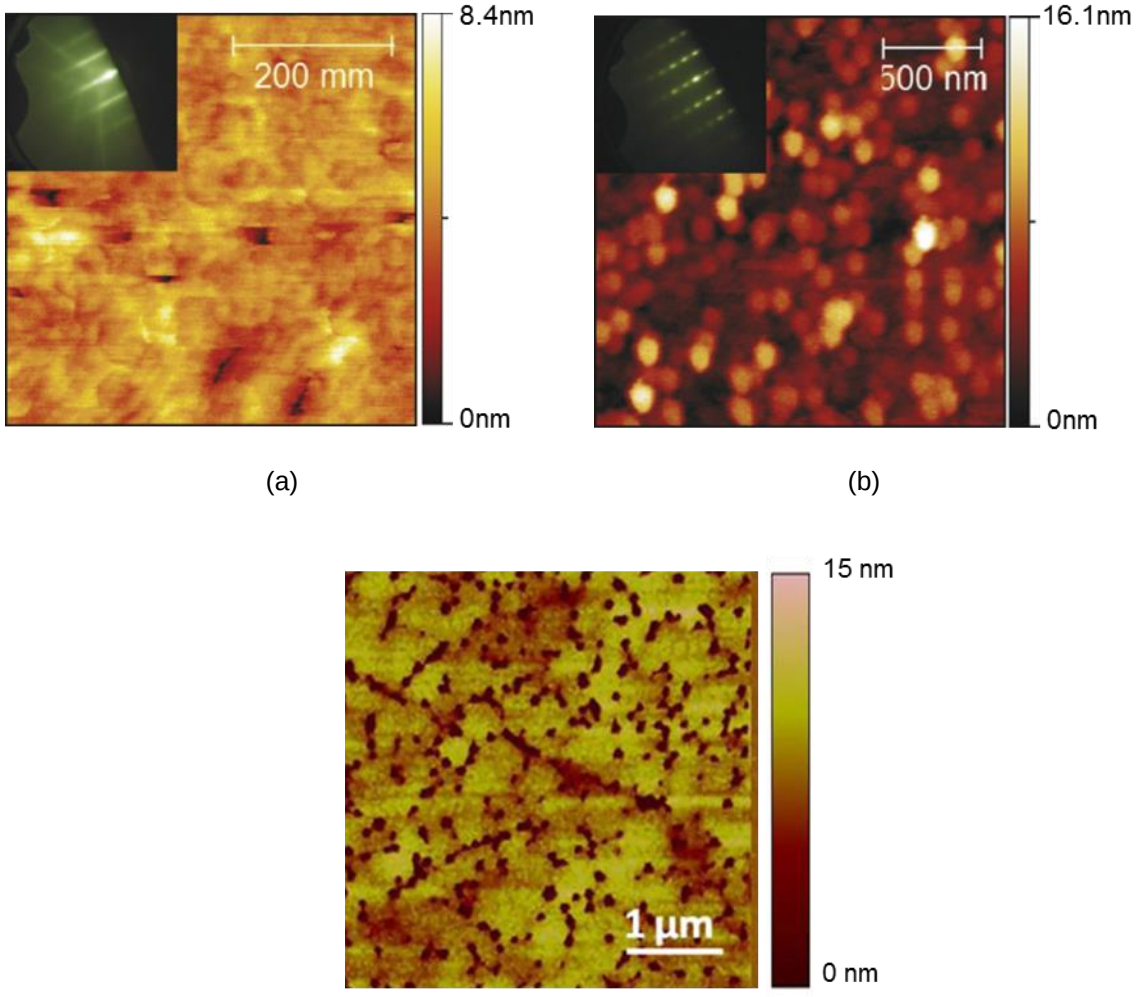

Figure 1.13: AFM image of an InGaN surface grown under (a) M-rich conditions showing a 2D growth mode [71], (b) N-rich conditions showing a 3D growth mode [71], and (c) intermediate M-rich conditions showing surface pits [66].

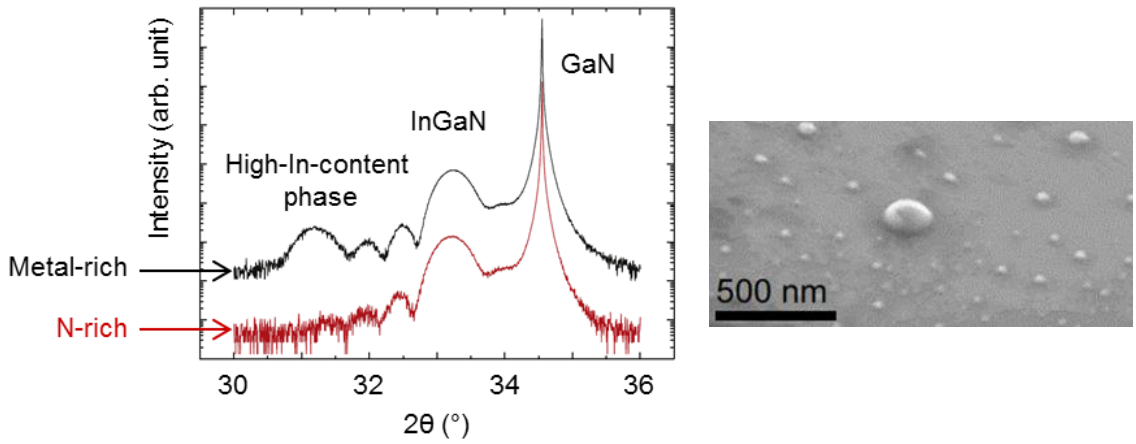

(a) (b)

Figure 1.14: (a) 2θ-ω scans of InGaN films grown under M-rich conditions showing additional peak indicating phase separation and N-rich conditions showing no phase separation [71]. (b) SEM image of an InGaN surface grown under M-rich conditions showing metal droplet accumulation at the growth front [76].

1.4 Objectives and Scope of the Dissertation

Despite the tremendous potential of InGaN alloys for PV applications, major progress needs to be achieved to overcome challenges related to practical implementation. The objective of the proposed research is to realize advances in design optimization and growth technology for high-efficiency InGaN-based PV. To evaluate the viability of InGaN alloys for PV applications, research in the areas of simulation, growth, and fabrication of InGaN-based solar cells has been conducted. The research objectives and accomplishments presented in this dissertation are described in detail in the following chapters.

Chapter 2 presents numerical simulations of InGaN *p-i-n* single-junction solar cells to provide guidelines for performance improvement through optimization of device structures given achievable material characteristics. The performance of both

InGaN/GaN heterojunction devices that are presently achievable and InGaN homojunction solar cells that should be feasible in the future are investigated.

Chapter 3 discusses the growth of single-phase InGaN films over the entire composition range by plasma-assisted MBE. High-quality single-phase InGaN films are needed as absorbing layers to produce photogenerated carriers. The surface morphology, microstructural, and optical properties of these films grown under low growth temperatures and slightly N-rich growth conditions are analyzed.

Chapter 4 examines the growth of doped III-nitride films that are required to separate and collect the photogenerated carriers. The MME-growth conditions and properties of *n*- and *p*-type GaN layers are presented to provide calibration for subsequent fabricated cells. The growth of *p*-InGaN films, required for homojunction structures, is investigated by N-rich MBE and MME.

Chapter 5 reviews various aspects needed for the fabrication of InGaN-based solar cells. A device processing sequence and a designed mask layout are presented. Metal contacts for both *n*- and *p*-type layers and optimization of the metallization grid pattern are also discussed.

Chapter 6 analyzes the growth, fabrication, and testing of InGaN/GaN double-heterojunction solar cells that employ the improved growth technology and the developed fabrication process.

Chapter 7 describes a hybrid MBE technique for thick InGaN layers. This novel growth method provides a pathway for homojunction cells that are identified by simulation and experimental results as the only viable structure for high-efficiency InGaN-based photovoltaics.

Chapter 8 investigates an advanced InGaN solar cell design based on InGaN quantum dots. Two methods to form InGaN quantum dots are described: *ex-situ* formation by electron-beam lithography and *in-situ* MBE growth. An attempt at InGaN quantum-dot intermediate-band solar cells was made.

Chapter 9 summarizes the work presented in this dissertation and presents recommendations for future work.

Included in this dissertation are five appendices. In Appendix A, the theory of X-ray diffraction of InGaN alloys is described. A fabrication process flow including the apparatus, the processing recipes, and the process flow, is given in Appendix B. Appendix C details the equations used to calculate and optimize the finger spacing for the top metallization pattern. Finally, the characteristics and performance of InGaN/GaN double-heterojunction solar cells reported in the literature are listed in Appendix D. Appendix E provides a MATLAB script required to control the source shutters independently.

CHAPTER 2

SIMULATIONS OF InGaN-BASED SOLAR CELLS

While previous simulations have already investigated the PV characteristics of InGaN-based *p*-*i*-*n* solar cells, few studies focused on optimizing the structure design. Chang *et al*. [41] demonstrated that appropriate band-engineered InGaN *p*-*i*-*n* solar-cell structures can efficiently moderate the detrimental polarization effects and achieve a conversion efficiency of ~14%. This study also investigated the influence of In composition on the device performance, but did not consider other material and structure parameters. Feng *et al*. [77] conducted numerical simulations to determine the effects of In content, thickness, and defect density of the intrinsic InGaN layer on the performance of homojunction solar cells. However, these simulations omitted major material limitations and growth issues such as appropriate *p*-type doping, background doping, and growth of thick InGaN. For this reason, the optimized structure proposed in [77] and exhibiting a conversion efficiency of 23% is not currently achievable. In the present work, the effect of In content, thickness, and background donor concentration of the InGaN absorbing layer on the performance of InGaN-based *p*-*i*-*n* solar cells are investigated. To improve the performance of InGaN-based solar cells, modified structures with suitable band engineering are also presented. These numerical simulations aim to provide guidelines for optimizing device design given specific material characteristics and present and future material limitations.

2.1 Simulation Parameters

In this study, the performance of *p-i-n* solar cells are investigated with the finite element analysis software APSYS [78]. The electrical and optical properties of GaN and InN used in the simulations are listed in Table 2.1. The references for the parameters can be found elsewhere [79]. The unstrained band gap of InGaN is expressed by

$$E_g(In_xGa_{1-x}N) = E_{g,InN}\,x + E_{g,GaN}(1-x) - b\,x(1-x), \tag{2.1}$$

where $E_{g,\,InN}$ = 0.65 eV and $E_{g,\,GaN}$ = 3.42 eV are the band gap energies of InN and GaN, respectively and b = 1.43 eV is the bowing parameter for $In_xGa_{1-x}N$ [80]. The electron and hole mobilities, μ_e and μ_h, respectively, are calculated using the Caughey-Thomas approximation [81] and can be expressed as

$$\mu_{e,h} = \mu_{min} + \frac{(\mu_{max} - \mu_{min})}{1 + \left(\frac{N}{N_g}\right)^{\gamma}}, \tag{2.2}$$

where N is the doping concentration and μ_{min}, μ_{max}, and γ are parameters specific to a given semiconductor [81]. The alloy mobility is calculated using a linear interpolation between the GaN and InN values. This approach does not take into account the influence of alloy disorder scattering, which reduces electron and hole mobilities. Minority carrier lifetimes of 5.4 ns and 6.5 ns have been measured in GaN and InN, respectively [82, 83]. However, $In_xGa_{1-x}N$ alloys are expected to have lower lifetimes due to inferior crystal quality. Thus, a conservative 1 ns minority carrier lifetime is used over the entire $In_xGa_{1-x}N$ composition. Shockley-Read-Hall and Auger recombination are included. A fixed Auger coefficient of $1.4\text{x}10^{-30}$ cm^6/s is used for electrons and holes [84]. The

simulations also account for surface recombination losses at various heterointerfaces. According to experimental measurements [85-87], a front surface recombination velocity of 10^4 cm/s is used. The bottom and top contacts are assumed to be ohmic and the electrode coverage is 5%. The absorption coefficient for each layer can be calculated by

$$\alpha(E) = 10^5 \times \sqrt{a(E - E_g) + b(E - E_g)^2}, \tag{2.3}$$

where E is the incoming photon energy and a and b are fitting parameters from experimental data [80, 88].

Table 2.1: Parameters of GaN and InN used in the simulations.

Parameter	**GaN**	**InN**
Band gap E_g (eV)	3.42	0.65
Dielectric constant $\varepsilon_s/\varepsilon_0$	8.9	10.5
Electron mass m_e/m_0	0.2	0.05
Hole mass m_h/m_0	1.25	0.6
Electron affinity E_a (eV)	4	5.6
Electron lifetime τ_e (ns)	1	1
Hole lifetime τ_h (ns)	1	1
$\mu_{min,\,e}$ ($cm^2/V{\cdot}s$)	55	30
$\mu_{max,\,e}$ ($cm^2/V{\cdot}s$)	1000	1100
γ_e	1	1
$N_{g,\,e}$ (cm^{-3})	2×10^{17}	8×10^{18}
$\mu_{min,\,h}$ ($cm^2/V{\cdot}s$)	3	3
$\mu_{max,\,h}$ ($cm^2/V{\cdot}s$)	170	340
γ_h	2	2
$N_{g,\,h}$ (cm^{-3})	3×10^{17}	3×10^{17}

Table 2.2 lists the fitting parameters used for the InGaN layers with various In compositions. In addition, the devices are under a one-sun AM1.5 illumination. Front surface reflection and light trapping effects are not included. Finally, the nonlinear equations developed by Fiorentini *et al.* [89] are used to determine the spontaneous and piezoelectric polarization. Previous experimental studies indicate lower polarization charge density than theoretically predicted [90, 91]. The difference between the theoretical and experimental values is attributed to partial compensation of the polarization by free carriers, fixed doping charges [92], and In segregation [93]. To account for these screening effects, the theoretical polarization is scaled by a factor of 0.4 in agreement with previous studies [40, 90].

Table 2.2: Fitting parameters used to calculate the absorption coefficients.

In composition	***a***	***b***
0	3.52517	-0.657999
0.25	2.02095	-0.094817
0.50	0.51672	0.468365
0.75	0.61831	0.677523
1	0.69642	0.460553

Conventional InGaN-based solar cells consist of a *p*-*i*-*n* double GaN heterojunction design [19-21]. This structure possesses an intrinsic InGaN absorbing layer inserted between *p*- and *n*-type GaN layers. Previous numerical simulations demonstrated that polarization effects arising from the presence of heterointerfaces have a detrimental impact on the performance of the conventional III-polar *n*-GaN/*i*-InGaN/

p-GaN solar cell [40, 41, 94]. The conversion efficiency drops because of two main factors. First, polarization charges create an electric field in the opposite direction to that of the built-in field, which is required for carrier drift. This polarization-induced field strongly affects band bending in the depletion region. The total electric field decreases, thereby reducing carrier collection efficiency. Second, polarization discontinuity creates potential barriers at the heterointerfaces, impeding carrier collection. For high-In-composition InGaN layers that are needed for longer wavelength absorption, the conversion efficiency dramatically declines as a result of polarization effects. For these reasons, the present study focuses on asymmetric InGaN/GaN heterojunction and InGaN homojunction devices.

2.2 Simulation Results and Discussion

2.2.1 InGaN/GaN Heterojunction Structure

To address this polarization issue, we investigate the photovoltaic characteristics of asymmetric heterojunction designs based on an *n*-GaN/*i*-$In_xGa_{1-x}N$/*p*-$In_{0.25}Ga_{0.75}N$ structure. The *p*-GaN layer in the conventional double GaN heterostructure has been replaced by a *p*-$In_{0.25}Ga_{0.75}N$ layer that moderates the polarization effects. In addition, *p*-InGaN exhibits several advantages over *p*-GaN including lower Mg activation energy [33] and lower etching damage resulting in lower contact resistance [34]. While *p*-type InGaN layers with In composition as high as 35% have been previously reported [33], $In_{0.25}Ga_{0.75}N$ was selected as the highest In composition that can consistently be doped *p*-type. Figure 2.1 depicts the 100 μm-wide *p-i-n* structure, which comprises a 1 μm-thick *n*-GaN layer, an unintentionally-doped (*UID*) $In_xGa_{1-x}N$ layer, and a 50 nm-thick

p-$In_{0.25}Ga_{0.75}N$ top layer. The thickness of the *p*-doped layer is limited to 50 nm to maximize absorption in the intrinsic region. The electron and hole concentrations in the *n*-GaN and *p*-InGaN layers are ~8×10^{18} cm^{-3} and ~4×10^{18} cm^{-3}, respectively. Similar hole concentrations in Mg-doped $In_{0.25}Ga_{0.75}N$ have already been experimentally achieved [33]. Thus, such devices are presently realizable using state-of-the-art nitride technology [19, 20].

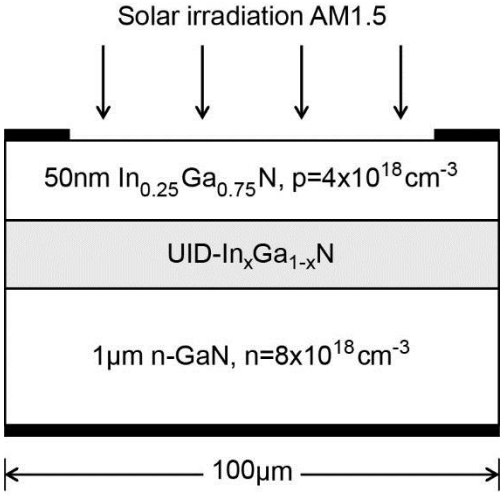

Figure 2.1: Schematic structure of an *n*-GaN/*UID*-$In_xGa_{1-x}N$/*p*-$In_{0.25}Ga_{0.75}$ heterojunction solar cell.

Figure 2.2 shows the energy-band diagrams and the corresponding *J*-*V* curves for an *n*-GaN/*UID*-$In_{0.25}Ga_{0.75}N$/*p*-$In_{0.25}Ga_{0.75}N$ solar cell structure with various *UID*-InGaN thicknesses and residual donor concentrations. As expected, no potential barriers are visible at the *UID*-InGaN/*p*-InGaN homointerface. However, the influence of

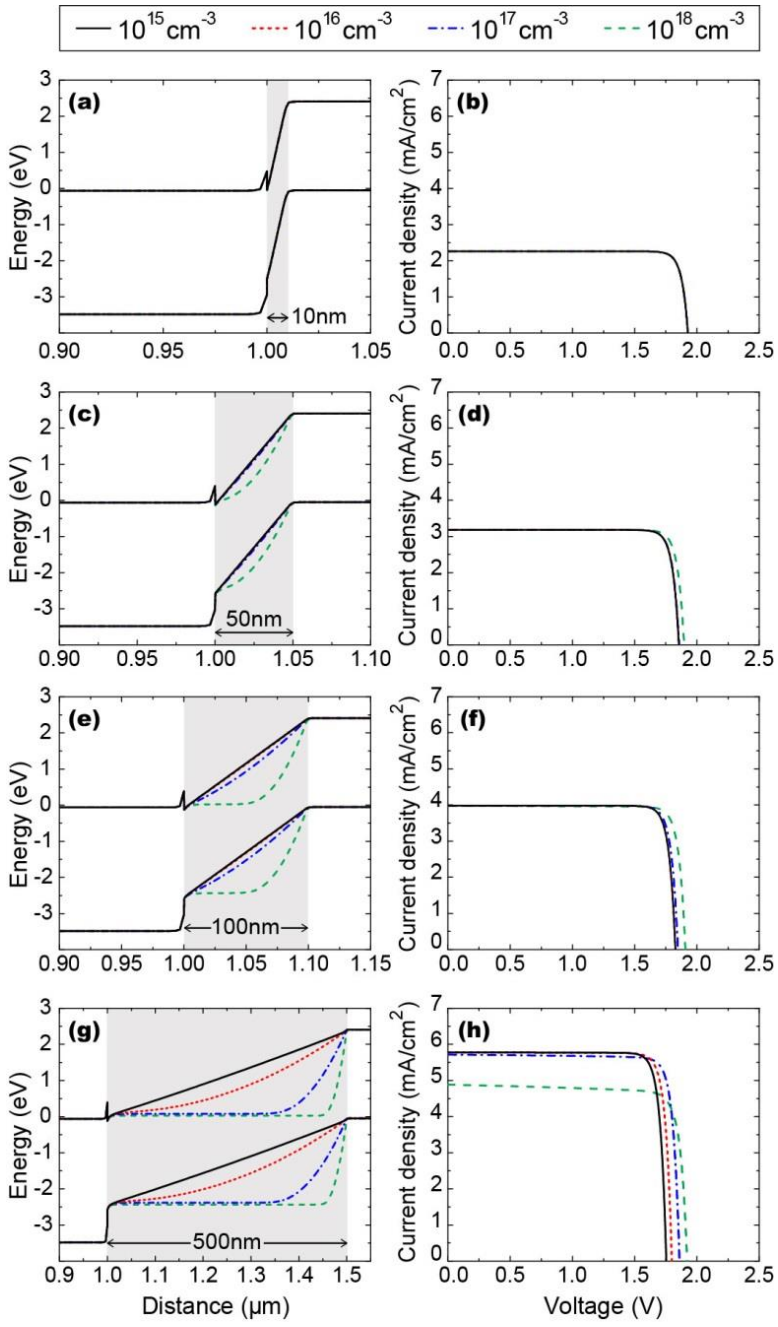

Figure 2.2: (a), (c), (e), (g) Energy-band diagrams at equilibrium for an *n*-GaN/*UID*-$In_{0.25}Ga_{0.75}N$/*p*-$In_{0.25}Ga_{0.75}N$ structure with various *UID*-InGaN thicknesses: 10 nm, 50 nm, 100 nm, and 500 nm, respectively. (b), (d), (f), (h) Corresponding *J*-*V* characteristics under AM1.5 illumination. The depletion width is affected by the thickness and the doping of the *UID*-layer.

polarization-induced charges still remains at the *n*-GaN/*UID*-InGaN heterointerface. The depletion width is affected by the thickness and the doping of the *UID*-layer. As the thickness of the *UID*-InGaN layer increases, the depletion region widens. For a 10 nm InGaN layer (Figure 2.2(a)-(b)), the background doping has a negligible impact on the band diagram and the *J*-*V* curve. However, for thicker *UID*-InGaN films (Figure 2.2(c)-(h)), the depletion region narrows as the background donor concentration increases.

Figure 2.3 shows the short-circuit current density (J_{sc}), the open-circuit voltage (V_{oc}), and the conversion efficiency (η) as a function of the thickness of the *UID*-InGaN layer with various residual donor concentrations. J_{sc} increases as the thickness increases, but decreases as the residual donor concentration increases. As the thickness of the *UID*-InGaN layer increases, the *UID*-InGaN layer can absorb more photons, resulting in increased photogenerated current. However, as the residual donor concentration increases, the collection efficiency drops due to narrower depletion width, leading to reduced photogenerated current. Contrary to J_{sc}, V_{oc} slightly decreases as the thickness increases, but it rises as the residual donor concentration increases. V_{oc} can be expressed as

$$V_{oc} = \frac{nkT}{q} \times ln\left(\frac{J_{sc}}{J_0} + 1\right), \tag{2.4}$$

where q is the elementary charge, k is the Boltzmann constant, n is the ideality factor, and J_0 is the saturation current. For a *p*-*i*-*n* solar cell, the Sah-Noyce-Shockley approximation is valid [77, 95] and J_0 can be expressed as

$$J_0 = \frac{qn_iW}{\sqrt{\tau_e\tau_h}}, \tag{2.5}$$

where n_i is the intrinsic carrier concentration, τ_e and τ_h are the electrons and holes lifetimes, respectively, and W is the width of the depletion region. Higher background doping in the *UID*-layer leads to narrower depletion width, and thus, smaller saturation current. As a result, V_{oc} increases in cells with higher background donor concentration. On the other hand, V_{oc} decreases in thicker cells due to larger saturation current density J_0.

The conversion efficiency η represents the combined effects of J_{sc} and V_{oc}. The efficiency improves as the thickness of the *UID*-InGaN layer increases. This enhancement in efficiency mainly results from the increase in J_{sc} because of the weaker influence of thickness on V_{oc}. Since doping only slightly influences J_{sc} at lower background donor concentrations, the efficiency demonstrates no significant variation for doping ranging from 10^{15} cm^{-3} to 10^{17} cm^{-3}. A background donor concentration of 10^{17} cm^{-3} slightly improves the performance of the solar cell due to improvement in V_{oc} for higher doping. However, the efficiency drastically declines as the background donor concentration reaches 10^{18} cm^{-3} for thicknesses higher than 200 nm due to decreased collection efficiency. Because of the relatively high band gap of $In_{0.25}Ga_{0.75}N$ (2.46 eV), the conversion efficiency of *n*-GaN/*UID*-$In_{0.25}Ga_{0.75}N$/*p*-$In_{0.25}Ga_{0.75}N$ devices is limited to 9.7%. To improve the conversion efficiency, InGaN absorbing layers with higher In contents need to be considered.

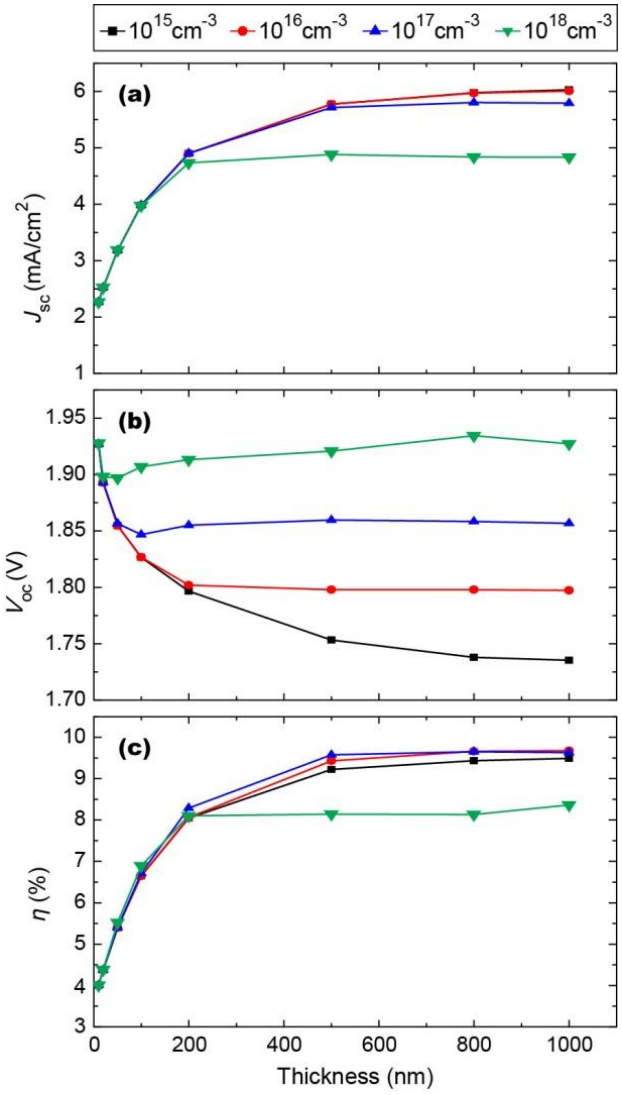

Figure 2.3: (a) Short-circuit current density J_{sc}, (b) open-circuit voltage V_{oc}, and (c) conversion efficiency η as a function of the *UID*-layer thickness for an *n*-GaN/*UID*-$In_{0.25}Ga_{0.75}N$/*p*-$In_{0.25}Ga_{0.75}N$ solar cell with various concentrations of background donors.

To determine the effect of the composition on the performance of *n*-GaN/ *UID*-$In_xGa_{1-x}N$/*p*-$In_{0.25}Ga_{0.75}N$ solar cells, In mole fractions ranging from 25% to 75% of the *UID*-$In_xGa_{1-x}N$ layer are considered. In this study, the In composition of the *p*-type layer remains 25% since the growth of *p*-doped InGaN with higher In fraction is presently extremely challenging. The thickness and the residual donor concentration of the *UID*-$In_xGa_{1-x}N$ are 500 nm and 1×10^{17} cm^{-3}, respectively. These values were selected from the previous section as the currently achievable metrics yielding maximum efficiency. Figure 2.4 shows the conversion efficiency as a function of the In composition. Efficiency initially increases due to increased photocurrent resulting from the reduced band gap of the InGaN absorbing layer, as shown by the band diagrams in Figure 2.5(a) for three cells with various In composition of the *UID*-layer: 25%, 50%, and 75% In. Figure 2.5(b) displays the optical generation rate for the structures with various In compositions of the *UID*-layer.

The generation rate is significantly enhanced in InGaN layers with larger In contents, leading to higher photocurrent and, thus, greater conversion efficiency. However, for In compositions higher than 30%, the efficiency decreases because of two polarization effects [40, 96]. First, the polarization discontinuity creates a potential barrier at the GaN/InGaN heterointerface as illustrated in Figure 2.5(a). As the In composition increases, this polarization-induced potential barrier becomes more prominent (Figure 2.5(a) inset). The barrier height in the conduction band between the *n*-GaN and the *UID*-$In_xGa_{1-x}N$ layers increases from 0.48 eV for x = 25%, 0.98 eV for x = 50%, to 2.33 eV for x = 75%. Second, the polarization-induced field that opposes drift transport increases.

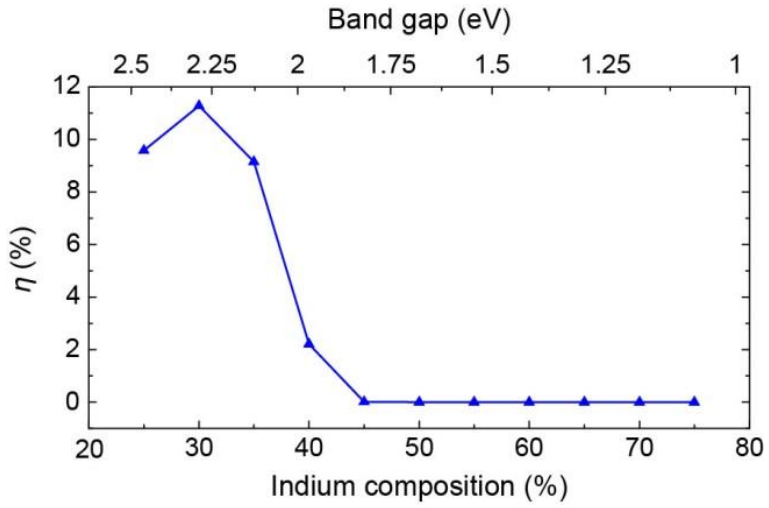

Figure 2.4: Conversion efficiency η of an *n*-GaN/*UID*-$In_xGa_{1-x}N$/*p*-$In_{0.25}Ga_{0.75}N$ structure as a function of the In composition (*i.e.* band gap) in the *UID*-InGaN layer. The efficiency is limited to 11.3% because of polarization effects.

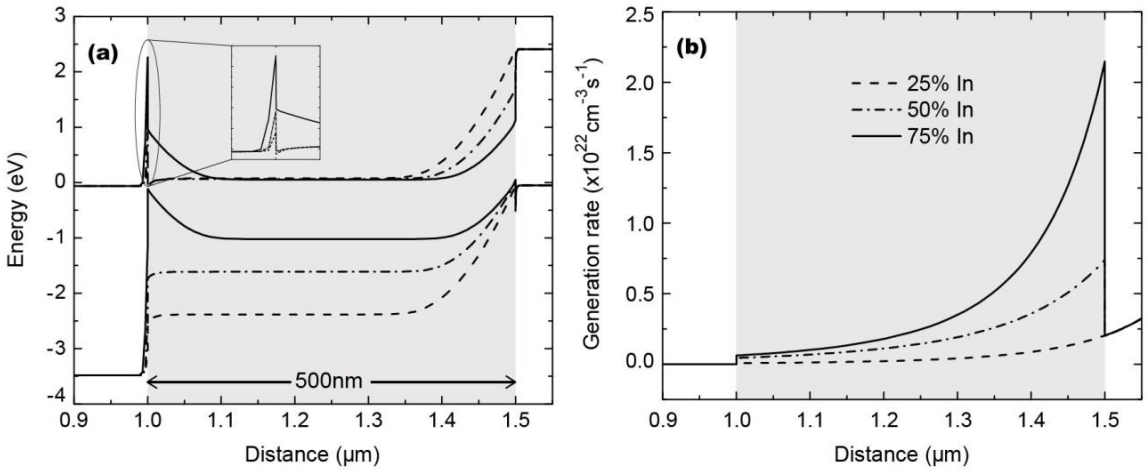

Figure 2.5: (a) Band diagrams at equilibrium and (b) optical carrier generation rates for an *n*-GaN/*UID*-$In_xGa_{1-x}N$/*p*-$In_{0.25}Ga_{0.75}N$ structure with various In compositions in the *UID*-layer. While the generation rate is enhanced for InGaN layers with higher In content, the polarization effects hinder the collection of photogenerated carriers. The inset shows a close-up view of the potential barriers at the GaN/InGaN interface.

The impact of these polarization effects on the *J-V* curves of the cells for In compositions ranging from of 30% to 45% is shown in Figure 2.6. The knee in the *J-V* curves, observed for In compositions of 35% and 40%, results from the abrupt drop in the current density as the forward bias increases due to reduction in the total electric field in the *UID*-InGaN layer. As the applied voltage increases, the energy band of the InGaN layer flattens, therefore hindering carrier separation and enhancing recombination in the InGaN layer. For an In composition of 40%, the conversion efficiency dramatically reduces to 2%. The device stops operating as a solar cell above an In composition of 45%. The conversion efficiency of the modeled InGaN/GaN heterojunction solar cell is limited to 11.3% for a *UID*-InGaN layer with an In fraction of 30%. While such cells would be suitable as subcells in multi-junction solar cells, particularly for 4- or more-junction devices [97], they are inadequate as single-junction devices.

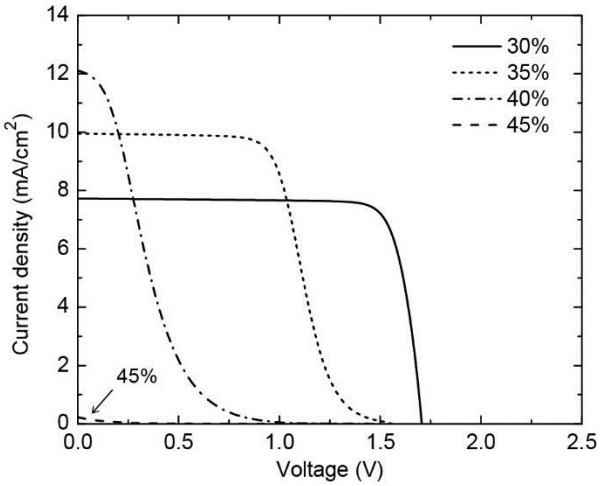

Figure 2.6: *J-V* characteristics under AM1.5 illumination for an *n*-GaN/*UID*-$In_xGa_{1-x}N$/*p*-$In_{0.25}Ga_{0.75}N$ structure with various In composition in the *UID*-layer. The polarization-induced electric field produces a knee in the *J-V* curve for In compositions of 35% and 40%. Above an In composition of 45%, the device stops operating as a solar cell.

In summary, the *n*-GaN/*i*-$In_xGa_{1-x}N$/*p*-$In_{0.25}Ga_{0.75}N$ solar-cell structure mitigates the influence of polarization charges and potential barriers for solar cells with low In compositions. However, for solar cells with high In compositions that are needed for longer wavelength absorption, polarization effects drastically degrade the photovoltaic performance.

2.2.2 InGaN *p-i-n* Homojunction Structure

To further mitigate the polarization effects, we study the photovoltaic performance of an InGaN *p-i-n* homojunction structure. Figure 2.7 displays the schematic structure of the *n*-$In_xGa_{1-x}N$/*UID*-$In_xGa_{1-x}N$/*p*-$In_xGa_{1-x}N$ cell used for simulations. In this design, an *n*-$In_xGa_{1-x}N$/*UID*-$In_xGa_{1-x}N$ homointerface replaces the *n*-GaN/*UID*-$In_xGa_{1-x}N$ heterointerface in the previous structure. The In composition throughout the cell is constant. The thicknesses and the doping concentrations of the *n*- and *p*-type InGaN layers are identical to those of the previous structure. In contrast to the previous design, such devices are presently challenging to fabricate. While InGaN *p-i-n* homojunction solar cells with In composition up to 20% have been previously demonstrated [23], the fabrication of *p-i-n* solar cells with higher In content requires further improvements in InGaN material. Major issues include *p*-doping at high In composition and growth of thick, high-quality InGaN layers.

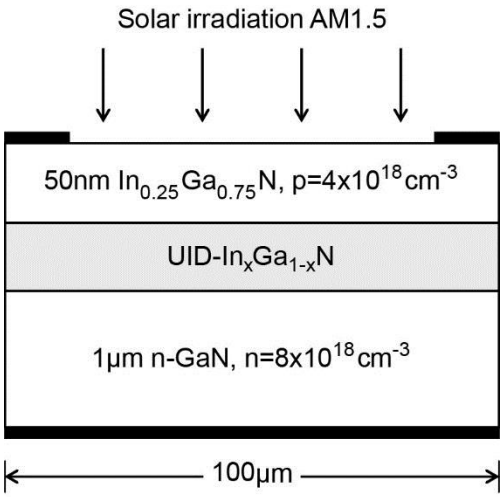

Figure 2.7: Schematic structure of an *n*-$In_xGa_{1-x}N$/*UID*-$In_xGa_{1-x}N$/*p*-$In_xGa_{1-x}N$ homojunction solar cell.

Figure 2.8 shows the energy-band diagrams and the *J*-*V* characteristics for an $In_{0.25}Ga_{0.75}N$ homojunction solar cell with various thicknesses and background donor concentrations of the *UID*-$In_{0.25}Ga_{0.75}N$ layer. As expected, all polarization-induced barriers that hinder carrier collection have been eliminated. The depletion width displays strong dependence on the thickness and the doping of the *UID*-layer. Similar to the effect of doping on the band diagram of the heterojunction structure, higher background donor concentration leads to narrower depletion regions.

Figure 2.9 shows the short-circuit current density J_{sc} of 25%, 50%, and 70% InGaN *p*-*i*-*n* homojunction solar cells. J_{sc} greatly depends on the In composition, the thickness, and doping of the *UID*-layer. The short-circuit current density of a homojunction solar cell exhibits similar trends compared to that of a heterojunction device (Figure 2.3(a)) indicating that the absorbing *UID*-InGaN layer predominantly

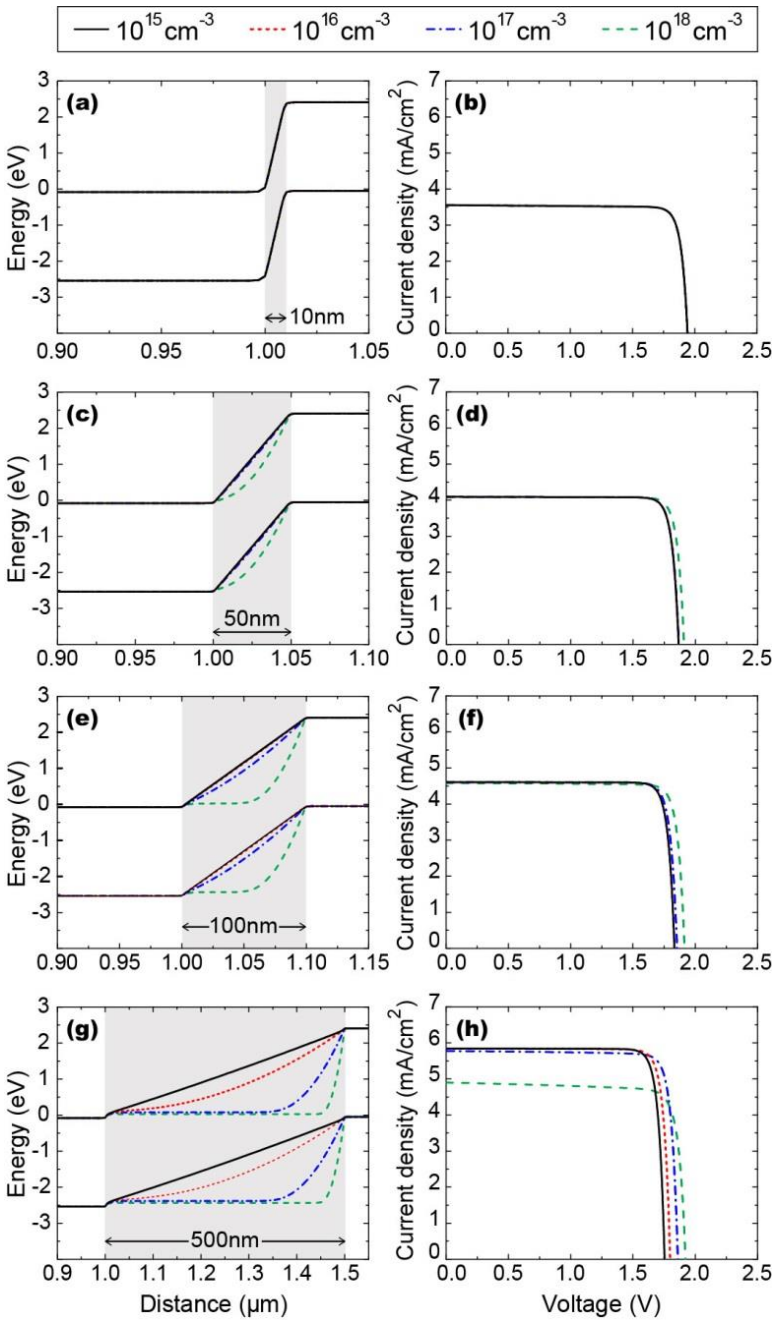

Figure 2.8: (a), (c), (e), (g) Energy-band diagrams at equilibrium for an *n*-$In_{0.25}Ga_{0.75}N$/*UID*-$In_{0.25}Ga_{0.75}N$/*p*-$In_{0.25}Ga_{0.75}N$ structure with various *UID*-InGaN thicknesses: 10 nm, 50 nm, 100 nm, and 500 nm, respectively. (b), (d), (f), (h) Corresponding *J-V* characteristics under AM1.5 illumination.

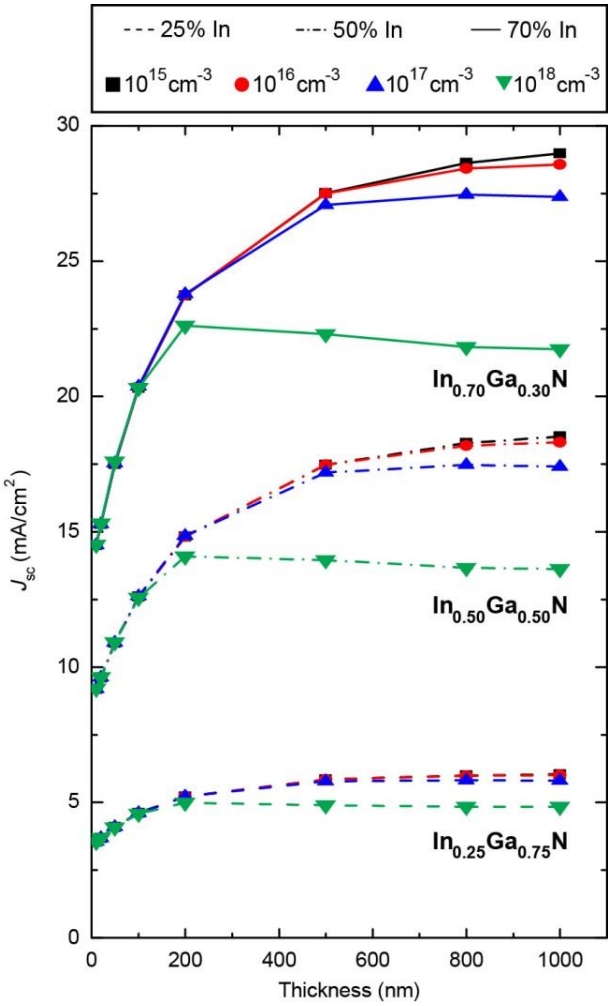

Figure 2.9: Short-circuit current density J_{sc} as a function of the *UID*-layer thickness for an *n*-$In_xGa_{1-x}N$/*UID*-$In_xGa_{1-x}N$/*p*-$In_xGa_{1-x}N$ solar cell with various In compositions and concentrations of background donors. J_{sc} increases for cells with larger thickness and higher In content because of enhanced light absorption, but decreases for cells with higher background doping because of reduced collection efficiency.

influences J_{sc} for both device structures. J_{sc} reduces in cells with higher residual donor concentrations due to degraded collection efficiency. On the other hand, J_{sc} increases in thicker cells due to improved light absorption. J_{sc} also improves for solar cells with higher In composition due to lower band gap.

Figure 2.10(a) illustrates the decrease in band gap of InGaN as the In content increases. Smaller band gaps allow enhanced absorption resulting in increased carrier generation rate (Figure 2.10(b)) and thus, higher J_{sc}.

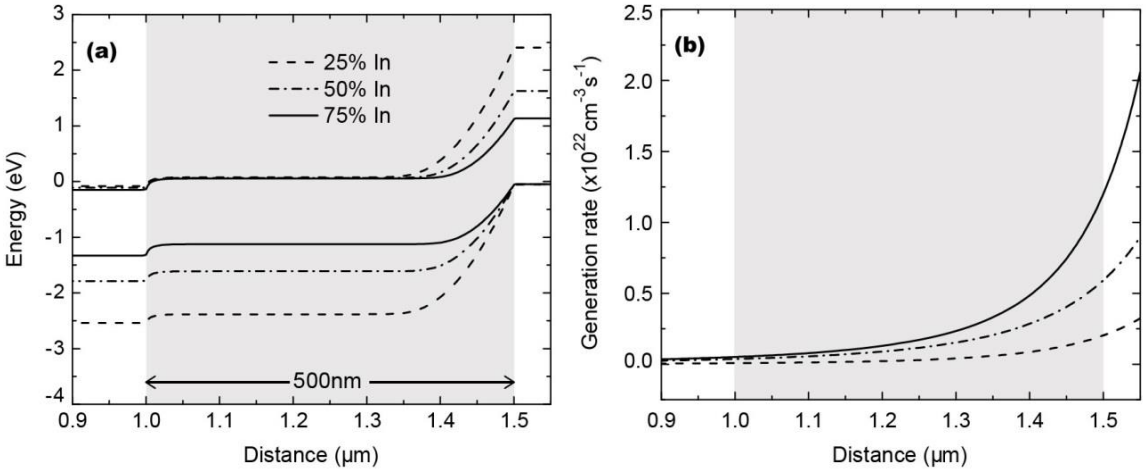

Figure 2.10: (a) Band diagrams at equilibrium and (b) optical carrier generation rate under AM1.5 illumination for an *n*-$In_xGa_{1-x}N$/*UID*-$In_xGa_{1-x}N$/*p*-$In_xGa_{1-x}N$ structure with various In compositions.

Figure 2.11 displays the open-circuit voltage V_{oc} as a function of the thickness of the *UID*-InGaN layer with various In contents and background donor concentrations. Simulation results demonstrate that V_{oc} strongly depends on the background doping and the In composition, but only slightly on the *UID*-layer thickness. Dependences on background doping and thickness are similar to those for the previous structure. Since the band gap represents an upper limit to the open-circuit voltage (neglecting Auger effects), V_{oc} decreases as the In content increases.

Figure 2.12(a)-(c) show the conversion efficiency η as a function of the *UID*-layer thickness for 25%, 50%, and 70% InGaN solar cells with various background donor concentrations. Similar to J_{sc}, the efficiency increases as the thickness increases for background donor concentrations smaller than 10^{18} cm^{-3}. The *UID*-layer doping only slightly affect the conversion efficiency for thin layers. However, moderate doping is beneficial to efficiency for thicker layers. This improvement in efficiency is mainly due to the increase in V_{oc} with increasing background doping and this effect is enhanced for solar cells with higher In compositions.

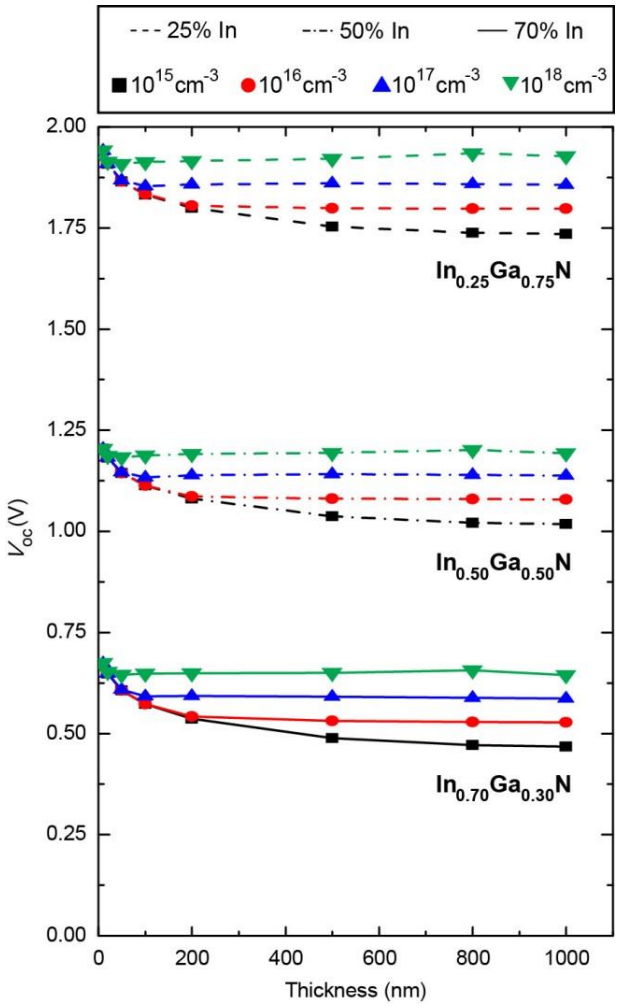

Figure 2.11: Open-circuit voltage V_{oc} as a function of the *UID*-layer thickness for an *n*-$In_xGa_{1-x}N$/*UID*-$In_xGa_{1-x}N$/*p*-$In_xGa_{1-x}N$ solar cell with various In compositions and concentrations of background donors. V_{oc} decreases for cells with higher In content due to reduced band gap, but increases for cells with higher background doping due to narrower depletion width.

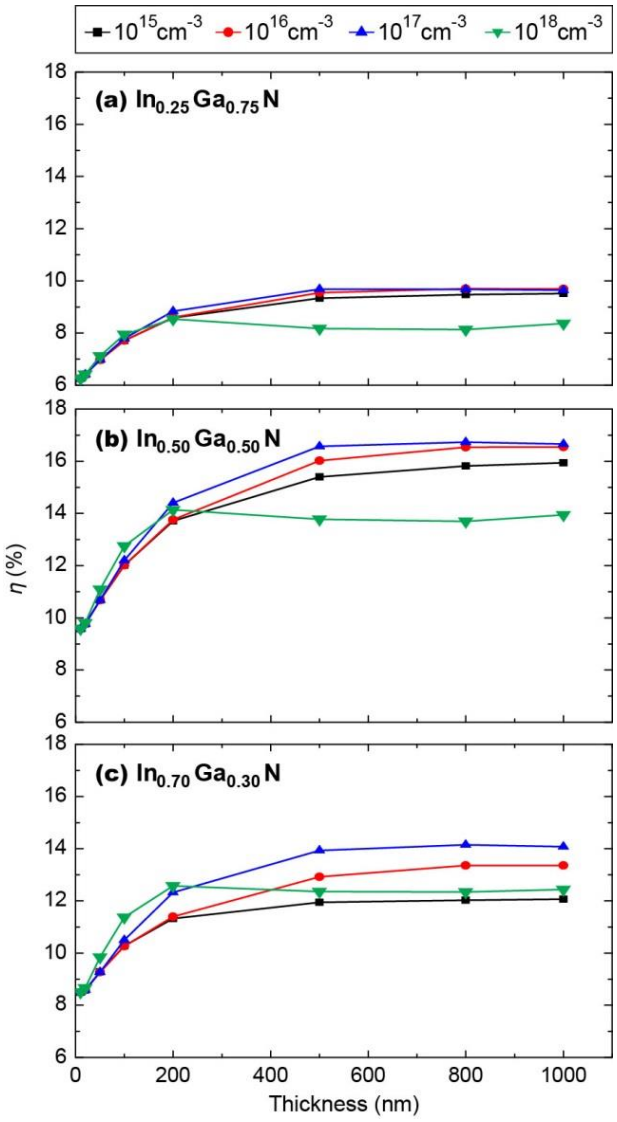

Figure 2.12: Conversion efficiency η as a function of the *UID*-layer thickness for (a) $In_{0.25}Ga_{0.75}N$ (b) $In_{0.50}Ga_{0.50}N$ (c) $In_{0.70}Ga_{0.30}N$ *p-i-n* homojunction solar cells with various concentrations of background donors. The conversion efficiency accounts for the tradeoff between the opposite trends of J_{sc} and V_{oc}.

While a residual donor concentration of 10^{18} cm^{-3} drastically degrades the performance of 25% and 50% InGaN solar cells due to reduced J_{sc}, such a high doping slightly improves the performance of a 70% InGaN solar cell due to increased V_{oc}. As the In content increases from 25% to 50%, η improves similar to J_{sc}. On the other hand, η decreases as the In content increases from 50% to 70%. Therefore, a finer investigation of the influence of composition is required to determine the optimal efficiency for an InGaN single homojunction device.

Figure 2.13(a)-(c) show the influence of composition and background doping on J_{sc}, V_{oc}, and η, respectively. These simulations do not include In content higher than 70% since polarization effects at these high In compositions create a surface inversion layer that induces lateral collection. The thickness of the *UID*-InGaN layer is set to 500 nm. As the In mole fraction increases, J_{sc} increases due to improved light absorption but V_{oc} decreases due to band gap reduction. These opposite trends lead to an optimum band gap for highest efficiency. For all background doping in the *UID*-layer, the maximum efficiency is within the range 14%-18% and occurs in the range 1.4 eV to 1.6 eV (*i.e.* 53-60% In) as predicted for a single-junction device [5, 95].

As the residual donor concentration increases, J_{sc} decreases but V_{oc} increases due to reduced depletion volumes. The optimal background doping, which accounts for the tradeoff between J_{sc} and V_{oc}, is 10^{17} cm^{-3}. Furthermore, as the background doping increases, the optimal band gap shifts to lower values, decreasing from 1.57 eV for 10^{15} cm^{-3} to 1.47 eV for 10^{18} cm^{-3} as illustrated in Figure 2.14. This change can be attributed to the opposite trends of J_{sc} and V_{oc} with both In composition and background doping as shown in Figure 2.13(a) and (b).

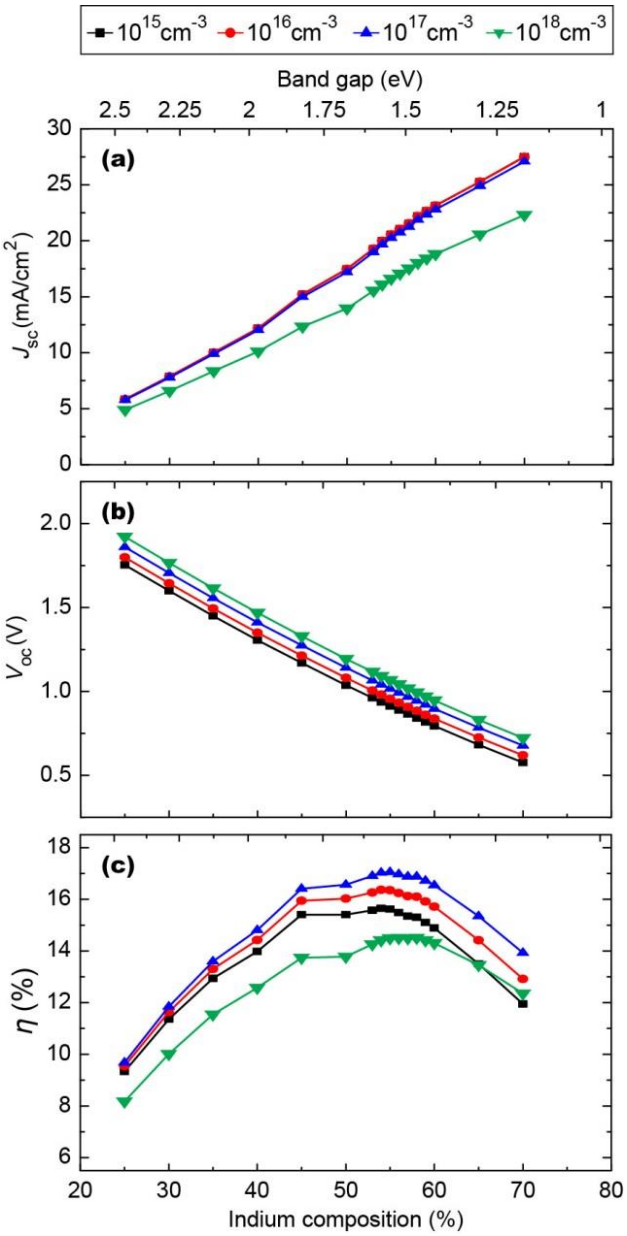

Figure 2.13: (a) Short-circuit current density J_{sc}, (b) open-circuit voltage V_{oc}, and (c) conversion efficiency η as a function of the In composition (*i.e.* band gap) for an *n*-$In_xGa_{1-x}N$/*UID*-$In_xGa_{1-x}N$/*p*-$In_xGa_{1-x}N$ structure with various residual donor concentrations. The thickness of the *UID*-InGaN is 500 nm.

The combination of these opposite trends displaces the optimal efficiency towards higher In compositions (*i.e.,* lower band gaps) as the background doping increases. The optimized structure consists of an InGaN *p-i-n* homojunction solar cell with an In composition of 55% (*i.e.* 1.54 eV), a *UID*-InGaN layer thickness of 500 nm, and a residual donor concentration of 10^{17} cm^{-3}. This homojunction with optimal parameter leads to a maximum conversion efficiency of ~17%, which is significantly lower than the theoretical maximum efficiency for a single-junction [98].

This efficiency is limited by presently achievable values of surface recombination velocity (10^4 cm/s) and minority carrier lifetime (1 ns). Figure 2.15 shows the conversion efficiency for identical InGaN *p-i-n* homojunction devices with various surface recombination velocity and various minority carrier lifetimes. Indeed, for an identical InGaN *p-i-n* homojunction device with unrealistic values of surface recombination velocity (10 cm/s) and minority carrier lifetime (1 μs), the conversion efficiency rises to 25.3% [99], which is closer to the ultimate efficiency. The simulation results demonstrate that the homojunction structure is the only practical design for high-efficiency single-junction InGaN solar cells. However, achieving high conversion efficiency still requires further improvements in material quality and surface passivation. Compared to present limits, a tenfold increase in both surface recombination velocity and minority carrier lifetime is needed to achieve efficiencies greater than 20%.

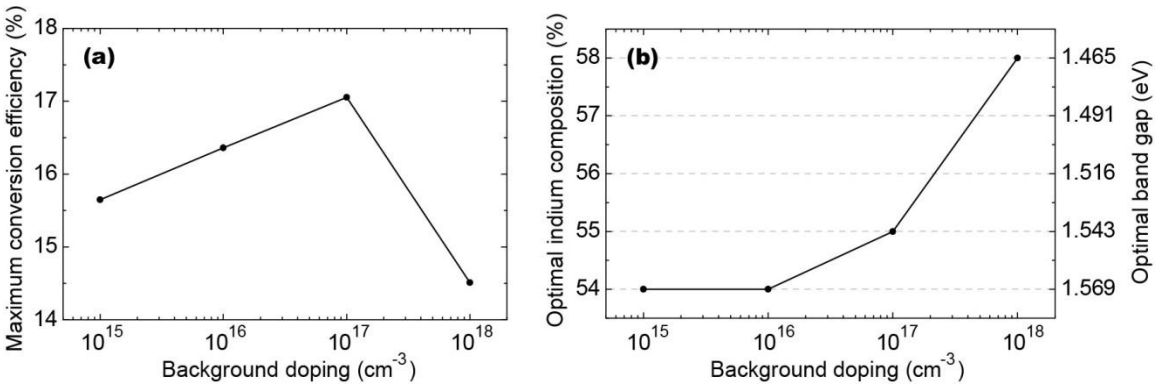

Figure 2.14: (a) Maximum conversion efficiency and (b) optimal In composition and band gap as a function of background doping in the *UID*-InGaN layer for an *n*-$In_xGa_{1-x}N$/*UID*-$In_xGa_{1-x}N$/*p*-$In_xGa_{1-x}N$ structure. As the background doping increases, the optimal band gap shifts to lower values.

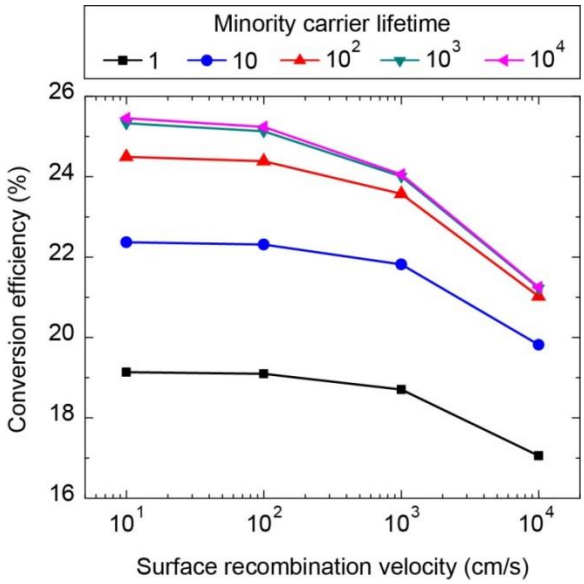

Figure 2.15: Conversion efficiency as a function of surface recombination velocity for a 55% InGaN *p-i-n* homojunction structure with various minority carrier lifetimes.

2.3 Summary

In summary, we numerically investigated the photovoltaic performance of InGaN *p*-*i*-*n* solar cells. Simulation results show that band diagram, short-circuit current density, open-circuit voltage, and conversion efficiency strongly depend on the In content, the thickness, and the background doping of the unintentionally-doped layer for both heterojunction and homojunction structures. Because of enhanced light absorption, J_{sc} increases for cells with larger thicknesses and higher In compositions. However, as doping increases, the depletion region narrows, leading to poor collection efficiency and thus, reduced J_{sc}. V_{oc} increases for cells with higher background donor concentrations due to reduced depletion volumes, but decreases for cells with higher In compositions due to band gap reduction. In addition, V_{oc} depends only slightly on the thickness of the *UID*-InGaN layer. The conversion efficiency accounts for the tradeoff between the opposite trends of J_{sc} and V_{oc}. For currently feasible *n*-GaN/*UID*-$In_xGa_{1-x}N$/ *p*-$In_{0.25}Ga_{0.75}N$ structures, the conversion efficiency is limited to 11.3% as a result of polarization effects that hinder carrier collection for high In compositions. These detrimental polarization effects can be eliminated by using InGaN *p*-*i*-*n* homojunction devices that are currently challenging to fabricate, but should be achievable in the future. For an optimized InGaN *p*-*i*-*n* homojunction solar cell with a 500 nm-thick absorbing layer, a background donor concentration of 10^{17} cm^{-3}, and an In content of 55%, the maximum conversion efficiency is ~17%. This conversion efficiency is limited below the theoretical limit for single-junction devices by presently achievable surface recombination velocities (10^4 cm/s) and minority carrier lifetimes (1 ns). With improved, but unrealistic values of surface recombination velocity and minority carrier

lifetime, the efficiency rises to ~25%. Finally, simulations show that the optimal band gap shifts to lower values as the background doping increases. Hence, by using appropriate device design, the performance of InGaN solar cells can be optimized given achievable material parameters.

CHAPTER 3

GROWTH OF InGaN FILMS OVER THE ENTIRE COMPOSITION RANGE BY N-RICH MBE

InGaN-based solar cells require high-quality InGaN layers to efficiently absorb photons and create photogenerated carriers. The growth of InGaN epitaxial layers has been already achieved by various growth techniques as listed in Table 3.1 but the material quality of the InGaN films are not completely satisfactory.

The material-quality limitations can be partially overcome using metal-modulated epitaxy (MME), a modified form of molecular beam epitaxy [28, 45]. MME has enabled the growth of InGaN films throughout the miscibility gap [44, 45]. While the moderate-In-content films (22-46% InGaN) display high density of dislocations and stacking faults, InGaN films with In content higher than 60% exhibit a significant improvement in the crystalline quality and optical properties due to a complete misfit strain relaxation through the formation of a uniform array of misfit dislocations at the InGaN/GaN interface [51]. However, it is unclear whether this complete misfit strain relaxation originates from (i) the fundamental lattice mismatch between In-rich InGaN films and GaN, (ii) the MME growth technique, or (iii) the use of low temperatures. This study presents the growth of InGaN films over the entire composition range under very low growth temperatures and slightly N-rich growth conditions. The growth of InGaN layers on both GaN and AlN are studied to investigate the effect of the underlayer on the relaxation of the InGaN films.

3.1 Growth of InGaN Films on GaN

3.1.1 Experimental Procedure

The InGaN films were grown in a Riber 32 MBE system using a standard effusion cell for In, a Veeco SUMO cell for Ga, and a Veeco Unibulb plasma source for N. Lumilog MOCVD-grown GaN (0001) templates on sapphire were used as substrates and were backside metallized with tantalum to enable radiative heating. Substrates were degreased in H_2SO_4:H_2O_2 (4:1) and outgassed in the introductory chamber at 150°C for 30 min. A ~130 nm GaN buffer was grown at 600°C via MME to bury the native surface oxide. Details on the growth of GaN by MME can be found elsewhere [100].

InGaN growth was performed at various low growth temperatures (360–450°C) depending on the targeted compositions. These growth temperatures are substantially lower than that traditionally used in the literature as described in Table 3.1. The table also compares the characteristics of InGaN films grown by various techniques and shows favorable figures of merit.

All InGaN films were grown under N-rich conditions using a constant III/N ratio of ~0.9 with group-III fluxes normalized by Z-number to account for differences in ion-gauge sensitivity between In and Ga. The In / (Ga + In) ratio was varied to obtain InGaN alloys over the entire composition range. Nitrogen flow rate and RF-plasma power were set at 1.3 sccm and 350 W, respectively. The growth rate was ~1 μm/hr and the nominal InGaN film thickness was 55 nm. The InGaN layers were then capped with a ~10 nm GaN film to prevent thermal decomposition of the surface upon cool down.

Table 3.1: Comparison of InGaN characteristics grown by various methods.

	Growth Technique	In Composition	Growth Temperature	Thickness	Single-Phase	Optical Response	XRD Rocking Curve (arcsec)	Surface Morphology
Chang 2004 [101]	MOCVD	70-100%	600°C		✓ for In > 92% × for In=80%	✓		13-67 nm RMS Pyramid morphology
Pantha 2008 [102]	MOCVD	25-63%	610-730°C	~200 nm	✓		(0002): 1500-3500	1.5-4 nm RMS Grainy morphology
Kim 2008 [103]	MOCVD	22-87%	640-670°C	100-500 nm	✓ @ 670°C × @ 640°C	✓		Small islands
Tsai 2014 [104]	MOCVD	13-38%	675-750°C	240-460 nm	× Pulling effect (relaxation)	✓		
Nanishi 2003 [17]	MBE	16-97%	550°C		✓ for In >53% × for In <53%	✓		
Che 2006 [74]	MBE	70%	450-600°C	400 nm	✓ for N-rich and modulated mode × for M-rich		(0002): 300-600 $(10\bar{1}2)$: 1700-3800	3-7.3 nm RMS pits
Komaki 2007 [70]	MBE	1-22%	575°C	350-750 nm	✓ for N-rich × for M-rich	✓		- M-rich: Flat with In droplets - N-rich: Rough with mesh structure

Table 3.1 (continued)

Kraus 2011 [46]	MBE	15-25%	520°C	25-60 nm	✓ for N-rich × for M-rich	✓		- M-rich: 2D/3D - N-rich: 3D with hexagonal hillocks
Moseley 2012 [45]	MBE MME	22-66%	400-450°C	50 nm	✓	✓ for In >60% × for In <60%	(0002): 350	0.2-0.8 nm
Gačević 2013 [66]	MBE	0-50%	460 - 645°C	60-120 nm				1-3 nm RMS - N-rich: 3D - Intermediate <1ML: pits - M-rich and intermediate>1ML: 2D
Valdueza 2014 [76]	MBE Excess In	13-48%	610-670°C	150-250 nm	Inhomogeneity: pulling effect	✓		1-5 nm RMS
Yamaguchi 2013 [75]	MBE DERI	25-75%	450-580°C	500 nm	✓			
Ju 2014 [69]	MBE Excess In	75-100%	450-630°C	0.6-1μm	✓ for low excess In and low temperature. × for high excess In and high temperature.	✓	(0002): 700-1450 $(10\bar{1}2)$: 1500-2900	1.2-6.5 nm metallic In droplets
Fabien 2014 [105]	**MBE**	**20-82%**	**360-450°C**	**55-65 nm**	✓	✓	**(0002): <340** **$(10\bar{1}5)$: 675-1100**	**<1 nm RMS** **2D/3D grainy morphology**

The growth of the InGaN films was monitored *in situ* by reflection high-energy electron diffraction (RHEED). The structural properties of the samples were characterized by X-ray diffraction (XRD) including 2θ–ω diffraction scans, ω rocking curves (RC), and reciprocal space maps (RSM). The surface morphology, microstructural, and optical properties of all these samples were analyzed by atomic force microscopy (AFM), transmission electron microscopy (TEM), and photoluminescence/cathodoluminescence (PL/CL), respectively.

3.1.2 Results and Discussion

Table 3.2 lists the InGaN layer characteristics. Figure 3.1 shows the In content determined by XRD as a function of the ratio of the In (In) to the total group-III (In + Ga) flux. The experimental data points follow a linear behavior with a slope equal to one. This slope can be interpreted as the incorporation efficiency of In into the InGaN layer, which depends on the desorption and the segregation of In atoms [71, 106]. At the low substrate temperatures used for these growths, desorption of In atoms from the surface is negligible. Under N-rich growth, the influence of In segregation is limited due to the reduced surface adatom mobility. Therefore, at low substrate temperatures and under slightly N-rich conditions, the In incorporation efficiency is approximately unity.

The 2θ-ω scans depicted in Figure 3.2 show the absence of phase separation for all the InGaN films grown throughout the miscibility gap. The suppression of phase separation can be attributed to kinetically-limited adatom diffusion enhanced by the N-rich growth regime [70] and the low substrate temperatures [73]. The full width at half maximum (FWHM) of the (0002) and XRD RCs, which are associated with dislocation density, are summarized in Table 3.2. The (0002) RC full widths at half maximum

(FWHMs) of all InGaN films are comparable to those of the underlying GaN templates, indicating negligible tilt. Film thicknesses were measured to be 52-60 nm from the Pendellösung fringes, which are also indicative of smooth interfaces.

Table 3.2: Characteristics of InGaN layers grown on GaN.

In content	Band gap (eV)	Wavelength (nm)	Growth temperature (°C)	(0002) RC FWHM (arcsec)	(10$\bar{1}$5) RC FWHM (arcsec)	Roughness (nm RMS)	Lattice mismatch
20%	2.64	470	450	324	675	0.495	2.2%
37%	2.06	601	425	322	1721	0.488	4.1%
52%	1.62	764	400	338	1770	0.559	5.8%
67%	1.25	994	400	331	976	0.632	7.5%
82%	0.94	1323	360	317	1088	0.670	9.2%

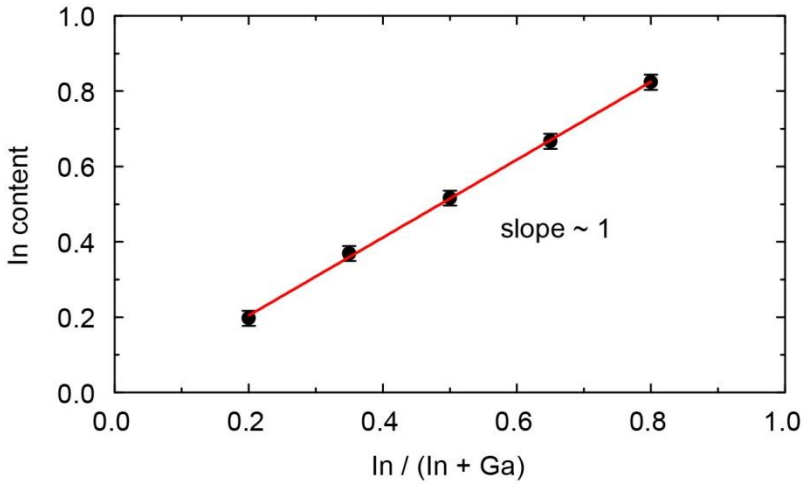

Figure 3.1: In content of InGaN films as a function of the ratio of In to total metal flux. The slope represents the In incorporation efficiency.

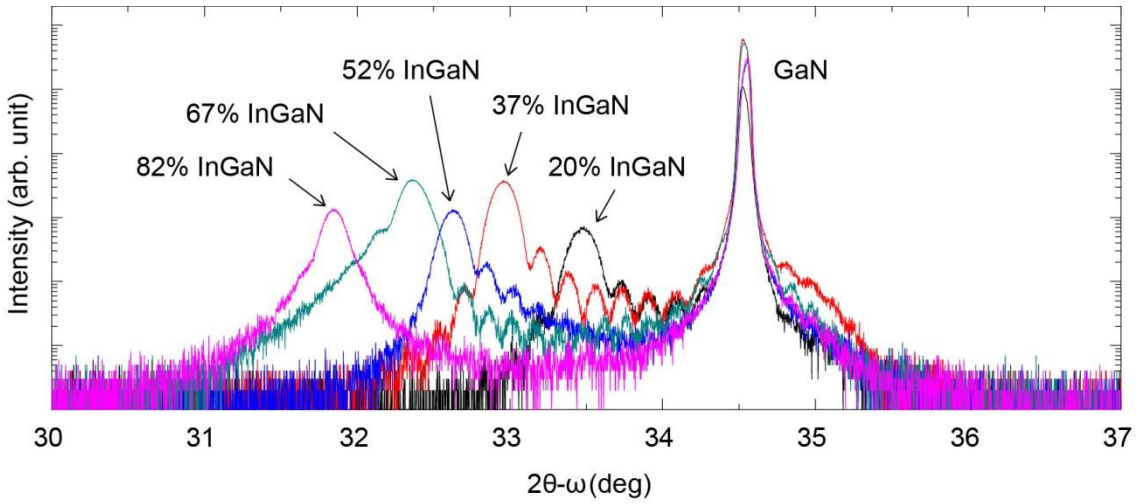

Figure 3.2: 2θ-ω diffraction scans along the (0002) reflection of single-phase InGaN films grown on GaN over the entire composition range.

The surface morphology of the InGaN films was investigated by AFM. The AFM images, shown in Figure 3.3, display smooth surfaces with sub-nm root-mean-square (RMS) roughnesses. The low adatom mobility from the slightly N-rich growth conditions results in a combination of long-range 2D atomic steps (Figure 3.3(a)) with short-range 3D granular domains (Figure 3.3(c)) that are 25-50 nm-diameter wide. This grainy morphology is confirmed by the slightly spotty RHEED pattern observed during growth as shown in Figure 3.3(d).

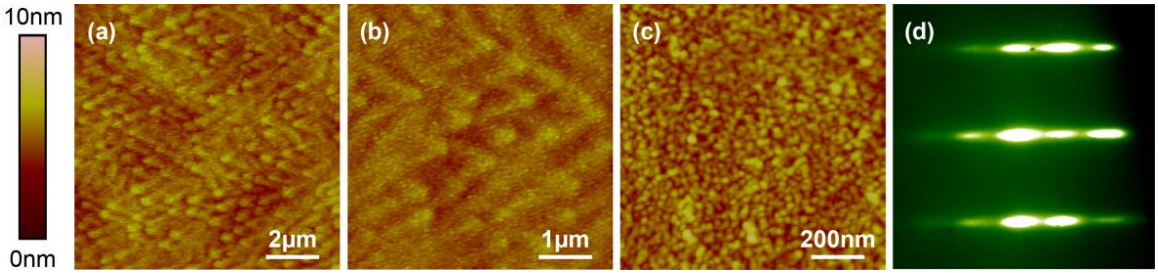

Figure 3.3: (a) 10×10 μm, (b) 5×5 μm, and (c) 1×1 μm representative AFM images of InGaN films grown on GaN under slightly N-rich conditions at low temperatures. (d) Typical RHEED pattern during growth.

The composition and strain of the InGaN films were derived from XRD RSMs. Details on the calculations are provided in Appendix A. Figure 3.4 depicts the InGaN/GaN RSMs for the $(10\bar{1}5)$ reflections of the five InGaN samples with In compositions ranging from 20% to 82%. The fully-strained and fully-relaxed lines are also represented as vertical and diagonal dashed lines, respectively. With increasing In content, the InGaN reciprocal lattice point shifts from a fully-strained to a fully-relaxed position. The 20% InGaN film is fully coherent to the GaN underlayer. The degree of relaxation increases for the 37% and the 52% InGaN films and for In composition of 67% and 82%, the films are fully relaxed.

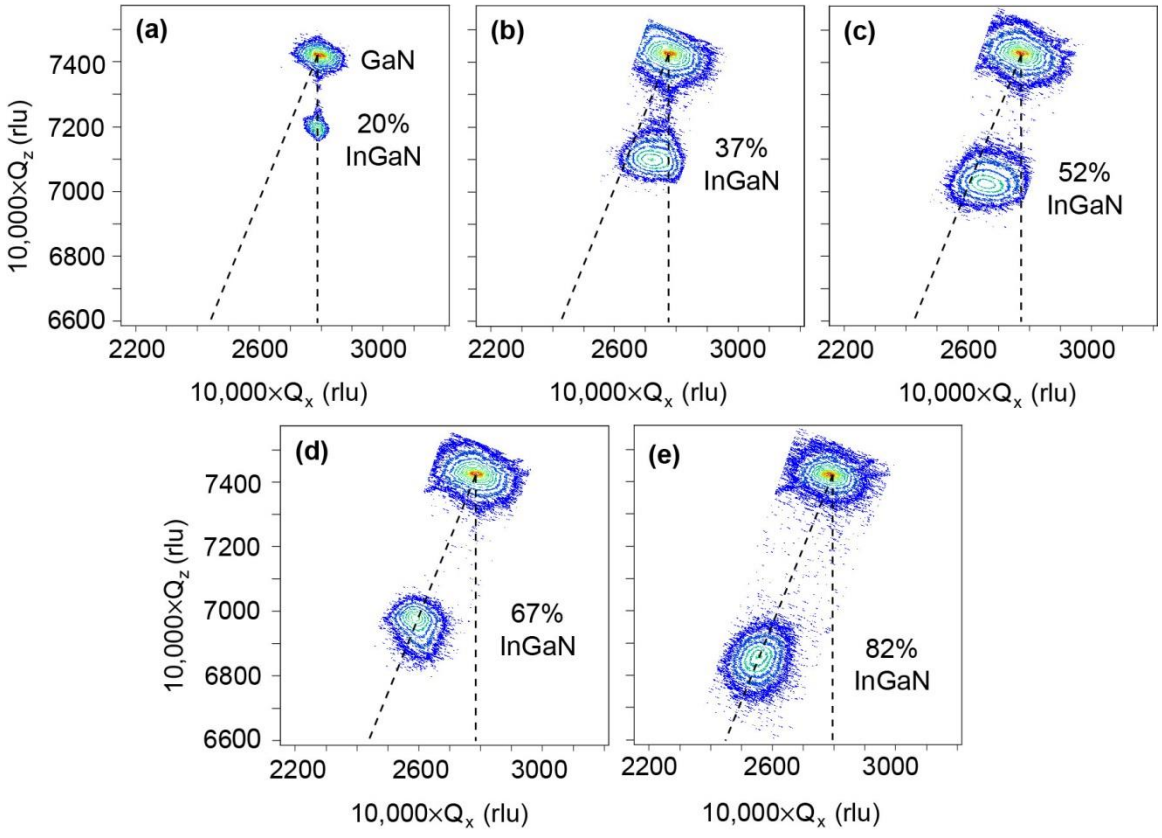

Figure 3.4: RSMs along the $(10\bar{1}5)$ reflection of the (a) 20%, (b) 37%, (c) 52%, (d) 67%, and (e) 82% InGaN films grown on GaN. The vertical and diagonal dashed lines correspond to the fully-strained and fully-relaxed positions, respectively.

This relaxation trend is confirmed by TEM as shown in Figure 3.5. The 20% InGaN film exhibits residual strain. The 37% InGaN layer follows an island-nucleation growth mechanism, resulting in isolated islands, with different tilt and twist, which coalesce. The onset of moiré fringes, which are associated with misfit dislocations, is observed at the GaN/InGaN interface for the 52% InGaN as demonstrated by the periodic peaks from the line scan (Figure 3.5(c) inset). The N-rich 67% InGaN sample clearly exhibits moiré fringes at the interface, indicating a complete misfit strain relaxation through misfit dislocations.

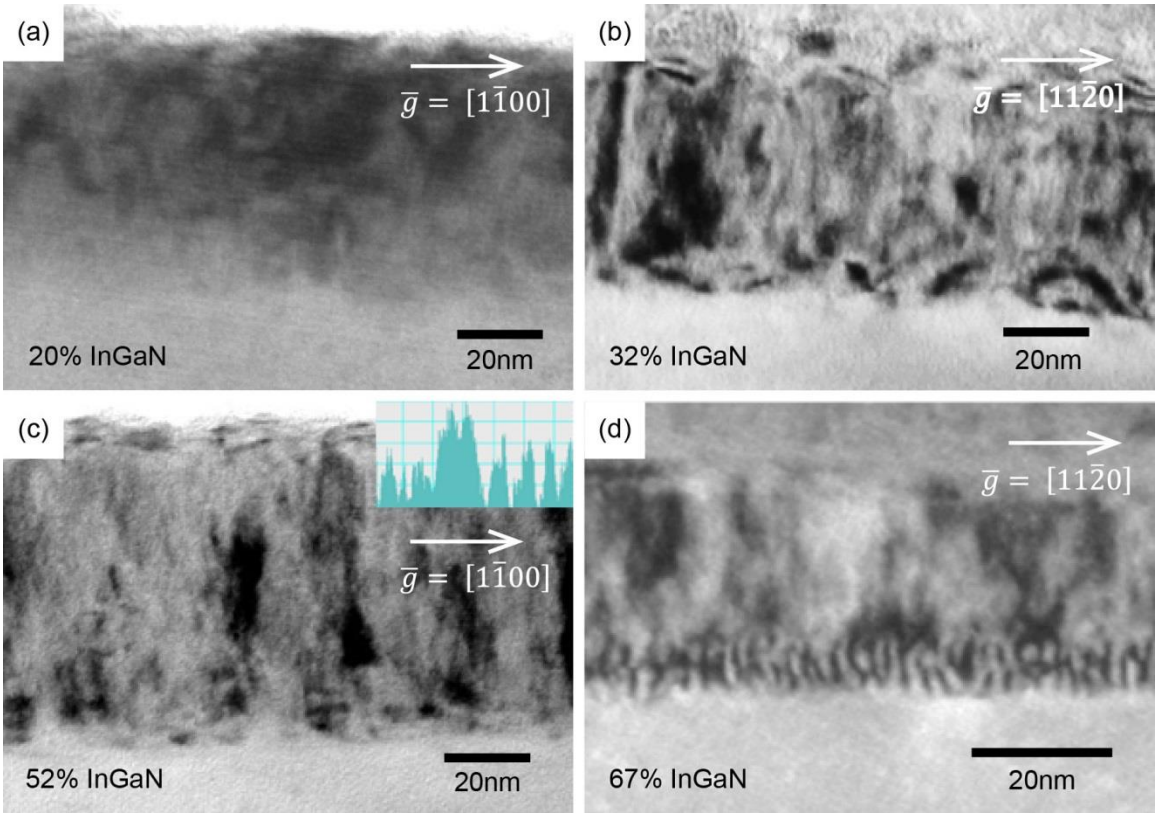

Figure 3.5: Cross-section TEM images of the InGaN films grown on GaN. Residual strain and island formation are observed for the (a) 20% and (b) 37% InGaN films, respectively. Moiré fringes indicating misfit strain relaxation are observed at the InGaN/GaN interfaces for the (c) 52% and (d) 67% InGaN films. The inset shows periodic peaks from the line scan at the bottom InGaN/GaN interface.

The distance D between two dark fringes, which is associated with the interplanar separation across InGaN/GaN interface is given by

$$D = \frac{d_{GaN}\, d_{InGaN}}{d_{InGaN} - d_{GaN}}, \tag{3.1}$$

where d_{GaN} and d_{InGaN} are the interplanar distances in the GaN and InGaN layers, respectively. The interplanar separation for moiré fringes arranged along the $\langle 1\bar{1}00 \rangle$ directions, is

$$d = \frac{a}{2}, \tag{3.2}$$

where *a* is the lattice parameter in the basal plane [107]. Using Equations (3.1) and (3.2), the lattice constant of the InGaN layer is calculated to be 3.41 Å, which corresponds to 64% InGaN. This result further confirms that the InGaN layer underwent a complete misfit strain relaxation within the first MLs.

Similar to the MME-grown InGaN samples [51], a transition in the structural properties of the N-rich InGaN films for In content higher than 50%-60% is observed. The critical thickness as a function of In content, calculated using various models, is depicted in Figure 3.6. The transition in the structural properties coincides with the calculated critical thickness reaching a value close to 1-2 monolayers (MLs) [108-110]. The lattice mismatch between the InGaN epitaxial layer and the GaN underlayer increases with In composition as shown in Table 3.2. At high In compositions, due to the large lattice mismatch between GaN and In-rich InGaN, the InGaN material spontaneously nucleates in a fully relaxed state, with the formation of a uniform array of misfit dislocations at the interface.

All these InGaN films exhibit luminescence either by CL (Figure 3.7(a)) or PL (Figure 3.7(b)) possibly due to reduced defect density compared to the MME-grown InGaN films [51], especially the absence of stacking faults as demonstrated by the TEM. The additional peaks and shoulders in the 67% and 82% InGaN spectra are attributed to Fabry-Pérot interferences from the GaN underlayer.

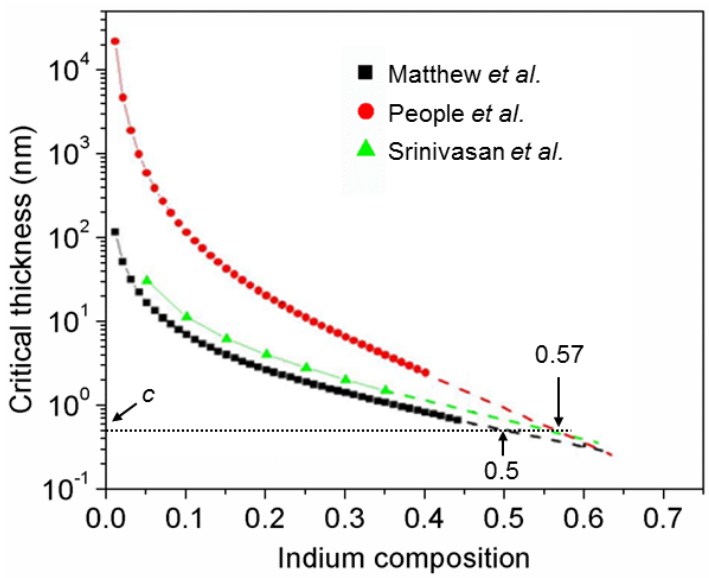

Figure 3.6: Critical thickness as a function of In composition for the InGaN/GaN system using various models [108-110]. The critical thickness of one lattice period *c* (horizontal dotted line) happens at 50-57% In composition [51].

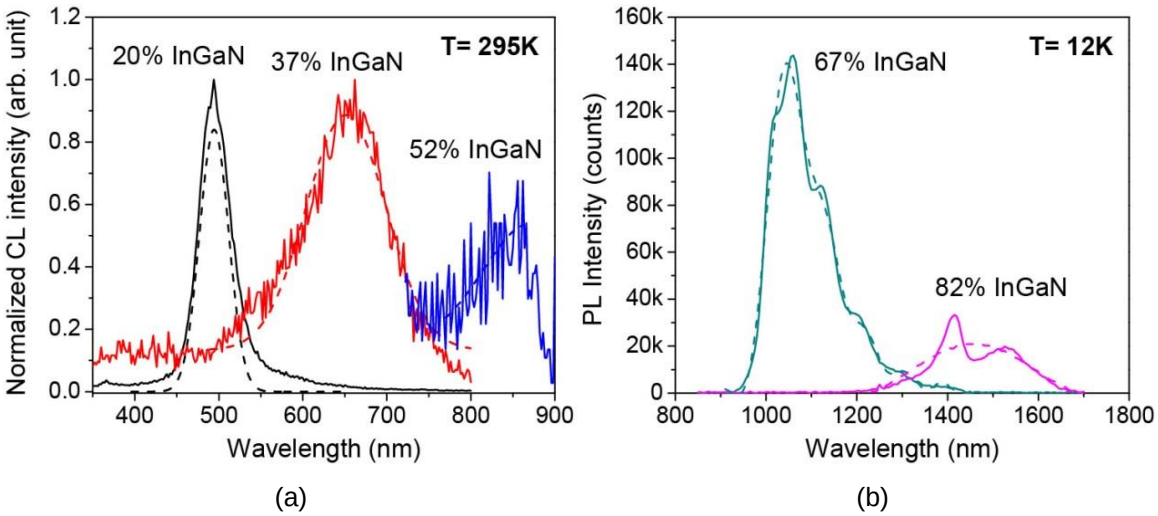

Figure 3.7: (a) CL spectra of the 20%, 37%, and 52% InGaN films and (b) PL spectra of the 67% and 82% InGaN films. The dashed lines represent the Gaussian fittings after removal of Fabry-Pérot interference effects.

3.1.3 Summary

In summary, the surface morphology, microstructural, and optical properties of InGaN films grown by plasma-assisted MBE under low growth temperatures and slightly N-rich growth conditions have been studied. The single-phase InGaN films exhibit improved defect density, an absence of stacking faults, efficient In incorporation, enhanced optical properties, but a grain-like morphology. An increase in the degree of relaxation with increasing In content and a complete misfit strain relaxation for InGaN films with In contents higher than 55-60% were observed. While the complete strain relaxation through misfit dislocations is independent of the growth method, further experiments are needed to determine the influence of low growth temperatures. The enhancement of In incorporation and the improvement in structural and optical properties of InGaN films over the entire composition range will benefit the development of InGaN-based optoelectronic devices, particularly solar cells.

3.2 Growth of InGaN Films on AlN

According to the previous study, the InGaN films grown by N-rich MBE on GaN reveal the formation of misfit dislocations at the InGaN/GaN interface for In content higher than 50%-60%, similar to the MME-grown samples. Therefore, the transition in the structural properties of the InGaN films is independent of the growth method employed (MME or N-rich MBE). This result confirms that the complete misfit strain relaxation originates from the fundamental lattice mismatch between In-rich InGaN films and GaN. The In composition at which this transition occurs depends on the lattice mismatch between the InGaN film and the underlayer. Therefore, this composition can be varied by employing various buffer layers. Since the in-plane lattice constant of AlN is lower than that of GaN, the lattice mismatch between InGaN and AlN is higher than that between InGaN and GaN for a given In composition. As a result, the In composition at which the complete lattice misfit relaxation happens is expected to be lower for InGaN on AlN than for InGaN on GaN. In this study, the relaxation mechanism of InGaN epitaxial layers grown on AlN is investigated.

3.2.1 Experimental Procedure

The InGaN films were grown under similar conditions as compared to the InGaN films grown on GaN underlayers. Lumilog MOCVD-grown GaN (0001) templates on sapphire were used as substrates. A low-temperature ~10 nm AlN layer was grown at 700°C via MME to prevent the decomposition of the GaN template followed by a ~130 nm AlN buffer layer grown at 800°C. Details on the growth of AlN by MME can be found elsewhere [111, 112]. All InGaN films were grown under N-rich conditions using a

constant III/N ratio of ~0.85 and at various low growth temperatures (355–415°C) depending on the targeted compositions (20-80% In). The growth rate was ~1 μm/hr and the nominal InGaN film thickness was 50 nm. The InGaN layers were then capped with a ~10 nm GaN film to prevent thermal decomposition of the surface upon cool down.

3.2.2 Results and Discussion

The characteristics of the InGaN layers grown on AlN are listed in Table 3.3. Figure 3.8 shows the 2θ-ω scans of the single-phase InGaN films grown throughout the miscibility gap with compositions ranging from 21% to 80%. Compared to the diffraction scans of InGaN on GaN shown in Figure 3.2, the Pendellösung fringes are less visible for InGaN on AlN, indicating rougher interfaces. This issue is due to the non-optimized AlN growth conditions, which results in surface voids at the InGaN/AlN interface.

Table 3.3: Characteristics of InGaN layers grown on AlN.

In content	Band gap (eV)	Wavelength (nm)	Growth temperature (°C)	Lattice mismatch
21%	2.6	477	415	4.9%
33%	2.19	566	400	6.2%
48%	1.73	715	385	8%
64%	1.32	941	380	9.8%
80%	0.98	1271	355	11.6%

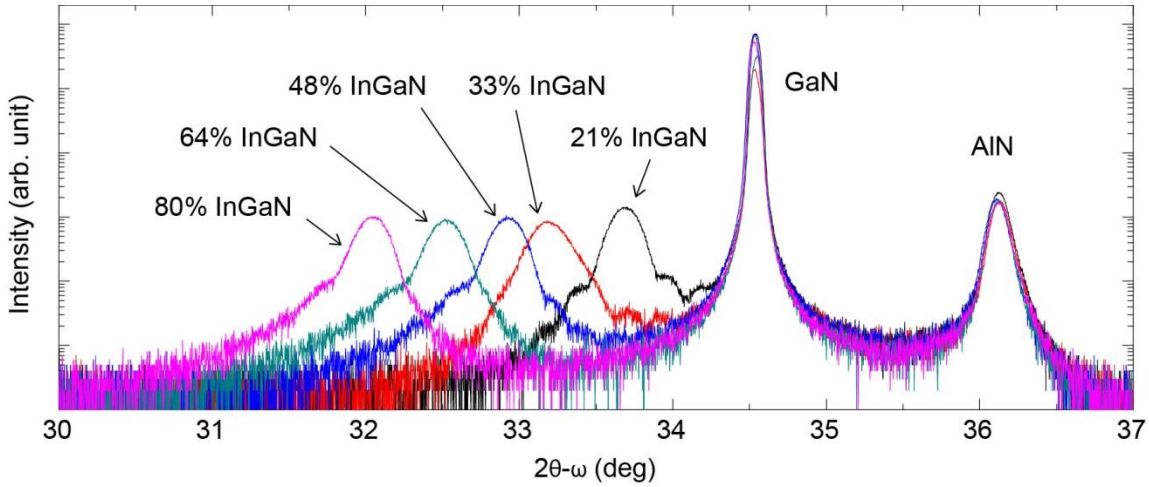

Figure 3.8: 2θ-ω diffraction scans along the (0002) reflection of single-phase InGaN films grown on AlN over the entire composition range.

The XRD RSMs along the $(10\bar{1}5)$ reflections depicted in Figure 3.9 were used to measure the composition and strain of the InGaN films. The fully-strained and fully-relaxed lines are represented as vertical and diagonal dashed lines, respectively. The fully-strained line originates from the AlN reciprocal lattice point since the AlN layer is the buffer layer. Unlike the 20% InGaN film that was fully strained to the GaN underlayer, the 21% InGaN film grown on AlN is mostly relaxed. For In composition of higher than 48%, the InGaN films are fully relaxed.

TEM was performed to determine at which In composition the complete misfit strain relaxation occurs. Moiré fringes, which are associated with misfit dislocations, are clearly observed at the InGaN/AlN interface for the 48% and 64% InGaN films as depicted in Figure 3.10. As predicted by lattice mismatch calculations, summarized in Table 3.3, the In composition at which the InGaN films exhibit a complete misfit relaxation is lower for InGaN on AlN than for InGaN on GaN.

Figure 3.11 shows the theoretical critical thickness for InGaN on AlN as a function of In content calculated using various models. The transition in the structural properties of the InGaN films on AlN happens for In content higher than ~45%. Similar to InGaN on GaN, this transition coincides with the calculated critical thickness reaching a value close to 1-2 MLs [108-110].

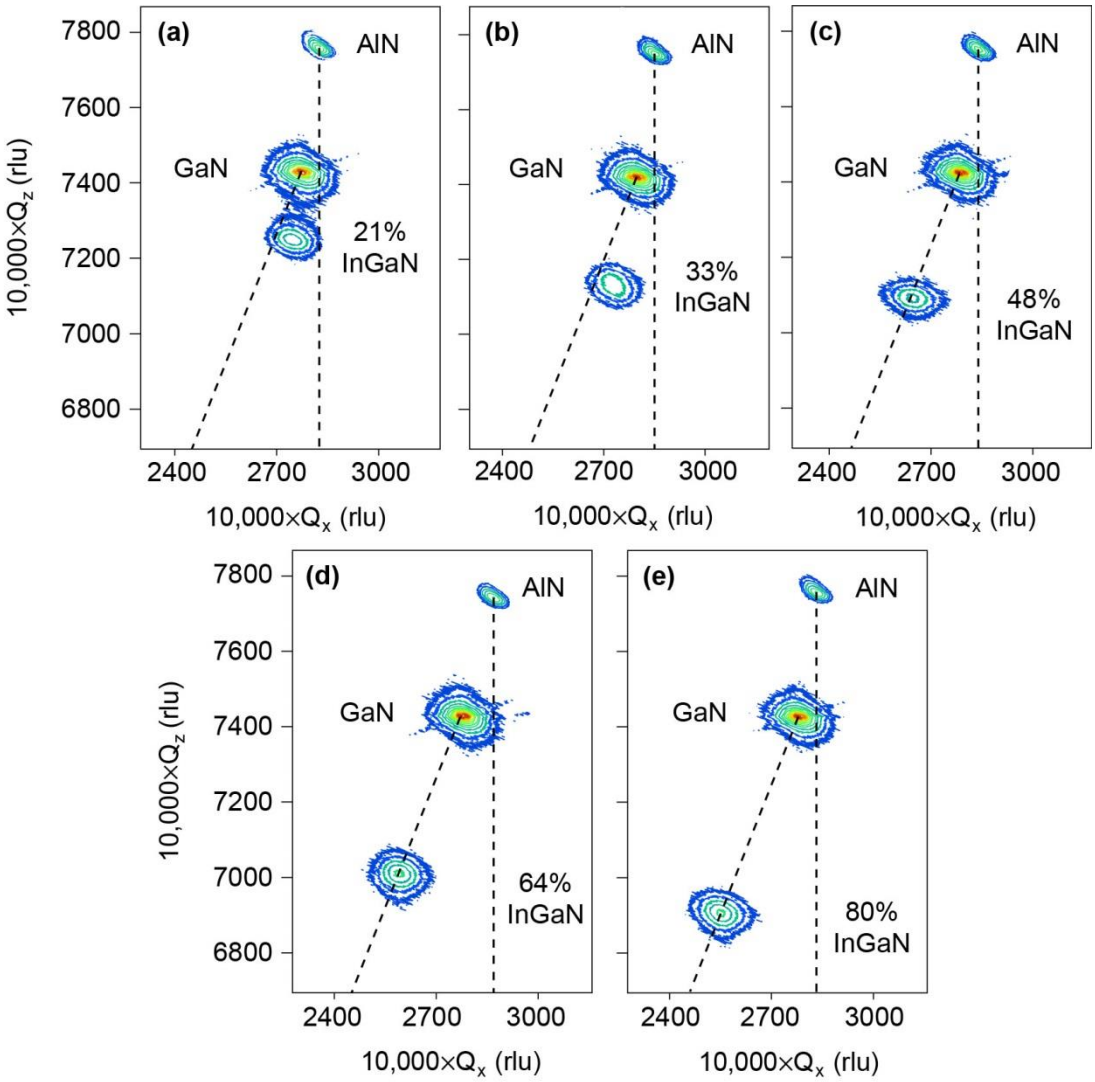

Figure 3.9: RSMs along the $(10\bar{1}5)$ reflection of the (a) 21%, (b) 33%, (c) 48%, (d) 64%, and (e) 80% InGaN films grown on AlN. The vertical and diagonal dashed lines correspond to the fully-strained and fully-relaxed positions, respectively.

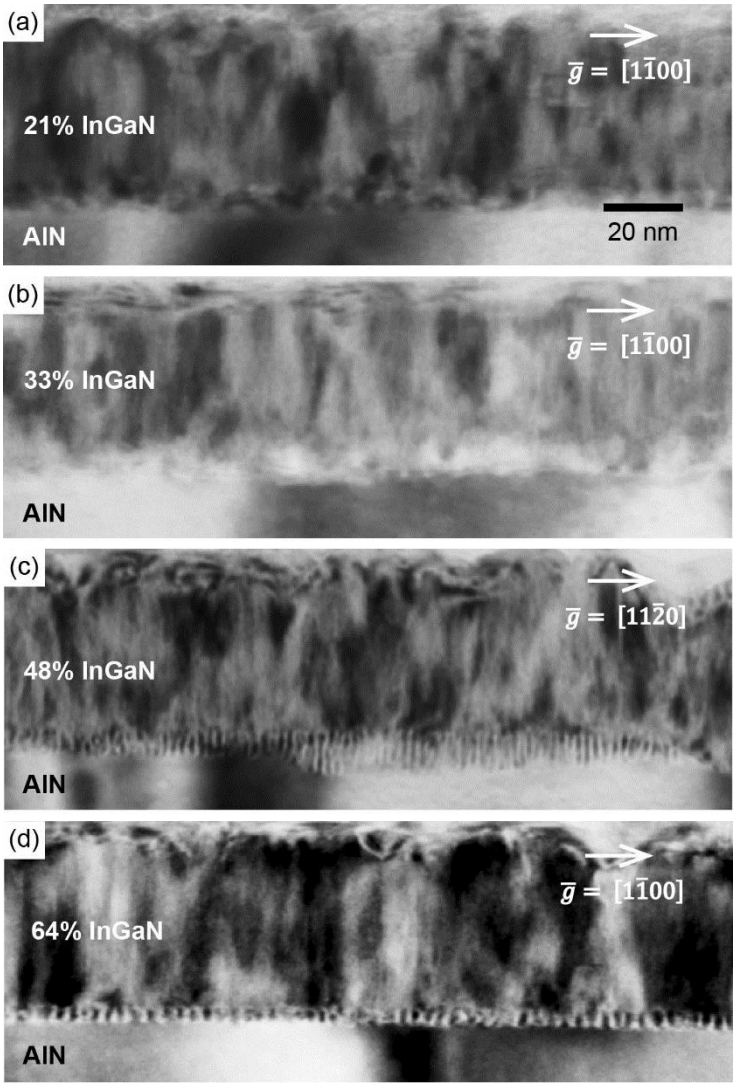

Figure 3.10: Cross-section TEM images of the (a) 20%, (b) 37%, (c) 48%, and (d) 64% InGaN films grown on AlN. Moiré fringes indicating misfit strain relaxation are observed at the InGaN/GaN interface for 48% and 64% InGaN films.

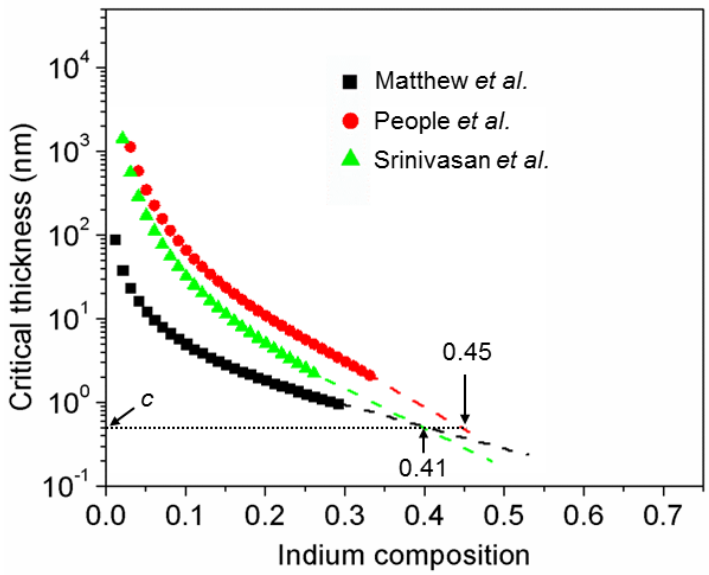

Figure 3.11: Critical thickness as a function of In composition for the InGaN/AlN system using various models [108-110]. The critical thickness of one lattice period *c* (horizontal dotted line) happens at 41-45% In composition.

3.2.3 Summary

In summary, the structural properties of single-phase InGaN films grown on AlN by plasma-assisted MBE under low growth temperatures and slightly N-rich growth conditions have been investigated. The complete misfit strain relaxation through the formation of a uniform array of misfit dislocations at the InGaN/AlN interface is observed for InGaN films with In contents higher than ~45%, which is lower than that observed for the InGaN/GaN system. Since the In content at which the transition in the structural properties occurs depends on the lattice mismatch between the InGaN layer and the underlayer, various buffer layers can be selected to shift the transition at various In compositions. This transition composition can be estimated by calculating the In content at which the critical thickness reaches a value close to 1-2 MLs.

CHAPTER 4

GROWTH OF DOPED GaN AND InGaN FILMS

The growth and fabrication of InGaN-based solar cells require doped layers to separate and collect the photogenerated carriers. The *p*- and *n*-doped layers establish a built-in electric field across the intrinsic layer to separate the photogenerated carriers. The intensity of the built-in electric field depends on the doping level in the doped layers. In addition, the doped layers create low-resistance contacts with external electrodes for carrier collection.

4.1 Metal-Modulated Epitaxy Growth of Si-Doped GaN

Highly Si-doped GaN films are necessary to form low-resistance *n*-type conductive layers in nitride-based optoelectronic devices. A systematic study was conducted to investigate *n*-GaN layers grown by metal-modulated epitaxy (MME). MME is a growth method in which the metal shutters are periodically opened and closed while the N flux is maintained constant. The present study describes the growth mechanisms of Si-doped GaN film by MME and the associated RHEED signatures observed during growth. The impact of the Si-doping concentration on the electrical and morphological properties of the GaN layers is studied using Hall-effect measurement and atomic force microscopy (AFM).

4.1.1 Experimental Procedure

The *n*-GaN samples were grown on Lumilog semi-insulating GaN:Fe (0001) templates. A 120 nm-thick AlN buffer layer was grown by MME to act as an insulating buffer layer. The AlN layer is used to bury the template native surface oxide and to avoid multi-layer conduction that will disturb the electrical measurement. The *n*-GaN epilayers were grown at 600°C via the MME technique with a 10 s open/10 s closed duty cycle as depicted in Figure 4.1. The Si shutter was not modulated because unlike Mg, Si does not segregate to the surface. The Ga flux was maintained constant at 1.8×10^{-6} torr beam equivalent pressure (BEP), resulting in a III/N ratio of ~1.8, while the Si cell temperature was varied from 975°C to 1240°C. The growth was monitored in real time by RHEED. To examine the RHEED transient signal, the analysis window was centered on the specular RHEED streak of the diffraction pattern. The correlation of RHEED signatures with surface characteristics has been previously studied for the growth of AlN [111, 112] and GaN [100].

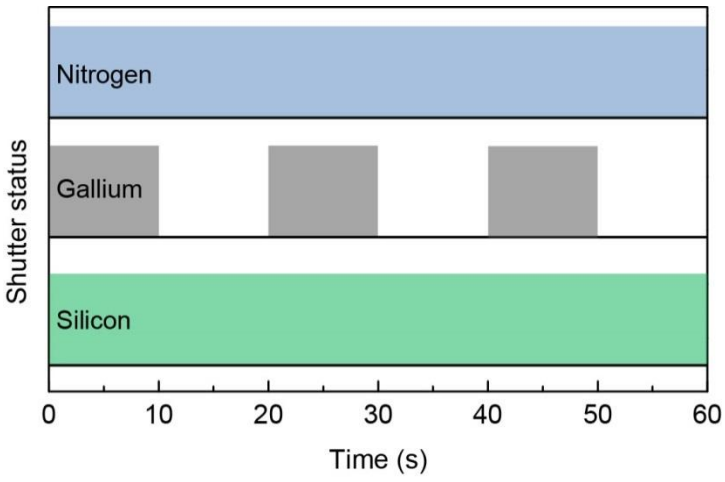

Figure 4.1: Simplified illustration of the modulation scheme used for MME Si-doped GaN.

4.1.2 Results and Discussion

The RHEED-transient features and the corresponding physical mechanisms that occur during the MME growth of Si-doped GaN layers at various portions of the modulation scheme are illustrated in Figure 4.2. Because of the metal-rich (M-rich) condition, a metal bilayer builds-up while the Ga shutter is open (Figure 4.2A). The formation of the Ga chemisorbed adlayer, which attenuates the reflection of the RHEED beam, is associated with the abrupt decay in the RHEED intensity labeled A. The RHEED intensity then reaches a saturation point labeled B, where the intensity decreases much more slowly. This slow decay corresponds to the formation and accumulation of Ga droplets on the surface (Figure 4.2B). After the Ga shutter is closed, a slow increase is observed in feature C as the Ga droplets are consumed by growth of GaN since N is still supplied to the surface (Figure 4.2C). Even if the Ga source is closed, the growth of GaN occurs from the excess metal accumulated during the open shutter period. The subsequent consumption of the Ga bilayer into the film (Figure 4.2D) results in a rapid increase in the signal intensity labeled D. Once the Ga adlayer is consumed, the dry GaN surface is exposed only to the impinging N, creating a N-adsorbed layer (Figure 4.2E). During this portion of the cycle, no growth occurs as there is no source of Ga. The exposure of the surface by the impinging N plasma leads to surface roughening, which is associated with a gradual increase in the RHEED intensity labeled E.

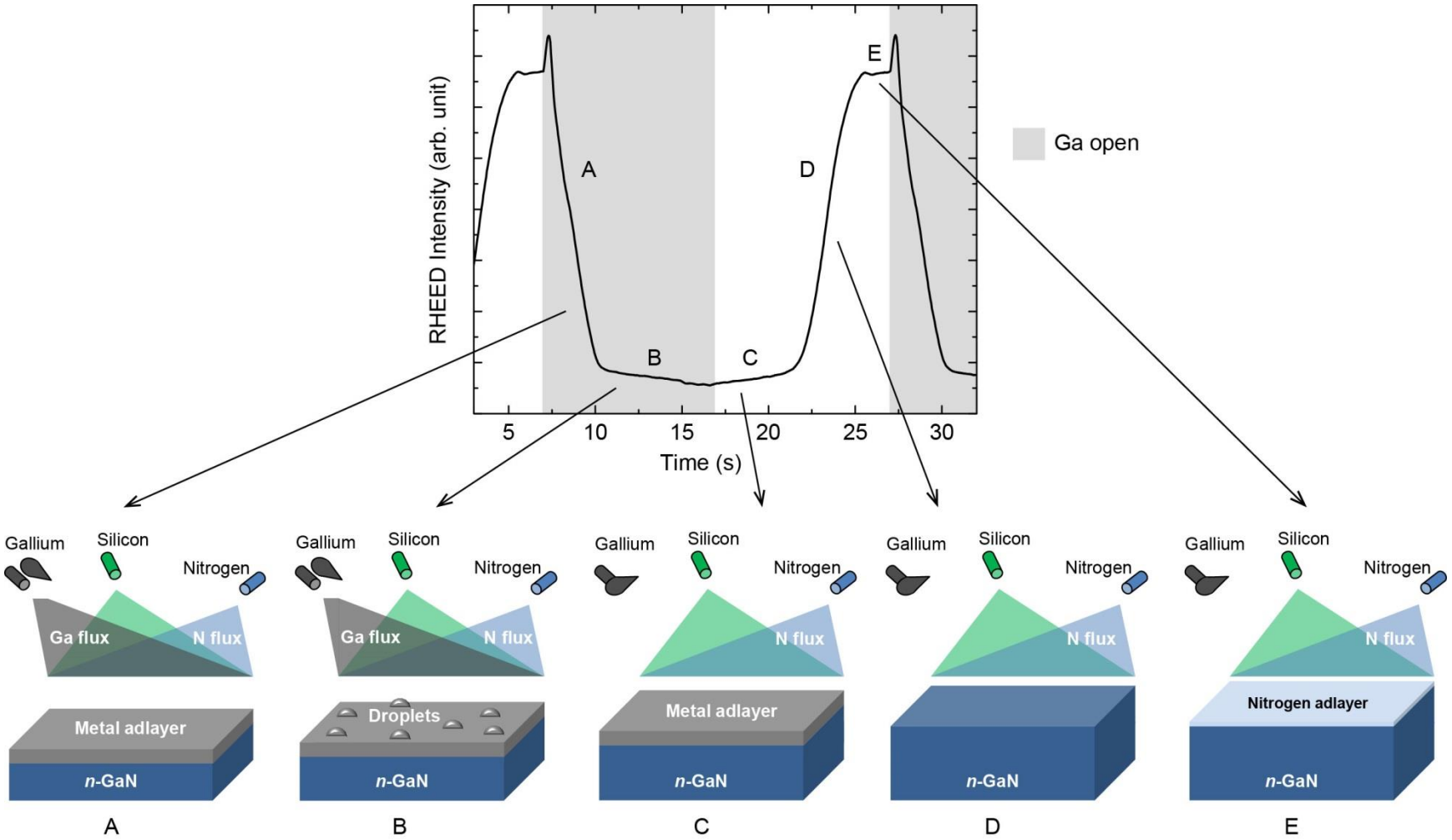

Figure 4.2: (Top) Representative transient RHEED signals for MME Si-doped GaN. Features are labeled and shaded regions indicate Ga-shutter open portions of the modulation scheme. (Bottom) Illustrations of the MME growth mechanisms of Si-doped GaN films. Each illustration corresponds to a feature labeled in the RHEED transient.

The electrical properties of the 500 nm-thick *n*-GaN films grown by MME were determined by Hall-effect measurements using a 0.3 T fixed magnet at room temperature. Indium dots were soldered to the samples as ohmic contacts. Figure 4.3 represents the electron concentration and resistivity as a function of the Si effusion cell temperature. By varying the cell temperature from 975 to 1240°C, electron concentration in the range 10^{17} cm^{-3}-10^{20} cm^{-3} and resistivity in the range 10^{-1}-10^{-4} Ω·cm can be obtained. With increasing the Si cell temperature, an increasing electron concentration in the doped layer is observed, up to a value of $n = 4.4\times10^{20}$ cm^{-3} for a cell temperature of 1240°C. The doping incorporation follows a trend similar to a vapor pressure curve, implying that the incorporation is governed by the impinging rate of dopant atoms. As expected, the resistivity decreases with increasing electron concentration.

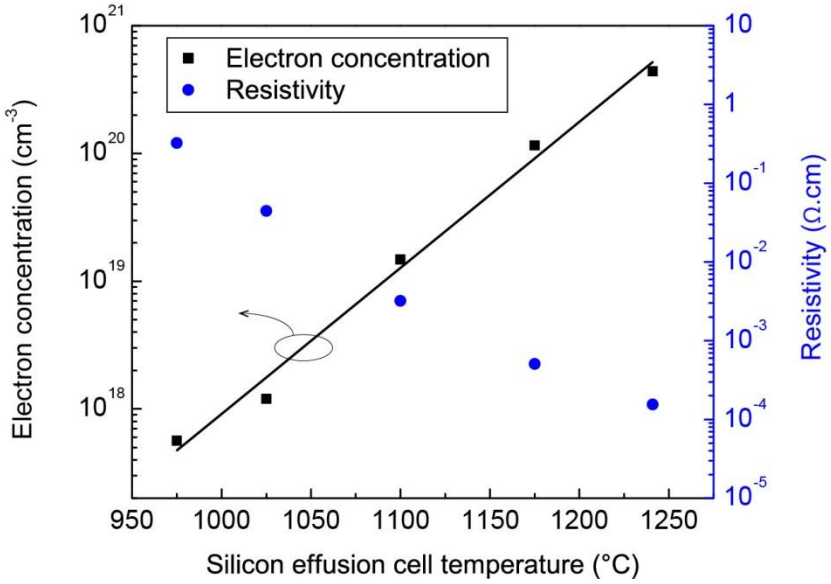

Figure 4.3: Electron concentration and resistivity as a function of Si effusion-cell temperature for Si-doped GaN films grown by MME.

The electron mobility as a function of electron concentration, given in Figure 4.4, follows a bell-shaped curve [113, 114]. This curve shape can be explained by the combined effects of dislocation and ionized-impurity scattering. At lower carrier concentrations, the mobility is limited by scattering by charged dislocations. At higher carrier concentrations, the limitation arises from scattering by ionized impurities.

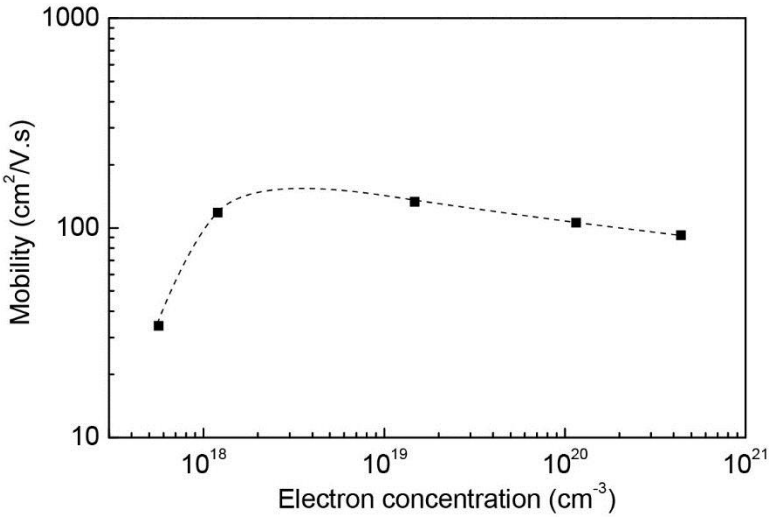

Figure 4.4: Mobility as a function of electron concentration for Si-doped GaN films grown by MME. The dashed line is a guide to the eye.

In general, the morphology of these Si-doped GaN layers is very smooth. The excessively metal-rich conditions typically used for MME-grown *n*-GaN produce a streaky RHEED pattern indicative of smooth surface as observed in Figure 4.2(b). Moreover, (2×2) reconstruction patterns are observed during GaN growth and during cooling after growth, further suggesting a flat and smooth surface [115]. The surface morphology of the *n*-GaN layers was determined after growth by AFM measurement as presented in Figure 4.5. The surface typically displays monolayer steps and

hexagonal-shaped spiral hillocks with a small pit in the center as shown in Figure 4.5(a). These hillocks are composed of monolayer-high steps and terraces that form around dislocations. This surface morphology is characteristic of MBE step-flow growth [116].

The samples with the highest Si concentration (n = 4.4×10^{20} cm^{-3}) exhibits substantial cracking as revealed in Figure 4.5(b). When incorporated at high doping levels, the Si *n*-type dopant introduces a significant amount of strain in the GaN layers, which can cause cracking of the layer [117-119]. Similar cracking has been previously observed for Si levels above 2×10^{19} cm^{-3} due to tensile stress occurring in the film [120]. This incorporation limit can be extended to the low-10^{20} cm^{-3} range via the MME technique by controlling the kinetics of Si incorporation using low substrate temperatures and metal-rich fluxes.

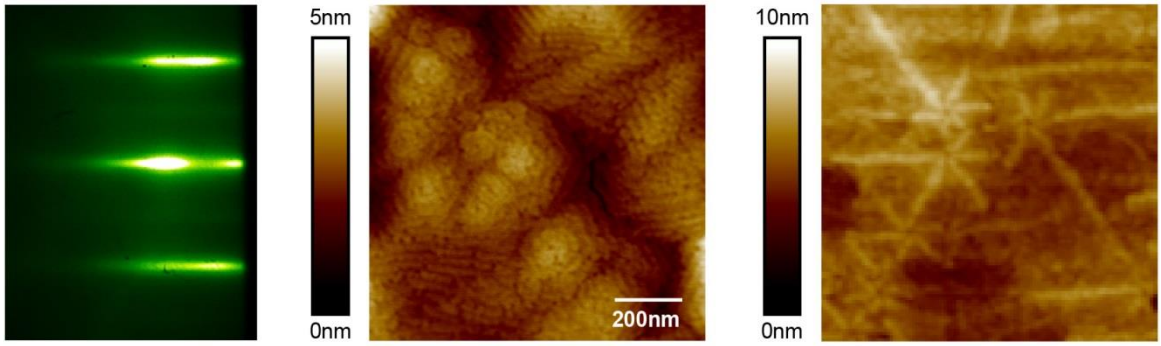

Figure 4.5: (a) Typical RHEED pattern during growth of MME Si-doped GaN. (b) 1×1 μm representative AFM image of Si-doped GaN films showing hexagonal hillocks typical of dislocation-mediated step-flow growth of GaN by MBE. (c) 1×1 μm AFM image of highly Si-doped GaN films showing cracking.

4.1.3 Summary

This study examined the growth of Si-doped GaN films by MME. The correlation between surface characteristics and RHEED signatures observed at various portions of the shutter cycle was studied. The doping as a function of the Si effusion-cell temperature was investigated to evaluate the impact of Si incorporation on the structural and electrical properties of *n*-GaN epilayers. This systematic study provides a useful calibration and baseline for subsequent *n*-GaN device layers.

4.2 Metal-Modulated Epitaxy Growth of Mg-Doped GaN

The ability to achieve high-quality *p*-type GaN films is essential for the improvement of nitride-based devices, such as LEDs, lasers, heterojunction bipolar transistors (HBTs), and solar cells. While Mg is the most commonly used *p*-type dopant, Mg-doped nitride-based devices have limited performance in part because of hole concentrations limited in the mid-10^{18} cm^{-3} range [24, 25] and highly resistive *p*-type layers resulting from low hole mobilities.

This *p*-doping issue can be significantly improved using MME [27, 28, 121]. MME allows for control of the kinetics of Mg incorporation while using low substrate temperatures, resulting in highly *p*-type nitride films with adequate crystal quality [29, 122]. Experimental studies have resulted in highly *p*-type III-nitride films with hole concentrations exceeding 7×10^{19} cm^{-3} in GaN and negligible carrier freeze-out [29]. By opening and closing the metal shutters, MME alternates between the N-rich and M-rich regimes. Under N-rich conditions, Mg dopants preferentially incorporate into Ga/In substitutional sites [123]. Furthermore, under N-rich conditions, the formation energy of

nitrogen vacancies that can act as compensating centers is higher than that under M-rich condition [124]. However, N-rich growth usually results in lower material quality due to surface faceting that can create crystalline defects such as grain boundaries and dislocations [27]. In contrast, M-rich growth results in smooth surfaces that prevent the formation of defects resulting from faceting. Under the M-rich regime, however, the formation energy of nitrogen vacancies decreases, leading to a higher density of compensating centers. By periodically modulating the metal fluxes, MME takes advantage of both N-rich and M-rich growth conditions.

4.2.1 Experimental Procedure

All Mg-doped GaN films were grown by MME on 1×1 cm semi-insulating MOCVD-grown GaN-on-sapphire template in a Riber 32 MBE system. Nitrogen was supplied by a Veeco UNI-Bulb RF plasma source with a RF power of 350 W and N_2 flow of 1.3 sccm, resulting in a N-limited growth rate of approximately 1 μm/hr. While a Veeco SUMO cell was used for Ga, a standard effusion cell was used for Mg with a cell temperature of 200°C. A 120 nm-thick AlN buffer layer was grown by MME to ensure that all electrical measurements resulted from the *p*-GaN layer. The *p*-type GaN:Mg films were grown by MME at 600°C with a III/N ratio of ~1.3. To avoid the formation of Mg clusters, Ga and Mg were shuttered simultaneously with a cycle of 5 s open/10 s closed. The modulation scheme is illustrated in Figure 4.6. RHEED patterns and transients were used to characterize the films *in situ*. Post-growth analysis was performed by AFM to determine the surface morphology and Hall-effect measurements to determine the electrical properties using indium-dot contacts. Similar to the previous study of Si-doped GaN films, the correlation between RHEED signal features and the

physical mechanisms occurring at various portions of the MME cycle has been investigated.

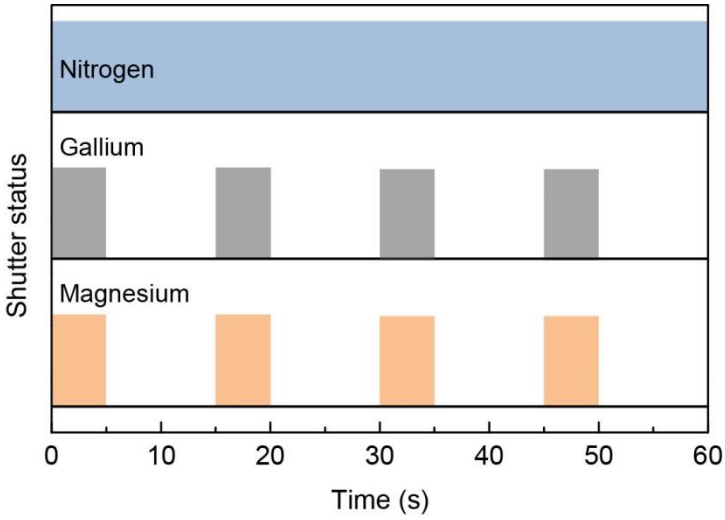

Figure 4.6: Simplified illustration of the modulation scheme used for MME Mg-doped GaN.

4.2.2 Results and Discussion

Figure 4.7 shows a typical transient RHEED signal for MME Mg-doped GaN with three characteristic features and the growth mechanisms associated with these signatures. The abrupt decay in the RHEED intensity labeled A is related to the formation of the excess-Ga adlayer (Figure 4.7A). Since the Ga flux is less M-rich and since the shutter open time is shorter than those used in the Si-doped case, the metal bilayer is not complete and no Ga droplets are formed. The absence of Ga-droplet accumulation is evidenced by the absence of the slow decay observed in feature B in Figure 4.2 for the case of Si-doped GaN.

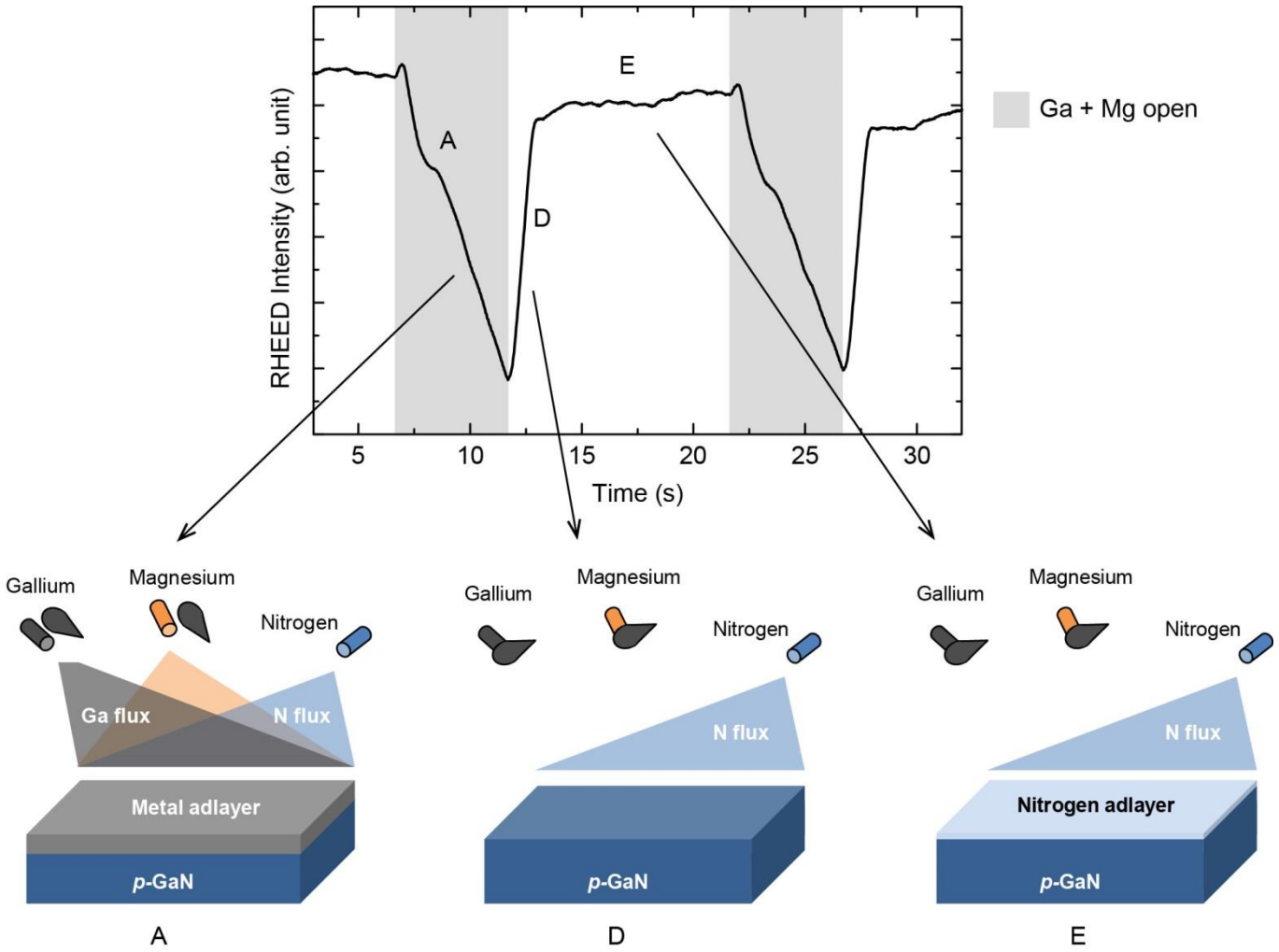

Figure 4.7: (Top) Representative transient RHEED signals for MME Mg-doped GaN. Features are labeled and shaded region indicates Ga and Mg shutter open portion of the modulation scheme. (Bottom) Illustrations of the MME growth mechanisms of Mg-doped GaN films. Each illustration corresponds to a feature labeled in the RHEED transient.

After the metal shutters are closed, the incomplete metal bilayer is consumed into the film (Figure 4.7D), leading to a rapid increase in the signal intensity visible in feature D. The absence of delay after shutter closing further confirms the absence of metal droplets on the surface. Once the metal adlayer is fully consumed, the RHEED intensity recovers to its starting value prior to shutter opening in feature E. The exposure of the GaN surface by the impinging N plasma results in the formation of a N adlayer (Figure 4.7E).

These growth conditions usually result in *p*-GaN films with hole concentrations in the $3\text{-}4\times10^{19}$ cm^{-3} range, resistivities of approximately 0.2 Ω·cm, and mobilities of ~0.9 $cm^2/V\cdot s$ measured at room temperature. Because of the high vapor pressure of Mg, the optimal Mg cell temperature fluctuates, rendering the use of a standard effusion cell unstable and unpractical. To address this instability issue, the use of a Veeco corrosive series valved cracker has been previously introduced [28, 29, 121, 122].

The surface morphology of Mg-doped GaN films is drastically different than that of undoped or Si-doped GaN films. This dissimilarity can be observed from the RHEED pattern depicted in Figure 4.8(a). While undoped and *n*-GaN layers exhibit a streaky pattern, *p*-GaN films reveal elongated spots that indicate rougher surfaces. Shown in Figure 4.8(b) is a representative 1×1 μm AFM image of a 100 nm-thick *p*-GaN layer. The sample displays a grainy surface morphology that is typical for MME-grown, highly *p*-doped GaN films. The pits are due to the non-optimized AlN growth conditions, which results in surface voids that propagate through the *p*-GaN layer.

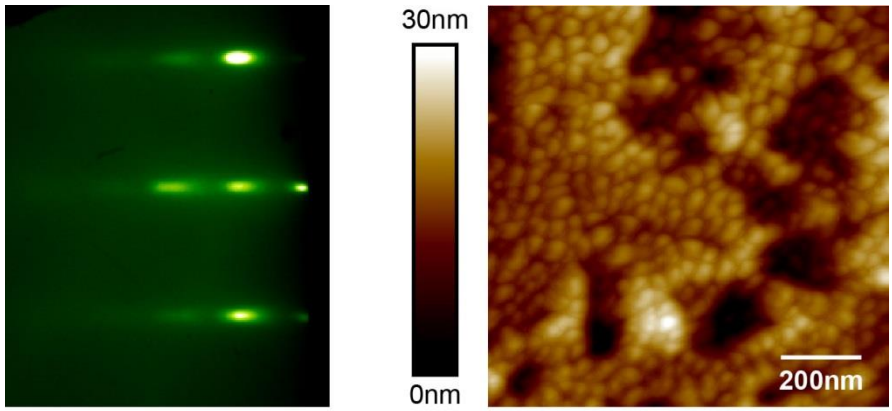

Figure 4.8: (a) Typical RHEED pattern during growth of MME Mg-doped GaN. (b) Representative AFM image of *p*-GaN films grown by MME.

4.2.3 Summary

In summary, this section describes the growth mechanisms and RHEED monitoring of Mg-doped GaN films grown by MME. The MME growth conditions with lower III/N ratio and shorter open-shutter cycle typically results in extremely-high hole concentrations and grainy morphologies. The increased hole concentration can be attributed to optimal incorporation of Mg dopants into Ga-substitutional sites with minimal formation of compensating defects. These highly-doped *p*-GaN films offer promise for future subcells and tunnel junctions.

4.3 Growth of Mg-Doped InGaN by Metal-Modulated Epitaxy and N-Rich MBE

While InGaN homojunction solar cells are the only design that can achieve suitable efficiencies according to simulation results, these devices are currently very challenging to achieve. The growth and fabrication of homojunction cells require major improvements in *p*-type doping of InGaN material. The electrical, optical, and structural properties of Mg-doped InGaN films, mainly grown by MOCVD, have been previously reported [33, 34, 125]. The hole concentration in *p*-InGaN depends on the growth conditions, the In content, and the crystal quality of the InGaN layers [126, 127]. As the In content increases, the Mg-acceptor activation energy decreases leading to higher hole concentrations [34, 128]. However, the concentration of background donors that compensate acceptors and thus, decrease the *p*-doping efficiency, increases with increasing In content [37]. At high Mg-doping level, the hole concentration decreases as a result of self-compensation due to the formation of a deep donor and/or the degradation of the crystal quality [126]. While *p*-type InGaN layers with In composition as high as 35% have been previously reported [33, 129], this work focuses on $In_{0.25}Ga_{0.75}N$ since this In composition is the highest composition that can consistently be doped *p*-type [127, 130-132]. In this study, the effect of the III/N ratio on the structural, electrical, and optical properties of *p*-InGaN films is investigated.

4.3.1 Experimental Procedure

The Mg-doped InGaN films were grown in a Riber 32 MBE system using a Veeco UNI-Bulb RF plasma source for N, a Veeco SUMO cell for Ga, a standard effusion cell for In, and a Veeco corrosive series valved cracker for Mg with a bulk temperature of

300°C and a valve opening of 240 mils. The substrates used for all films were 1×1 cm semi-insulating MOCVD-grown GaN-on-sapphire templates. The targeted structure, depicted in Figure 4.9, consists of a 50 nm-thick 25% *p*-InGaN layer followed by a 25 nm-thick composition-graded *p*-InGaN film and a 5 nm *p*-GaN cap. The growth temperature was maintained at 450°C for the 25% InGaN films and linearly graded to 550°C during the growth of the composition-graded layer.

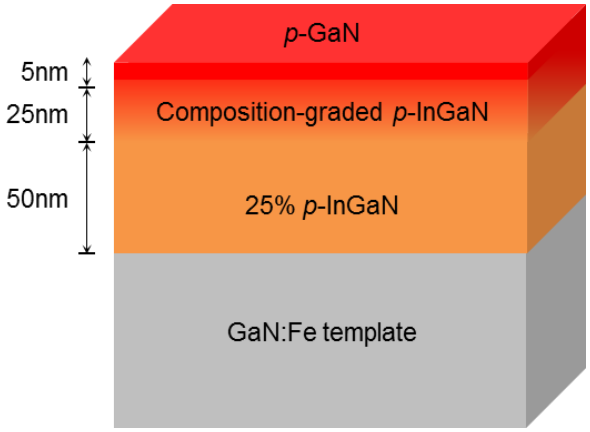

Figure 4.9: Schematic structure of the *p*-InGaN/composition-graded *p*-InGaN/*p*-GaN samples.

While maintaining a constant In to Ga flux ratio to produce a fixed In composition of 25%, the total normalized metal flux was varied to investigate the impact of the III/N ratio on the characteristics of the Mg-doped InGaN layers. Four samples with various III/N ratios were grown: one N-rich *p*-InGaN film with III/N = 0.9 and three MME *p*-InGaN films with III/N = 1.2, 1.3, and 1.6. In the case of the N-rich *p*-InGaN film, the In, Ga, and Mg shutters are opened simultaneously and maintained open throughout the growth (no modulation of the metal sources). In the case of the MME *p*-InGaN films, the Mg source is modulated concurrently with the In and Ga sources. The open/close time of

the modulation scheme, illustrated in Figure 4.10, was varied depending on the III/N ratio to ensure that the thickness of the excess-metal adlayer did not exceed a ML to avoid In surface segregation [45]. The adlayer buildup and the film morphology were monitored *in situ* by RHEED transient and RHEED pattern respectively. The structural, electrical, and optical properties of the films were investigated *ex situ* by XRD, AFM, hot-probe measurement, four-point-probe measurement, TEM, and CL.

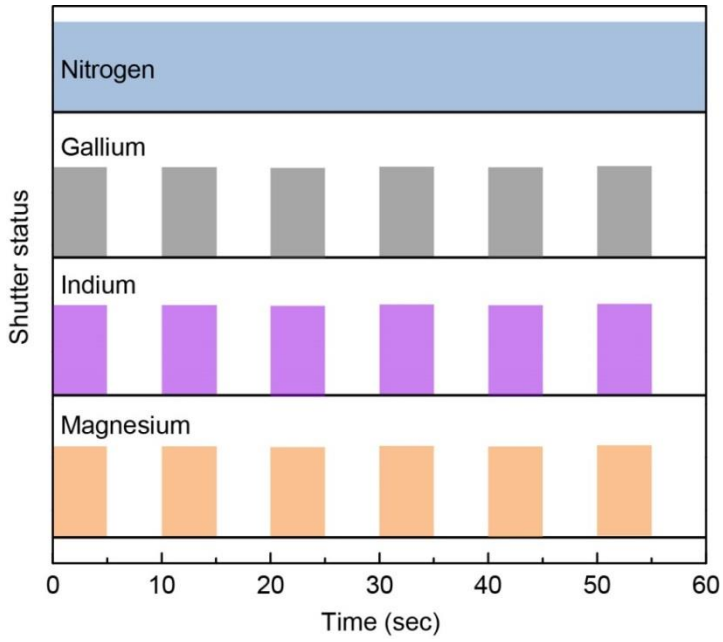

Figure 4.10: Simplified illustration of the modulation scheme used for the MME Mg-doped InGaN.

4.3.2 Results and Discussion

The characteristics of the *p*-InGaN films grown under various methods and III/N ratios are listed in Table 4.1. Figure 4.11 shows representative RHEED patterns for the Mg-doped InGaN films with various III/N ratios. The N-rich layer with III/N = 0.9 displays a spotty RHEED pattern, indicative of a rough surface (Figure 4.11(a)) as expected for a Mg-doped N-rich film. As the III/N ratio increases, the spots become more elongated, suggesting smoother surfaces. The MME layer with III/N = 1.6 displays a streaky RHEED pattern indicative of a flat surface (Figure 4.11(d)).

Table 4.1: Characteristics of Mg-doped InGaN layers.

Growth method	III/N	(0002) RC FWHM (arcsec)	(10$\bar{1}$5) RC FWHM (arcsec)	Fringe thickness (nm)	In content	Roughness 5×5μm (nm RMS)	Resistivity (Ω·cm)
N-rich	0.9	537	1453	NA	27.7%	5.99	~24
	1.2	562	1987	65	27.5%	2.12	~11
MME	1.3	527	2205	70	23%	0.97	~20
	1.6	374	1567	71	18.7%		~360

The MME RHEED transients shown in Figure 4.12 also give information on the surface morphology and surface kinetics. The shaded regions correspond to the metal-shutter open portions of the modulation scheme. The RHEED oscillations are attributed to the accumulation and subsequent consumption of the excess-metal adlayer [45]. A minimum intensity corresponds to destructive interference caused by an

incomplete adlayer, and a maximum intensity corresponds to constructive interference caused by a complete adlayer. Upon opening the metal shutters, a RHEED oscillation associated with the adsorption of an incomplete metal adlayer is observed. For all MME samples, the metal shutters are closed before a full ML forms to prevent In surface segregation. Thus, only a minimum intensity is observed in the shaded region of the modulation scheme. After the metal shutters are closed, a RHEED signal that resembles the time-opposite of the shaded region occurs. This behavior corresponds to the consumption of the incomplete metal adlayer [45]. After the metal adlayer is consumed, a steady state is reached. The gradual increase in RHEED intensity over time, observed in Figure 4.12(a) and (b) but not observed in Figure 4.12(c), demonstrates the roughening of the surface with decreasing III/N ratio.

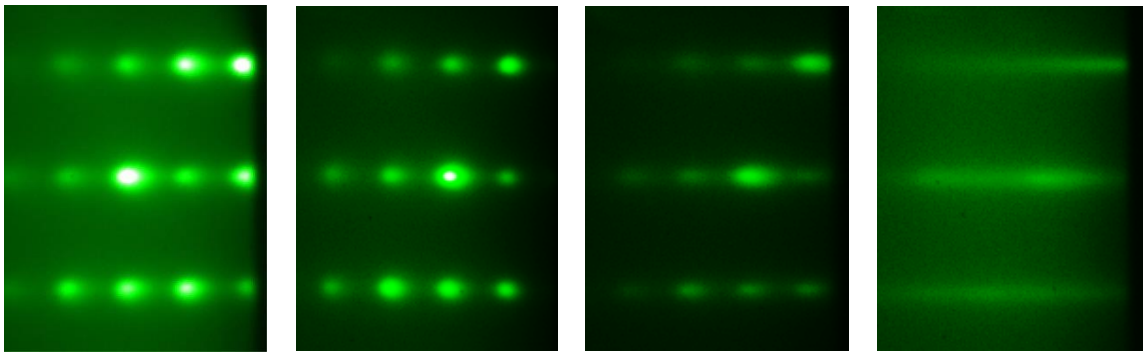

Figure 4.11: RHEED patterns during growth of Mg-doped InGaN grown under (a) N-rich III/N = 0.9, (b) MME III/N = 1.2, (c) MME III/N = 1.3, and (d) MME III/N = 1.6 conditions.

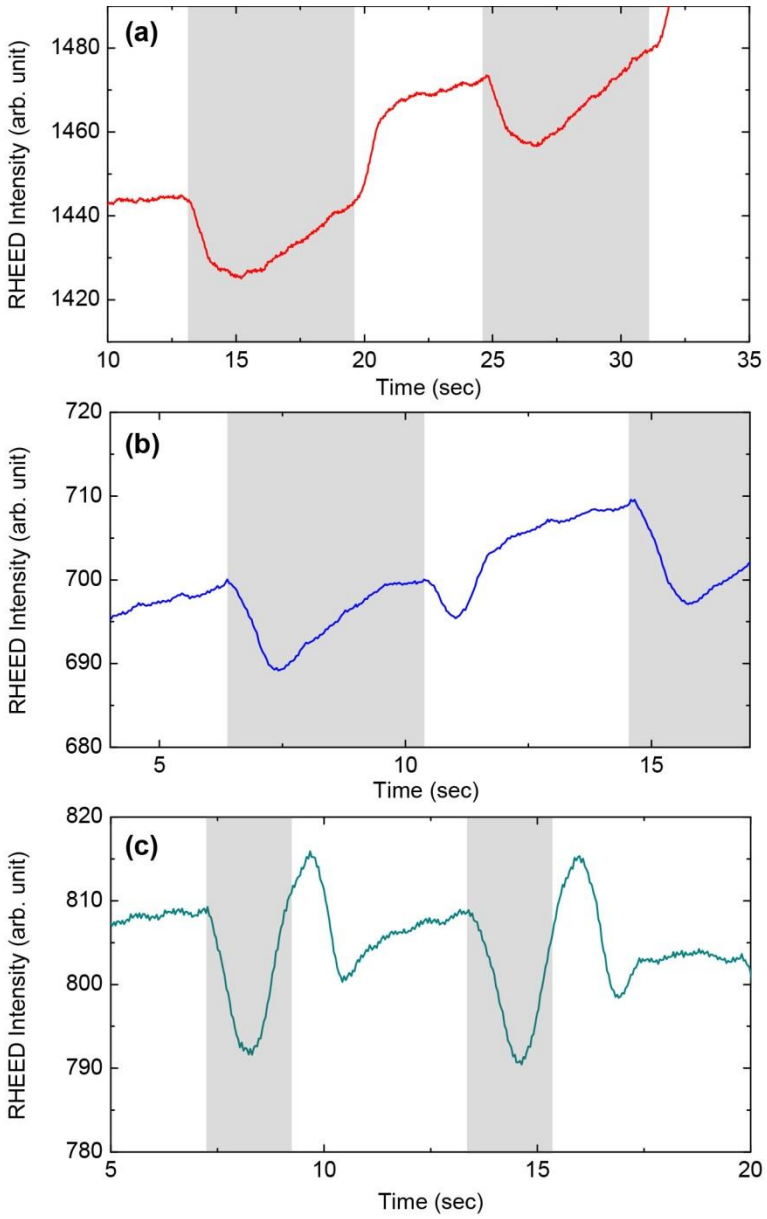

Figure 4.12: Transient RHEED signals for MME Mg-doped InGaN grown under (a) MME III/N = 1.2, (b) MME III/N = 1.3, and (c) MME III/N = 1.6 conditions. The shaded regions indicate the Ga, In, and Mg shutter open portions of the modulation scheme.

All Mg-doped InGaN films were determined to be *p*-type as measured by hot-probe measurements. Hall-effect measurements, used to determine the hole concentration, lead to inconclusive results possibly due to the reduced mobility of the InGaN layers and/or the native oxide at the GaN:Fe/InGaN interface that typically induces *n*-type conductivity. This native surface oxide can result in a multi-layer conduction that can disturb the electrical measurement. The resistivity of the *p*-InGaN samples, listed in Table 4.1, was measured by the Van der Pauw method. For the MME samples, the resistivity increases as the III/N ratio increases. Since the Mg cracker conditions (temperature and valve opening) are similar for all samples, the Mg / (In + Ga) ratio decreases as the (In + Ga) flux, *i.e.* the III/N ratio, increases leading to lower Mg concentration and thus, higher resistivity. The MME-grown film with III/N = 1.6 displays a resistivity of ~360 Ω·cm, suggesting that the *n*-doping from the background donors is compensated by the low Mg doping. Such a compensated InGaN layer could be used in the active region of a solar cell to extend the width of the depletion region.

The structural property of the *p*-InGaN layers was analyzed by XRD. Figure 4.13 depicts the (0002) diffraction scans of the *p*-InGaN films grown under various conditions. The single-phase InGaN films do not display In segregation as evidenced by the absence of peaks corresponding to InN or metallic In. As the III/N ratio increases, the Pendellösung fringes become more pronounced, suggesting smoother surfaces. This behavior is also evidenced by the 5×5 μm AFM images of *p*-InGaN shown in Figure 4.14. The root-mean-square (RMS) roughness, listed in Table 4.1, decreases with increasing the III/N ratio. The N-rich sample is significantly rougher than the MME-grown samples since it does not benefit from the smoothing effect of the wetting layer.

However, independent of the growth conditions, the *p*-InGaN films display a grainy morphology, shown in Figure 4.15, typical for N-rich and MME *p*-doped III-nitride films.

The composition and degree of relaxation of the InGaN:Mg layers were determined from XRD RSMs as illustrated in Figure 4.16. All InGaN films are mostly relaxed, but no clear trend in the relaxation as a function of the III/N ratio is observed.

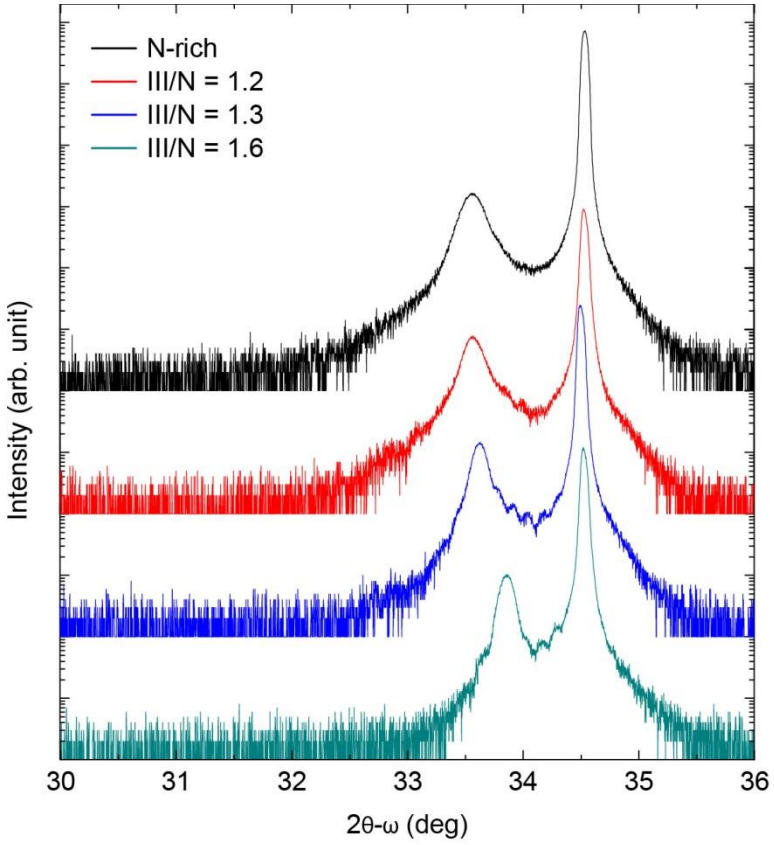

Figure 4.13: XRD (0002) diffraction scans of *p*-InGaN grown under N-rich III/N = 0.9, MME III/N = 1.2, MME III/N = 1.3, and MME III/N = 1.6 conditions.

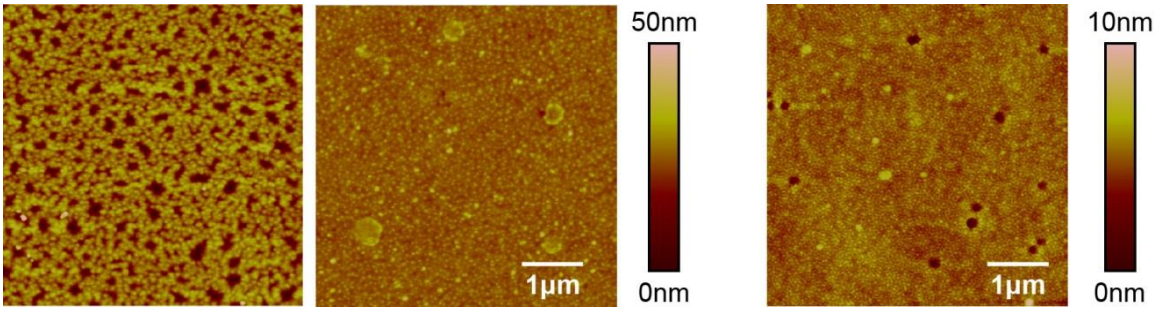

Figure 4.14: 5×5 μm AFM images of *p*-InGaN grown under (a) N-rich III/N = 0.9, (b) MME III/N = 1.2, and (c) MME III/N = 1.3 conditions.

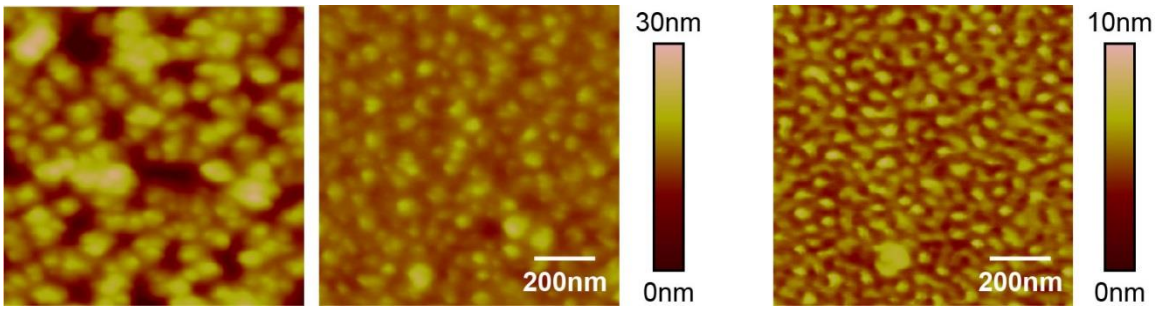

Figure 4.15: 1×1 μm AFM images of *p*-InGaN grown under (a) N-rich rich III/N = 0.9, (b) MME III/N = 1.2, and (c) MME III/N = 1.3 conditions.

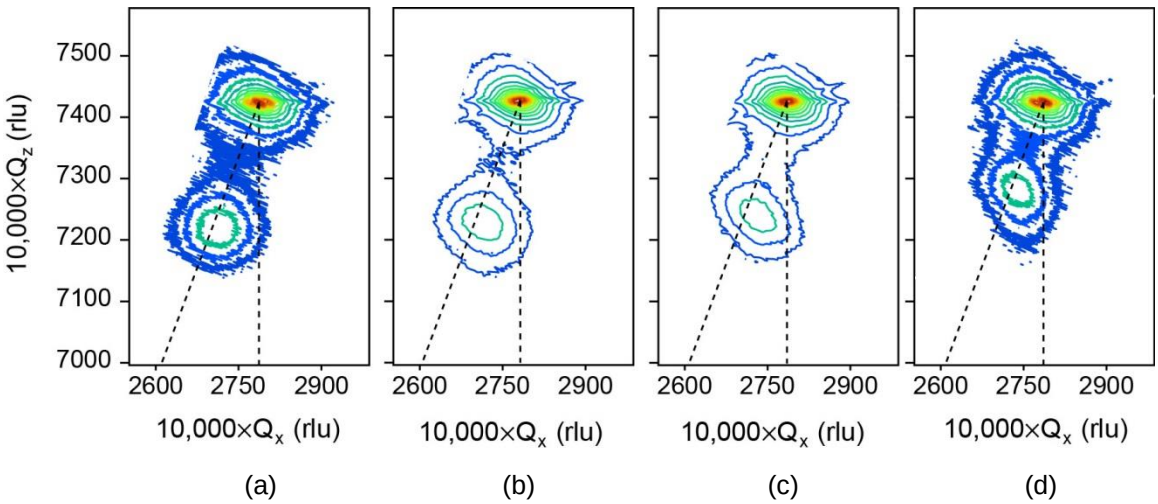

Figure 4.16: RSMs along the $(10\bar{1}5)$ reflection of *p*-InGaN grown under (a) N-rich III/N = 0.9, (b) MME III/N = 1.2, (c) MME III/N = 1.3, and (d) MME III/N = 1.6 conditions.

TEM was performed to assess the crystal quality and defect structures of the *p*-InGaN layers. Figure 4.17 depicts the cross-section TEM images with a diffraction contrast set at $\bar{g}$ = [0002], which reveals threading dislocations. For all samples, the InGaN films demonstrate a columnar structure with large V-pits at the surface. While the GaN/InGaN interfaces are sharp, the InGaN films exhibit threading dislocations, represented by dark vertical lines that originated at the interfaces. These dislocations are located at the domain boundaries of the columnar structures. Figure 4.18 depicts the cross-section TEM images with a diffraction contrast set at $\bar{g} = [1\bar{1}00]$, which reveals stacking faults. All films exhibit stacking faults, which are cubic inclusions in the hexagonal lattice. The density of stacking faults in the N-rich sample is lower than in all MME samples, confirming the results observed previously for undoped InGaN films [51, 105] and described in Chapter 3. The density of stacking faults increases with increasing the III/N ratio, suggesting that their formation is promoted by the M-rich growth condition. The MME InGaN layers display an initial high density of short stacking faults near the GaN/InGaN interface. As the thickness of the InGaN film increases and as the In composition decreases through the composition-graded layer, the stacking faults elongate and become sparser.

The optical properties of the *p*-InGaN films were studied by CL spectroscopy at room temperature. The N-rich InGaN layer exhibits CL as shown in Figure 4.19(a). The CL spectrum can be fitted by two Gaussian curves. The main peak centered at 552 nm is associated with the *p*-InGaN films, while the peak centered at 600 nm is associated with yellow luminescence from the MOCVD-grown GaN template. In contrast with the N-rich film, negligible luminescence was observed for the MME-grown samples as

shown in Figure 4.19(b). The absence of luminescence for MME InGaN film with low In content is concordant with previous observations [51], and can be explained by the high density of stacking faults.

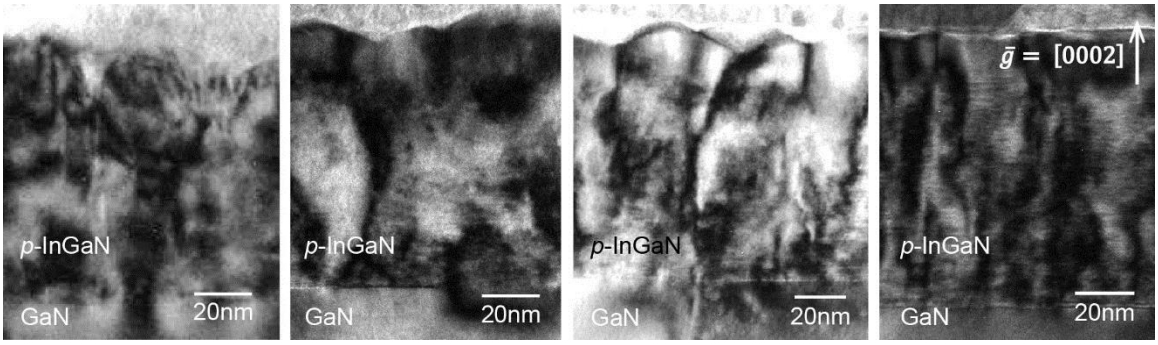

(a) (b) (c) (d)

Figure 4.17: Cross-section TEM images of *p*-InGaN grown under (a) N-rich III/N = 0.9, (b) MME III/N = 1.2, (c) MME III/N = 1.3, and (d) MME III/N = 1.6 conditions showing threading dislocations.

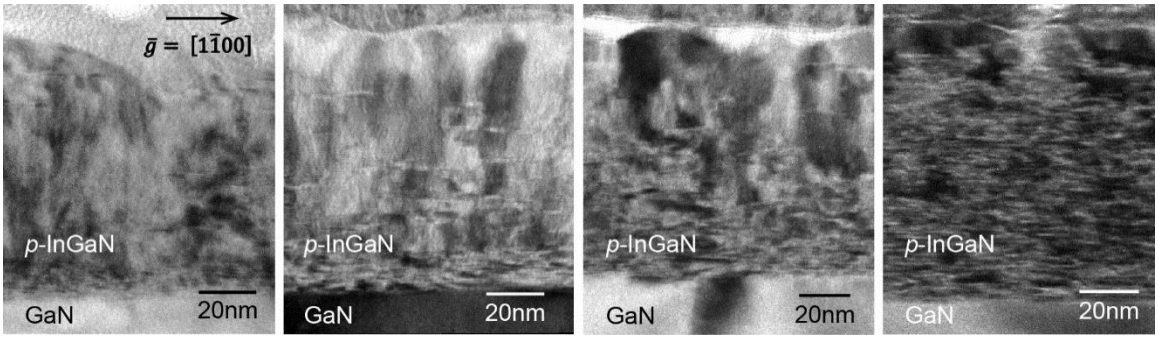

(a) (b) (c) (d)

Figure 4.18: Cross-section TEM images of *p*-InGaN grown under (a) N-rich III/N = 0.9, (b) MME III/N = 1.2, (c) MME III/N = 1.3, and (d) MME III/N = 1.6 conditions showing stacking faults.

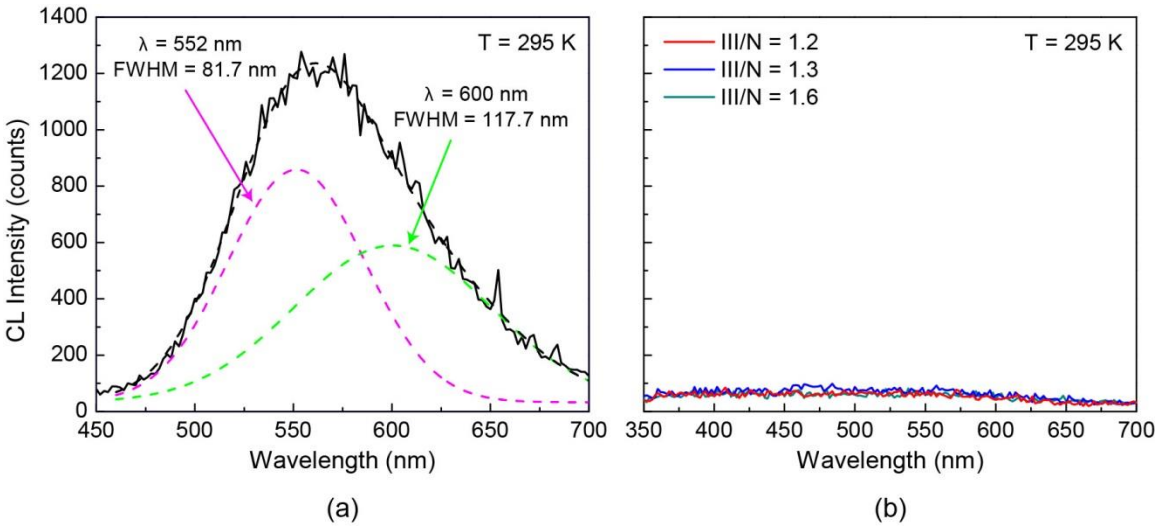

Figure 4.19: (a) CL spectrum of N-rich Mg-doped InGaN film. The dashed lines represent the Gaussian fittings. (b) CL spectra of MME Mg-doped InGaN films.

4.3.3 Summary

This study investigated the growth of Mg-doped InGaN films by N-rich MBE and MME. The effect of III/N ratio on the electrical, structural, and optical properties of *p*-InGaN films was examined. Independent of the growth technique, all Mg-doped InGaN layers exhibit *p*-type conductivity as determined by hot-probe measurements, a grainy morphology as determined by AFM, and no phase separation as determined by XRD. As the III/N ratio increases, the films become more resistive. The M-rich conditions result in smoother surfaces but higher stacking-fault densities. While the MME-grown samples do not display optical emission due to these crystalline defects, the N-rich film shows enhanced optical properties. The growth of these *p*-InGaN films offer promise for future InGaN homojunction solar cells, but further effort is required to extend *p*-type doping to higher In composition.

CHAPTER 5

FABRICATION PROCESS OF III-NITRIDE SOLAR CELLS

In addition to growth, InGaN solar cells demand a process to fabricate and optimize devices. A processing sequence is developed to fabricate III-nitride devices. A mask set with multiple analysis structures is designed to investigate the device performance and determine pathways for improvement. Ohmic contacts to both *n*- and *p*-GaN are studied using the circular transmission line model (CTLM). Finally, optimization of the grid contact to minimize the combined optical and resistive losses is considered.

5.1 Fabrication Process Sequence

To fabricate InGaN-based solar cells, a process based on a standard nitride-semiconductor processing technique was developed. A typical device processing sequence for an InGaN *p*-*i*-*n* solar cell is depicted in Figure 5.1. The fabrication of the solar cell uses traditional optical lithography, dry etching, metal deposition, and lift-off. A standard solvent clean followed by deionized-water (DI) rinsing and N_2 blow drying is used to clean the wafer before and between processing steps to clear the sample of any grease, dust, or organic impurities. First, a mesa pattern is formed by photolithography on the *p*-*i*-*n* structure to define the area of the cell structure. The thick photoresist (PR) layer, cured at 120°C for 30 minutes to harden it, serves as a mask for the pattern transfer. The mesa structure is transferred via inductively coupled plasma (ICP) etching using a BCl_3/Cl_2 chemistry to expose the *n*-type layer (Figure 5.1(b)). The pattern transfer requires dry etching due to the high chemical stability and the high bond strength of

nitride semiconductors. Next, the *n*-ohmic contact, which consists of titanium/aluminum/titanium/gold (Ti/Al/Ti/Au 30/100/30/50 nm), is formed by photolithography and electron-beam evaporation (Figure 5.1(c)). Prior to the metallization, the sample is dipped in buffered oxide etch (BOE) for 30 s to etch native oxides. After another photolithography step and a hydrochloric acid (HCl) treatment, a thin layer of nickel/gold (Ni/Au 5/5 nm) is then deposited on the resistive *p*-type layer to serve as a semitransparent current-spreading layer to promote lateral conduction and thus, enhance carrier collection (Figure 5.1(d)). Finally, a Ni/Au (30/50 nm) grid with 5 μm-wide fingers is deposited to form *p*-contact metal schemes by electron-beam evaporation (Figure 5.1(e)). Figure 5.2 shows a top-view micrograph of a fabricated 1×1 mm device with the grid contact. A detailed process flow for a typical *p*-*i*-*n* InGaN solar-cell fabrication is provided in Appendix B.

To test this fabrication process, several III-nitride devices including a simple *p*-*i*-*n* diode and an InGaN/GaN multi-quantum well (MQW) light-emitting diode (LED) structure were fabricated without contact anneal. Figure 5.3(a) and (b) represent the *J*-*V* curves of the diode and the LED, respectively. The devices exhibit clear rectification and low leakage current. The LED structure displays electroluminescence, PV, and photoconductance effects measured with a UV-deficient light, but shunt resistance appears to be the main issue, leading to a poor V_{oc}. While this fabrication process requires further optimization, particularly regarding the contact-annealing steps, these results attest its viability for the fabrication of future InGaN solar cells.

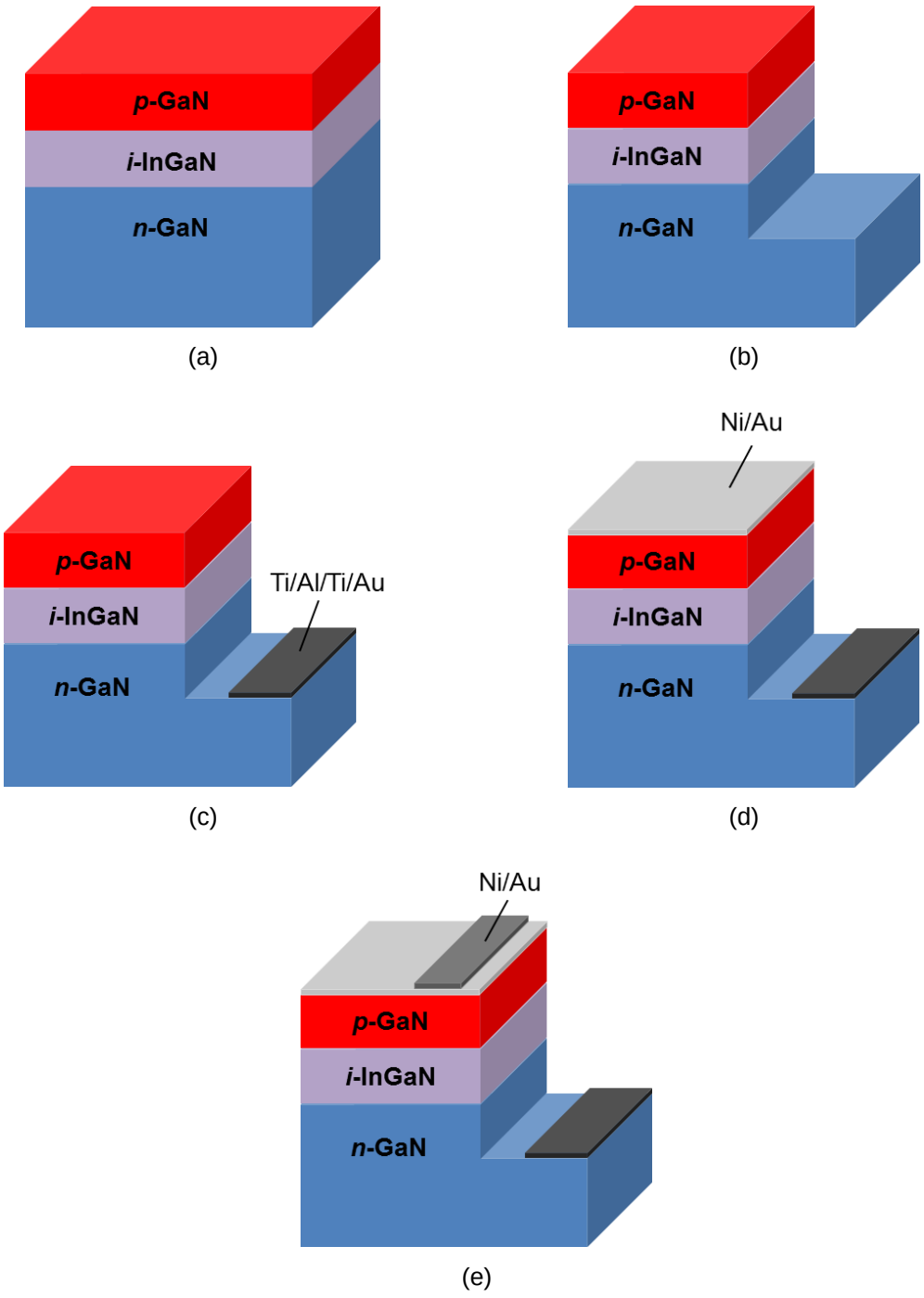

Figure 5.1: Schematic of the fabrication process: (a) as-grown InGaN *p*-*i*-*n* structure, (b) mesa etch, (c) *n*-type metal deposition, (d) spreading metal deposition, (e) *p*-type metal deposition.

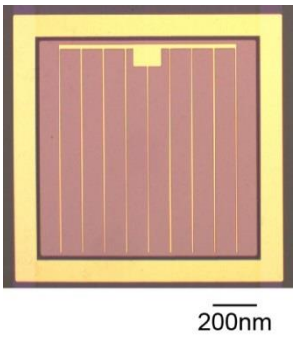

Figure 5.2: Top-view micrograph of an example 1×1 mm device.

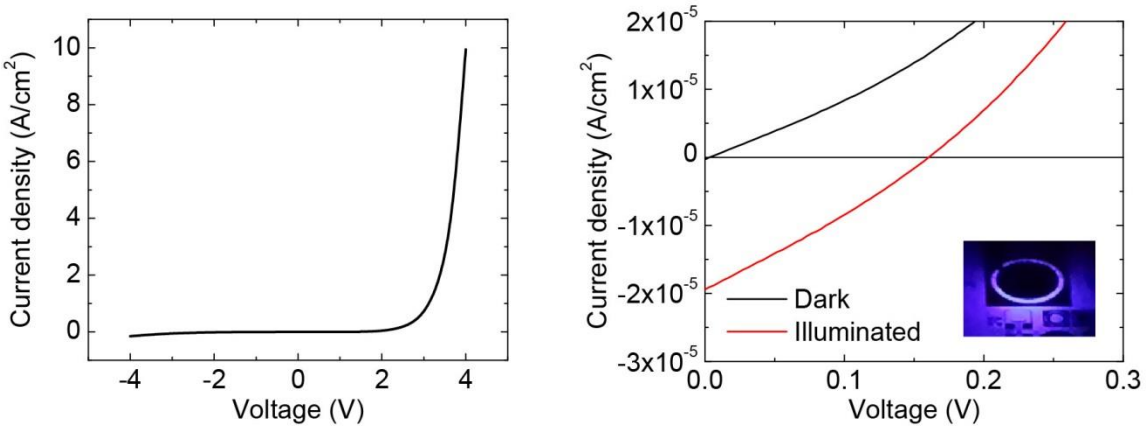

(a) (b)

Figure 5.3: *J-V* curves of the fabricated (a) *p-i-n* diode and (b) MQW LED under dark and illuminated conditions [122]. The inset shows the blue electroluminescence of the MQW LED.

5.2 Mask Layout

The mask set was developed using the physical layout editor Clewin and was fabricated by laser writing on a 4"x4" quartz photomask blank coated with chromium and PR. The total pattern dimension was designed to pattern a 1×1 cm sample. The designed mask set includes 20 solar-cell devices with various areas (500×500 μm, 750×750 μm, and 1×1 mm) and grid-spacing values ranging from 100 to 300 μm. Figure 5.4 shows the mask layout used for the solar-cell structures.

The grey features represent the mesa structure, the blue features represent the *p*-type metal, and the green features represent the *n*-type contact. The current-spreading layer for the *p*-type contact is not included for clarity. The mask also contains various diagnostic structures including CTLM patterns, metal-resistance measurement, and diodes with various sizes.

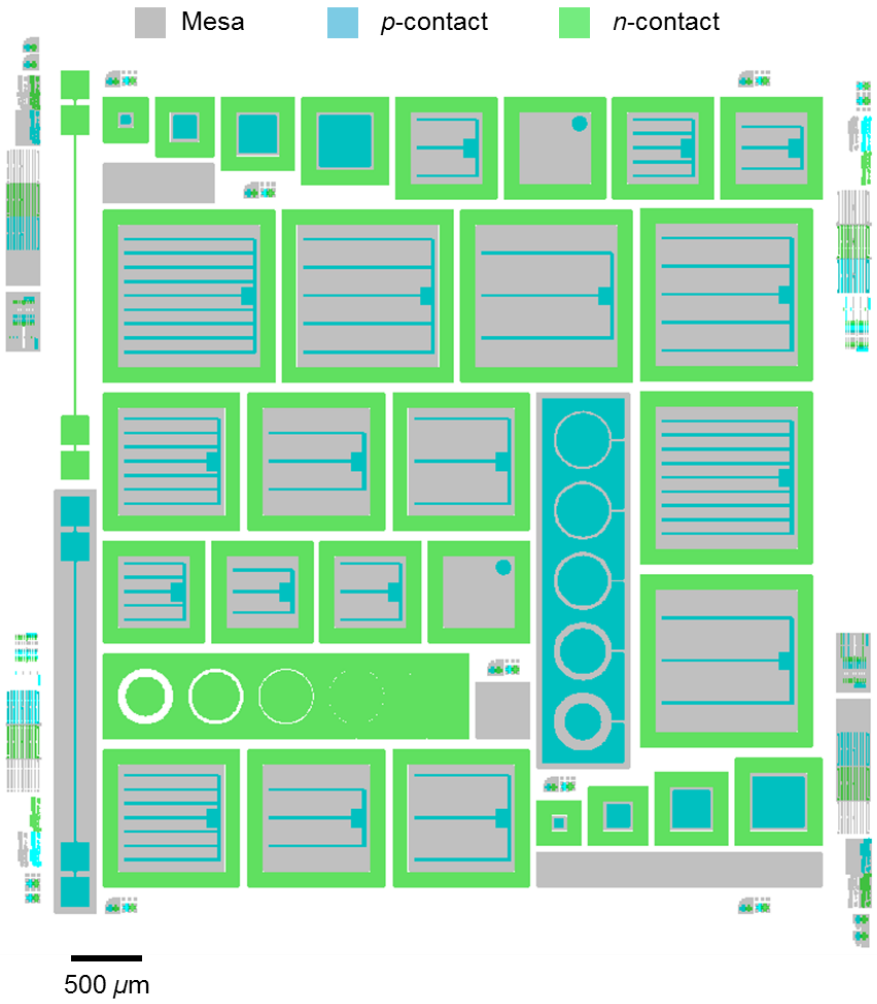

Figure 5.4: Mask layout for a 1×1 cm sample showing solar cell devices with various areas and various grid-spacing values.

5.3 Metal Contacts for III-Nitride Devices

5.3.1 Circular Transmission Line Model

Ohmic-contact formation to III-nitride films is a critical step for the fabrication of InGaN solar cells. To enhance carrier collection, the *n*- and *p*-type contact resistances need to be minimized. While *n*-type contacts typically show ohmic behaviors with suitable contact resistances, satisfactory *p*-type contacts are challenging. The metal-semiconductor contact can be characterized using the circular transmission line model (CTLM). The CTLM pattern, illustrated in Figure 5.5(a), consists of a conductive (metal) inner region of radius *r*, a gap of width *d* (semiconductor), and a conducting outer region of radius *R*. The test structure is designed with a constant outer radius R = 200 μm and gap d = 4, 8, 16, 32, and 64 μm as depicted in Figure 5.5(a). The total resistance R_t between the internal and the external contacts is given by

$$R_t = \frac{R_{sh}}{2\pi} \times \left[ln\left(\frac{R}{r}\right) + L_t\left(\frac{1}{R} + \frac{1}{r}\right)\right], \tag{5.1}$$

where R_{sh} is the sheet resistance (Ω/□) of the semiconductor layer and L_t is the transfer length (cm) [133, 134]. Equation (5.1) is valid for $r >> 4L_t$. Figure 5.5(b) shows the plot of the total resistance measured for various gap values as a function of ln(R/r). The data can then be fitted to obtain a straight line plot of R_t vs ln(R/r). The slope of the linear regression leads to R_{sh} and the intercept at ln(R/r) = 0 (corresponding to $R = r$) is $R_{sh}\cdot L_t/R\pi$, giving L_t. The specific contact resistivity, ρ_c (Ω·cm^2), can be obtained using the following equation:

$$L_t = \sqrt{\frac{\rho_c}{R_{sh}}}\,, \tag{5.2}$$

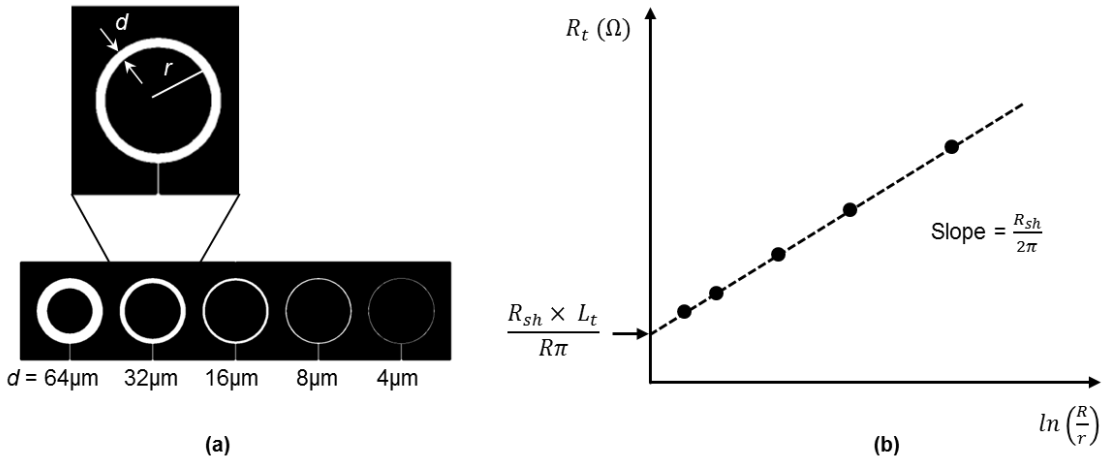

Figure 5.5: (a) Circular contact resistance patterns with various gap values. The dark regions represent metallic regions. The inset shows a structure with a gap *d* and an inner radius *r*, and (b) plot of the total resistance as a function of ln(*R*/*r*) [133].

5.3.2 Ohmic contact to *n*-GaN

For ohmic contacts to *n*-GaN, Ti- and Al-based metallization schemes (*e.g.*, Ti, Ti/Al, Ti/Au, Ti/Al/Ni/Au, and Ti/Al/Ti/Au) have been widely investigated [135-137]. Using such metallization schemes, low specific contact resistivities ranging from 10^{-5} to $10^{-8}\ \Omega\cdot cm^2$ have been reported, which are satisfactory for the operation of optoelectronic devices. To evaluate metal contacts to *n*-GaN films, the CTLM structures described previously were patterned on MOCVD-grown *n*-GaN (0001) templates on sapphire with electron concentration $1\text{-}2\times10^{18}\ cm^{-3}$ by standard lithography, electron-beam

evaporation, and lift-off. Before photolithography, the samples were degreased with a solvent clean and dipped in BOE for 3 min to etch the native surface oxide layer that would act as a barrier to electrical current flow through the GaN/metal contact interface. After the photolithography step, an O_2-plasma descum was performed to remove PR residue that would affect the contact performance. Prior to the metallization, the samples were dipped in BOE:DI 1:1 for 30 s to ensure that the surface oxide was removed. The metal films, which consist of Ti/Al/Ti/Au (30/100/30/50 nm), were deposited consecutively using an electron-beam evaporator with a base pressure lower than 3×10^{-6} torr. The *I-V* measurements were carried out by a four-point probe method, and the specific contact resistivity ρ_c, transfer length L_t, and sheet resistance of the *n*-GaN R_{sh} were measured by CTLM.

The *I-V* characteristics of the as-deposited CTLM patterns, shown in Figure 5.6(a), exhibit a linear behavior, indicating that the metal contacts are ohmic even without post-metallization annealing. To calculate ρ_c, the total resistance R_t, extracted from the *I-V* characteristics, is plotted as a function of ln(*R/r*) as illustrated in Figure 5.6(b) [133, 134]. Using equations (5.1) and (5.2), ρ_c and L_t were determined to be $\sim5\times10^{-5}\ \Omega\cdot cm^2$ and 10-15 μm, respectively. The sheet resistance of the *n*-GaN epilayer was calculated to be ~40 Ω/□, which is consistent with the value obtained from Hall measurement. These low-resistance ohmic contacts to *n*-GaN offer a great baseline for future nitride-based solar cells. The specific contact resistivity of similar contacts to MME-grown *n*-GaN films used in devices is expected to be lower due to higher electron concentration [138]. While these preliminary results are very promising, metal-contact

schemes and annealing conditions can be further optimized to improve the contact resistance and stability.

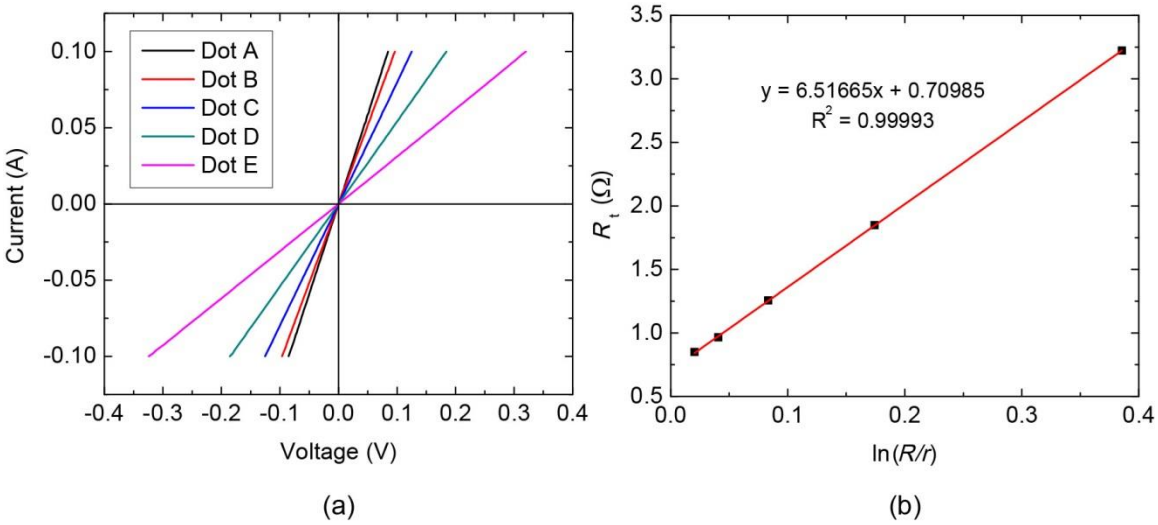

Figure 5.6: (a) CTLM *I-V* characteristics of non-annealed Ti/Al/Ti/Au (30/100/30/50 nm) ohmic contacts to *n*-GaN. Dots A, B, C, D, and E correspond to spacing values of 4, 8, 16, 32, and 64 μm, respectively. (b) R_t as a function of ln(*R*/*r*). The experimental data points are fitted using linear regression (red line) to determine the specific contact resistivity.

5.3.3 Ohmic contact to *p*-GaN

The formation of low-resistance ohmic contacts to *p*-GaN is essential for further improvement in electrical and optical performance of GaN-based optoelectronic devices [139]. Various methods to achieve low-resistance contacts to *p*-GaN including the use of large work function [140, 141], surface treatments [141, 142], and superlattice and strained layers [143, 144], have been employed. Ni/Au contacts have been commonly used as ohmic contact to *p*-GaN. The ohmic formation usually requires an annealing process to cause interfacial reaction and Ni oxidation [145]. The effect of annealing

atmosphere and temperature on the structural and electrical properties of Ni/Au contacts has been widely investigated [134, 146]. To evaluate metal contacts to *p*-GaN films with high hole concentrations, CTLM structures were patterned on MME-grown *p*-GaN films with hole concentration 2-3$\times 10^{19}$ cm^{-3} grown on AlN on sapphire. The CTLM structures used in this study have a constant outer radius R = 185 μm and spacing values of 20, 30, 50, and 90 μm. The cleaning, lithography, and descum steps were similar to those for the metal contacts to *n*-GaN. However, prior to metallization, the *p*-GaN samples were dipped in HCl for 30 s to etch the surface oxide. The metal films, which consist of Ni/Au (50/50 nm), were deposited consecutively using an electron-beam evaporator with a base pressure lower than 3×10^{-6} torr. The metallized samples were then annealed in a MILA 5000 mini-annealer at 500°C for 10 min in dry air.

Figure 5.7(a) depicts the *I-V* characteristics of the as-deposited CTLM patterns on MME-grown *p*-GaN. The *I-V* curves are almost linear even without post-metallization annealing due to the high hole concentration in the *p*-GaN layer. The dependence of R_t as on ln(R/r) for contacts before and after annealing is illustrated in Figure 5.7(b). The extracted values of ρ_c for the contact before and after annealing were 1.2×10^{-2} $\Omega\cdot cm^2$ and 8.5×10^{-3} $\Omega\cdot cm^2$, respectively. The *I-V* after annealing display a linear behavior that demonstrates an ohmic contact to *p*-GaN. While the contact resistivity improved with the annealing step and is suitable for solar cell operation, a more detailed study is needed to optimize the annealing conditions and obtain low-resistance ohmic contact to *p*-GaN.

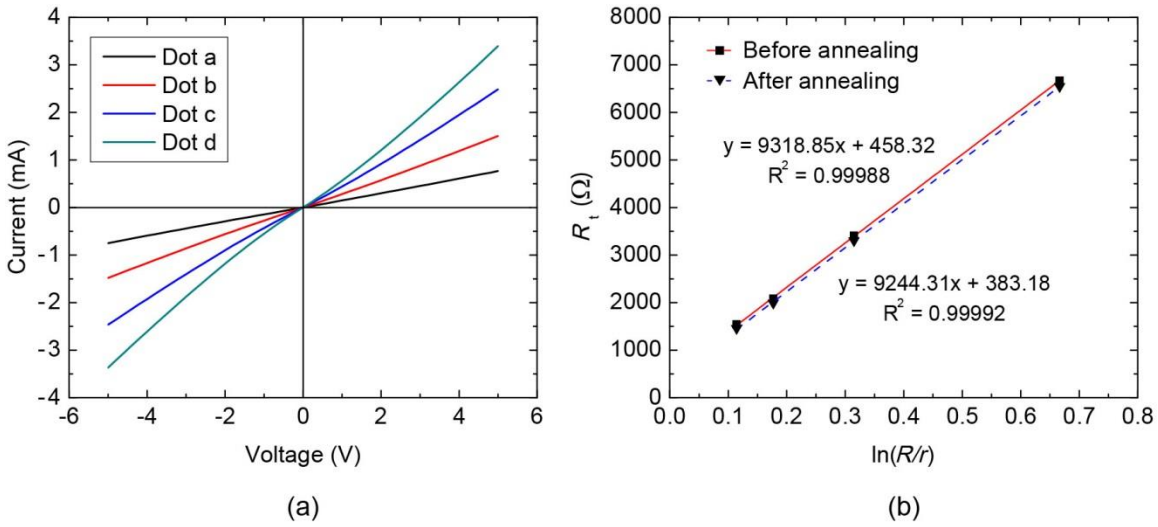

Figure 5.7: (a) CTLM *I-V* characteristics of as-deposited Ni/Au (50/50 nm) contacts to *p*-GaN. Dots a, b, c, and d correspond to spacing values of 20, 30, 50, and 90 μm, respectively. (b) R_t as a function of ln(*R/r*) for the contacts before and after annealing. The experimental data points are fitted using linear regression (red line) to determine the specific contact resistivity.

5.4 Optimization of Metallization grid pattern

The metallization grid pattern is an essential design element for high-efficiency solar cells. While a variety of grid geometries exists, metallization grid patterns are usually simple and highly symmetrical for practical reasons. A typical top contact grid configuration consists of parallel grid lines or fingers as depicted in Figure 5.8(a) and (b). The optimized grid pattern minimizes the combined effect of four loss mechanisms directly associated with the grid, which are (i) the optical loss due to shading, (ii) the resistive loss in fingers, (iii) the resistive loss in the emitter or current-spreading layer, and (iv) the resistive loss due to the metal/semiconductor contact. The shading losses P_s, which are due to the presence of metal on the top surface that prevents light absorption, are determined by the fraction of the top surface covered by metal. The resistive losses in

fingers P_f depend on the resistivity of the metal ρ_f, the pattern of the metallization and the aspect ratio of the metallization scheme. The resistive losses in the top layer P_e, which are due to lateral current flow to the fingers, are characterized by the sheet resistance R_{sh}. The contact resistance losses P_c, which occur at the interface between the semiconductor and the metal contact, are characterized by the specific contact resistivity ρ_c. The equations and derivations used to estimate the power losses are detailed in Appendix C.

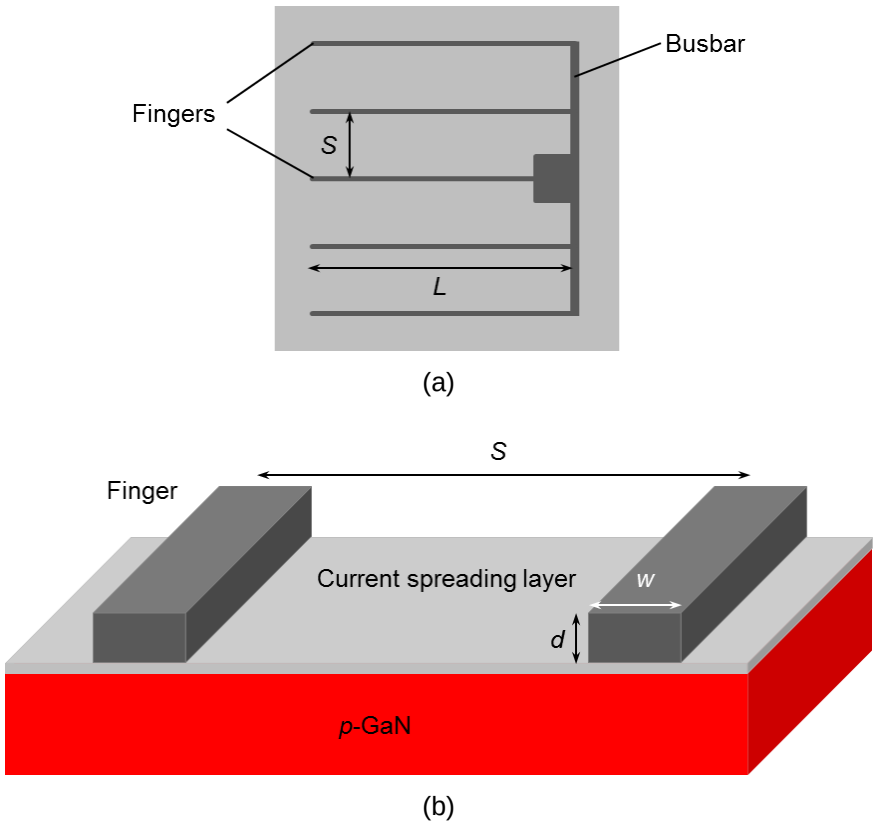

Figure 5.8: (a) Top and (b) isometric schematic view of the grid-pattern scheme for the solar cell under study. The schematics also show the finger parameters.

The equations for optical and electrical losses can be combined to determine the total power loss in the top contact grid. The total power loss P_{tot} is given by

$$P_{tot} = P_s + P_f + P_e + P_c, \tag{5.3}$$

This calculation does not include the resistive losses in the bus bars. By numerically minimizing the total power losses in the metallization grid pattern, the optimal finger spacing can be determined as illustrated in Figure 5.9. The losses shown in Figure 5.9 were calculated using realistic material and fabrication parameters for InGaN-based solar cells as listed in Table 5.1. The optimal finger spacing must account for a tradeoff between resistive losses that decrease with decreasing finger spacing and shading losses that increase with decreasing finger spacing. Through the optimization of the grid-pattern designs, the power losses can be minimized, leading to higher cell efficiencies. For the modeled InGaN-based solar cell, the minimal total power loss is ~2%, which corresponds to an optimal finger spacing of 410 μm. Since the current density at maximum power point J_{mp} is relatively low, the influence of the resistive losses is minor and the predominant component of the total power loss is the optical loss due to shading.

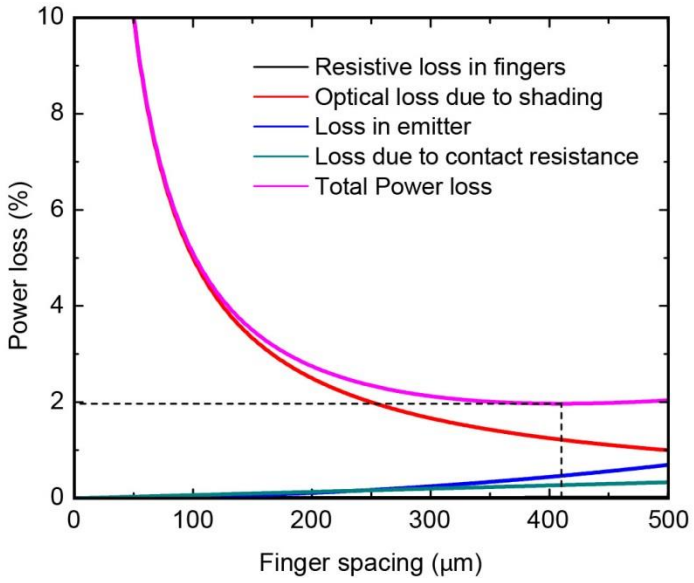

Figure 5.9: Fractional power losses associated with the grid pattern as a function of the finger spacing. The horizontal and vertical dashed lines correspond to the minimal total power loss and the optimal finger spacing, respectively.

Table 5.1: Material and fabrication parameters used to estimate the power losses and to calculate the optimal finger spacing.

Parameter	Value
Finger length L (μm)	450
Emitter sheet resistance R_{sh} (Ω/□)	10^4
Metal resistivity ρ_f (Ω·cm)	5×10^{-6}
Finger width w (μm)	5
Finger thickness d (nm)	100
Specific contact resistivity ρ_c (Ω·cm^2)	1×10^{-2}
Current density at maximum power point J_{mp} (mA/cm^2)	5
Voltage at maximum power point V_{mp} (V)	1.5
Minimal total power loss (%)	1.97
Optimal finger spacing (μm)	410

By differentiating Equation (5.3), an expression of the optimal finger spacing can be derived and the effect of various material and device parameters can be assessed. The effect of the sheet resistance R_{sh} on the optimal finger spacing is depicted in Figure 5.10. R_{sh} values for a Ni/Au (5/5 nm) current-spreading layers are typically in the 1-10 Ω/□ range whereas R_{sh} values for *p*-GaN layers are in the low-to-mid 10^4 Ω/□ range. As expected, the optimal finger spacing decreases with increasing R_{sh}. For all tested values of J_{mp}, the impact of R_{sh} is negligible for R_{sh} values lower than 10^2 Ω/□. Valdueza-Felip *et al.* investigated the effect of grid spacing (100, 150, and 200 μm) on the performance of InGaN MQW solar cells [147]. The experimental results reveal that the finger spacing does not influence considerably the device performance, suggesting a satisfactory majority-carrier lateral conduction in the *p*-GaN and/or current-spreading layer.

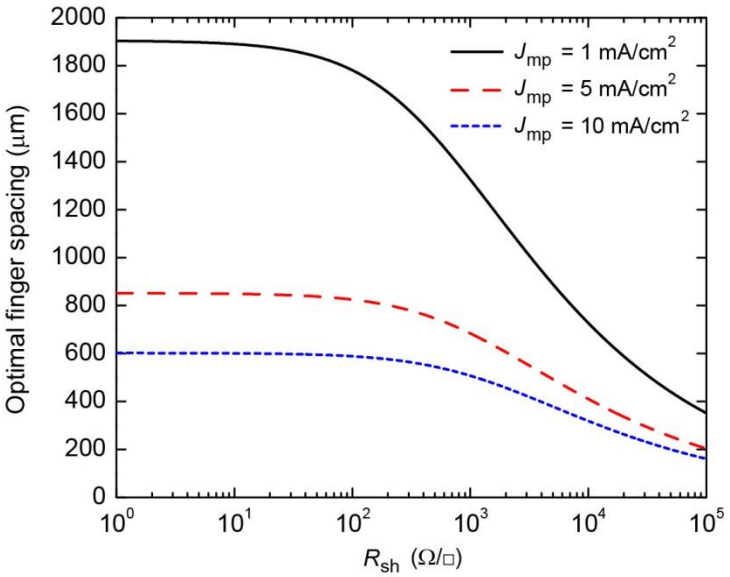

Figure 5.10: Optimal finger spacing as a function of R_{sh} for various values of J_{mp}.

Figure 5.11 shows the influence of J_{mp} and V_{mp} on the optimal finger spacing. As J_{mp} increases, the effect of resistive losses becomes more significant, shifting the optimal finger spacing to lower values. However, the optimum depends only slightly on V_{mp}. J_{mp} and V_{mp} highly depend on the solar cell structure, InGaN composition, and absorbing layer thickness as demonstrated in Chapter 2. While a ~50% InGaN homojunction solar cell under 1 sun would typically yield a J_{mp} in the tens of mA/cm^2 range, a similar structure under 100 suns would yield a J_{mp} in the 1000 mA/cm^2 range.

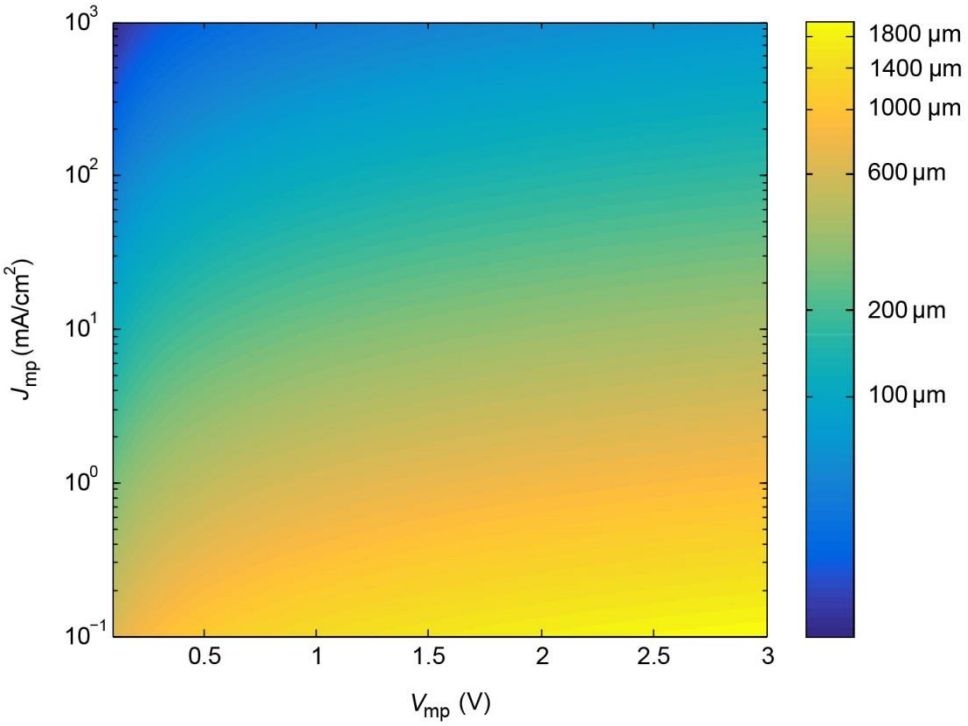

Figure 5.11: Optimal finger spacing as a function of J_{mp} and V_{mp}.

5.5 Summary

This chapter discussed several aspects of device processing and design of InGaN-based solar cells. A processing sequence was developed to fabricate III-nitride devices. A mask set that comprises devices with variable sizes and contact configurations was designed to optimize the conversion efficiency of InGaN-based solar cells. Using CTLM, ohmic-contact formation to III-nitride films was investigated. Finally, a design method for metallization patterns is presented to minimize power losses. While the developed fabrication process is viable for the fabrication of future InGaN solar cells, it requires further optimization, notably for the contact-annealing steps.

CHAPTER 6

III-NITRIDE DOUBLE-HETEROJUNCTION SOLAR CELLS WITH HIGH In-CONTENT InGaN ABSORBING LAYERS

Using the improved growth technology and the developed fabrication process, the growth and fabrication of InGaN/GaN double-heterojunction (DHJ) was investigated. While homojunction devices are predicted to exhibit superior performance than DHJ structures [99], experimental results show that DHJ structures are currently the most viable design because of numerous material challenges [148]. Nitride-based devices are typically grown by metalorganic chemical vapor deposition (MOCVD) or molecular beam epitaxy (MBE). Numerous studies of MOCVD-grown DHJ structures have been reported [7], but very few reports exist on MBE-grown DHJ devices [19]. The characteristics and performance of InGaN/GaN DHJ solar cells found in the literature are summarized in Appendix D. In this work, we present InGaN/GaN DHJ solar cells with various InGaN film thicknesses and compositions grown by RF-plasma MBE including a functional DHJ cell with a record-high In content of 22%.

6.1 Experimental Procedure

The *n*-GaN/*i*-InGaN/*p*-GaN DHJ solar cells were grown in a Riber 32 MBE system using a Veeco Unibulb plasma source. MOCVD-grown *n*-GaN (0001) templates on sapphire with electron concentration 1-2$\times 10^{18}$ cm^{-3} and threading-dislocation density ~3$\times 10^{8}$ cm^{-2} were used as substrates. The *p*-*i*-*n* junction consists of a 500 nm n^{+}-GaN, an unintentionally-doped InGaN absorption layer with various thicknesses and

compositions, and a 90 nm *p*-GaN. The InGaN layers were grown under N-rich growth conditions and low growth temperatures (450-500°C) [105]. The *n*- and *p*-GaN layers were grown at 600°C using metal-modulated epitaxy, a shuttered growth technique that allows for high doping while maintaining good crystal quality [29, 122]. Si and Mg were used as *n*- and *p*-type dopants, respectively. Electron and hole concentrations were calibrated using room-temperature Hall-effect measurements and the carrier concentrations in the n^+- and p^+-GaN were 5×10^{19} cm^{-3} and 3×10^{19} cm^{-3}, respectively. The heavy doping in the n^+- and p^+-GaN layers is intended to counterbalance the detrimental polarization effects. The high concentrations of ionized-dopant charge at the hetero-interfaces is expected to impede the polarization-induced field that opposes carrier collection [149]. Since defect generation due to strain relaxation increases with both In composition and thickness, four devices (A, B, C, and D) with various combinations of InGaN thickness and In composition were grown, characterized, fabricated, and tested. Samples A and B are comprised of a 35 nm- and 200 nm-thick ~10% InGaN absorbing layer, respectively. Samples C and D are comprised of a 50 nm- and 200 nm-thick ~20% InGaN absorbing layer, respectively. The photovoltaic characteristics of both large-area (1×1 cm) and small-area (500×500 μm) devices were compared. The large-area devices use indium dots as metal contacts for both *n*- and *p*-GaN layers and had no anti-reflection coating or current spreading layers. The small-area devices were processed into 500×500 μm mesas by photolithography and inductively coupled plasma etching using a BCl_3/Cl_2 chemistry. A thin layer of Ni/Au was deposited on the moderately-resistive *p*-type layer to serve as a semitransparent current-spreading layer to promote lateral conduction and thus, enhance carrier collection. Ti/Al/Ti/Au and Ni/Au were used for

the *n*- and *p*-contact pads, respectively, without post-metallization annealing. Due to the extremely-high doping achieved via RF-plasma MBE, the as-deposited contacts displayed ohmic behavior as measured with circular transmission line model patterns. A typical device structure for the small-area devices is shown in Figure 6.1.

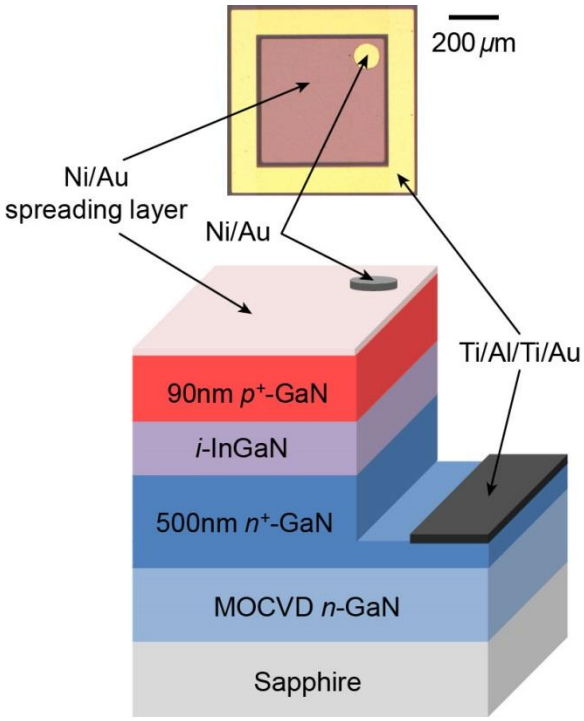

Figure 6.1: Structure of the fabricated InGaN/GaN DHJ solar cells. The inset is a top-view micrograph of an example 500×500 μm device.

The structural properties and the surface morphology of the epitaxial layers were characterized by X-ray diffraction (XRD) and atomic force microscopy (AFM), respectively. The *I-V* characteristics of the small-area devices were measured using a continuous-wave Oriel Class A solar simulator equipped with a Xenon ARC lamp (AM1.5 – 1 sun). A reference solar cell was used to calibrate the spectral intensity. The

power of the lamp was changed accordingly to obtain the desired concentration. The external quantum efficiency (EQE) was measured using an Oriel IQE-200. The performance of both large-area and small-area devices were tested and compared using a Solux broad-spectrum lamp (4700K) with ultra-low UV and under concentration (~20×). Due to the deficiency of the blue/UV light of the Solux lamp, the performance of the devices presented herein is underestimated.

6.2 Results and Discussions

XRD (0002) 2θ-ω scans shown in Figure 6.2 indicate the absence of phase separation for all samples. The presence of Pendellösung fringes around the main peaks is indicative of smooth interfaces. Film thicknesses for both the InGaN and the *p*-GaN films were confirmed by calculating the average interference fringe spacing based on the Bragg equation. The rocking curves (RCs) for the (0002) and $(10\bar{1}5)$ reflections were measured to further characterize the crystalline quality of the InGaN absorbing layers. The full width at half maximum (FWHM) of these XRD RCs, which are associated with dislocation density, are summarized in Table 6.1.

The composition and degree of relaxation of the InGaN films were measured from reciprocal space maps (RSMs) in the vicinity of the $(10\bar{1}5)$ reflection (Figure 6.3). The fully-strained and fully-relaxed lines are represented as vertical and diagonal dashed lines, respectively. The InGaN layers in samples A, B, and C are fully coherent to the *n*-GaN underlayer. As the thickness increases to 200 nm, the degree of relaxation in the 20% InGaN film (sample D) increases slightly to 28%, but is substantially lower than in other growth techniques [76, 104, 150]. The ability to grow InGaN films with In

composition up to 22% and negligible relaxation is attributed to the N-rich MBE growth under low temperature that results in efficient In incorporation, improved defect density, and enhanced optical properties [105]. While the InGaN film remains mostly strained, the slight relaxation degrades the crystal quality as demonstrated by the increase in the RC FWHM. Since strain relaxation results in defect formation that can increase non-radiative recombination and leakage current and thus, degrade the solar cell performance, the growth of fully-strained InGaN films is critical for DHJ cells. Thick, fully-strained InGaN layers are required to maximize light absorption while maintaining good crystal quality.

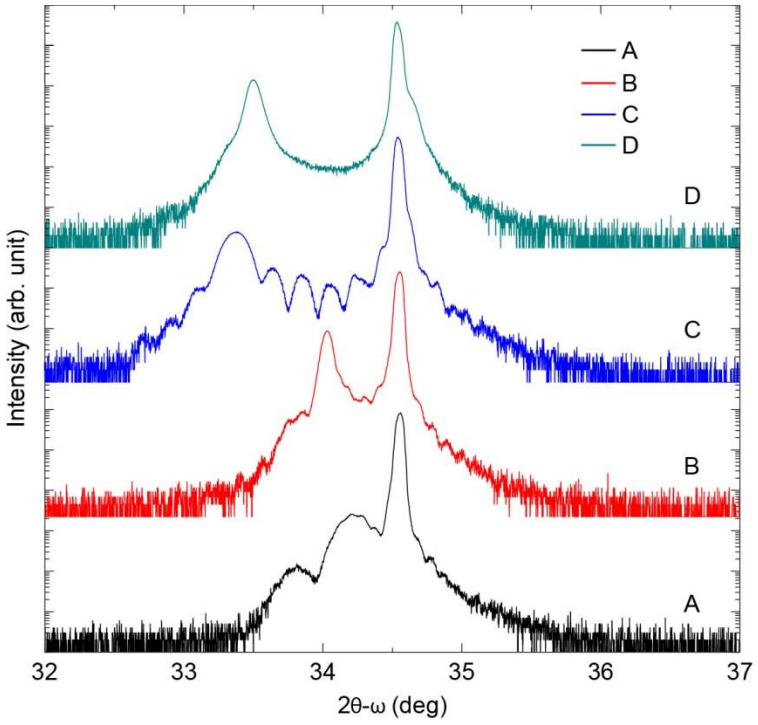

Figure 6.2: (0002) 2θ-ω diffraction scans of samples A, B, C, and D showing the absence of phase separation for all samples. The presence of Pendellösung fringes around the main peaks indicates smooth interfaces.

Table 6.1: Characteristics of InGaN/GaN double-heterostructures.

	Composition (%)	Band gap (eV)	Wavelength (nm)	Thickness (nm)	Relaxation (%)	Roughness (nm RMS)	(0002) RC (arcsec)	(10$\bar{1}$5) RC (arcsec)
A	9.4	3	409	35	0	1.1	270	485
B	9.5	3	409	188	0	3.11	265	410
C	22	2.56	483	48	1	2.18	296	902
D	20	2.64	470	192	28	3.27	490	1030

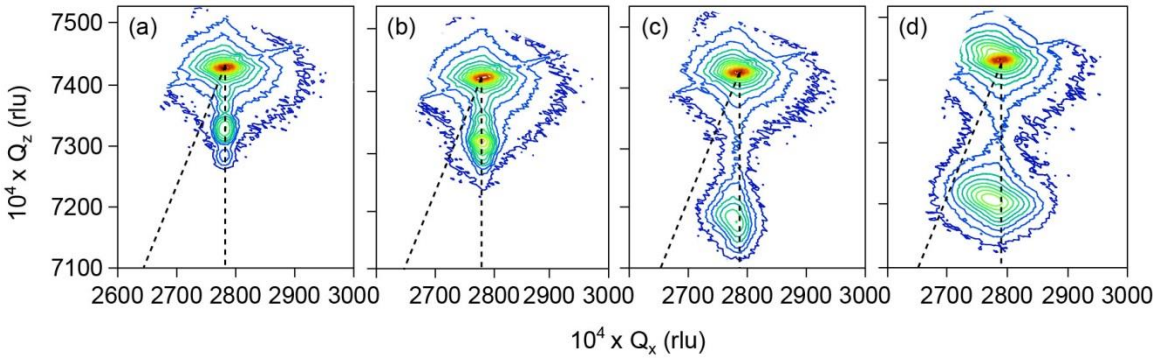

Figure 6.3: RSMs along the (10$\bar{1}$5) reflection of samples (a) A, (b) B, (c) C, and (d) D. The vertical and diagonal dashed lines represented the fully-strained and fully-relaxed lines, respectively.

The surface morphology of the devices was investigated by AFM. The AFM images shown in Figure 6.4 display smooth surfaces with grainy morphologies typical for N-rich InGaN and p^+-GaN films [105, 122]. The root-mean-square (RMS) roughness increases with thickness and In content. In sample A and B, pits located at the center of spiral hillocks and associated with threading dislocations are clearly visible. These pits become wider and deeper as the thickness of the InGaN film increases.

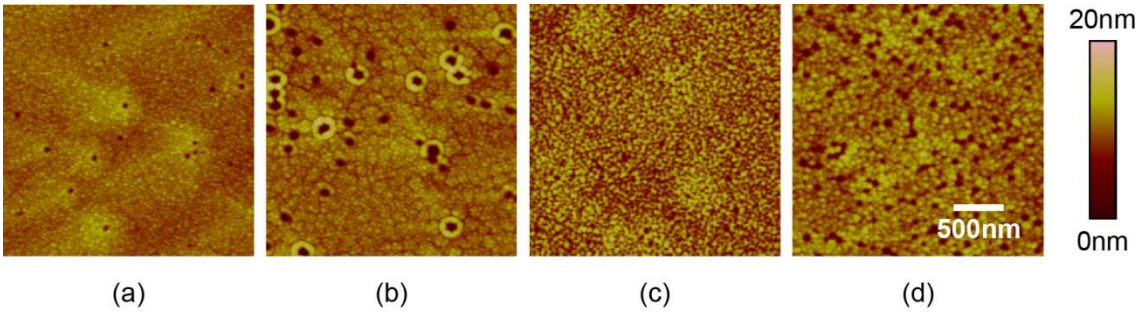

Figure 6.4: AFM images of samples (a) A, (b) B, (c) C, and (d) D. The samples exhibit a grainy morphology.

The *J-V* characteristics of the small-area DHJs measured under 1sun AM1.5 are depicted in Figure 6.5(a). All InGaN/GaN DHJs display photovoltaic and photoconductance effects. To the best of our knowledge, these devices are the first reported InGaN/GaN DHJs grown by RF-plasma MBE. While functional DHJ cells with In content up to 17% have been previously reported [151], this work presents the InGaN/GaN DHJ with the highest In content (22%). Table 6.2 summarizes the performance characteristics of the various small-area devices under 1 sun AM1.5. As expected, the short-circuit current density (J_{sc}) increases for thicker cells for both compositions due to enhanced light absorption. As the composition increases from 10% to 20%, J_{sc} is impacted by competing effects. On one hand, light absorption improves due to the reduced band gap of the InGaN absorbing layer. On the other hand, carrier collection efficiency is impeded by stronger polarizations effects [152] and degraded crystalline quality. These competing effects can be observed in the cells EQE as shown in Figure 6.5(b). While the main spectral response of sample A and B occurs in the range of 360-440 nm, that of sample C and D extends up to ~500 nm. All these values are

consistent with the estimated band gaps of the absorbing InGaN layers. However, the peak EQE of sample C and D are substantially lower than that of sample A and B. The drop in EQE below 360 nm for all samples corresponds to the absorption edge of the *p*-GaN top layer.

Table 6.2: Photovoltaic properties of small-area InGaN/GaN DHJ devices under 1 sun AM1.5 illumination.

	J_{sc} (mA/cm^2)	V_{oc} (V)	*FF* (%)	η (%)	Peak EQE (%)
A	0.39	0.42	37.3	0.06	11.7
B	0.71	0.96	48.4	0.33	24.4
C	0.66	0.5	51.5	0.17	9
D	0.67	0.36	45.8	0.11	10.6

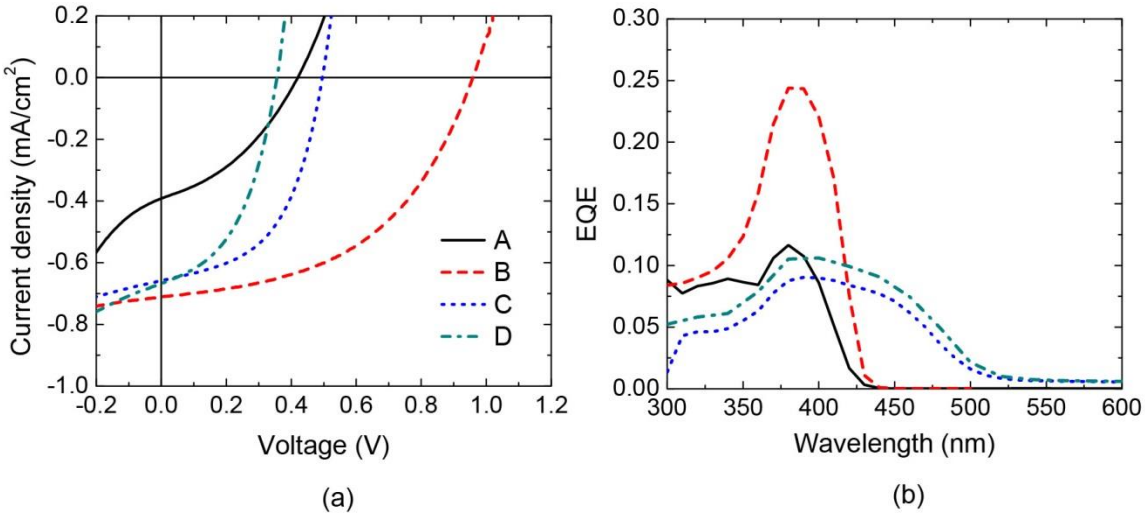

Figure 6.5: (a) *J-V* characteristics of the small-area InGaN/GaN DHJ devices under 1 sun AM1.5 illumination. (b) EQE vs wavelength for the small-area InGaN/GaN DHJ cells.

The performance of large-area and small-area devices was then compared. Figure 6.6 shows the dark and light *I-V* characteristics of both types of solar cells measured with a UV-deficient light under ~20× light concentration. The cell series resistance (R_s) calculated from the linear portion of the dark *I-V* characteristics and the shunt resistance (R_{sh}) determined from the slope of the light *I-V* curve near I_{sc} are listed in Table 6.3. The cells show clear rectifying behaviors with turn-on voltages of 2.7-3 V for sample A and B (10% InGaN) and 1.7-2.2 V for sample C and D (20% InGaN). As expected, the small-area device demonstrated dramatically sharper turn-ons with lower R_s.

Table 6.3: Comparison of large-area and small-area device characteristics illuminated with a UV-deficient light under 20× concentration.

	Large-area devices				**Small-area devices**			
	R_s **(Ω)**	R_{sh} **(kΩ)**	**FF (%)**	V_{oc} **(V)**	R_s **(Ω)**	R_{sh} **(kΩ)**	**FF (%)**	V_{oc} **(V)**
A	18.6	6.8	30.6	0.61	5	423	51.1	1
B	52.9	13.4	25.2	1.13	5.2	197	51.1	1.50
C	25.1	9.1	33.3	0.56	5.2	80.3	53.5	0.72
D	17.2	3.1	27.9	0.19	9.9	50.9	46.9	0.45

The large-area devices face leakage-current issues as demonstrated by the low R_{sh} values that negatively affect the open-circuit voltage (V_{oc}). The shunt issue is modestly improved in small-area devices where R_{sh} drastically increases, leading to higher values of V_{oc}. The improvement in both R_s and R_{sh} results in a rise in the fill factor (*FF*) for small-area devices.

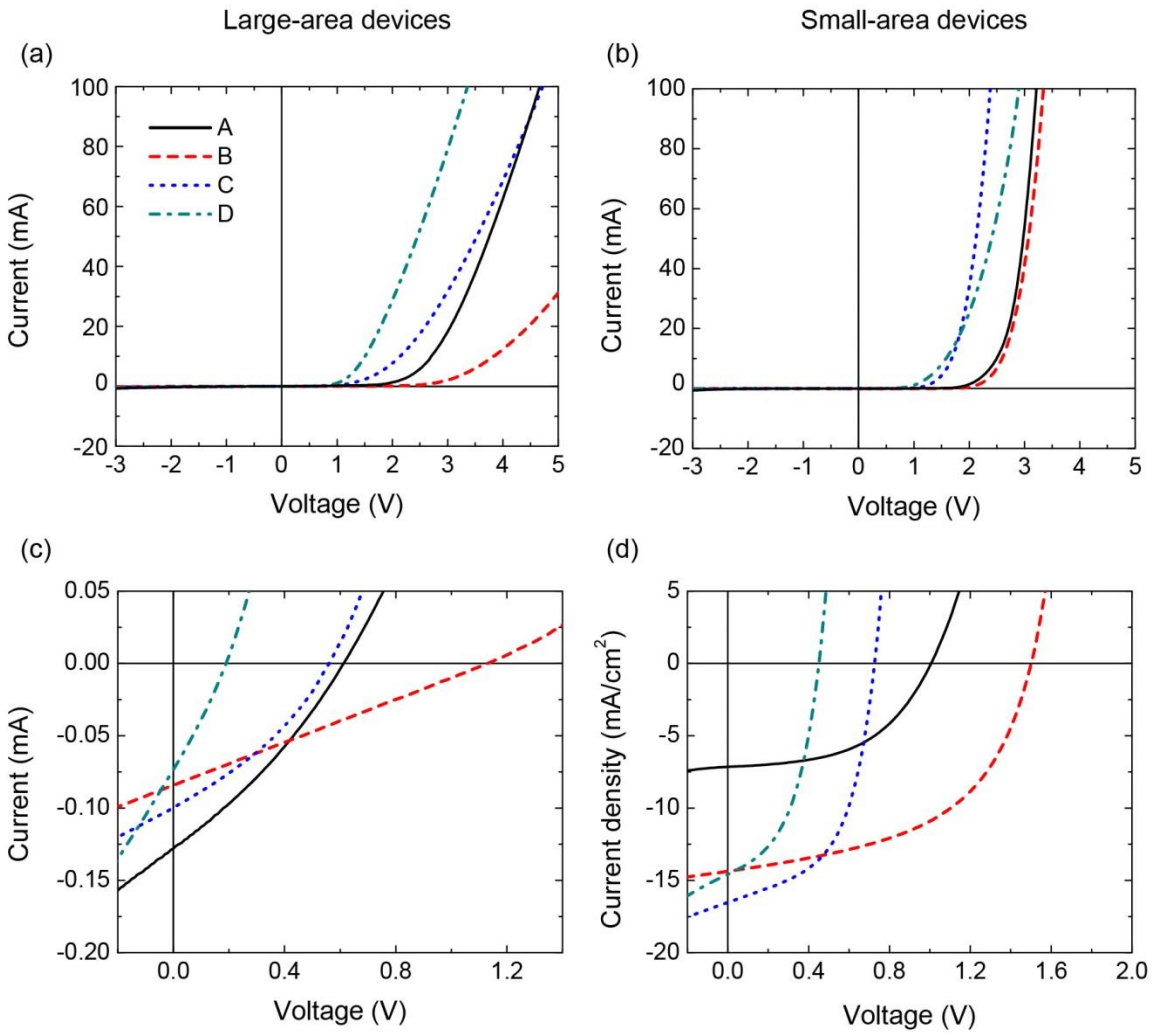

Figure 6.6: (a) and (b) Dark *I-V* curves of the large-area and small-area solar cells, respectively. (c) and (d) Characteristics of the large-area and small-area solar cells, respectively, illuminated with a UV-deficient light under 20× concentration.

The effect of light intensity on V_{oc} is depicted in Figure 6.7 for sample B. As the concentration factor increases, V_{oc} drastically increases for both large-area and small-area devices. The experimental data is fitted with a logarithmic function with a slope $S = nkT/q$ corresponding to an ideality factor n ~ 9.4 for the large-area device and n ~ 6.8 for the small-area device. These high ideality factors are most likely due to tunneling

through *p*-GaN/*i*-InGaN interface states [153, 154]. The interface states may also result in lower R_{sh}. The combined effects of leakage current and tunneling through interface states due to the formation of defects in the InGaN absorbing layer, have a detrimental impact on J_{sc} and V_{oc}. Despite these issues, sample B shows a highly promising V_{oc} of 1.5 V under ~20× light concentration.

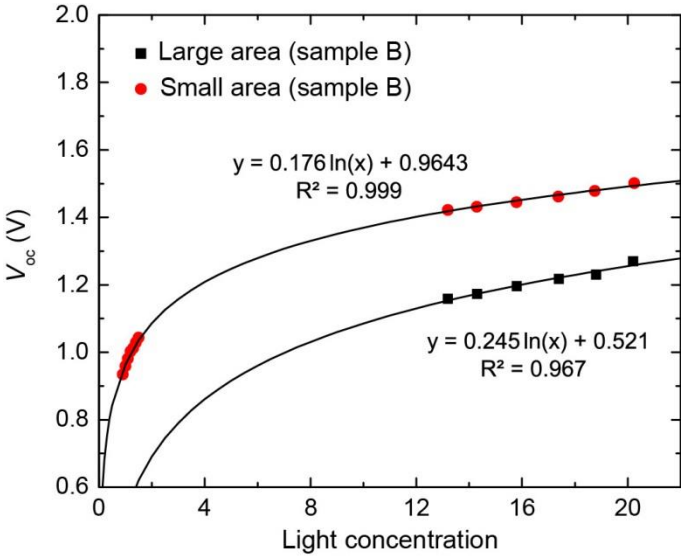

Figure 6.7: V_{oc} as a function of the concentration factor of sample B for both the large-area and the small-area devices.

Finally, the growth and fabrication of a DHJ solar cell with a 35% InGaN absorbing layer was attempted. The 200 nm-thick 35% InGaN layer is mostly relaxed as detected by the XRD RSM shown in Figure 6.8. This strain relaxation generates defects and thus, degrades the crystal quality of the InGaN film. The formation of defects due to strain relaxation seriously affects the performance of the cell. The dark *I*-*V* curve, depicted in Figure 6.9(a), displays a very high reverse current possibly due to defects that

act as shunt pathways. Under illumination, while the DHJ demonstrates photoconductance as illustrated by the light *I-V* curve in Figure 6.9(b), the device does not exhibit a PV effect. This lack of a PV effect results most likely from a combination of two phenomena: (i) the formation of defects due to strain relaxation that increases leakage current and (ii) the polarization effects due to the heterointerfaces that impedes carrier collection. This experimental observation of the lack of PV effect is consistent with predictions reported for DHJ. Indeed, simulation results show that DHJ structures stop operating as solar cells for InGaN absorbing layers with In content higher than 25-30% due to polarization effects [41, 94, 96, 99, 152].

The efficiency of DHJ solar cells is limited by detrimental polarization effects, strain relaxation generating defects, and tunneling through interface states. All these effects are inherent to the double-heterojunction structure. These experimental results

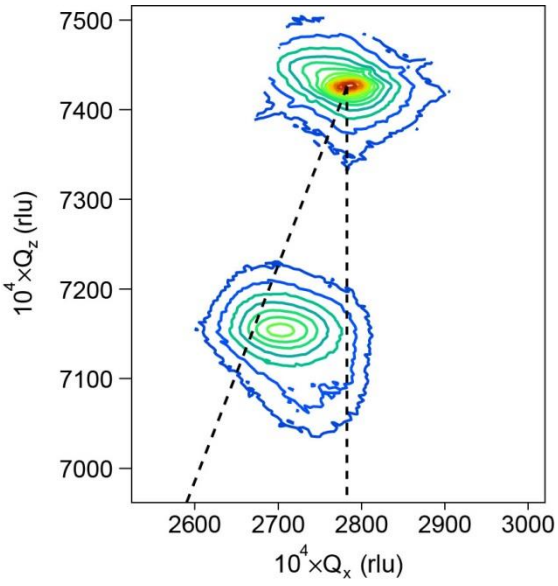

Figure 6.8: RSM along the $(10\bar{1}5)$ reflection of the DHJ solar cell with a 35% InGaN absorbing layer. The vertical and diagonal dashed lines correspond to the fully-strained and fully-relaxed positions, respectively. The InGaN film is mostly relaxed.

indicate that the pathway for improved III-nitride solar cell performance is thick homojunction structures as predicted previously by simulations performed in this work [99].

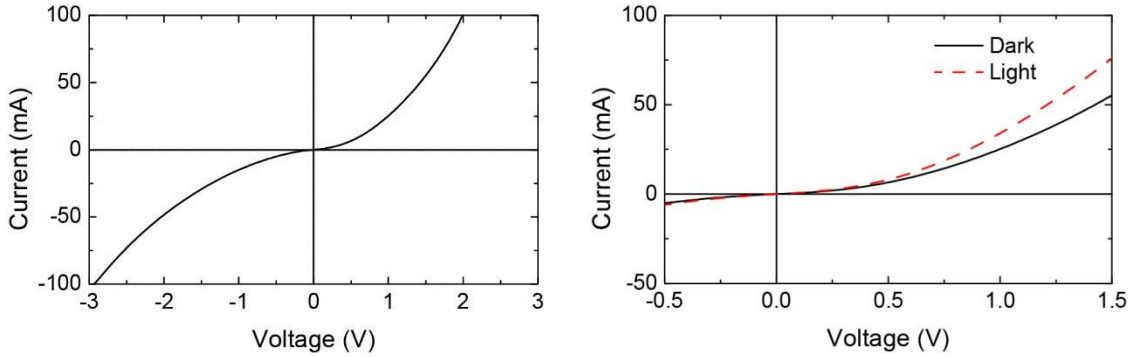

Figure 6.9: (a) Dark *I-V* curve of the DHJ solar cell with a 35% InGaN absorbing layer showing high reverse current and (b) Light *I-V* curve showing photoconductance but no PV effect.

6.3 Summary

The growth, characterization, and testing of InGaN/GaN DHJ solar cells with ~50 nm- and ~200 nm-thick InGaN films with ~10% and ~20% In content has been demonstrated. While leakage current and poor ideality factors are limiting the performance of the cells, the four devices exhibit promising photovoltaic and photoconductance effects. The performance of large-area and small-area devices was compared. As expected, the shunt issue is improved in small-area cells leading to higher V_{oc}. To the best of our knowledge, the 22% InGaN cell presented in this work is the InGaN/GaN DHJ device with the highest In content reported in the literature.

CHAPTER 7

GROWTH OF THICK InGaN LAYERS BY A HYBRID MBE GROWTH TECHNIQUE

According to simulation and experimental results detailed in Chapter 2 and Chapter 6, respectively, the preferred pathway for high-efficiency III-nitride solar cells is thick homojunction structures. While very promising, homojunction devices are currently extremely challenging to fabricate because they require thick, high-quality InGaN films. Due to strain relaxation, epitaxial InGaN films grown on lattice-mismatched substrates beyond the critical thickness usually display a high density of defects. The defect density can be reduced by increasing the film thickness via the defect-annihilation mechanism. Threading dislocations and other crystalline defects formed in heteroepitaxially-grown nitride films can bend and intersect as the film is grown thicker. By intersecting, the dislocations are annihilated leading to lower defect densities. The growth of thicker films enables substantial defect-density reduction and thus, improved electrical and optical properties. While the low-temperature N-rich growth described in Chapter 3 has produced high-quality 50 nm-thick InGaN layers, InGaN films are expected to roughen as the thickness increases. To address the need for thick, high-quality InGaN layers, a hybrid MBE growth technique that combines nitrogen-rich (N-rich) and metal-rich (M-rich) InGaN interlayers is presented. The hybrid growth method takes advantage of the high crystal quality of N-rich InGaN films as well as the smoothing effect of M-rich InGaN interlayers. The alternation of roughening and smoothing effects of N-rich and M-rich growth conditions, respectively, is intended to bend and annihilate dislocations.

7.1 Experimental Procedure

InGaN films were grown in a Riber 32 MBE system using a Veeco UNI-Bulb RF plasma source for N, a Veeco SUMO cell for Ga, and two standard effusion cells for In (In1 and In2). The substrates used were 1×1 cm MOCVD-grown GaN-on-sapphire templates. Nitrogen flow rate and RF-plasma power were set at 1.3 sccm and 350 W, respectively, resulting in a ~1 μm/hr growth rate. The growth temperature was maintained at 450°C. The N-rich InGaN interlayers were grown using a III/N ratio of ~0.9 with a normalized-flux ratio In2 / (Ga + In2) equal to 25%. The In1 source was modulated to grow the M-rich InGaN interlayers. When the In1 shutter is closed, the total metal flux (Ga + In2) is lower than that of active N, leading to N-rich growth conditions. When the In1 shutter is open, the total metal flux (Ga + In2 + In1) becomes larger than that of the active N, leading to M-rich growth conditions. The open/close time of the modulation scheme, illustrated in Figure 7.1, and the In1 flux were calculated to ensure that the thickness of the excess-metal adlayer did not exceed one ML to avoid In surface segregation [45]. The adlayer buildup and the film morphology were monitored *in situ* by reflection high-energy electron diffraction (RHEED) transient and RHEED pattern respectively. The structural properties and surface morphology of the films were investigated *ex situ* by X-ray diffraction (XRD), atomic force microscopy (AFM), and scanning electron microscopy (SEM).

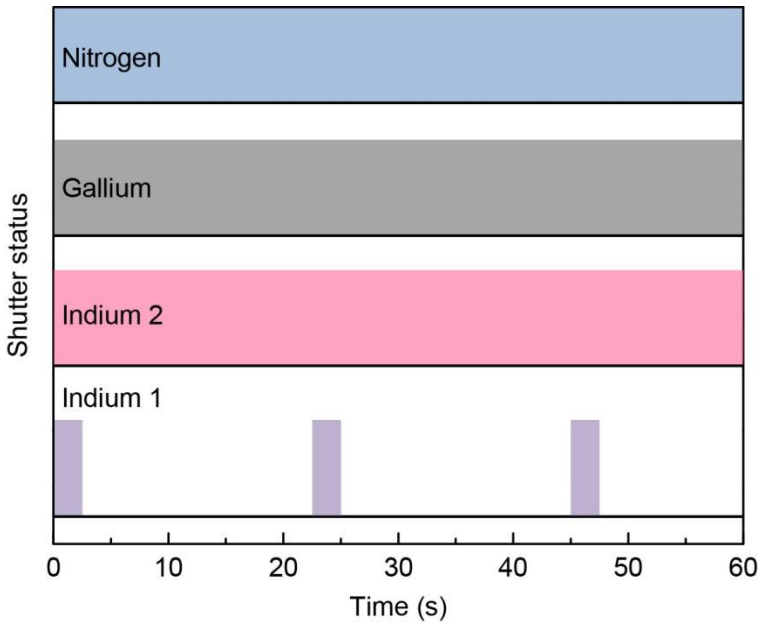

Figure 7.1: Simplified illustration of the modulation scheme used for the growth of InGaN using the hybrid growth technique.

7.2 Results and Discussions

The RHEED-transient features and the corresponding physical mechanisms that occur during the hybrid growth of InGaN layers at various portions of the modulation scheme are illustrated in Figure 7.2. The abrupt decay in the RHEED intensity labeled A is related to the formation of the metal adlayer (Figure 7.2A) that originates from the M-rich condition when the In1 shutter is open. After the In1 shutter is closed, the metal adlayer is consumed into the film (Figure 7.2B), leading to an increase in the signal intensity visible in feature B. Once the metal adlayer is fully consumed, the RHEED intensity steadily increases indicating slight roughening labeled C due to the N-rich growth conditions. This roughening is also demonstrated by the gradual increase in RHEED intensity over time. While the N-rich growth conditions occur during the

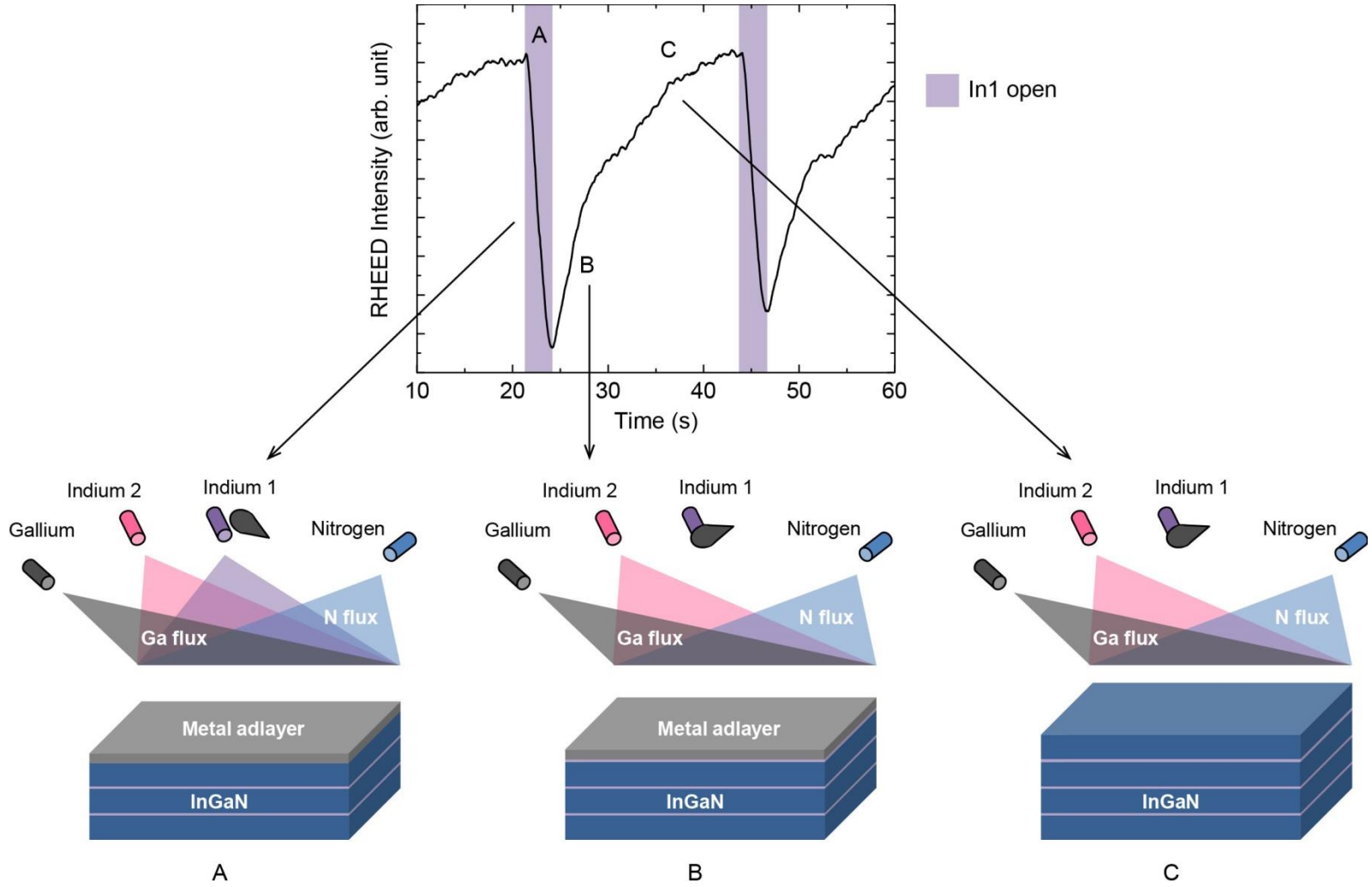

Figure 7.2: (Top) Representative transient RHEED signals for hybrid growth of InGaN. Features are labeled and shaded region indicates In1 shutter open portion of the modulation scheme. (Bottom) Illustrations of the hybrid growth mechanisms for InGaN films.

portion of the cycle labeled C, the M-rich growth conditions happen during portion A and B. Because the source of In from both the impinging In flux and the metal adlayer differ during the three portions of the cycle, the In content will vary in the different interlayers.

Figure 7.3(a) and (b) show the (0002) and (0004) 2θ-ω scans, respectively, of a 250 nm-thick InGaN sample grown using this hybrid technique. The (0002) diffraction scan reveals a single InGaN peak at 32.3°, but a weak InN peak at 31.3° that suggests In surface segregation possibly due to an excess-metal dose slightly exceeding the onset dose [45]. The presence of Pendellösung fringes around the InGaN peak is indicative of smooth interfaces. The peak at 31.8° is the satellite peak of order -1 produced by the periodicity of the superlattice. The satellite peak of order +1 is not visible since it is superimposed to the GaN peak. The superlattice nature of the sample is further evidenced by the satellite peaks of order -1 and +1 visible the (0004) diffraction scan. The period Λ of the multi-layer can be calculated by

$$\Lambda = \frac{(i-j)\lambda}{2(\sin(\omega_i) - \sin(\omega_j))}, \tag{7.1}$$

where i and j are the satellite orders, ω_i and ω_j are the peak positions, and λ the wavelength of the incident X-ray beam. Using both diffraction scans, the superlattice period is estimated to be 6.5 nm, which is consistent with the growth rate and the period of the modulation scheme. The average In composition and the relaxation degree of the superlattice structure, determined from the XRD reciprocal space map (RSM) along the $(10\bar{1}5)$ reflection shown in Figure 7.4, are 32% and 61%, respectively. The RSM also display two satellite peaks that confirm the multi-layer structure.

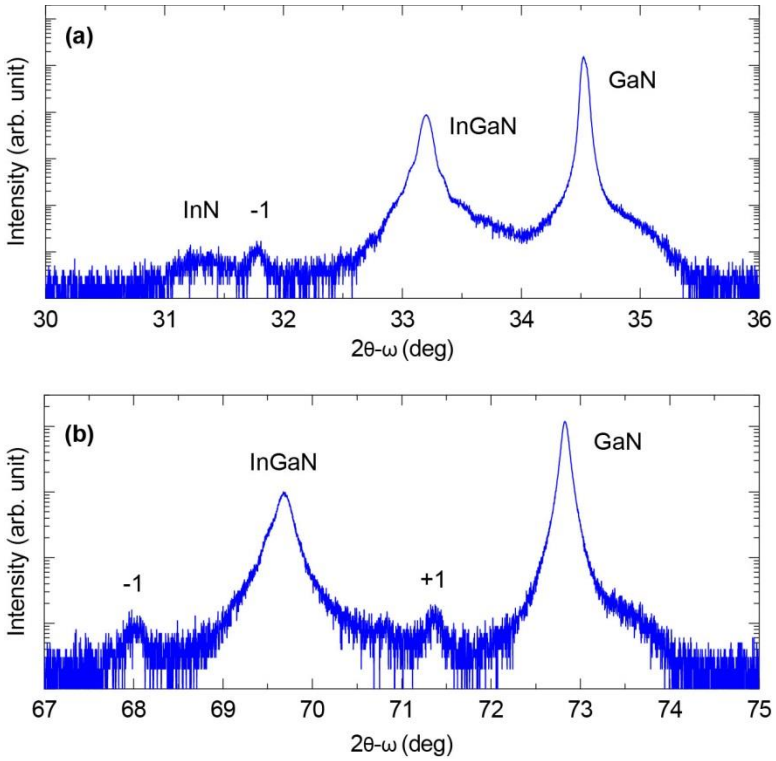

Figure 7.3: (a) XRD (0002) and (b) XRD (0004) diffraction scans of 32% InGaN grown by the hybrid growth technique showing superlattice peaks.

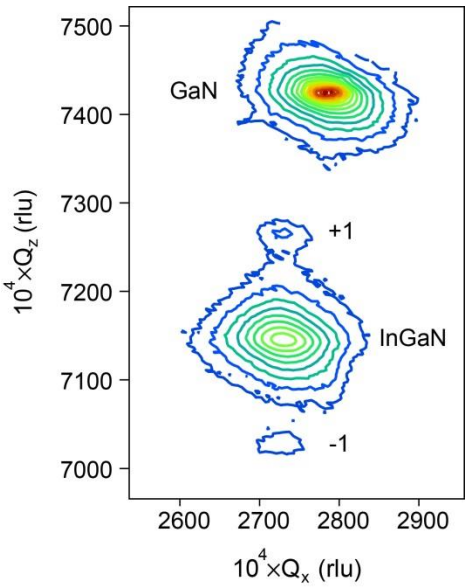

Figure 7.4: RSM along the $(10\bar{1}5)$ reflection of 32% InGaN grown by the hybrid growth technique.

The surface morphology of the InGaN superlattice structure grown by the hybrid technique was investigated *in situ* by RHEED and *ex situ* by AFM. The combination of M-rich and N-rich growth regime resulted in a smooth surface as evidenced by the elongated spots visible in the RHEED pattern (Figure 7.5(a)) and by the 5×5 μm and 1×1 μm AFM scans showing 1.1 and 0.6 nm RMS, respectively (Figure 7.5(b) and (c)). Further investigations of the surface morphology by SEM revealed the presence of round mounds as shown in Figure 7.6 that could be associated with In surface segregation. However, the nitridation of In resulting from decomposition upon cool down cannot be excluded.

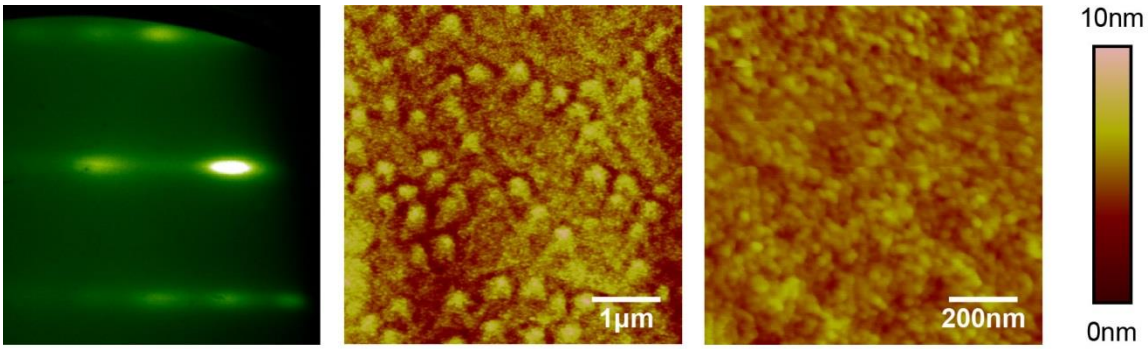

Figure 7.5: (a) RHEED pattern during growth of InGaN by the hybrid growth technique. (b) and (c) 5×5 μm and 1×1 μm AFM scan of InGaN grown by the hybrid growth technique showing 1.1 and 0.6 nm RMS, respectively.

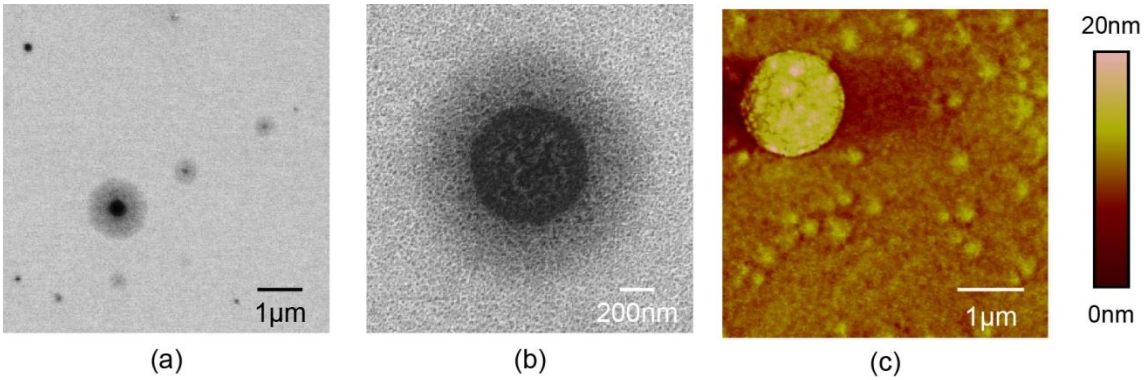

Figure 7.6: (a) and (b) SEM images and (c) AFM scan of the InGaN sample grown by the hybrid technique showing round mounds on the surface.

7.3 Summary

In summary, a hybrid growth technique that combines M-rich and N-rich growth conditions was presented. The 250 nm-thick, 32% InGaN film grown using this technique displays a superlattice structure detected by the XRD satellite peaks, a smooth surface confirmed by the XRD Pendellösung fringes and AFM, but In surface segregation suggested by XRD and SEM.

CHAPTER 8

INVESTIGATION OF InGaN QUANTUM DOTS FOR INTERMEDIATE-BAND SOLAR CELLS

Advanced InGaN-based solar cell designs include multi-junction solar cells, III-nitride/Si tandem cells, and intermediate-band (IB) solar cells. In IB solar cells, a narrow density of states within the band gap of the semiconductor enables sub-band-gap absorption of multiple photons while theoretically maintaining the same open-circuit voltage. A possible approach to form the IB is to use quantum dots (QD). In this type of structure, the QDs, which have a lower band gap than the barrier regions, form a discrete energy level due to quantum confinement. Because of the periodic arrangement and close proximity of the QDs, the discrete energy levels overlap and form mini-bands that enable sub-band-gap absorption [155]. Therefore, the IB structure strongly depends on the size and density of the QDs. InGaN QDs inserted in a GaN matrix offer great potential to create additional energy levels in the band gap extending the absorption below the GaN band gap energy. In this study, two techniques to obtain InGaN QDs are studied. The first method involves *ex-situ* patterning of an InGaN quantum well (QW) via electron-beam lithography (EBL). The second method is *in-situ* MBE growth using surface kinetics to form the QDs at various temperatures. The QD shape, size, height, and density are evaluated by AFM and SEM.

8.1 *Ex-situ* Formation of InGaN Quantum Dots by Electron-Beam Lithography

In this method, InGaN QDs are formed by patterning an InGaN QW using EBL and inductively coupled plasma (ICP) etching. The structure consists of a ~3 nm InGaN QW with an In content of ~65%, sandwiched between GaN layers. The structure is grown by MBE and then patterned by EBL with various doses. The impact of electron-beam (e-beam) exposure dose on the dot diameter is evaluated.

8.1.1 Experimental Procedure

The QD fabrication process is illustrated in Figure 8.1. Figure 8.1(a) shows the grown GaN/InGaN QW/GaN cap structure. All InGaN films were grown in a Riber 32 MBE system under N-rich conditions. Lumilog *n*-GaN templates were used as substrates and were back-side sputtered with 1 μm of tantalum (Ta) to provide uniform heating. The InGaN films were capped with a 5 nm-GaN layer to prevent phase separation upon cool down. After solvent clean, the samples were immersed in SurPass 3000 for 5 min to promote resist adhesion. The films were then coated with 35 nm of hydrogen silsesquioxane (HSQ) 2% resist and baked at 80°C for 4 min (Figure 8.1(b)). E-beam writing was achieved in a JEOL JBX-9300FS EBL system at 100 kV and 0.6 nA. After EBL exposure, the HSQ was developed in 25% TMAH for 30 s, and then rinsed in running deionized water to remove unexposed HSQ (Figure 8.1(c)). The dot patterns were then transferred into the underlying InGaN layer by ICP etching in a Plasma-Therm ICP system. The etching was performed in a BCl_3/Cl_2 mixture (8/32 sccm) with 5 sccm of Ar at 5 mTorr chamber pressure. The platen (RF1) and coil (RF2) powers were 70 W and 50 W, respectively, resulting in an etch rate of ~50 nm/min. After etching, the HSQ

was stripped in buffered hydrofluoric acid for 1 min. The final InGaN QD structure is depicted in Figure 8.1(d). The dot size, spacing and shape were characterized by SEM in a Zeiss Ultra60 FE-SEM. The etch step was measured by AFM.

As a preliminary step for EBL processing, the e-beam dose was optimized to provide efficient exposure of QDs. For this purpose, a range of e-beam exposure dose was evaluated on test samples. The pattern, which consists of 20×20 μm array of dots, was written on HVPE-grown GaN templates. The doses were varied between 13,000 and 20,000 μC/cm^2.

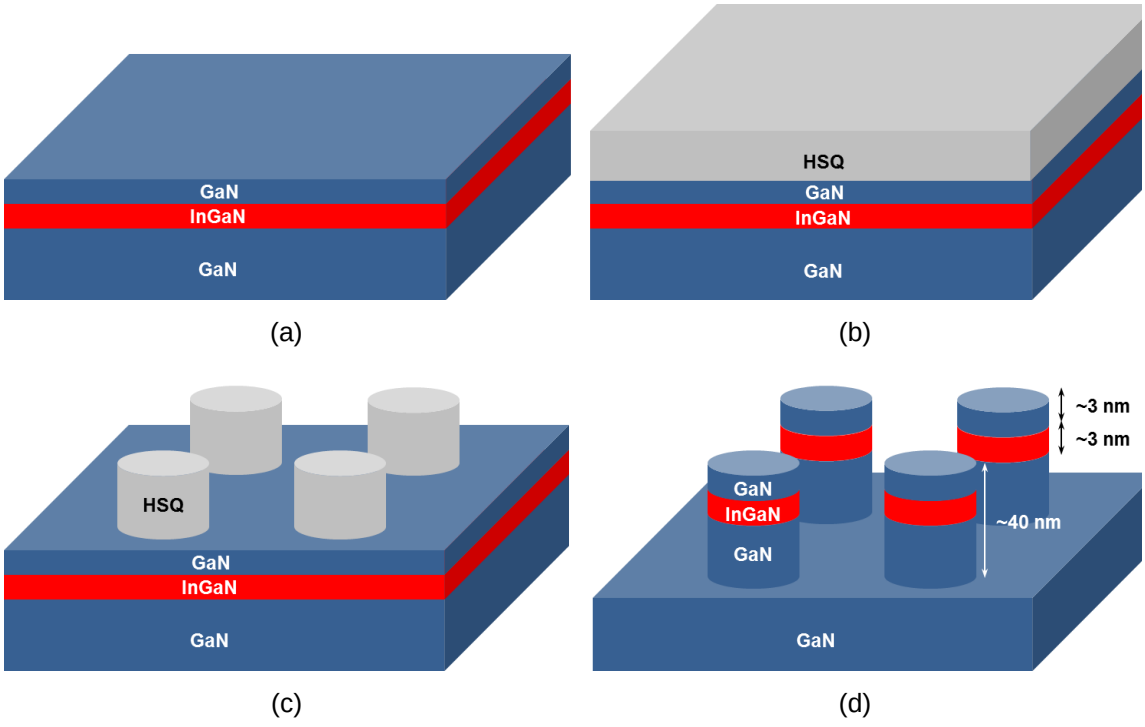

Figure 8.1: Formation of InGaN QD by EBL: (a) GaN/InGaN QW/GaN cap structure grown by MBE, (b) HSQ coating, (c) EBL exposure and development, and (d) pattern transfer by ICP etch.

8.1.2 Results and Discussion

The preliminary step for EBL processing was to determine the adequate e-beam dose for efficient writing of QDs. Several dose test were performed on GaN templates. The optimal dose depends on the dot size, dot pitch, and test area. Figure 8.2(a) and Figure 8.2(c) shows examples of underexposed and overexposed patterns, respectively. While some dots in the underexposed pattern are missing, dots in the overexposed pattern are merged together. Figure 8.2(b) shows well-defined dots obtained using an optimized dose. This optimized dose was used as a baseline for subsequent e-beam writing experiments on InGaN QW structures. This optimized condition leads to uniform arrays of dots with diameter ranging from 25 to 50 nm. The distorted oval shape of the dots is due to the curvature of the electron beam during the writing of the pattern since the pattern was positioned in the top left corner of the beam writing area. This shape issue was resolved by centering the pattern in the electron beam writing area.

After optimizing the EBL processing, the QD features were written on a 3 nm-$In_{0.65}Ga_{0.35}N$ layer grown on a GaN template and capped with 3 nm of GaN. The pattern, which consists of 8 20×20 μm regions, is depicted in Figure 8.3 (a). Each region was exposed with a different dose. Table 8.1 lists the dose for each pattern region and the corresponding dot diameter after exposure and after etching. Figure 8.3(b) shows a SEM image of the HSQ pattern after exposure and development. All the QD regions are very uniform and do not show proximity effects. This uniformity is confirmed by the SEM image of an example QD region shown in the inset of Figure 8.3(b).

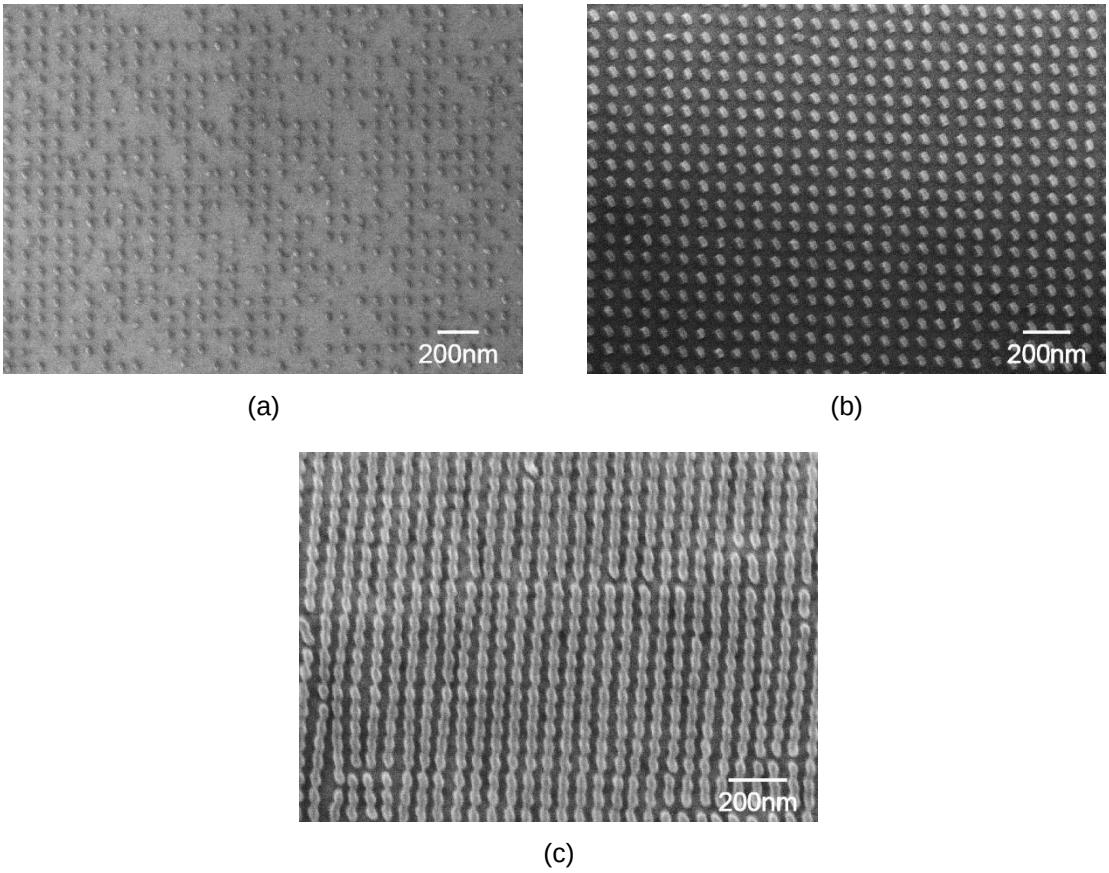

Figure 8.2: SEM images of (a) an underexposed pattern, (b) a pattern exposed with the optimized dose, and (c) an overexposed pattern.

Table 8.1: List of e-beam doses and corresponding dot diameters.

	Dose 1	Dose 2	Dose 3	Dose 4	Dose 5	Dose 6	Dose 7	Dose 8
Dose ($\mu C/cm^2$)	13,000	14,000	15,000	16,000	17,000	18,000	19,000	20,000
Dot diameter after exposure (nm)	30-32	30-33	28-32	30-35	35-38	38-40	26-35	23-36
Dot diameter after etching (nm)	32-38	32-35	32-35	34-38	39-44	39-42	35-39	35-37

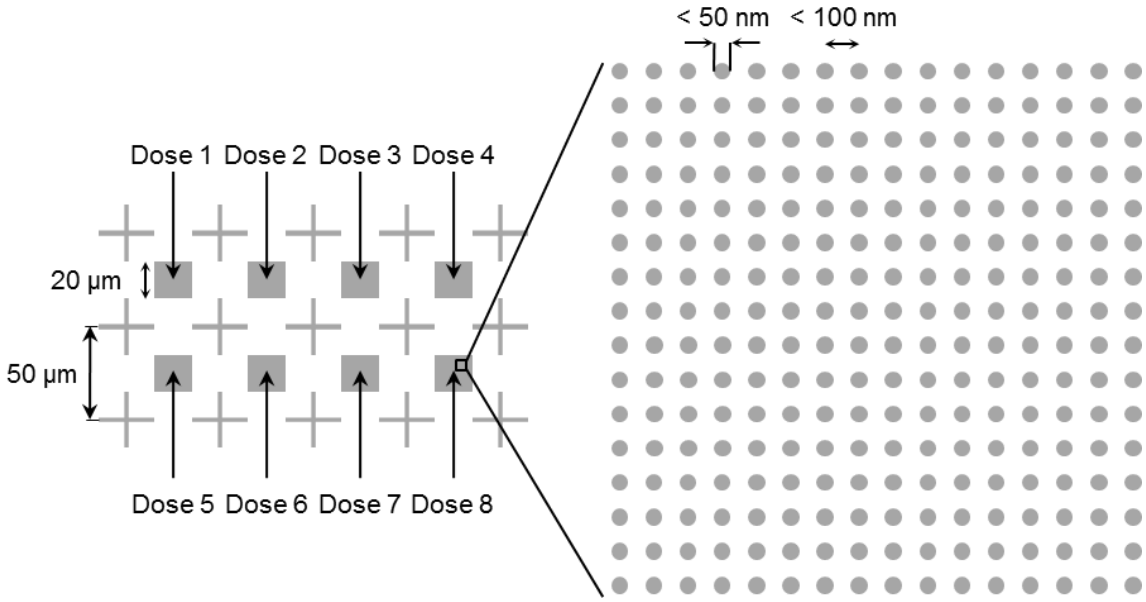

(a)

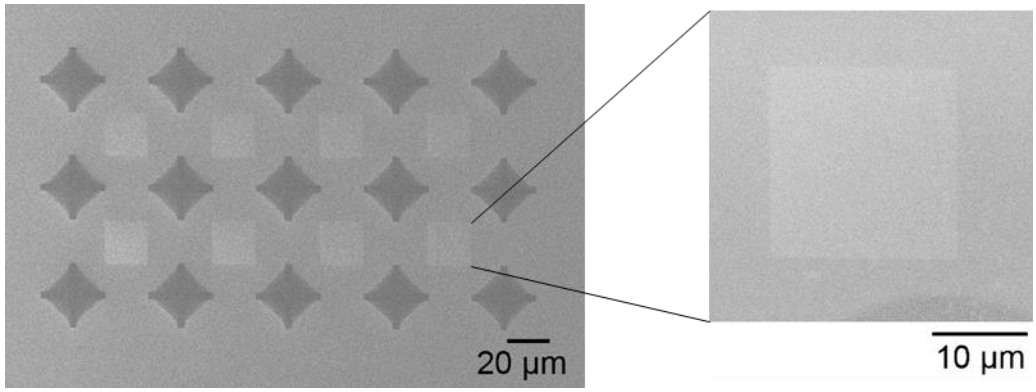

(b)

Figure 8.3: (a) Diagram and (b) SEM image after exposure development of the pattern with various doses. The inset in (a) shows a magnified view of the QDs and the inset in (b) shows a magnified SEM view of a 20×20 μm region of QDs.

The pattern was transferred to the InGaN quantum well by ICP etching for 50 s, resulting in a step height of ~40 nm as demonstrated by the step height profile of a test structure measured by AFM and depicted in Figure 8.4. Figure 8.5 compares the surface of the sample before and after etching. The etch process slightly roughened the GaN underlayer as illustrated by the AFM scan in Figure 8.5, but the surface is still relatively smooth with an RMS roughness of 0.97 nm.

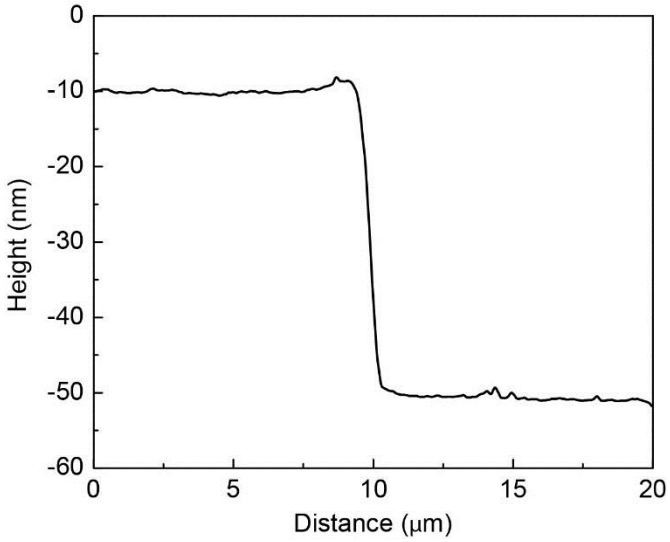

Figure 8.4: Step height profile after ICP etch measured by AFM. The step height is ~40 nm.

The QDs in the various regions were characterized using SEM to determine the diameter and spacing of the dots. Representative SEM images of QDs in regions 1-8 are shown in Figure 8.6. The dots are very uniform and round. As expected, the pitch is <100 nm for all regions but the dot diameter slightly varies with the exposure dose.

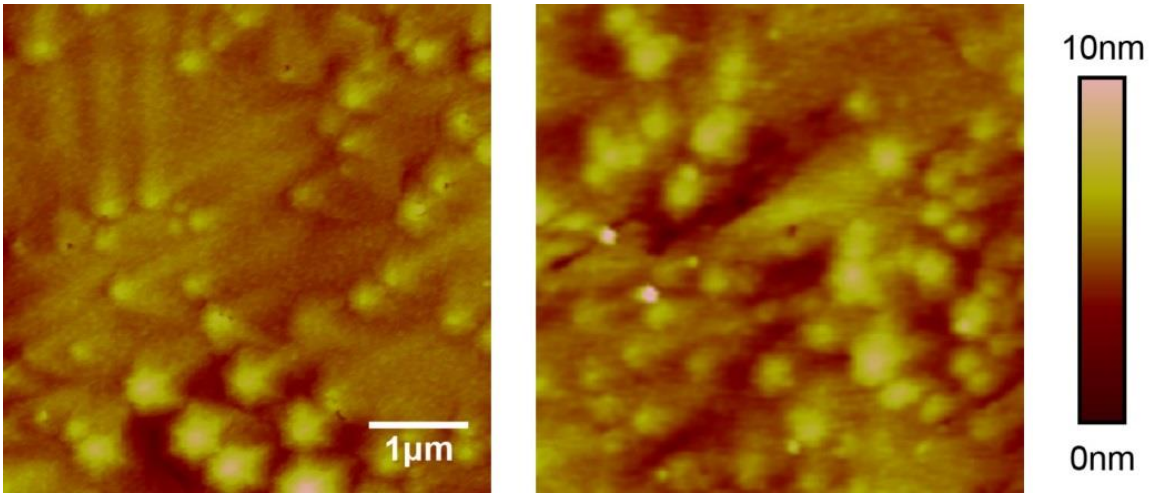

(a) (b)

Figure 8.5: 5×5μm AFM images of the sample surface (a) after growth of the GaN/InGaN/GaN structure (0.75 nm RMS) and (b) after the ICP etch (0.97 nm RMS). The surface roughened slightly due to etching.

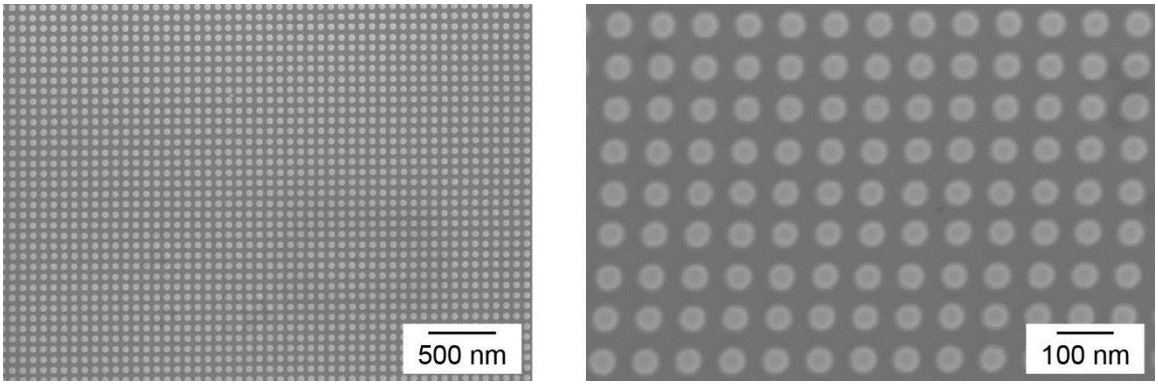

(a) (b)

Figure 8.6: SEM images of InGaN QD pattern after ICP etching showing superior uniformity and dot shape.

Figure 8.7 displays an SEM image of QDs after etching with a sample tilt of 45°. The top diameter is larger than the bottom diameter is 46-49 nm. The dot sidewalls are not vertical indicating that the etching process was not anisotropic. This phenomenon can be explained by the low RF power needed for a slow-enough etch rate to ensure

timed etch control. The diameter of the dots after etching is larger for each region than that before etching as listed in Table 8.1. Because of the etch isotropy, the InGaN dots will have a smaller diameter than that of the bottom diameter.

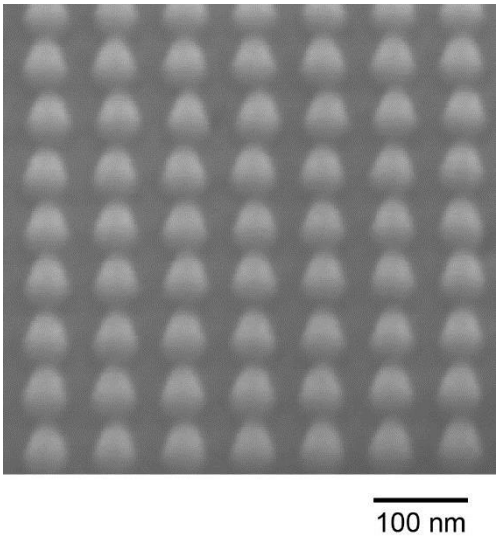

Figure 8.7: SEM image of QDs in after etching. The sample is tilted 45°.

8.1.3 Summary

In summary, the fabrication of InGaN QDs with an In content of 65%, a height of ~3 nm, a diameter of <50 nm, and a pitch of <100 nm by EBL was demonstrated. The EBL processing was optimized on GaN templates to determine the appropriate dose. After calibration and optimization, the QD patterns were written on a MBE-grown GaN/InGaN QW/GaN structure by EBL and transferred by ICP etching resulting in uniform array of QDs with minor etch damage.

8.2 *In-situ* Growth of InGaN Quantum Dots by Molecular Beam Epitaxy

While the *ex-situ* formation of InGaN QD by EBL allows for a precise control and uniformity of the dot size and density, this method is time-consuming, can produce etch damage, and requires multiple steps. To address this issue, a second method, which consists of *in-situ* MBE growth of QDs, is considered. The growth of InGaN self-assembled QD by MBE [156, 157] and MOCVD [158] has been previously investigated. In this study, the effect of the growth temperature on the density and size of the QDs is examined.

8.2.1 Experimental Procedure

The metal dose required for the MBE growth can be estimated through the QD surface coverage. A surface coverage of ~20% is desired to obtain a high-density of InGaN QDs with a diameter < 30 nm. Taking into account the height of the QDs, the required dose to form the targeted structure can be estimated and corresponds to ~2 monolayers of 65% InGaN. The 65% InGaN QDs were grown by MBE on GaN templates under very N-rich conditions with a 5 s open/10 s closed shutter duty cycle. To evaluate the impact of the growth temperature on the size and density of the InGaN QD, the QD growth was performed at various low growth temperatures ranging from 290°C to 370°C. The growth temperature was reduced to 200°C, while maintaining N flow as soon as the InGaN deposition was complete. The formation of QD was characterized in real-time by RHEED and post-growth by AFM.

8.2.2 Results and Discussion

The morphology of 65% InGaN QDs deposited at various substrate temperatures can be qualitatively assessed by the RHEED patterns depicted in Figure 8.8. As the growth temperature increases, the RHEED pattern evolves from elongated spots, associated with rough 2D films, to chevron-shape spots, associated with 3D islands. The chevron shape originates from the refraction of the electron beam when transmitted through the crystals facets. The pattern evolution with increasing temperature indicates a transition from a 2D growth mode to a 3D growth mode. Another noticeable feature of the RHEED patterns is the appearance of two distinct RHEED patterns as the temperature increases. For growth temperatures of 350°C and 370°C, the RHEED patterns, visible in Figure 8.8(d) and (e), respectively, consist of a juxtaposition of streaks and spots that are slightly shifted vertically. This shift corresponds to a difference in lattice-spacing values. The streaks are attributed to the smooth GaN underlayer and the spots are attributed to the InGaN QDs. With increasing growth temperature, the migration of In and Ga atoms is enhanced, leading to the formation of larger and sparser QDs. The InGaN surface coverage decreases and the GaN-underlayer surface becomes more exposed to the RHEED beam, leading to a stronger corresponding RHEED signal.

The trends observed by RHEED during the QD formation are confirmed by post-growth AFM measurements. 500×500 nm AFM scans of the InGaN QD formed at various growth temperatures are shown in Figure 8.9.

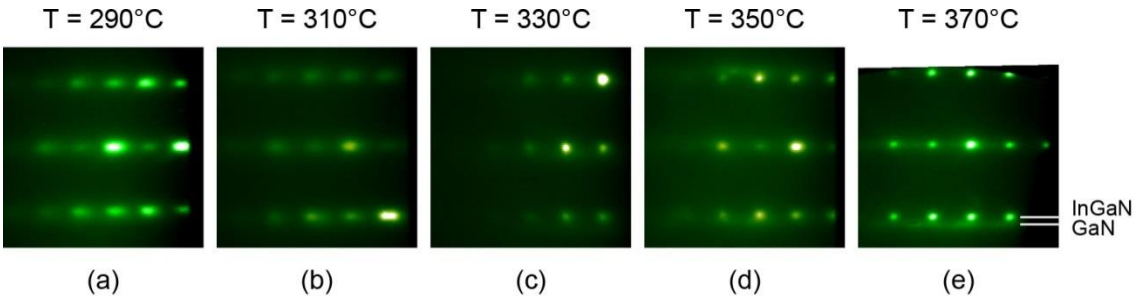

Figure 8.8: RHEED patterns during MBE growth of InGaN QDs grown at (a) 290°C, (b) 310°C, (c) 330°C, (d) 350°C, and (e) 370°C.

The extracted dot density N is plotted as a function of growth temperature in Figure 8.10(a). As the growth temperature increases, the density of InGaN self-assembled QD decreases from 6.72×10^{10} cm^{-2} to 1×10^{10} cm^{-2} because of the enhanced migration of In and Ga atoms. For high temperatures, the dot density drops drastically due to island coarsening by eliminating small islands while increasing the size of large ones [159]. This mechanism is driven by the thermodynamic tendency of the system to reduce its free energy through a decrease in the island total surface area. The analytical relationship between the dot density N and the diffusion coefficient D indicates that $D \propto N^{-3}$ for isotropic two-dimensional diffusion [159, 160]. The diffusion coefficient D follows an Arrhenius relationship with the growth temperature as illustrated in Figure 8.10(b). The slope of the curve yields an activation energy for surface diffusion of adatoms of 1.2 eV.

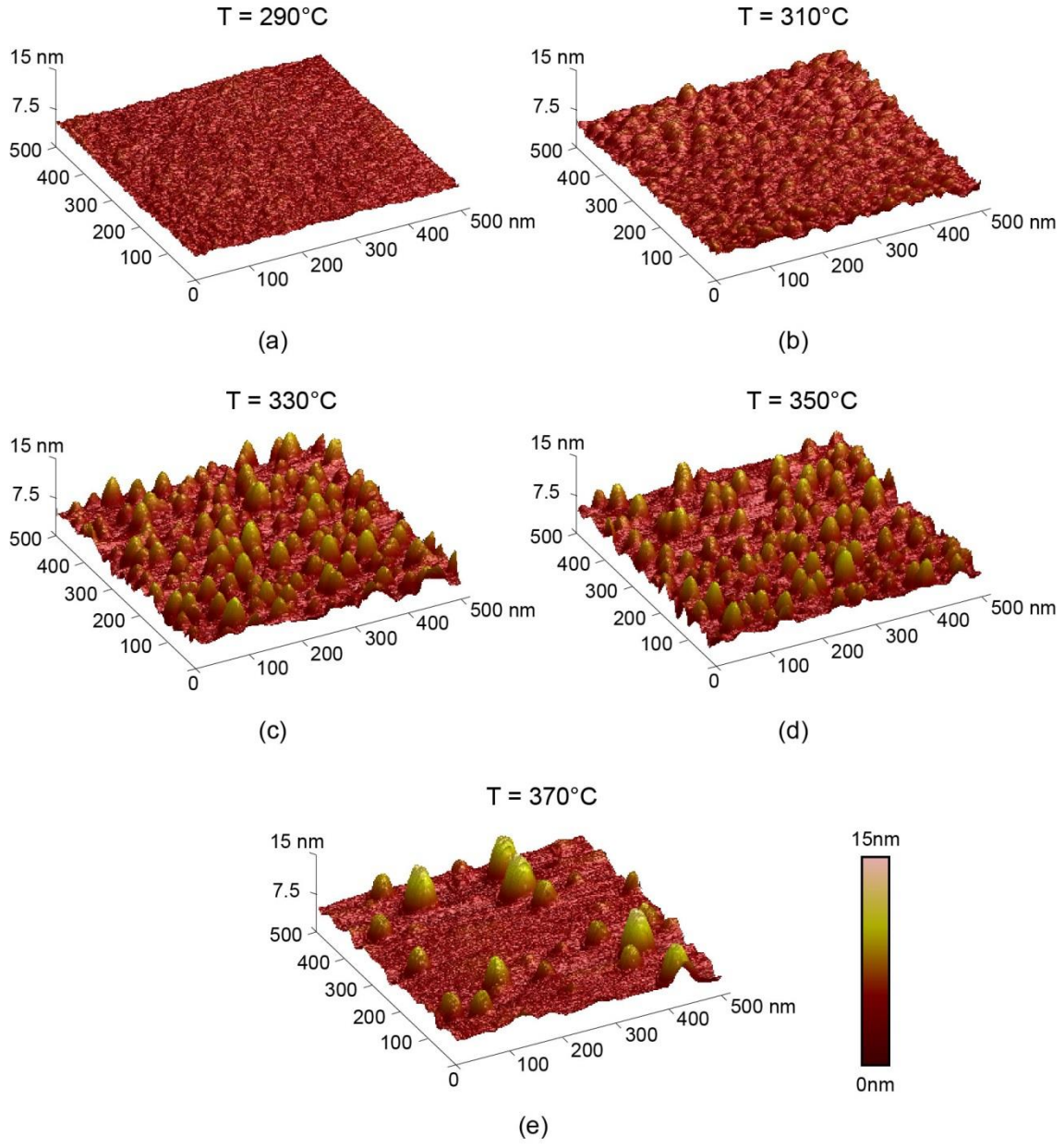

Figure 8.9: 500×500 nm AFM images of InGaN QDs grown by MBE at (a) 290°C, (b) 310°C, (c) 330°C, (d) 350°C, and (e) 370°C.

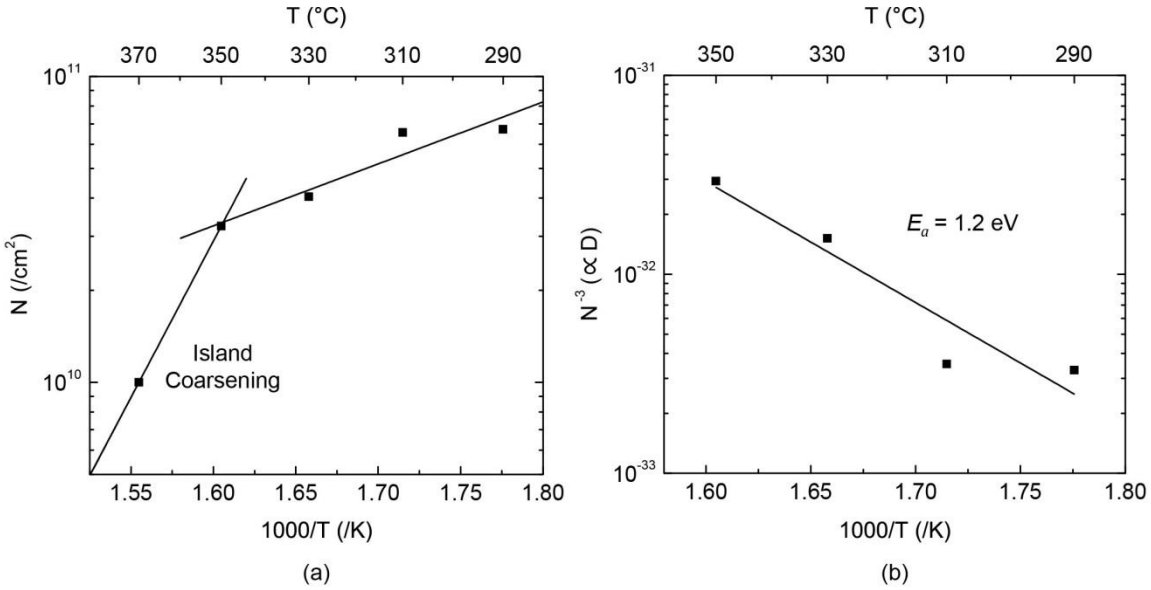

Figure 8.10: (a) Density N of InGaN self-assembled QDs as a function of growth temperature and (b) N^{-3}, which is proportional to the diffusion coefficient D, as a function of growth temperature.

Figure 8.11 shows the effect of the growth temperature on the height and diameter of the QDs. With increasing temperature, the average height rises from 0.4 nm to 3.6 nm while the average diameter rises from 13 nm to 30 nm. Note that for all these samples, the equivalent dose of InGaN material remained constant at 2 MLs. Therefore, the size of the QDs can be adjusted by varying solely the growth temperature. The standard deviations of the height and diameter, shown by error bars in Figure 8.11, are relatively large. Since the formation of the self-assembled QDs depends on the random thermal migration of metal atoms, the size of the QD is highly variable. Thus, the InGaN self-assembled QDs produced by this *in-situ* MBE technique are randomly distributed and not uniform.

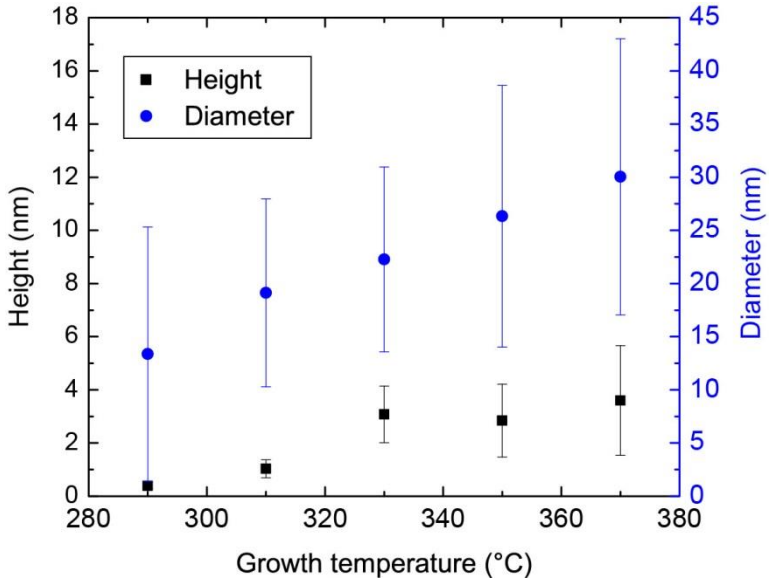

Figure 8.11: Height and diameter of InGaN self-assembled QDs grown by MBE as a function of growth temperature.

8.2.3 Summary

In summary, the formation of 65% InGaN self-assembled QDs by MBE was demonstrated. The effect of growth temperature on the QD density, height, and diameter was studied. While the *in-situ* MBE growth is more time-efficient and more practical for device integration than the *ex-situ* EBL formation, this technique does not allow for a precise control and uniformity of the dot size and distribution.

8.3 Attempted Fabrication of InGaN Quantum Dots Solar Cells

The theoretical performance of IB solar cells based on InGaN QD has been previously investigated [161, 162]. Simulations predict that the conversion efficiency of such cells strongly depends on the dot size, spacing, composition, and number of QD layers. Sang *et al.* [163] recently demonstrated experimentally the MOCVD growth and fabrication of a multi-level IB solar cell by embedding multi-stacked InGaN QDs with varying size and In content in a GaN matrix between a *p-n* junction. The photocurrent is enhanced due to sub-band-gap absorption originated from the multi-level transitions of the multi-QDs. However, the open-circuit voltage is considerably reduced possibly due to leakage current, recombination, and tunneling through energy levels introduced by the QDs. Using the QD calibration performed by the *in-situ* MBE technique and described in the previous section, InGaN QDs were incorporated in a *p-n* junction to make an attempt at InGaN QD IB solar cells.

8.3.1 Experimental Procedure

A solar cell with 5 periods of 65% InGaN QDs/GaN superlattices (SL) was grown, fabricated, and tested. A schematic structure of the attempted (5×) InGaN QD solar cell is depicted in Figure 8.12. The InGaN QDs with a targeted In content of 65% were grown by MBE at 310°C. Each layer of InGaN QDs was capped with 10-12 nm of MME-grown GaN. The SL structure was sandwiched between a ~350 nm-thick *n*-GaN and a ~60 nm-thick *p*-GaN layers. The solar cell was then fabricated using the fabrication process and the mask described in Chapter 5.

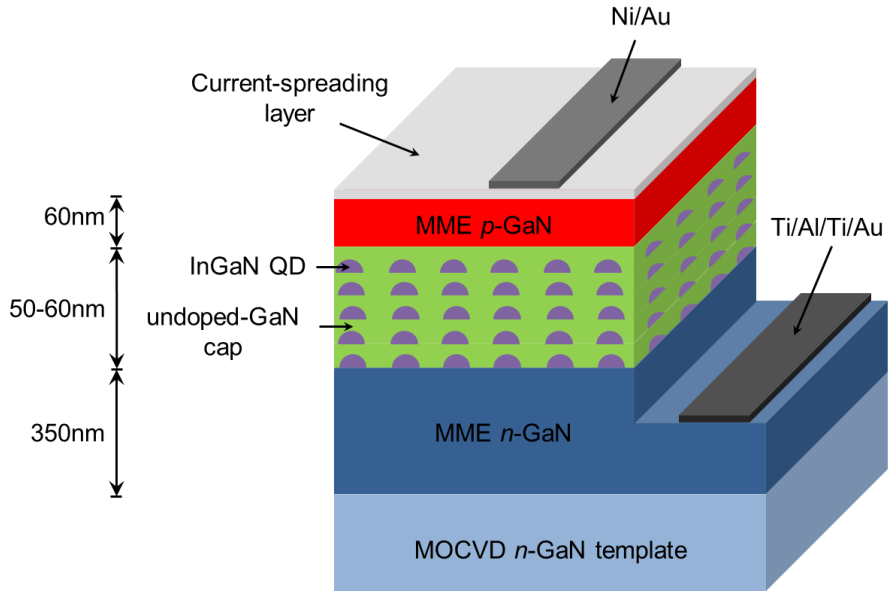

Figure 8.12: Schematic structure of the InGaN QD/GaN (5×) SL solar cell.

8.3.2 Results and Discussion

Figure 8.13 displays typical RHEED patterns at various stages of the growth of the InGaN QD solar cell structure. As expected, the RHEED pattern produced after the *n*-GaN layer consists of streaks with (2×2) reconstruction patterns as observed in Figure 8.13(a), that correspond to a smooth surface. The RHEED pattern after the QD formation is a juxtaposition of spots and streaks, produced by the InGaN QDs and the GaN underlayer, respectively. After covering the InGaN QDs by a GaN capping layer, the RHEED pattern becomes streaky as illustrated in Figure 8.13(c). The RHEED pattern after the growth of the *p*-GaN layer shows elongated spots that are typical of MME-grown *p*-GaN film as discussed in Section 4.2.

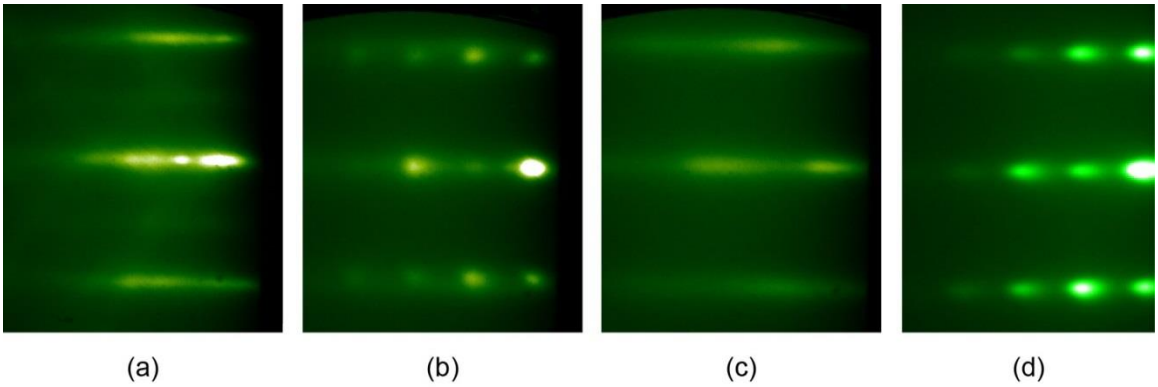

Figure 8.13: Typical RHEED patterns at various stages of growth of the InGaN QD solar cell: (a) after the *n*-GaN layer, (b) after the InGaN QDs, (c) after the undoped-GaN cap, and (d) after the *p*-GaN layer.

The presence of the InGaN QDs in the 5-period structure was confirmed by XRD measurement. The (0002) diffraction scan, depicted in Figure 8.14, shows InGaN satellite peaks that originate from the periodicity of the InGaN QDs/GaN SL. The surface morphology of the solar-cell structures was examined by SEM and AFM, as illustrated in Figure 8.15. While the surface is grainy, as expected due to the *p*-GaN layers, it is relatively smooth given the presence of the QDs (1.44 nm RMS).

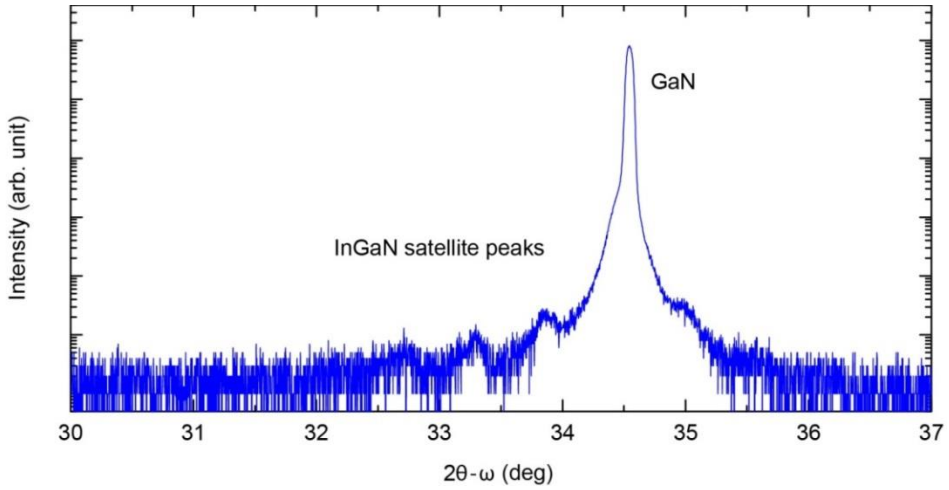

Figure 8.14: XRD (0002) diffraction scan of the InGaN QD/GaN (5×) SL solar cell.

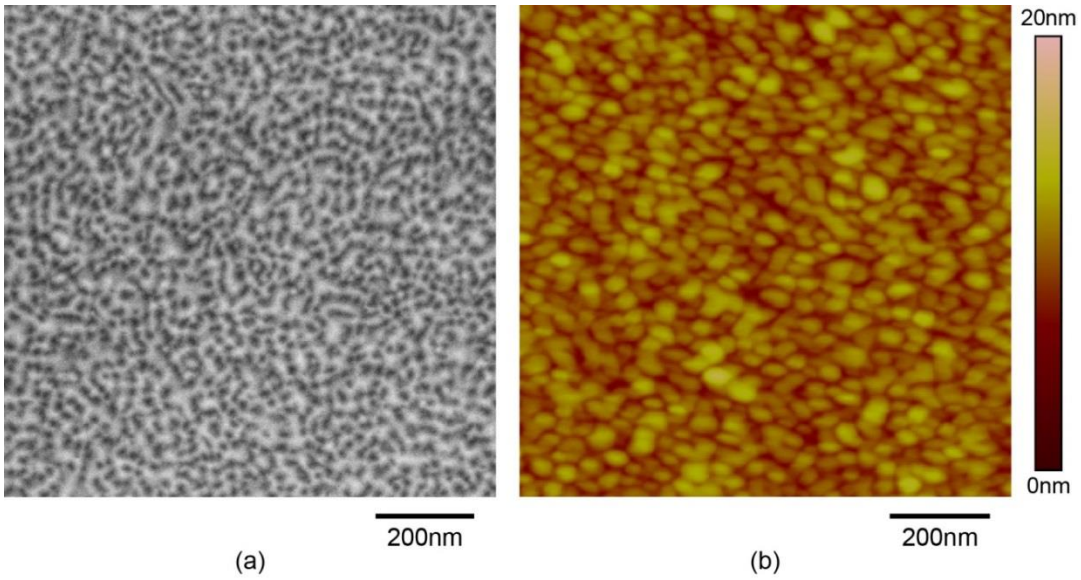

Figure 8.15: (a) SEM image and (b) AFM scan of InGaN QD/GaN (5×) SL solar cell surface (1.44 nm RMS).

The performance of the attempted InGaN QD IB solar cell was tested using a Solux broad-spectrum lamp (4700K) with ultra-low UV and under concentration (~20×). An example of dark and light *I-V* characteristics of 5-period structure are depicted in Figure 8.16. The *I-V* characteristics show a very high reverse current and no PV effect. This lack of PV effect could result from leakage current, recombination, and/or tunneling possibly due to non-fully capped QDs. Other issues might arise from the GaN-cap low growth temperature that is necessary to prevent any alteration of the InGaN QDs and that will most likely result in low-quality defective GaN interlayers.

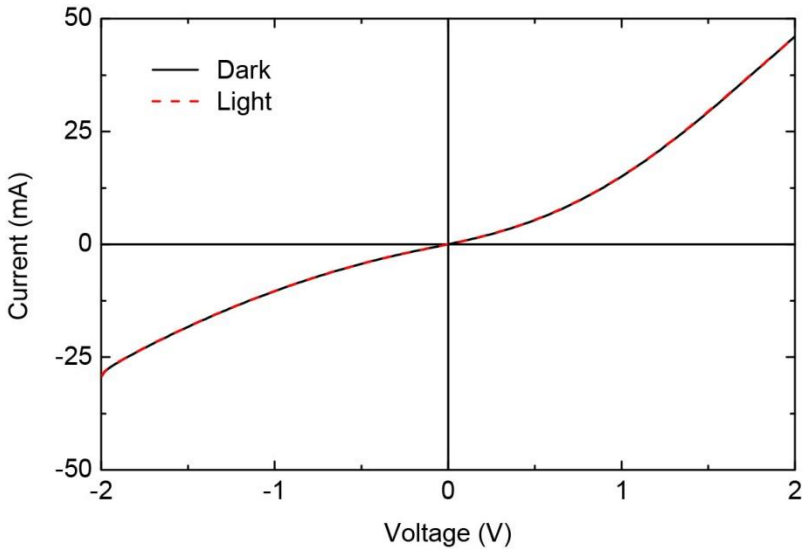

Figure 8.16: Dark and light *I-V* curve of the InGaN QD/GaN (5×) SL solar cell showing high reverse current and no PV effect.

8.3.3 Summary

In summary, the growth and fabrication of InGaN QD IB solar cell was attempted. Using the MBE-growth calibration for the formation of InGaN QDs, a solar cell structure with a 5-period InGaN QDs/GaN SL was grown by MBE. The growth was monitored *in situ* by RHEED and the structural properties and the surface morphology were characterized *ex situ* by XRD, SEM, and AFM. Under illumination, the device demonstrated no PV effect possibly due to leakage current, recombination, and/or tunneling as evidenced by high reverse current.

CHAPTER 9

CONCLUSIONS AND RECOMMENDATIONS

The objective of this dissertation has been to realize advances in design optimization and growth technology for high-efficiency InGaN-based photovoltaics through performance simulation, MBE growth, and device fabrication. In this chapter, research results and accomplishments are summarized and discussed. Future research recommendations are presented as well.

9.1 Conclusions

While InGaN alloys are a promising candidate for high-efficiency solar applications, their full potential requires significant progress in the areas of device design, material growth, and device fabrication.

Using numerical simulations, the performance of InGaN *p-i-n* single-junction solar cells were investigated to provide guidelines for optimizing device design given specific material characteristics. The performance of both InGaN/GaN heterojunction devices that are presently achievable and InGaN homojunction solar cells that should be feasible in the future were investigated using realistic constraints on growth and fabrication. The simulations studied the effect of In content, thickness, and background doping of the InGaN absorbing layer on the performance of both InGaN solar-cell designs. The conversion efficiency of currently-feasible heterojunction structures is limited by polarization effects that hinder carrier collection for high In composition. These detrimental polarization effects can be eliminated by using InGaN homojunction

devices. For an optimized InGaN *p-i-n* homojunction solar cell, the maximum conversion efficiency is limited below the theoretical limit for single-junction devices by presently achievable surface recombination velocities and minority carrier lifetimes. Using improved but unrealistic parameter values, the efficiency reaches a value closer to the predicted theoretical maximum efficiency. The results demonstrated that the only viable design for a high-efficiency single-junction InGaN solar cell is the homojunction structure. This design is currently challenging to fabricate, but should be achievable in the future assuming challenges in material quality and *p*-type doping can be overcome.

InGaN-based solar cells require high-quality InGaN layers to efficiently absorb photons and create photogenerated carriers. To address this need, the MBE growth of InGaN film over the entire composition was investigated. The surface morphology, microstructural, and optical properties of InGaN films grown by plasma-assisted MBE under low growth temperatures and slightly N-rich growth conditions were studied. The single-phase InGaN films exhibit improved defect density, an absence of stacking faults, efficient In incorporation, enhanced optical properties, but a grain-like morphology. The relaxation mechanism of InGaN epitaxial layers grown on both GaN and AlN was examined and compared. With increasing In content, a complete misfit strain relaxation through the formation of a uniform array of misfit dislocations at the InGaN/GaN and InGaN/AlN interface were observed for InGaN films with In contents higher than 55-60% and 40-45%, respectively. The complete misfit strain relaxation originates from the fundamental lattice mismatch between the InGaN film and the buffer layer. The In composition at which this structural transition happens is lower for InGaN on AlN than for InGaN on GaN due to the larger lattice mismatch resulting from the difference in

in-plane lattice constant. The transition composition can be estimated for various buffer layers by calculating the In content at which the critical thickness reaches a value close to 1-2 monolayers. These InGaN films with improved structural and optical properties are very beneficial for use as absorbing layers in InGaN-based solar cells.

In addition to the growth of InGaN absorbing layers, the growth of doped GaN and InGaN films, required for photogenerated-carrier separation and collection, was studied. The growth of both *n*- and *p*-GaN films by MME was investigated to provide a useful calibration and baseline for III-nitride solar cells. The correlation between growth mechanisms and RHEED signatures observed at various portions of the shutter cycle was analyzed for both Si-doped and Mg-doped GaN epilayers. The impact of Si and Mg incorporation on the structural and electrical properties of the films were described. The increased incorporation limit for both dopants is attributed to the MME technique that enables the control of the kinetics of dopant incorporation using low substrate temperatures and metal-rich fluxes. The growth of *p*-InGaN films by N-rich MBE and MME for use in homojunction structures was also investigated. The effect of the growth technique and the III/N ratio on the electrical, structural, and optical properties of Mg-doped 25% InGaN films was examined. Independent of the growth method, the Mg-doped InGaN layers were measured to be *p*-type by hot-probe measurements. All *p*-InGaN films exhibited no phase separation and a grainy morphology. The metal-rich conditions lead to smoother surfaces but higher stacking-fault densities that resulted in the absence of optical emission. On the other hand, the N-rich growth conditions resulted in rougher surfaces but enhanced optical properties. While these *p*-type 25% InGaN

films are promising for future InGaN homojunction solar cells, further progress needs to be achieved to extend *p*-type doping to higher In composition.

Among the requirements to demonstrate InGaN solar cells is a process to fabricate and optimize devices. A fabrication process that uses optical lithography, dry etching, metal deposition, and lift-off was developed. A new mask set that comprises cells with various sizes and grid spacings as well as diagnostic structures was designed and fabricated. To attest the viability of this process, several III-nitride devices were fabricated and showed promising *J-V* characteristics and photovoltaic responses. The formation of ohmic contacts to III-nitride films, which is a critical step for the fabrication of InGaN solar cells, was also discussed. While *n*-type contacts typically showed ohmic behaviors with suitable contact resistivities, satisfactory *p*-type contacts were more challenging and involved an annealing step. Another essential design element for high-efficiency solar cells is the metallization grid pattern. A method for quantifying the power losses due to the metallization grid pattern and optimizing the finger spacing was presented. The power losses for InGaN-based solar cells were calculated using realistic parameters and the effect of various material and fabrication parameters on the optimal finger spacing was assessed. Since the produced current density is relatively low, the influence of resistive losses is minor and the predominant component of the total power loss is optical losses due to shading.

Using the improved growth technology and the developed fabrication process, the MBE growth, material characterization, and performance testing of InGaN/GaN double-heterojunction solar cells was investigated as a preliminary step towards device fabrication and as a comparison to the existing literature. Structures with varying

thicknesses and compositions of the InGaN absorbing layer were studied. The N-rich MBE growth at low temperatures enables the growth of thick 10% and 20% InGaN films with minimal strain relaxation and defect generation. The characteristics of both large-area and small-area devices were compared. While leakage current and high ideality factors remain major issues, the double-heterojunction cell with a record-high In content of 22% shows a promising photovoltaic response. An attempt at an InGaN/GaN double-heterojunction solar cell with a 35% InGaN absorbing layer was also made. The device does not show photovoltaic effect as a result of the formation of defects due to strain relaxation and polarization effects due to heterointerfaces. This experimental observation of the lack of photovoltaic effect is consistent with predictions reported by simulations for double-heterojunction with high-In content InGaN absorbing layers. The efficiency of double-heterojunction solar cells is limited by detrimental effects (polarization effects impeding carrier collection, strain relaxation generating defects, and tunneling through interface states) associated with the double-heterojunction structure. These experimental results, which are concordant with simulation results, further confirm that the pathway for high-efficiency III-nitride solar cells is thick homojunction structures.

While very promising, homojunction devices are currently extremely challenging to fabricate because of the need for thick, high-quality InGaN films. To address this requirement, a hybrid growth technique that combines metal-rich and nitrogen-rich growth regime was presented. The superlattice InGaN film displays encouraging structural and morphological properties, but exhibits In surface segregation.

Finally, an advanced InGaN-based solar-cell design that employs InGaN quantum dots was explored. Two methods to fabricate InGaN quantum dots were considered: an *ex-situ* patterning of InGaN quantum well by electron-beam lithography and an *in-situ* MBE growth of quantum dots. For the first method, the effect of the exposure dose on the dot diameter was studied. After calibration and optimization, the quantum-dot patterns were written on a MBE-grown GaN/InGaN quantum well/GaN structure by electron-beam lithography and transferred by plasma etching resulting in uniform array of dots with minor etch damage. For the second method, the effect of growth temperature on the dot size and density was studied. Unlike the *in-situ* MBE growth, which resulted in dots with highly variable shape and distribution, the *ex-situ* formation of InGaN quantum dots by electron-beam lithography allowed for a precise control and uniformity of the dot size and density. However, the electron-beam lithography patterning method is time-consuming and requires multiple steps while the MBE growth is more time-efficient and more practical for device integration. Using the QD calibration performed by the *in-situ* MBE technique, InGaN quantum dots were incorporated in a *p-n* junction to make an attempt at an InGaN intermediate-band solar cell. Under illumination, the device demonstrated no photovoltaic effect possibly due leakage current, recombination, and/or tunneling as evidenced by high reverse current. Further efforts are necessary to optimize the growth conditions to obtain functioning InGaN quantum-dot intermediate-band solar cell grown by MBE.

9.2 Contributions

The results presented in this thesis resulted in the following accomplishments and contributions:

1. Provided guidelines for high-efficiency InGaN solar cells using realistic properties [99, 152].

2. Identified present and future material limitations for InGaN solar cells [99, 152].

3. Demonstrated the growth of single-phase InGaN films by N-rich MBE [105].

4. Improved the structural and optical quality of InGaN layers at solar-relevant composition (20-60% In content) [105].

5. Identified the origin of the complete misfit strain relaxation as the fundamental lattice mismatch between In-rich InGaN films and GaN/AlN underlayers [51, 105].

6. Presented a method to estimate the In composition at which the transition in the structural properties occurs depending on the buffer layer [51, 105].

7. Calibrated *n*- and *p*-type doping for III-nitride solar cells [122].

8. Demonstrated the growth of *p*-type 25% InGaN layers by N-rich and MME.

9. Developed a fabrication process for III-nitride optoelectronic devices [122].

10. Designed and fabricated a photomask dedicated to III-nitride based solar cells.

11. Calculated and optimized the metallization grid pattern for InGaN-based solar cells.

12. Reported the first InGaN/GaN double-heterojunction solar cells grown by RF-plasma MBE [164].

13. Demonstrated the growth and fabrication of functioning InGaN/GaN double-heterojunction solar cells with record-high In content of 22% [164].

14. Developed and optimized an electron-beam lithography process to pattern 30 nm-diameter InGaN quantum dots.

15. Investigated the effect of growth temperature on the size and density of InGaN quantum dots by N-rich MBE growth.

9.3 Recommendations for Future Work

Although this dissertation aimed at advancing InGaN-based solar cells, numerous research aspects require further improvements. Potential future research areas are presented in this section.

9.3.1 Growth of *p*-InGaN Films with High In Content

The growth of *p*-InGaN films with high In content is critical for the fabrication of homojunction solar cells. While the *p*-type 25% InGaN films demonstrated in this dissertation are promising, further advances are required to achieve *p*-type InGaN over the entire composition range. Extending *p*-type doping to higher In composition is very difficult since undoped InGaN epilayers usually show *n*-type conductivities with high residual electron concentrations due to donor-type impurities and defects. Another challenge is the presence of the surface accumulation layer in In-rich InGaN due to the extremely large electron affinity of InN. This layer renders the detection of *p*-type conductivity complex.

9.3.2 Optimization of Fabrication Process

The fabrication process developed in this dissertation is a useful starting point for producing III-nitride solar cells, but would benefit from add-ons and optimization. Suggested areas of research include the optimization of metal contacts, the optimization of the current spreading layer, the use of an antireflection coating (ARC), and the use of sidewall passivation. Metal-contact schemes and annealing conditions for both *p*- and *n*-type GaN can be further optimized to improve the contact resistance and stability. The current spreading layer is a critical aspect of nitride-based optoelectronic devices that also requires optimization. The electrical and optical properties of various films, for instance Ni/Au or transparent conductive oxides such as indium tin oxide (ITO), and the effect of annealing conditions on their properties should be studied. The ARC, which aims to enhance light coupling into the device, should have excellent surface passivation qualities and a matching refractive index. Thin layers of SiO_2 or SiN could be employed for sidewall passivation to eliminate current leakage path along the mesa sidewalls.

9.3.3 Investigation of Graded Structures for Photovoltaic Applications

As demonstrated by simulation results, InGaN/GaN heterojunction devices are limited by polarization effects. To mitigate these detrimental effects, composition-graded layers can be introduced to replace the abrupt InGaN/GaN heterointerfaces. Compared to the double-heterojunction design, these devices contain *n*- and *p*-type composition-graded layers. While this structure hinders detrimental polarization effects, the graded layers can have an unfavorable impact on the solar cell due to the introduction of defects that can act as shunt pathways.

9.3.4 Investigation of Thick InGaN layers for Homojunction Solar Cells

Thick InGaN layers grown by the hybrid MBE growth technique are very promising for high-efficiency solar cells. However, further research efforts are necessary to determine the full potential of these layers. To solve the In segregation issue, an alternative solution that consists of periodic ultra-thin metal-rich (M-rich) GaN interlayers inserted during the nitrogen-rich (N-rich) InGaN growth, is proposed. A similar semi-bulk approach has been previously investigated by MOCVD [165, 166]. This method replaces the M-rich InGaN interlayers used in Chapter 7, by M-rich GaN interlayers to avoid the formation of InN clusters. The alternative modulation scheme, which requires the control of source shutters independently, is illustrated in Figure 9.1. To implement this technique, a MATLAB script, provided in Appendix E, was written [167]. The effect of the M-rich GaN interlayers on the structural, optical, and electrical properties of these films needs to be investigated. Thick InGaN buffer layers with optimized properties can then be integrated in homojunction solar cells.

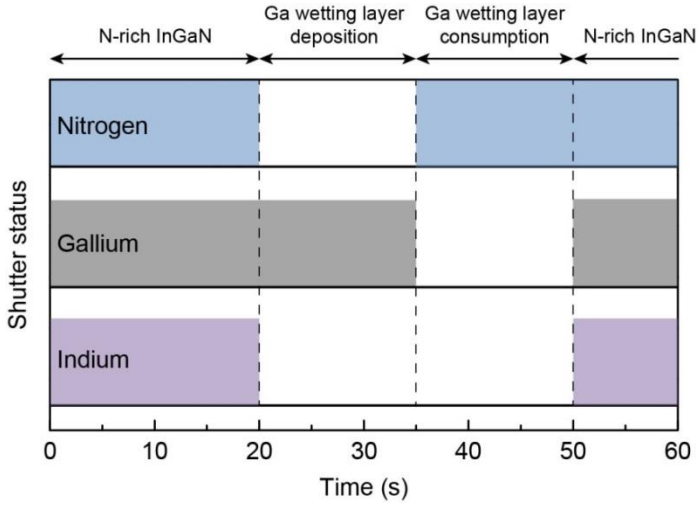

Figure 9.1: Simplified illustration of an alternative modulation scheme for the growth of InGaN using the hybrid growth technique.

APPENDIX A

X-RAY DIFFRACTION OF InGaN ALLOYS

X-ray diffraction (XRD) is a non-destructive technique used to determine the composition, strain, thickness, lattice parameters, and defect densities of III-nitride films and device structures. The diffraction of X-rays by matter results from the combination of the X-ray scattering by each atom in the crystal and the constructive interference of the scattered waves. Bragg's law, which describes the condition for constructive interferences, relates the spacing d_{hkl} between the planes of atoms from which diffraction occurs, to the angle θ between the incident monochromatic ray and the scattering planes required for constructive interference:

$$2d_{hkl}\, sin\, \theta = n\lambda, \tag{A.1}$$

where n is an integer and λ is the wavelength of the incident X-ray beam (λ = 1.54056 Å for CuKα). Each set of (hkl) crystal planes associated with real space will produce a diffraction spot associated with reciprocal space. In thin epitaxial semiconductor alloy films, variation of strain and chemical composition may both lead to a variation of interplanar separations, and thus, to a variation of the reciprocal lattice point (RLP) location.

For symmetric Bragg reflections (h and k = 0), only variations in lattice constant perpendicular to the sample surface can be detected. The physical origin (strain or composition) of the variation of the RLP position cannot be determined in this case as

illustrated in Figure A.1. Considering only symmetrical X-ray reflection may result in uncertainties on the In content and the strain.

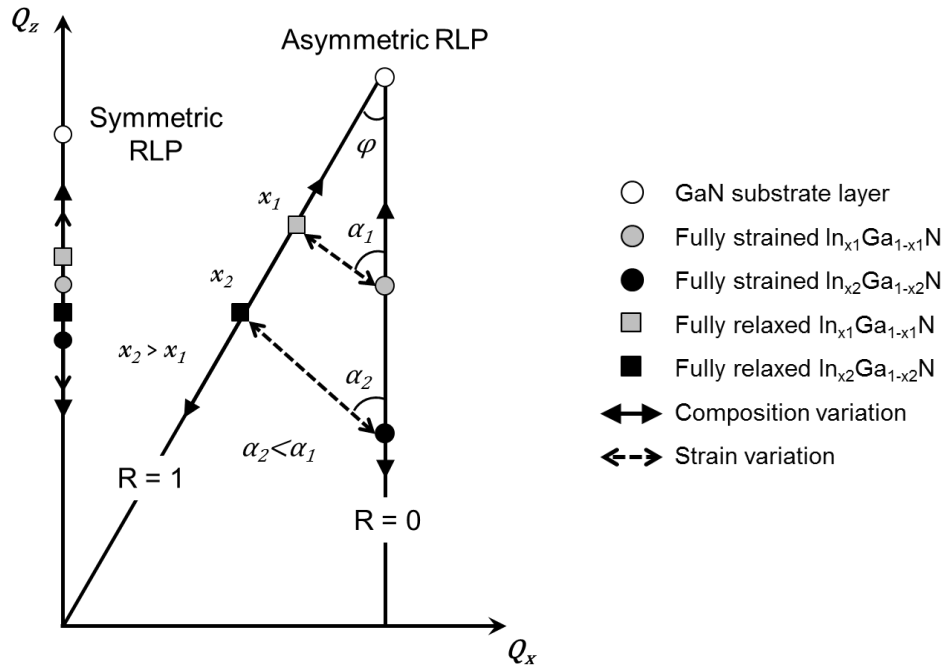

Figure A.1: Schematic diagram illustrating the effect of strain and composition variation on the position of symmetric and asymmetric RLPs of In_xGa_xN [150].

However, in the asymmetric case, the RLP shifts due to strain and composition differ significantly. Information on the in-plane and out-of-plane lattice constants can be obtained using an asymmetrical reciprocal space map (RSM) that allows the separation of the two effects. A RSM, which is a 2D section of reciprocal space, can be obtained by taking a series of 2θ-ω scans at successive values of ω, the angle between the incident beam and the sample surface. For asymmetric Bragg reflections, the value of ω will differ from that of θ. In order to plot RSMs, the angles ω and 2θ are converted into coordinates in reciprocal space Q_x and Q_z using the following equations [168, 169]:

$$Q_x = sin\,\theta\ sin(\theta - \omega) = \frac{1}{2}\,[cos\,\omega - cos(2\theta - \omega)] = \frac{\lambda}{2d_{\parallel}} \tag{A.2}$$

$$Q_z = sin\,\theta\ cos(\theta - \omega) = \frac{1}{2}\,[sin\,\omega + sin(2\theta - \omega)] = \frac{\lambda}{2d_{\perp}} \tag{A.3}$$

where $d_{\perp}$ and $d_{\parallel}$ are the average lattice spacing perpendicular to the layers and in the plane of the layer, respectively. In hexagonal lattices, the relation between the lattice spacing d_{hkl} and the lattice parameters *a* and *c* is

$$\frac{1}{d_{hkl}^2} = \frac{4}{3}\frac{h^2 + hk + k^2}{a^2} + \frac{l^2}{c^2} = \frac{1}{d_{\parallel}^2} + \frac{1}{d_{\perp}^2}, \tag{A.4}$$

Because the *c*-axis is parallel to $d_{\perp}$, *a* and *c* are given by

$$a = d_{\parallel}\sqrt{\frac{4}{3}(h^2 + hk + k^2)} = \frac{\lambda}{Q_x}\sqrt{\frac{h^2 + hk + k^2}{3}} \tag{A.5}$$

$$c = d_{\perp}l = \frac{\lambda l}{2Q_z} \tag{A.6}$$

Thus, any pair of coordinates (Q_x, Q_z) in the map corresponds to a pair of lattice constants (*a*, *c*) of the wurtzite structure.

In heteroepitaxy, the lattice constants of relaxed InGaN differ from those of the underlying substrate, creating a biaxial strain. In an InGaN layer, the strain components ε_{xx} and ε_{zz} are defined as

$$\varepsilon_{xx} = \frac{a - a_0(x)}{a_0(x)} \tag{A.7}$$

$$\varepsilon_{zz} = \frac{c - c_0(x)}{c_0(x)} \tag{A.8}$$

where a and c are the measured lattice parameters, and $c_0(x)$ and a_0 (x) are the relaxed parameters given by Vegard's law. The biaxial strain causes the distortion of the hexagonal unit cell. According to the biaxial elastic model, the in-plane strain ε_{xx} shows a linear relationship with the out-of-plane strain ε_{zz} by the distortion factor D as expressed by the following formula:

$$\varepsilon_{zz} = -D(x)\varepsilon_{xx} = -2\frac{C_{13}(x)}{C_{33}(x)}\varepsilon_{xx}, \tag{A.9}$$

where $C_{13}(x)$ and $C_{33}(x)$ are the elastic constants linearly interpolated from the binary values. For epitaxial films, the degree of the strain relaxation R is defined as

$$R = \frac{a(x) - a(S)}{a_0(x) - a(S)}, \tag{A.10}$$

where a and $a_0(x)$ are the measured and relaxed in-plane lattice constants of the layer of composition x, respectively, and a(S) is the lattice constant of the substrate. R = 0 means that the in-plane lattice constant in the layer is equal to the in-plane lattice constant of the substrate, *i.e.* the epitaxial film is completely strained to the substrate. On the other hand, R = 1 means that the lattice constant equals to that of the free-standing layer, *i.e.* the epitaxial film is fully relaxed.

The effects of strain and composition on the position of the symmetric and asymmetric RLPs are illustrated in Figure A.1 [150]. The variation in composition of a layer with fixed strain follows an isostrain composition line. The isostrain composition line corresponding to R = 0 and R = 1 are shown in Figure A.1. The relaxation process of a layer with a fixed composition from fully strained to fully relaxed follows an isocomposition relaxation line inclined at an angle α with respect to the Q_z axis. Two isocomposition lines along which relaxation varies from R = 0 to R = 1 are shown in Figure A.1 as two dashed lines at the angles α_1 and α_2.

The angle α can be expressed by

$$\alpha(x) = \tan^{-1}\left(\frac{\tan\varphi}{D(x)}\right), \tag{A.11}$$

where φ is the inclination angle of the (*hkl*) diffraction plane with respect to the surface normal given by [170]

$$tan\,\varphi = \frac{c}{a}\sqrt{\frac{4}{3}\frac{(h^2+hk+k^2)}{l^2}} \tag{A.12}$$

The strain and composition can be calculated analytically by solving

$$\frac{c-[c_0^{InN}x + c_0^{GaN}(1-x)]}{c_0^{InN}x + c_0^{GaN}(1-x)} = -2\frac{C_{13}^{InN}x + C_{13}^{GaN}(1-x)}{C_{33}^{InN}x + C_{33}^{InN}(1-x)}\,\frac{a-[a_0^{InN}x + a_0^{GaN}(1-x)]}{a_0^{InN}x + a_0^{GaN}(1-x)} \tag{A.13}$$

The input parameters used to perform the calculation are listed in Table A.1.

Table A.1: Lattice parameters and elastic constants for InN and GaN [171].

Parameter	GaN	InN
c_0 (Å)	5.185	5.703
a_0 (Å)	3.189	3.545
C_{13}	106	92
C_{33}	398	224

APPENDIX B

FABRICATION PROCESS FLOW

The following procedure was used for fabricating solar cell devices using five masks depicted in Figure B.1. Samples were degreased with a solvent clean before any photolithography step. Before processing the samples, the tantalum (Ta) backside metal was removed for consistent results.

B.1 Apparatus

B.1.1 Facilities

- Van Leer cleanroom
- Pettit cleanroom
- Marcus inorganic cleanroom

B.1.2 Materials

- Mask set
- Cleanroom supplies: beakers, tweezers, wipes, swabs, etc.

B.1.3 Chemicals

- Cleaning: trichloroethylene (TCE), Acetone, Methanol, deionized (DI) Water
- Photoresist (PR): AZ 5214
- Developer: AZ 400K or AZ 300MIF
- Stripper: AZ 400T
- Buffered Oxide Etch (BOE)
- Hydrofluoric acid (HF)
- Nitric acid (HNO_3)
- Hydrochloric acid (HCl)

B.1.4 Tools

- Wet bench and fume hood
- Spin coater
- Mask aligner: SUSS MJB3 (Exposure wavelength: 365 nm)
- Etcher: Plasma-Therm ICP (Gases: Cl_2, BCl_3, Ar)
- Asher: Plasma-Therm RIE (Gas: O_2)
- Profilometer: Tencor KLA, Dektak 150
- Electron-beam evaporator: Denton Explorer, CVC, CHA 2, VL evaporator (Metals: Ni, Au, Ti, Al, Pd)
- Mini-annealer: MILA-5000 (Gases: N_2, air)

B.2 Processing Recipes

B.2.1 Solvent Clean

- TCE for 5 min
- Acetone for 5 min
- Methanol for 5 min
- Dry with N_2
- Rinse with DI water

B.2.2 Photoresist Positive Recipe

- Solvent clean
- Dehydration Bake @ 120°C for >5 min to remove any solvent moisture - hot block in oven
- Spin AZ 5214 PR – spread: 500 rpm for 5 s; spin: 3500 rpm for 30 s
- Soft bake @ 115°C for 90 s - hot block in oven
- Exposure @ 100 mJ/cm^2 - use 365 nm detector to determine power and calculate exposure time
- Development in AZ 400K or AZ 300MIF developer for 20-30 s - Mild agitation
- Rinse in DI water for 30 s
- Dry with N_2

B.2.3 Photoresist Negative Recipe

- Solvent clean
- Dehydration Bake @ 120°C for >5 min to remove any solvent moisture - hot block in oven
- Spin AZ 5214 PR - spread: 500 rpm for 5 s; spin: 3500 rpm for 30 s
- Soft bake @ 115°C for 90 s - hot block in oven
- Exposure @ 60 mJ/cm^2 - use 365 nm detector to determine power and calculate exposure time
- Post exposure bake @ 100°C for 30 s - hot block in oven
- Flood exposure @ 600 mJ/cm^2
- Development in AZ 400K or AZ 300MIF developer for 20-30 s - Mild agitation
- Rinse in DI water for 30 s
- Dry with N_2

B.2.4 Plasma Etching Recipe

- Plasma-Therm ICP etcher – Left chamber
- Mount samples on 4" carrier wafer with cool grease
- Gases: Cl_2 = 32 sccm, BCl_3 = 8 sccm, Ar = 5 sccm
- Power: RF1 = 70 W, RF2 = 500 W
- GaN etch rate = 400-450 nm/min – PR etch rate ~500 nm/min
- Remove cool grease on the backside using a swab dampened with acetone

B.2.5 Plasma Descum Recipe to Remove Cured Photoresist

- Plasma-Therm RIE etcher – Right chamber
- Gases: O_2 = 80 sccm
- Power: RF = 200 W
- Pressure: P = 200 mTorr

B.2.6 Plasma Descum Recipe before Metallization

- Plasma-Therm RIE etcher – Right chamber
- Gases: O_2 = 10 sccm
- Power: RF = 10 W
- Pressure: P = 100 mTorr

B.3 Process Flow

B.3.1 Ta Backside Metal Etch

- Spin PR on epi side for protection
- Cure PR 30 min @ 120°C
- Etch in HF:HNO_3:DI 1:1:5 for 5-10 min
- Rinse in DI water
- Dry with N_2
- Soak in acetone using ultra-sonic bath to remove protective PR
- Solvent clean
- Rinse in DI water
- Dry with N_2

B.3.2 Mesa Isolation - Photolithography

- Solvent clean
- Photolithography: AZ 5214 PR positive process (see above) - mesa isolation mask (Mask 1 in Figure B.1(a))
- Cure PR by baking @ 120°C for ~30 min in oven
- Determine PR thickness with profilometer (~1.8 μm)

B.3.3 Mesa Isolation - Etch

- Plasma-Therm ICP to etch III-N
- Determine PR + mesa thickness with profilometer
- Remove AZ 5214 PR mask using acetone and swab
- Descum Plasma-Therm RIE to remove cured PR for 2min
- Determine mesa height/etch depth with profilometer

B.3.4 Recess Contact - Photolithography

- Solvent clean or piranha etch to clean sample and remove cured PR residue
- BOE dip 3 min - Rinse DI
- Optional: NH_4OH 80°C 15 min - Rinse DI
- Photolithography: AZ 5214 PR Negative Recipe (see above) - Recess contact mask (Mask 2 in Figure B.1(b))
- Descum Plasma-Therm RIE 1 min

- Determine PR thickness with profilometer

B.3.5 Recess Contact - Metallization

- BOE:DI 1:1 dip 30 s for better contacts immediately before loading samples in e-beam evaporator
- Recessed contact metallization - E-beam evaporator (*n*-type metal):
  Ti (300 Å)/Al (1000 Å)/Ti (300 Å)/Au (500 Å)
- Metal lift-off – Acetone or AZ 400T stripper soak, ultra-sonic bath if needed
- Solvent clean - Rinse DI
- Determine metal thickness with profilometer
- Optional: Ohmic contact anneal – Mini-annealer in Van Leer - Recipe: 700-800°C for 30 s in N_2

B.3.6 Current Spreading Layer - Photolithography

- Photolithography: AZ 5214 PR Negative Recipe (see above) - Top spreading metal (Mask 3 in Figure B.1(c))
- Descum Plasma-Therm RIE 1 min
- Determine PR thickness with profilometer

B.3.7 Current Spreading Layer - Metallization

- HCl dip 30 s for better contacts immediately before loading samples in e-beam evaporator
- Current spreading layer metallization - E-beam evaporator (*p*-type metal)
- Ni (50 Å)/Au (50 Å)
- Metal lift-off – Acetone or AZ 400T stripper soak, ultra-sonic bath if needed
- Solvent clean - Rinse DI
- Determine metal thickness with profilometer

B.3.8 Top Contact - Photolithography

- Photolithography: AZ 5214 PR Negative Recipe (see above) - Top spreading metal (Mask 4 in Figure B.1(d))
- Descum Plasma-Therm RIE 1 min
- Determine PR thickness with profilometer

B.3.9 Top Contact - Metallization

- Top contact metallization - Electron-beam evaporator (*p*-type metal)
- Ni (500 Å)/Au (500 Å)
- Metal lift-off – Acetone or AZ 400T stripper soak, ultra-sonic bath if needed
- Solvent clean - Rinse DI
- Determine metal thickness with profilometer
- Ohmic contact anneal - Mini annealer in Van Leer - Recipe: 550°C for 3 min in air

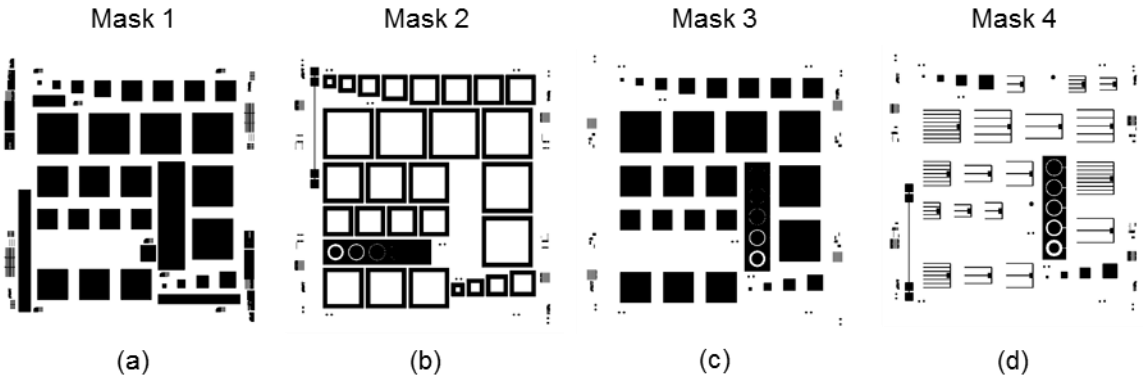

Figure B.1: Schematics of the masks used for the solar-cell fabrication: (a) Mask 1 for mesa isolation, (b) mask 2 for recess contact, (c) mask 3 for current spreading layer, and (d) mask 4 for top contact.

APPENDIX C

OPTIMIZATION OF FINGER SPACING

A method for quantifying the fractional power losses of the metallization grid pattern for InGaN-based solar cells is presented. The model is based on the unit-cell approach to accurately quantify the optical and electrical power losses associated with the metallization grid [172]. The unit cell approach consists of calculating the power loss due to a particular mechanism by integrating the loss and then dividing it by the total power generated in the relevant unit cell to give a fractional power loss. This approach effectively normalizes the power loss to per unit area and allows for a fair comparison of loss mechanisms within the metallization. The power losses include shading losses, resistive losses in the top layer, resistive losses in the metal finger, and resistive losses due to the metal/semiconductor contact.

C.1 Shading Losses

Shading losses are simply proportional to the coverage fraction. Therefore, considering the unit cell illustrated in Figure C.1, the fractional optical losses p_s due to shading can be expressed as

$$p_s = \frac{w}{S}, \tag{C.1}$$

where w is the finger width and S is the finger spacing.

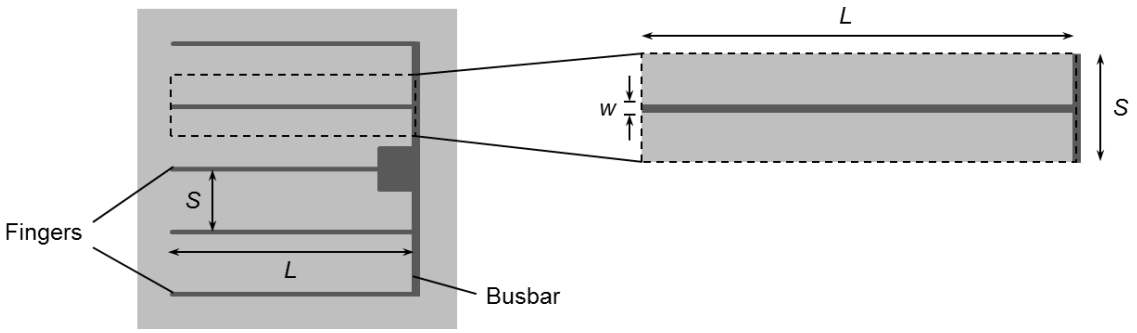

Figure C.1: Top view of the grid-pattern scheme for the solar cell under study. The inset shows a unit cell used for calculation.

C.2 Resistive Finger Losses

The derivation for the fractional resistive losses along the finger is as follows: The resistance *dR* in an element *dx* at a position *x* along the finger (Figure C.2) is

$$dR = \frac{\rho_f dx}{wd}, \tag{C.2}$$

where *d* is the finger thickness and ρ_f is the effective resistivity of the finger metal.

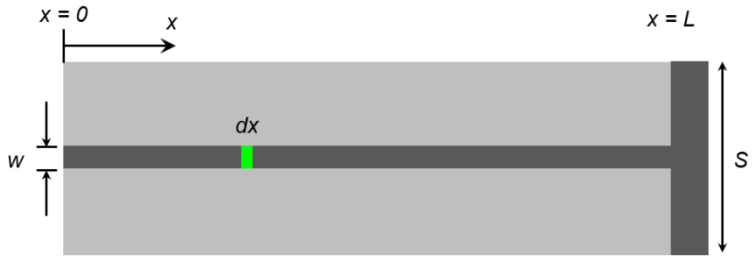

Figure C.2: Finger diagram showing the element *dx* used to calculate the resistive losses in fingers.

Considering the unit cell depicted in Figure C.2, the current flow I at any position x along the finger is

$$I = J_{mp} x S, \tag{C.3}$$

where J_{mp} is the current-density value at maximum power point. The resistive losses in fingers P_f can be calculated by integrating the electrical power losses over the entire finger length L:

$$P_f = \int_0^L I^2 dR = \frac{1}{3} L^3 J_{mp}^2 S^2 \frac{\rho_f}{wd} \tag{C.4}$$

At the maximum power point, the generated power P_{gen} in the unit cell of area SL is

$$P_{gen} = LSJ_{mp}V_{mp}, \tag{C.5}$$

where V_{mp} is the voltage value at maximum power point. The fractional resistive losses in fingers p_f is obtained by dividing the absolute power losses by the generated power:

$$p_f = \frac{P_f}{P_{gen}} = \frac{L^2 J_{mp} S \rho_f}{3 V_{mp} wd} \tag{C.6}$$

C.3 Resistive Emitter Losses

The resistive losses P_e in the top layer can be estimated by integrating the electrical power losses due to the lateral current flow from the midpoint between two finger lines to the finger line [173]. The differential resistance along the y axis as defined in Figure C.3 is given by

$$dR = \frac{R_{sh}}{L} dy, \tag{C.7}$$

where R_{sh} is the sheet resistance of the *p*-GaN or the current-spreading layer. Considering the unit cell depicted in Figure C.3, the current flow *I* at any position *y* is

$$I = J_{mp} y L \tag{C.8}$$

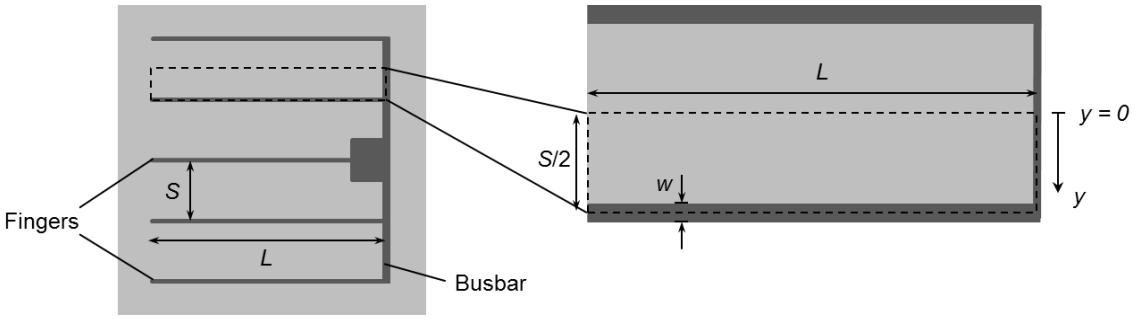

Figure C.3: Top view of the grid-pattern scheme for the solar cell under study. The inset shows a unit cell used for calculation of resistive emitter losses.

The resistive emitter losses P_e can be calculated by integrating the electrical power losses over the width of the unit cell:

$$P_e = \int_0^{S/2} I^2 dR = \frac{J_{mp}^2 R_{sh} S^3 L}{24} \tag{C.9}$$

At the maximum power point, the generated power P_{gen} in the unit cell of area *Sl*/2 is

$$P_{gen} = L\frac{S}{2}J_{mp}V_{mp} \tag{C.10}$$

The fractional resistive losses in fingers p_e is thus, given by

$$p_e = \frac{P_e}{P_{gen}} = \frac{S^2 J_{mp} R_{sh}}{12 V_{mp}} \tag{C.11}$$

C.4 Resistive Losses due to Semiconductor-Metal Contact

Finally, the resistive losses due to semiconductor-metal contact P_c resulting from current flowing from both sides of the finger can be estimated by considering the unit cell depicted in Figure C.1 [5]. The resistance *R* due to the semiconductor-metal contact is given by

$$R = \frac{\rho_c}{Lw}, \tag{C.12}$$

where ρ_c is the specific contact resistivity. The current flow *I* over the unit cell of area *SL* is

$$I = J_{mp} SL \tag{C.13}$$

Therefore, the resistive losses due to semiconductor-metal contact P_c is

$$P_c = \frac{\rho_c}{Lw} J_{mp}^2 S^2 L^2, \tag{C.14}$$

where ρ_c is the specific contact resistivity. The generated power P_{gen}, which account for the current collection over an area *SL* for each finger is

$$P_{gen} = LSJ_{mp}V_{mp} \tag{C.15}$$

The fractional resistive losses in fingers p_c is thus, given by

$$p_c = \frac{P_c}{P_{gen}} = \frac{SJ_{mp}\rho_c}{wV_{mp}} \tag{C.16}$$

C.5 Total Power Losses

The equations for optical and electrical losses can be combined to determine the total power losses in the top contact grid. The total power losses is given by

$$p_{tot} = p_s + p_f + p_e + p_c \tag{C.17}$$

By numerically minimizing the total power losses in the metallization grid pattern, the optimal finger spacing can be calculated.

APPENDIX D

REPORTS ON InGaN/GaN DOUBLE-HETEROJUNCTION SOLAR CELLS

Table D.1: Comparison of InGaN/GaN double-heterojunction solar cell characteristics and performance.

	Growth Technique	In content (Thickness)	Structure	Performance (Excitation)
Jani 2007 [174]	MOCVD	0.04–0.05 (200 nm)	*p*-GaN: 100 nm – 5×10^{17} cm^{-3} *n*-GaN: 200 nm – 5×10^{18} cm^{-3}	J_{sc} ~3.8 mA/cm^2 V_{oc} = 2.4 V *FF* = 78-80% (UV-enhanced light) IQE = 60%
Neufeld 2008 [175]	MOCVD	0.12 (200 nm) strained	*p*-GaN: 150 nm – 5×10^{17} cm^{-3} *n*-GaN: 2×10^{18} cm^{-3}	J_{sc} = 4.2 mA/cm^2 V_{oc} = 1.81 V *FF* = 75% P_{max} = 5.7 mW/cm^2 (concentrated AM0) EQE = 63%
Zheng 2008 [176]	MOCVD	0.1 (150 nm) strained	*p*-GaN: 150 nm	J_{sc} = 0.46 mA/cm^2 V_{oc} = 2.1 V *FF* = 81% η = 0.5% (AM1.5)
Horng 2009 [177]	MOCVD	0.1 (150 nm)	*p*-GaN: 150 nm *n*-GaN: 3 μm	J_{sc} = 0.52 mA/cm^2 V_{oc} = 2.09 V η = 0.8% (AM1.5)
Tsai 2010 [178]	MOCVD	0.085 (150 nm)	*p*-GaN: 50 nm	J_{sc} = 0.5 mA/cm2 V_{oc} = 1.79 V *FF* = 64% η = 0.57% (AM1.5G – 100 mW/cm^2)

Table D.1 (continued)

Kuwahara 2010 [179]	MOCVD	0.1 (250 nm) strained	*p*-GaN: 150 nm – 3.6×10^{18} cm^{-3} *n*-GaN: 2 μm – 4.5×10^{18} cm^{-3}	J_{sc} = 1.59 mA/cm^2 V_{oc} = 2.23 V *FF* = 61% η = 1.41% (AM1.5 – 1.5sun) EQE = 55%
Horng 2010 [180]	MOCVD	0.1 (150 nm)	*p*-GaN: 150 nm *n*-GaN: 2 μm	J_{sc} = 0.65 mA/cm^2 V_{oc} = 2.2 V *FF* =75% η = 1.03% (AM1.5G – 1 sun)
Shim 2010 [181]	MOCVD	0.108 (200 nm)	*p*-GaN: 100 nm *n*-GaN: 2.2 μm	J_{sc} = 0.644 mA/cm^2 V_{oc} = 2.0 V *FF* =79.5% η = 1% (AM1.5) EQE = 74.1%
Matioli 2011 [20]	MOCVD	0.12 (60 nm)	*p*-GaN: 300 nm – [Mg]~8×10^{19} cm^{-3} *n*-GaN: [Si]~6×10^{18} cm^{-3}	J_{sc} = 1.06 mA/cm^2 V_{oc} = 1.89 V *FF* = 78.6% P_{max} = 1.57 mW/cm^2 (Xe lamp AM1.5G 1 sun) EQE = 72% IQE = 93%
Lee 2011 [182]	MOCVD	0.11 (200 nm)	*p*-GaN: 100 nm – 4×10^{17} cm^{-3} *n*-GaN: 1.5 μm – 5×10^{18} cm^{-3}	J_{sc} = 0.59 mA/cm^2 V_{oc} = 1.33 V *FF* = 65% η = 0.51% (AM1.5G – 1 sun) QE = 76.8%
Lang 2011 [19]	NH_3 MBE	0.11 (90 nm)	*p*-GaN: 100 nm – [Mg]~5×10^{19} cm^{-3} *n*-GaN: 100 nm – [Si]~4×10^{18} cm^{-3}	J_{sc} = 1.11 mA/cm^2 V_{oc} = 1.75 V *FF* =73% (AM0 – 1 sun) IQE peak >95%

Table D.1 (continued)

Shim 2011 [21]	MOCVD	0.108 (200 nm)	*p*-GaN: 100 nm *n*-GaN: 2.2 μm	J_{sc} = 0.83 mA/cm^2 V_{oc} = 2.0 V *FF* =75.2% η = 1.2% (AM1.5G – 1 sun) EQE = 63.6%
Zheng 2011 [183]	MOCVD	0.1 (50 nm)	*p*-GaN: 200 nm *n*-GaN: 2.5 μm	J_{sc} = 0.42 mA/cm^2 V_{oc} = 2.1 V *FF* =77.8% (AM1.5G – 1 sun) EQE = 55%
Chu 2011 [151]	MOCVD	0.17 (95 nm)	*p*-InGaN (0.037): 100 nm p^+-GaN: 10 nm *n*-GaN: 2 μm	J_{sc} = 0.74 mA/cm^2 V_{oc} = 2.08 V *FF* = 70.5% η = 1.09% (AM1.5 – 1 sun) EQE = 45%
Wu 2012 [184]	MOCVD	0.1 - 0.12 - 0.14 (150 nm)	*p*-GaN: 100 nm *n*-GaN: 3 μm	J_{sc} = 0.31 mA/cm^2 V_{oc} = 2.07 V *FF* =80% η = 0.51% (AM1.5G – 1 sun)
Wu 2012 [185]	MOCVD	0.05 (200 nm)	*p*-GaN: 100 nm – 5×10^{16} cm^{-3} AlGaN(10%)/GaN: 10 pairs 2.5/2.5 nm *i*-GaN: 10 nm *i*-InGaN: 200 nm – 10^{16} cm^{-3} *n*-GaN: 100 nm – 5×10^{8} cm^{-3} *n*-AlGaN (10%): 100 nm – 5×10^{18} cm^{-3} *n*-GaN: 200 nm – 5×10^{18} cm^{-3}	J_{sc} = 26.8 mA/cm^2 V_{oc} = 2.19 V *FF* =74% η = 0.362% (AM1.5 – 1 & 120 suns)

Table D.1 (continued)

Li 2013 [186]	MOCVD	0.095 (120 nm)	*p*-GaN: 100 nm Low-temperature GaN interlayer: 5 nm *n*-GaN: 5 μm	J_{sc} = 0.54 mA/cm^2 V_{oc} = 1.3 V η = 0.38% (Xe lamp) EQE = 29%
Cai 2013 [187]	MOCVD	0.135 (150 nm)	*p*-GaN: 70 nm – 10^{17} cm^{-3} *n*-GaN: 2 μm – 10^{18} cm^{-3}	J_{sc} = 0.792 mA/cm^2 V_{oc} = 1.42 V *FF* = 74.6% η = 0.841% (AM1.5G – 1 sun) EQE = 48.1%
Cai 2013 [148]	MOCVD	0.16 (150 nm)	*p*-GaN: 70 nm – 10^{17} cm^{-3} *n*-GaN: 2 μm – 10^{18} cm^{-3}	J_{sc} = 0.796 mA/cm^2 V_{oc} = 1.23 V *FF* = 61.02% η = 0.6% (AM1.5G – 1 sun) EQE = 38.8%
Farrell 2013 [188]	MOCVD	(60 nm)	*p*-GaN: 300 nm (intentionally rough) *n*-GaN: 2 μm	J_{sc} = 2.1 mA/cm^2 V_{oc} = 1.54 V (AM1.5G – 1.5 sun) EQE = 77.5%
Li 2013 [189]	MOCVD	0.12 (75-150-300 nm)	*p*-GaN: 200 nm – 3×10^{17} cm^{-3} *n*-GaN: 3 μm – 5×10^{18} cm^{-3}	J_{sc} = 0.45 mA/cm^2 V_{oc} = 1.6 V *FF* = 64.6% (Concentrated AM0) EQE = 57%
Zhang 2013 [190]	MOCVD	0.125 (200 nm) strained	*n*-GaN: 5×10^{18} cm^{-3}	J_{sc} = 1.12 mA/cm^2 V_{oc} = 0.48 V *FF* = 30.2% P_{max} = 0.162 mW/cm^2 (AM1.5 Xe lamp) EQE = 29.8%
Sumiya 2015 [149]		0.08 (150 nm)	*n*-GaN: 100 nm – 5×10^{17} cm^{-3}	J_{sc} = 0.12 mA/cm^2 V_{oc} = 2.3 V *FF* = 80% η = 1.05% (AM1.5 – 100 mW/cm^2)

APPENDIX E

MATLAB CODE FOR INDEPENDENT SHUTTER CONTROL

The following MATLAB script is used to implement the alternative modulation scheme of the hybrid growth presented in Chapter 9.

```
% s: serial port object associated with the shutter-control box
s = serial('COM32','BaudRate',9600,'DataBits',8);
set(s,'Terminator','CR/LF');
fopen(s);
% Shutter address number: In1 = 6 | In2 = 3 | Ga = 4 | Si = 5 |
% plasma = 2
% m: Ga accumulation time
m = 5;
% c: GaN consumption time
c = 7;
% N-rich InGaN growth
n = 20;
% i: total growth time
i=0;
itot = 2560;
% Open Si
fprintf(s,'/5e7R');
pause(0.2)
while i<itot
   % N-rich InGaN | open In2 and Ga
   fprintf(s,'/3e7R');
   fprintf(s,'/4e7R');
   disp('N-rich InGaN')
   pause(n)
   i=i+n;
   % Ga wetting layer | Close In2 and plasma
   fprintf(s,'/3e8R');
   fprintf(s,'/2e8R');
   disp('Ga wetting layer')
   pause(m)
   i=i+m;
   % Consume Ga metal | close Ga and open plasma
   fprintf(s,'/4e8R');
   fprintf(s,'/2e7R');
   disp('consume Ga metal')
   pause(c)
   i=i+c;
   disp([num2str(floor(i/60)), 'min ', num2str(mod(i,60)) , 'sec over
   ', num2str(floor(itot/60)), 'min ', num2str(mod(itot,60)) , 'sec '])
   disp([num2str(100*i/itot), '%'])
end
```

```
% N-rich InGaN | open In2 and Ga
fprintf(s,'/4e7R');
fprintf(s,'/3e7R');
disp('LAST N-rich InGaN')
pause(n)

% GaN cap | close In2
fprintf(s,'/3e8R');
disp('GaN cap')
pause(90);
fprintf(s,'/4e8R');
fprintf(s,'/5e8R');

fclose(s);
```

REFERENCES

[1] I. E. Agency, "World Energy Outlook 2014," 978-92-64-20804-9, 2014.

[2] U. S. E. I. Administration, "International Energy Outlook 2013," 2013.

[3] A. E. Becquerel, "Mémoire sur les effets électriques produits sous l'influence des rayons solaires," *Comptes Rendus des Séances Hebdomadaires,* vol. 9, pp. 561-567, 1839.

[4] D. M. Chapin, C. S. Fuller, and G. L. Pearson, "A New Silicon p-n Junction Photocell for Converting Solar Radiation into Electrical Power," *Journal of Applied Physics,* vol. 25, pp. 676-677, 1954.

[5] M. A. Green, *Solar cells: operating principles, technology, and system applications*. Englewood Cliffs, NJ: Prentice-Hall, 1982.

[6] N. R. E. Laboratory, ed. http://www.nrel.gov/ncpv/images/efficiency_chart.jpg, 2015.

[7] A. Bhuiyan, K. Sugita, A. Hashimoto, and A. Yamamoto, "InGaN Solar Cells: Present State of the Art and Important Challenges," *IEEE Journal of Photovoltaics,* vol. 2, pp. 276-293, 2012.

[8] E. Trybus, G. Namkoong, W. Henderson, S. Burnham, W. A. Doolittle, M. Cheung, and A. Cartwright, "InN: A material with photovoltaic promise and challenges," *Journal of Crystal Growth,* vol. 288, pp. 218-224, 2006.

[9] T. M. Research, "GaN Semiconductor Devices Market (Power semiconductors, Opto semiconductors) - Global Industry Analysis, Size, Share, Growth, Trends and Forecast, 2013 - 2019," 2014.

[10] J. Wu, "When group-III nitrides go infrared: New properties and perspectives," *Journal of Applied Physics,* vol. 106, pp. 011101-1–011101-28, 2009.

[11] A. S. Bouazzi, H. Hamzaoui, and B. Rezig, "Theoretical possibilities of $In_xGa_{1-x}N$ tandem PV structures," *Solar Energy Materials and Solar Cells,* vol. 87, pp. 595-603, 2005.

[12] L. Hsu and W. Walukiewicz, "Modeling of InGaN/Si tandem solar cells," *Journal of Applied Physics,* vol. 104, p. 024507, 2008.

[13] M. E. Nell and A. M. Barnett, "The spectral p-n junction model for tandem solar-cell design," *IEEE Transactions on Electron Devices,* vol. 34, pp. 257-266, 1987.

[14] J. F. Muth, A. J. H. Lee, I. K. Shmagin, R. M. Kolbas, H. C. Casey, Jr., B. P. Keller, U. K. Mishra, and S. P. DenBaars, "Absorption coefficient, energy gap, exciton binding energy, and recombination lifetime of GaN obtained from transmission measurements," *Applied Physics Letters*, vol. 71, pp. 2572-2574, 1997.

[15] R. Singh, D. Doppalapudi, T. D. Moustakas, and L. T. Romano, "Phase separation in InGaN thick films and formation of InGaN/GaN double heterostructures in the entire alloy composition," *Applied Physics Letters*, vol. 70, pp. 1089-1091, 1997.

[16] T. H. Wang, T. F. Ciszek, C. R. Schwerdtfeger, H. Moutinho, and R. Matson, "Growth of silicon thin layers on cast MG-Si from metal solutions for solar cells," *Solar Energy Materials and Solar Cells*, vol. 41–42, pp. 19-30, 1996.

[17] Y. Nanishi, Y. Saito, and T. Yamaguchi, "RF-molecular beam epitaxy growth and properties of InN and related alloys," *Japanese Journal of Applied Physics*, vol. 42, pp. 2549-2559, 2003.

[18] J. Wu, W. Walukiewicz, K. M. Yu, W. Shan, J. W. Ager, E. E. Haller, L. Hai, W. J. Schaff, W. K. Metzger, and S. Kurtz, "Superior radiation resistance of $In_{1-x}Ga_xN$ alloys: Full-solar-spectrum photovoltaic material system," *Journal of Applied Physics*, vol. 94, pp. 6477-6482, 2003.

[19] J. R. Lang, C. J. Neufeld, C. A. Hurni, S. C. Cruz, E. Matioli, U. K. Mishra, and J. S. Speck, "High external quantum efficiency and fill-factor InGaN/GaN heterojunction solar cells grown by NH3-based molecular beam epitaxy," *Applied Physics Letters*, vol. 98, pp. 131115-1–131115-3, 2011.

[20] E. Matioli, C. Neufeld, M. Iza, S. C. Cruz, A. A. Al-Heji, C. Xu, R. M. Farrell, S. Keller, S. DenBaars, U. Mishra, S. Nakamura, J. Speck, and C. Weisbuch, "High internal and external quantum efficiency InGaN/GaN solar cells," *Applied Physics Letters*, vol. 98, p. 021102, 2011.

[21] J. P. Shim, M. Choe, S. R. Jeon, D. Seo, T. Lee, and D. S. Lee, "InGaN-Based p-i-n Solar Cells with Graphene Electrodes," *Applied Physics Express*, vol. 4, pp. 052302-1–052302-1, 2011.

[22] L. Sang, M. Liao, N. Ikeda, Y. Koide, and M. Sumiya, "Enhanced performance of InGaN solar cell by using a super-thin AlN interlayer," *Applied Physics Letters*, vol. 99, pp. 161109-1–161109-3, 2011.

[23] X.-M. Cai, S.-W. Zeng, and B.-P. Zhang, "Fabrication and characterization of InGaN p-i-n homojunction solar cell," *Applied Physics Letters*, vol. 95, p. 173504, 2009.

[24] S.-N. Lee, T. Sakong, W. Lee, H. Paek, J. Son, E. Yoon, O. Nam, and Y. Park, "Characterization of optical and electrical quality of Mg-doped $In_xGa_{1-x}N$ grown by MOCVD," *Journal of Crystal Growth*, vol. 261, pp. 249-252, 2004.

[25] S. Brochen, J. Brault, S. Chenot, A. Dussaigne, M. Leroux, and B. Damilano, "Dependence of the Mg-related acceptor ionization energy with the acceptor concentration in p-type GaN layers grown by molecular beam epitaxy," *Applied Physics Letters,* vol. 103, p. 032102, 2013.

[26] C. G. Van de Walle, C. Stampfl, and J. Neugebauer, "Theory of doping and defects in III–V nitrides," *Journal of Crystal Growth,* vol. 189–190, pp. 505-510, 1998.

[27] G. Namkoong, E. Trybus, K. K. Lee, M. Moseley, W. A. Doolittle, and D. C. Look, "Metal modulation epitaxy growth for extremely high hole concentrations above 10^{19} cm^{-3} in GaN," *Applied Physics Letters,* vol. 93, p. 172112, 2008.

[28] E. Trybus, W. A. Doolittle, M. Moseley, W. Henderson, D. Billingsley, G. Namkoong, and D. C. Look, "Extremely high hole concentrations in c-plane GaN," *Physica Status Solidi (c),* vol. 6, pp. S788-S791, 2009.

[29] B. Gunning, J. Lowder, M. Moseley, and W. A. Doolittle, "Negligible carrier freeze-out facilitated by impurity band conduction in highly p-type GaN," *Applied Physics Letters,* vol. 101, pp. 082106-1–082106-5, 2012.

[30] A. Bell, R. Liu, F. A. Ponce, H. Amano, I. Akasaki, and D. Cherns, "Light emission and microstructure of Mg-doped AlGaN grown on patterned sapphire," *Applied Physics Letters,* vol. 82, pp. 349-351, 2003.

[31] S. Fischer, C. Wetzel, E. E. Haller, and B. K. Meyer, "On p-type doping in GaN-acceptor binding energies," *Applied Physics Letters,* vol. 67, pp. 1298-1300, 1995.

[32] A. Bhattacharyya, W. Li, J. Cabalu, T. D. Moustakas, D. J. Smith, and R. L. Hervig, "Efficient p-type doping of GaN films by plasma-assisted molecular beam epitaxy," *Applied Physics Letters,* vol. 85, pp. 4956-4958, 2004.

[33] B. N. Pantha, A. Sedhain, J. Li, J. Y. Lin, and H. X. Jiang, "Electrical and optical properties of p-type InGaN," *Applied Physics Letters,* vol. 95, p. 261904, 2009.

[34] K. Kumakura, T. Makimoto, and N. Kobayashi, "Mg-acceptor activation mechanism and transport characteristics in p-type InGaN grown by metalorganic vapor phase epitaxy," *Journal of Applied Physics,* vol. 93, pp. 3370-3375, 2003.

[35] D. C. Look, D. C. Reynolds, J. W. Hemsky, J. R. Sizelove, R. L. Jones, and R. J. Molnar, "Defect Donor and Acceptor in GaN," *Physical Review Letters,* vol. 79, pp. 2273-2276, 1997.

[36] S. Nakamura, N. Iwasa, M. Senoh, and T. Mukai, "Hole compensation mechanism of P-type GaN films," *Japanese Journal of Applied Physics,* vol. 31, pp. 1258-66, 1992.

[37] B. N. Pantha, H. Wang, N. Khan, J. Y. Lin, and H. X. Jiang, "Origin of background electron concentration in $In_xGa_{1-x}N$ alloys," *Physical Review B,* vol. 84, p. 075327, 2011.

[38] E. T. Yu, X. Z. Dang, P. M. Asbeck, S. S. Lau, and G. J. Sullivan, "Spontaneous and piezoelectric polarization effects in III-V nitride heterostructures," *Journal of Vacuum Science & Technology B,* vol. 17, pp. 1742-1749, 1999.

[39] S. Y. Karpov, "Spontaneous polarization in III-nitride materials: crystallographic revision," *Physica Status Solidi (c),* vol. 7, pp. 1841-1843, 2010.

[40] Z. Q. Li, M. Lestradet, Y. G. Xiao, and S. Li, "Effects of polarization charge on the photovoltaic properties of InGaN solar cells," *Physica Status Solidi (a),* vol. 208, pp. 928-31, 2011.

[41] J.-Y. Chang, S.-H. Yen, Y.-A. Chang, and Y.-K. Kuo, "Simulation of high-efficiency GaN/InGaN p-i-n solar cell with suppressed polarization and barrier effects," *IEEE Journal of Quantum Electronics,* vol. 49, pp. 17-23, 2013.

[42] O. Ambacher, J. Smart, J. R. Shealy, N. G. Weimann, K. Chu, M. Murphy, W. J. Schaff, L. F. Eastman, R. Dimitrov, L. Wittmer, M. Stutzmann, W. Rieger, and J. Hilsenbeck, "Two-dimensional electron gases induced by spontaneous and piezoelectric polarization charges in N- and Ga-face AlGaN/GaN heterostructures," *Journal of Applied Physics,* vol. 85, pp. 3222-3233, 1999.

[43] G. B. Stringfellow, "Microstructures produced during the epitaxial growth of InGaN alloys," *Journal of Crystal Growth,* vol. 312, pp. 735-749, 2010.

[44] M. Moseley, J. Lowder, D. Billingsley, and W. A. Doolittle, "Control of surface adatom kinetics for the growth of high-indium content InGaN throughout the miscibility gap," *Applied Physics Letters,* vol. 97, p. 191902, 2010.

[45] M. Moseley, B. Gunning, J. Greenlee, J. Lowder, G. Namkoong, and W. A. Doolittle, "Observation and control of the surface kinetics of InGaN for the elimination of phase separation," *Journal of Applied Physics,* vol. 112, p. 014909, 2012.

[46] M. Rao, D. Kim, and S. Mahajan, "Compositional dependence of phase separation in InGaN layers," *Applied Physics Letters,* vol. 85, pp. 1961-1963, 2004.

[47] P. Kozodoy, J. P. Ibbetson, H. Marchand, P. T. Fini, S. Keller, J. S. Speck, S. P. DenBaars, and U. K. Mishra, "Electrical characterization of GaN p-n junctions with and without threading dislocations," *Applied Physics Letters,* vol. 73, pp. 975-977, 1998.

[48] J. Abell and T. D. Moustakas, "The role of dislocations as nonradiative recombination centers in InGaN quantum wells," *Applied Physics Letters,* vol. 92, p. 091901, 2008.

[49] J. Jasinski and Z. Liliental-Weber, "Extended defects and polarity of hydride vapor phase epitaxy GaN," *Journal of Electronic Materials,* vol. 31, pp. 429-436, 2002.

[50] D. Holec, P. M. F. J. Costa, M. J. Kappers, and C. J. Humphreys, "Critical thickness calculations for InGaN/GaN," *Journal of Crystal Growth,* vol. 303, pp. 314-317, 2007.

[51] A. M. Fischer, Y. O. Wei, F. A. Ponce, M. Moseley, B. Gunning, and W. A. Doolittle, "Highly luminescent, high-indium-content InGaN film with uniform composition and full misfit-strain relaxation," *Applied Physics Letters,* vol. 103, p. 131101, 2013.

[52] J. S. Speck and S. J. Rosner, "The role of threading dislocations in the physical properties of GaN and its alloys," *Physica B: Condensed Matter,* vol. 273–274, pp. 24-32, 1999.

[53] M. Mahat, A. Llopis, R. D. Schaller, I. Watson, S. Periera, and A. Neogi, "Carrier-induced nonlinearities in InGaN/GaN quantum wells with V-pits," *MRS Communications,* vol. 2, pp. 55-60, 2012.

[54] M. R. Brozel and G. E. Stillman, *Properties of Gallium Arsenide,* third ed. London: Institution of Engineering and Technology, 1996.

[55] K. Kumakura, T. Makimoto, N. Kobayashi, T. Hashizume, T. Fukui, and H. Hasegawa, "Minority carrier diffusion length in GaN: dislocation density and doping concentration dependence," *Applied Physics Letters,* vol. 86, p. 52105, 2005.

[56] Z. Z. Bandić, P. M. Bridger, E. C. Piquette, and T. C. McGill, "The values of minority carrier diffusion lengths and lifetimes in GaN and their implications for bipolar devices," *Solid-State Electronics,* vol. 44, pp. 221-228, 2000.

[57] J. Poortmans and V. Arkhipov, *Thin film solar cells: fabrication, characterization and applications*. Chichester, England: Wiley, 2006.

[58] F. Rinaldi, "Basics of Molecular Beam Epitaxy (MBE)," University of Ulm Annual Report Optoelectronics Department, 2002.

[59] P. J. Dobson, "An introduction to reflection high energy electron diffraction," in *Surface and interface characterization by electron optical methods*, A. Howie and U. Valdrè, ed Plenum Press published in cooperation with the NATO Scientific Affairs Division: New York, 1988.

[60] T. D. Moustakas, "Growth of III-V Nitrides by Molecular Beam Epitaxy," in *Gallium Nitride (GaN) II*, J. I. Pankove and T. D. Moustakas, ed: Academic Press, 1999.

[61] J. R. Arthur, "Molecular beam epitaxy," *Surface Science,* vol. 500, pp. 189-217, 2002.

[62] P. J. Dobson, B. A. Joyce, J. H. Neave, and J. Zhang, "Intensity oscillations in reflection high energy electron diffraction during epitaxial growth," in *Surface and interface characterization by electron optical methods*, A. Howie and U. Valdrè, ed Plenum Press published in cooperation with the NATO Scientific Affairs Division: New York, 1988.

[63] J. R. Arthur, "Molecular beam epitaxy," *Surface Science,* vol. 500, pp. 189-217, 2002.

[64] L. Liu and J. H. Edgar, "Substrates for gallium nitride epitaxy," *Materials Science and Engineering Reports,* vol. 37, pp. 61-127, 2002.

[65] F. K. Yam and Z. Hassan, "InGaN: An overview of the growth kinetics, physical properties and emission mechanisms," *Superlattices and Microstructures,* vol. 43, pp. 1-23, 2008.

[66] Ž. Gačević, V. J. Gómez, N. G. Lepetit, P. E. D. Soto Rodríguez, A. Bengoechea, S. Fernández-Garrido, R. Nötzel, and E. Calleja, "A comprehensive diagram to grow (0001)InGaN alloys by molecular beam epitaxy," *Journal of Crystal Growth,* vol. 364, pp. 123-127, 2013.

[67] C. Adelmann, J. Brault, E. Martinez-Guerrero, G. Mula, H. Mariette, L. Si Dang, and B. Daudin, "Molecular-Beam Epitaxy of GaN: A Phase Diagram," *Physica Status Solidi (a),* vol. 188, pp. 575-578, 2001.

[68] C. S. Gallinat, G. Koblmüller, J. S. Brown, and J. S. Speck, "A growth diagram for plasma-assisted molecular beam epitaxy of In-face InN," *Journal of Applied Physics,* vol. 102, p. 064907, 2007.

[69] J. Ju, B. Loitsch, T. Stettner, F. Schuster, M. Stutzmann, and G. Koblmüller, "Trade-off between morphology, extended defects, and compositional fluctuation induced carrier localization in high In-content InGaN films," *Journal of Applied Physics,* vol. 116, p. 053501, 2014.

[70] H. Komaki, R. Katayama, K. Onabe, M. Ozeki, and T. Ikari, "Nitrogen supply rate dependence of InGaN growth properties, by RF-MBE," *Journal of Crystal Growth,* vol. 305, pp. 12-18, 2007.

[71] A. Kraus, S. Hammadi, J. Hisek, R. Buß, H. Jönen, H. Bremers, U. Rossow, E. Sakalauskas, R. Goldhahn, and A. Hangleiter, "Growth and characterization of InGaN by RF-MBE," *Journal of Crystal Growth,* vol. 323, pp. 72-75, 2011.

[72] G. Koblmüller, J. Brown, R. Averbeck, H. Riechert, P. Pongratz, and J. S. Speck, "Ga Adlayer Governed Surface Defect Evolution of (0001)GaN Films Grown by

Plasma-Assisted Molecular Beam Epitaxy," *Japanese Journal of Applied Physics,* vol. 44, p. L906, 2005.

[73] H. Komaki, T. Nakamura, R. Katayama, K. Onabe, M. Ozeki, and T. Ikari, "Growth of In-rich InGaN films on sapphire via GaN layer by RF-MBE," *Journal of Crystal Growth,* vol. 301–302, pp. 473-477, 2007.

[74] S.-B. Che, T. Shinada, T. Mizuno, X. Wang, Y. Ishitani, and A. Yoshikawa, "Effect of Precise Control of V/III Ratio on In-Rich InGaN Epitaxial Growth," *Japanese Journal of Applied Physics,* vol. 45, p. L1259, 2006.

[75] T. Yamaguchi, N. Uematsu, T. Araki, T. Honda, E. Yoon, and Y. Nanishi, "Growth of thick InGaN films with entire alloy composition using droplet elimination by radical-beam irradiation," *Journal of Crystal Growth,* vol. 377, pp. 123-126, 2013.

[76] S. Valdueza-Felip, E. Bellet-Amalric, A. Núñez-Cascajero, Y. Wang, M.-P. Chauvat, P. Ruterana, S. Pouget, K. Lorenz, E. Alves, and E. Monroy, "High In-content InGaN layers synthesized by plasma-assisted molecular-beam epitaxy: Growth conditions, strain relaxation, and In incorporation kinetics," *Journal of Applied Physics,* vol. 116, pp. 233504-1–233504-9, 2014.

[77] S.-W. Feng, C.-M. Lai, C.-H. Chen, W.-C. Sun, and L.-W. Tu, "Theoretical simulations of the effects of the indium content, thickness, and defect density of the i-layer on the performance of p-i-n InGaN single homojunction solar cells," *Journal of Applied Physics,* vol. 108, p. 093118, 2010.

[78] *APSYS* [Online]. Available: http://www.crosslight.com

[79] G. F. Brown, J. W. Ager III, W. Walukiewicz, and J. Wu, "Finite element simulations of compositionally graded InGaN solar cells," *Solar Energy Materials and Solar Cells,* vol. 94, pp. 478-483, 2010.

[80] J. Wu, W. Walukiewicz, K. M. Yu, J. W. Ager, E. E. Haller, L. Hai, and W. J. Schaff, "Small band gap bowing in $In_{1-x}Ga_xN$ alloys," *Applied Physics Letters,* vol. 80, pp. 4741-4743, 2002.

[81] D. M. Caughey and R. E. Thomas, "Carrier mobilities in silicon empirically related to doping and field," *Proceedings of the IEEE,* vol. 55, pp. 2192-2193, 1967.

[82] Z. Z. Bandic, P. M. Bridger, E. C. Piquette, and T. C. McGill, "Minority carrier diffusion length and lifetime in GaN," *Applied Physics Letters,* vol. 72, pp. 3166-3168, 1998.

[83] F. Chen, A. N. Cartwright, H. Lu, and W. J. Schaff, "Temperature dependence of carrier lifetimes in InN," *Physica Status Solidi (a),* vol. 202, pp. 768-772, 2005.

[84] Y. C. Shen, G. O. Mueller, S. Watanabe, N. F. Gardner, A. Munkholm, and M. R. Krames, "Auger recombination in InGaN measured by photoluminescence," *Applied Physics Letters,* vol. 91, p. 141101, 2007.

[85] P. Scajev, K. Jarasiunas, S. Okur, U. Ozgur, and H. Morkoc, "Carrier dynamics in bulk GaN," *Journal of Applied Physics,* vol. 111, p. 023702, 2012.

[86] M. Boroditsky, I. Gontijo, M. Jackson, R. Vrijen, E. Yablonovitch, T. Krauss, C.-C. Cheng, A. Scherer, R. Bhat, and M. Krames, "Surface recombination measurements on III-V candidate materials for nanostructure light-emitting diodes," *Journal of Applied Physics,* vol. 87, pp. 3497-3504, 2000.

[87] H. Kitagawa, T. Suto, M. Fujita, Y. Tanaka, T. Asano, and S. Noda, "Green Photoluminescence from GaInN Photonic Crystals," *Applied Physics Express,* vol. 1, p. 032004, 2008.

[88] W. Walukiewicz, J. W. Ager III, K. M. Yu, Z. Liliental-Weber, J. Wu, S. X. Li, R. E. Jones, and J. D. Denlinger, "Structure and electronic properties of InN and In-rich group III-nitride alloys " *Journal of Physics D: Applied Physics,* vol. 39, pp. R83-R99, 2006.

[89] V. Fiorentini, F. Bernardini, and O. Ambacher, "Evidence for nonlinear macroscopic polarization in III-V nitride alloy heterostructures," *Applied Physics Letters,* vol. 80, pp. 1204-1206, 2002.

[90] H. Zhang, E. J. Miller, E. T. Yu, C. Poblenz, and J. S. Speck, "Measurement of polarization charge and conduction-band offset at $In_xGa_{1-x}N$/GaN heterojunction interfaces," *Applied Physics Letters,* vol. 84, pp. 4644-6, 2004.

[91] C. A. Flory and G. Hasnain, "Modeling of GaN optoelectronic devices and strain-induced piezoelectric effects," *IEEE Journal of Quantum Electronics,* vol. 37, pp. 244-53, 2001.

[92] F. D. Sala, A. D. Carlo, P. Lugli, R. Cingolani, G. Coli', M. Lomascolo, A. Botchkarev, H. Tang, and H. Morkoc, "Carrier screening and polarization fields in nitride-based heterostructure devices," *Physica B,* vol. 272, pp. 397-401, 1999.

[93] O. Mayrock, H. J. Wunsche, and F. Henneberger, "Polarization charge screening and indium surface segregation in (In,Ga)N/GaN single and multiple quantum wells," *Physical Review B,* vol. 62, pp. 16870-80, 2000.

[94] K. A. Bulashevich and S. Y. Karpov, "Assessment of factors limiting conversion efficiency of single-junction III-nitride solar cells," *Physica Status Solidi (c),* vol. 11, pp. 640-643, 2014.

[95] J. Nelson, *The Physics of Solar Cells*. UK: Imperial College Press, 2003.

[96] J.-Y. Chang and Y.-K. Kuo, "Numerical Study on the Influence of Piezoelectric Polarization on the Performance of p-on-n (0001)-Face GaN/InGaN p-i-n Solar Cells," *IEEE Electron Device Letters,* vol. 32, pp. 937-939, 2011.

[97] C. Honsberg, O. Jani, A. Doolittle, E. Trybus, G. Namkoong, I. Ferguson, D. Nicol, and A. Payne, "InGaN - A new solar cell material," in *Proceedings of the 19th EU PVSEC,* Paris, France, 2004.

[98] M. A. Green, "Limiting photovoltaic efficiency under new ASTM International G173-based reference spectra," *Progress in Photovoltaics: Research and Applications,* vol. 20, pp. 954-959, 2012.

[99] C. A. M. Fabien, M. Moseley, B. Gunning, W. A. Doolittle, A. M. Fischer, Y. O. Wei, and F. A. Ponce, "Simulations, practical limitations and novel growth technology for InGaN-based solar cells," *IEEE Journal of Photovoltaics,* vol. 4, pp. 601-606, 2013.

[100] M. Moseley, D. Billingsley, W. Henderson, E. Trybus, and W. A. Doolittle, "Transient atomic behavior and surface kinetics of GaN," *Journal of Applied Physics,* vol. 106, p. 014905, 2009.

[101] C.-A. Chang, C.-F. Shih, N.-C. Chen, T. Y. Lin, and K.-S. Liu, "In-rich $In_{1-x}Ga_xN$ films by metalorganic vapor phase epitaxy," *Applied Physics Letters,* vol. 85, pp. 6131-6133, 2004.

[102] B. N. Pantha, J. Li, J. Y. Lin, and H. X. Jiang, "Single phase $In_xGa_{1-x}N$ ($0.25 \leq x \leq 0.63$) alloys synthesized by metal organic chemical vapor deposition," *Applied Physics Letters,* vol. 93, p. 182107, 2008.

[103] H. J. Kim, Y. Shin, S.-Y. Kwon, H. Jin Kim, S. Choi, S. Hong, C. S. Kim, J.-W. Yoon, H. Cheong, and E. Yoon, "Compositional analysis of In-rich InGaN layers grown on GaN templates by metalorganic chemical vapor deposition," *Journal of Crystal Growth,* vol. 310, pp. 3004-3008, 2008.

[104] W.-C. Tsai, C.-H. Hsu, S.-F. Fu, F.-W. Lee, C.-Y. Chen, W.-C. Chou, W.-K. Chen, and W.-H. Chang, "Optical properties associated with strain relaxations in thick InGaN epitaxial films," *Optics Express,* vol. 22, pp. A416-A424, 2014.

[105] C. A. M. Fabien, B. P. Gunning, W. Alan Doolittle, A. M. Fischer, Y. O. Wei, H. Xie, and F. A. Ponce, "Low-temperature growth of InGaN films over the entire composition range by MBE," *Journal of Crystal Growth,* vol. 425, pp. 115-118, 2015.

[106] E. Iliopoulos, A. Georgakilas, E. Dimakis, A. Adikimenakis, K. Tsagaraki, M. Androulidaki, and N. T. Pelekanos, "InGaN(0001) alloys grown in the entire composition range by plasma assisted molecular beam epitaxy," *Physica Status Solidi (a),* vol. 203, pp. 102-105, 2006.

[107] F. A. Ponce, "Microstructure of Epitaxial III-V Nitride Thin Films," in *GaN and related materials*, S. J. Pearton, ed Gordon and Breach: Amsterdam, 1997.

[108] J. W. Matthews and A. E. Blakeslee, "Defects in epitaxial multilayers: I. Misfit dislocations," *Journal of Crystal Growth*, vol. 27, pp. 118-125, 1974.

[109] R. People and J. C. Bean, "Calculation of critical layer thickness versus lattice mismatch for Ge_xSi_{1-x}/Si strained-layer heterostructures," *Applied Physics Letters*, vol. 47, pp. 322-324, 1985.

[110] S. Srinivasan, L. Geng, R. Liu, F. A. Ponce, Y. Narukawa, and S. Tanaka, "Slip systems and misfit dislocations in InGaN epilayers," *Applied Physics Letters*, vol. 83, pp. 5187-5189, 2003.

[111] S. D. Burnham, G. Namkoong, K.-K. Lee, and W. A. Doolittle, "Reproducible reflection high energy electron diffraction signatures for improvement of AlN using in situ growth regime characterization," *Journal of Vacuum Science & Technology B*, vol. 25, pp. 1009-1013, 2007.

[112] S. D. Burnham and W. Alan Doolittle, "In situ growth regime characterization of AlN using reflection high energy electron diffraction," *Journal of Vacuum Science & Technology B*, vol. 24, pp. 2100-2104, 2006.

[113] N. G. Weimann, L. F. Eastman, D. Doppalapudi, H. M. Ng, and T. D. Moustakas, "Scattering of electrons at threading dislocations in GaN," *Journal of Applied Physics*, vol. 83, pp. 3656-3659, 1998.

[114] H. M. Ng, D. Doppalapudi, T. D. Moustakas, N. G. Weimann, and L. F. Eastman, "The role of dislocation scattering in n-type GaN films," *Applied Physics Letters*, vol. 73, pp. 821-823, 1998.

[115] K. Iwata, H. Asahi, K. Asami, M. Fushida, S. I. Gonda, S. J. Yu, and H. Fujita, "High quality GaN growth on (0001) sapphire by ion-removed electron cyclotron resonance molecular beam epitaxy and first observation of (2×2) and (4×4) reflection high energy electron diffraction patterns," *Japanese Journal of Applied Physics, Part 2: Letters*, vol. 35, pp. L289-L292, 1996.

[116] B. Heying, E. J. Tarsa, C. R. Elsass, P. Fini, S. P. DenBaars, and J. S. Speck, "Dislocation mediated surface morphology of GaN," *Journal of Applied Physics*, vol. 85, pp. 6470-6476, 1999.

[117] S. Fritze, A. Dadgar, H. Witte, M. Bügler, A. Rohrbeck, J. Bläsing, A. Hoffmann, and A. Krost, "High Si and Ge n-type doping of GaN doping - Limits and impact on stress," *Applied Physics Letters*, vol. 100, p. 122104, 2012.

[118] C.-R. Lee, "N-type doping behavior of A10.15Ga0.85N:Si with various Si incorporations," *Journal of Crystal Growth*, vol. 246, pp. 25-30, 2002.

[119] P. R. Hageman, W. J. Schaff, J. Janinski, and Z. Liliental-Weber, "n-type doping of wurtzite GaN with germanium grown with plasma-assisted molecular beam epitaxy," *Journal of Crystal Growth,* vol. 267, pp. 123-128, 2004.

[120] L. T. Romano, C. G. Van de Walle, J. W. Ager, W. Götz, and R. S. Kern, "Effect of Si doping on strain, cracking, and microstructure in GaN thin films grown by metalorganic chemical vapor deposition," *Journal of Applied Physics,* vol. 87, pp. 7745-7752, 2000.

[121] S. D. Burnham, G. Namkoong, D. C. Look, B. Clafin, and W. A. Doolittle, "Reproducible increased Mg incorporation and large hole concentration in GaN using metal modulated epitaxy," *Journal of Applied Physics,* vol. 104, p. 024902, 2008.

[122] B. P. Gunning, C. A. M. Fabien, J. J. Merola, E. A. Clinton, W. A. Doolittle, S. Wang, A. M. Fischer, and F. A. Ponce, "Comprehensive study of the electronic and optical behavior of highly degenerate p-type Mg-doped GaN and AlGaN," *Journal of Applied Physics,* vol. 117, pp. 045710-1–045710-11, 2015.

[123] N. Sipe and R. Venkat, "Modeling GaN growth by plasma assisted MBE in the presence of low Mg flux," *Mrs Internet Journal of Nitride Semiconductor Research,* vol. 7, pp. 1-11, 2002.

[124] C. G. Van de Walle and J. Neugebauer, "Defects, impurities and doping levels in wide-band-gap semiconductors," *Brazilian Journal of Physics,* vol. 26, pp. 163-166, 1996.

[125] P.-C. Chen, C.-H. Chen, S.-J. Chang, Y.-K. Su, P.-C. Chang, and B.-R. Huang, "High hole concentration of p-type InGaN epitaxial layers grown by MOCVD," *Thin Solid Films,* vol. 498, pp. 113-117, 2006.

[126] K. Kumakura, T. Makimoto, and N. Kobayashi, "High hole concentrations in Mg-doped InGaN grown by MOVPE," *Journal of Crystal Growth,* vol. 221, pp. 267-270, 2000.

[127] K. Sasamoto, T. Hotta, K. Sugita, A. G. Bhuiyan, A. Hashimoto, A. Yamamoto, K. Kinoshita, and Y. Kohji, "MOVPE growth of high quality p-type InGaN with intermediate In compositions," *Journal of Crystal Growth,* vol. 318, pp. 492-495, 2011.

[128] S.-N. Lee, J. Son, T. Sakong, W. Lee, H. Paek, E. Yoon, J. Kim, Y.-H. Cho, O. Nam, and Y. Park, "Investigation of optical and electrical properties of Mg-doped p-$In_xGa_{1-x}N$, p-GaN and p-$Al_yGa_{1-y}N$ grown by MOCVD," *Journal of Crystal Growth,* vol. 272, pp. 455-459, 2004.

[129] A. Yamamoto, T. M. Hasan, K. Kodama, N. Shigekawa, and M. Kuzuhara, "Thick (~1 μm) p-type $In_xGa_{1-x}N$ ($x \sim 0.36$) grown by MOVPE at a low temperature (~570 °C)," *Physica Status Solidi (b),* vol. 252, pp. 909-912, 2015.

[130] M. R. Islam, K. Sugita, M. Horie, A. Hashimoto, and A. Yamamoto, "Mg doping behavior of MOVPE $In_xGa_{1-x}N$ (x~0.4)," *Journal of Crystal Growth,* vol. 311, pp. 2817-2820, 2009.

[131] C.-A. Chang, T.-Y. Tang, P.-H. Chang, N.-C. Chen, and C.-T. Liang, "Magnesium Doping of In-rich InGaN," *Japanese Journal of Applied Physics,* vol. 46, p. 2840, 2007.

[132] M. Moseley, B. Gunning, J. Lowder, W. A. Doolittle, and G. Namkoong, "Structural and electrical characterization of InN, InGaN, and p-InGaN grown by metal-modulated epitaxy," *Journal of Vacuum Science & Technology B: Microelectronics and Nanometer Structures,* vol. 31, pp. 03C104-6, 2013.

[133] D. K. Schroder, "Contact Resistance and Schottky Barriers," in *Semiconductor Material and Device Characterizatione*d: John Wiley & Sons, Inc., 2005, pp. 127-184.

[134] J.-K. Ho, C.-S. Jong, C. C. Chiu, C.-N. Huang, K.-K. Shih, L.-C. Chen, F.-R. Chen, and J.-J. Kai, "Low-resistance ohmic contacts to p-type GaN achieved by the oxidation of Ni/Au films," *Journal of Applied Physics,* vol. 86, pp. 4491-4497, 1999.

[135] B. P. Luther, S. E. Mohney, T. N. Jackson, M. Asif Khan, Q. Chen, and J. W. Yang, "Investigation of the mechanism for Ohmic contact formation in Al and Ti/Al contacts to n-type GaN," *Applied Physics Letters,* vol. 70, pp. 57-59, 1997.

[136] A. Motayed, R. Bathe, M. C. Wood, O. S. Diouf, R. D. Vispute, and S. N. Mohammad, "Electrical, thermal, and microstructural characteristics of Ti/Al/Ti/Au multilayer Ohmic contacts to n-type GaN," *Journal of Applied Physics,* vol. 93, pp. 1087-1094, 2003.

[137] Z. Fan, S. N. Mohammad, W. Kim, Ö. Aktas, A. E. Botchkarev, and H. Morkoç, "Very low resistance multilayer Ohmic contact to n-GaN," *Applied Physics Letters,* vol. 68, pp. 1672-1674, 1996.

[138] D.-F. Wang, F. Shiwei, C. Lu, A. Motayed, M. Jah, S. N. Mohammad, K. A. Jones, and L. Salamanca-Riba, "Low-resistance Ti/Al/Ti/Au multilayer ohmic contact to n-GaN," *Journal of Applied Physics,* vol. 89, pp. 6214-6217, 2001.

[139] J. O. Song, H. Jun-Seok, and T.-Y. Seong, "Ohmic-Contact Technology for GaN-Based Light-Emitting Diodes: Role of P-Type Contact," *Electron Devices, IEEE Transactions on,* vol. 57, pp. 42-59, 2010.

[140] J. T. Trexler, S. J. Pearton, P. H. Holloway, M. G. Mier, K. R. Evans, and R. F. Karlicek, "Comparison of Ni/Au, Pd/Au, and Cr/Au Metallizations for Ohmic Contacts to p-GaN," *MRS Online Proceedings Library,* vol. 449, pp. 1091-1096, 1996.

[141] H. Ishikawa, S. Kobayashi, Y. Koide, S. Yamasaki, S. Nagai, J. Umezaki, M. Koike, and M. Murakami, "Effects of surface treatments and metal work functions on electrical properties at p-GaN/metal interfaces," *Journal of Applied Physics,* vol. 81, pp. 1315-1322, 1997.

[142] Z. Z. Chen, Z. X. Qin, Y. Z. Tong, X. D. Hu, T. J. Yu, Z. J. Yang, L. S. Yu, G. Y. Zhang, W. L. Zheng, Q. J. Jia, and X. M. Jiang, "Effects of oxidation by O2 plasma on formation of Ni/Au ohmic contact to p-GaN," *Journal of Applied Physics,* vol. 96, pp. 2091-2094, 2004.

[143] P. Kozodoy, Y. P. Smorchkova, M. Hansen, H. Xing, S. P. DenBaars, U. K. Mishra, A. W. Saxler, R. Perrin, and W. C. Mitchel, "Polarization-enhanced Mg doping of AlGaN/GaN superlattices," *Applied Physics Letters,* vol. 75, pp. 2444-2446, 1999.

[144] K. Kazuhide, M. Toshiki, and K. Naoki, "Efficient Hole Generation above 10^{19} cm^{-3} in Mg-Doped InGaN/GaN Superlattices at Room Temperature," *Japanese Journal of Applied Physics,* vol. 39, p. L195, 2000.

[145] Y. Koide, T. Maeda, T. Kawakami, S. Fujita, T. Uemura, N. Shibata, and M. Murakami, "Effects of annealing in an oxygen ambient on electrical properties of ohmic contacts to p-type GaN," *Journal of Electronic Materials,* vol. 28, pp. 341-346, 1999.

[146] D. Mistele, F. Fedler, H. Klausing, T. Rotter, J. Stemmer, O. K. Semchinova, and J. Aderhold, "Investigation of Ni/Au-contacts on p-GaN annealed in different atmospheres," *Journal of Crystal Growth,* vol. 230, pp. 564-568, 2001.

[147] S. Valdueza-Felip, A. Mukhtarova, Q. Pan, G. Altamura, L. Grenet, C. Durand, C. Bougerol, D. Peyrade, F. González-Posada, J. Eymery, and E. Monroy, "Photovoltaic Response of InGaN/GaN Multiple-Quantum Well Solar Cells," *Japanese Journal of Applied Physics,* vol. 52, p. 08JH05, 2013.

[148] X. Cai, Y. Wang, B. Chen, M.-M. Liang, W.-J. Liu, J.-Y. Zhang, X.-Q. Lv, L.-Y. Ying, and B.-P. Zhang, "Investigation of InGaN p-i-n Homojunction and Heterojunction Solar Cells," *IEEE Photonics Technology Letters,* vol. 25, pp. 59-62, 2013.

[149] M. Sumiya, T. Honda, L. Sang, Y. Nakano, K. Watanabe, and F. Hasegawa, "Improvement of strained InGaN solar cell performance with a heavily doped n^+-GaN substrate," *Physica Status Solidi (a),* pp. 1033-1038, 2015.

[150] S. Pereira, M. R. Correia, E. Pereira, K. P. O'Donnell, E. Alves, A. D. Sequeira, N. Franco, I. M. Watson, and C. J. Deatcher, "Strain and composition distributions in wurtzite InGaN/GaN layers extracted from x-ray reciprocal space mapping," *Applied Physics Letters,* vol. 80, pp. 3913-3915, 2002.

[151] M.-T. Chu, W.-Y. Liao, R.-H. Horng, T.-Y. Tsai, T.-B. Wu, S.-P. Liu, M.-H. Wu, and R.-M. Lin, "Growth and Characterization of p-InGaN/i-InGaN/n-GaN Double-Heterojunction Solar Cells on Patterned Sapphire Substrates," *IEEE Electron Device Letters,* vol. 32, pp. 922-924, 2011.

[152] C. A. M. Fabien and W. A. Doolittle, "Guidelines and limitations for the design of high-efficiency InGaN single-junction solar cells," *Solar Energy Materials and Solar Cells,* vol. 130, pp. 354-363, 2014.

[153] P. Perlin, M. Osiński, P. G. Eliseev, V. A. Smagley, J. Mu, M. Banas, and P. Sartori, "Low-temperature study of current and electroluminescence in InGaN/AlGaN/GaN double-heterostructure blue light-emitting diodes," *Applied Physics Letters,* vol. 69, pp. 1680-1682, 1996.

[154] X. A. Cao, E. B. Stokes, P. M. Sandvik, S. F. LeBoeuf, J. Kretchmer, and D. Walker, "Diffusion and tunneling currents in GaN/InGaN multiple quantum well light-emitting diodes," *IEEE Electron Device Letters*, vol. 23, pp. 535-537, 2002.

[155] G. F. Brown and J. Wu, "Third generation photovoltaics," *Laser & Photonics Reviews* vol. 3, pp. 394-405, 2009.

[156] S. Dalmasso, B. Damilano, N. Grandjean, J. Massies, M. Leroux, J. L. Reverchon, and J. Y. Duboz, "MBE grown InGaN quantum dots and quantum wells: effects of in-plane localization," *Thin Solid Films,* vol. 380, pp. 195-197, 2000.

[157] C. Adelmann, J. Simon, G. Feuillet, N. T. Pelekanos, B. Daudin, and G. Fishman, "Self-assembled InGaN quantum dots grown by molecular-beam epitaxy," *Applied Physics Letters,* vol. 76, pp. 1570-1572, 2000.

[158] K. Tachibana, T. Someya, and Y. Arakawa, "Nanometer-scale InGaN self-assembled quantum dots grown by metalorganic chemical vapor deposition," *Applied Physics Letters,* vol. 74, pp. 383-385, 1999.

[159] Y. W. Mo, J. Kleiner, M. B. Webb, and M. G. Lagally, "Activation energy for surface diffusion of Si on Si(001): A scanning-tunneling-microscopy study," *Physical Review Letters,* vol. 66, pp. 1998-2001, 1991.

[160] H. Yang, V. P. LaBella, D. W. Bullock, Z. Ding, J. B. Smathers, and P. M. Thibado, "Activation energy for Ga diffusion on the GaAs(0 0 1)-(2×4) surface: an MBE-STM study," *Journal of Crystal Growth,* vol. 201–202, pp. 88-92, 1999.

[161] Q. Deng, X. Wang, C. Yang, H. Xiao, C. Wang, H. Yin, Q. Hou, J. Li, Z. Wang, and X. Hou, "Theoretical study on $In_xGa_{1-x}N$/GaN quantum dots solar cell," *Physica B: Condensed Matter* vol. 406, pp. 73-76, 2011.

[162] N. Es'haghi Gorji, H. Movla, F. Sohrabi, A. Hosseinpour, M. Rezaei, and H. Babaei, "The effects of recombination lifetime on efficiency and *J–V* characteristics of $In_xGa_{1-x}N$/GaN quantum dot intermediate band solar cell,"

Physica E: Low-dimensional Systems and Nanostructures vol. 42, pp. 2353-2357, 2010.

[163] L. Sang, M. Liao, Q. Liang, M. Takeguchi, B. Dierre, B. Shen, T. Sekiguchi, Y. Koide, and M. Sumiya, "A Multilevel Intermediate-Band Solar Cell by InGaN/GaN Quantum Dots with a Strain-Modulated Structure," *Advanced Materials* vol. 26, pp. 1414-1420, 2014.

[164] Chloe A. M. Fabien, Aymeric Maros, Christiana B. Honsberg, and W. A. Doolittle, "III-Nitride Double-Heterojunction Solar Cells with High In-content InGaN Absorbing Layers: Comparison of Large-Area and Small-Area Devices," *accepted in IEEE Journal of Photovoltaics,* 2015.

[165] K. Pantzas, Y. El Gmili, J. Dickerson, S. Gautier, L. Largeau, O. Mauguin, G. Patriarche, S. Suresh, T. Moudakir, C. Bishop, A. Ahaitouf, T. Rivera, C. Tanguy, P. L. Voss, and A. Ougazzaden, "Semibulk InGaN: A novel approach for thick, single phase, epitaxial InGaN layers grown by MOVPE," *Journal of Crystal Growth,* vol. 370, pp. 57-62, 2013.

[166] Y. El Gmili, G. Orsal, K. Pantzas, T. Moudakir, S. Sundaram, G. Patriarche, J. Hester, A. Ahaitouf, J. P. Salvestrini, and A. Ougazzaden, "Multilayered InGaN/GaN structure vs. single InGaN layer for solar cell applications: A comparative study," *Acta Materialia* vol. 61, pp. 6587-6596, 2013.

[167] *MATLAB* [Online]. Available: http://www.mathworks.com/products/matlab/

[168] M. A. Moram and M. E. Vickers, "X-ray diffraction of III-nitrides," *Reports on Progress in Physics,* vol. 72, p. 036502, 2009.

[169] J. Birch, J.-E. Sundgren, and P. F. Fewster, "Measurement of the lattice parameters in the individual layers of single-crystal superlattices," *Journal of Applied Physics,* vol. 78, pp. 6562-6568, 1995.

[170] X. Guo, H. Wang, D.-S. Jiang, Y.-T. Wang, D.-G. Zhao, J.-J. Zhu, Z.-S. Liu, S.-M. Zhang, and H. Yang, "Evaluation of both composition and strain distributions in InGaN epitaxial film using x-ray diffraction techniques," *Chinese Physics B,* vol. 19, p. 106802, 2010.

[171] T. Hanada, "Basic Properties of ZnO, GaN, and Related Materials," in *Oxide and Nitride Semiconductors*. vol. 12, T. Yao and S.-K. Hong, ed: Springer Berlin Heidelberg, 2009, pp. 1-19.

[172] P. J. Gress and S. Varlamov, "Quantification of Power Losses of the Interdigitated Metallization of Crystalline Silicon Thin-Film Solar Cells on Glass," *International Journal of Photoenergy* vol. 2012, p. 6, 2012.

[173] A. R. Burgers, "How to design optimal metallization patterns for solar cells," *Progress in Photovoltaics: Research and Applications,* vol. 7, pp. 457-461, 1999.

[174] O. Jani, I. Ferguson, C. Honsberg, and S. Kurtz, "Design and characterization of GaN/InGaN solar cells," *Applied Physics Letters,* vol. 91, p. 132117, 2007.

[175] C. J. Neufeld, N. G. Toledo, S. C. Cruz, M. Iza, S. P. DenBaars, and U. K. Mishra, "High quantum efficiency InGaN/GaN solar cells with 2.95 eV band gap," *Applied Physics Letters,* vol. 93, p. 143502, 2008.

[176] X. Zheng, R.-H. Horng, D.-S. Wuu, M.-T. Chu, W.-Y. Liao, M.-H. Wu, R.-M. Lin, and Y.-C. Lu, "High-quality InGaN/GaN heterojunctions and their photovoltaic effects," *Applied Physics Letters,* vol. 93, p. 261108, 2008.

[177] R.-H. Horng, S.-T. Lin, Y.-L. Tsai, M.-T. Chu, W.-Y. Liao, M.-H. Wu, R.-M. Lin, and Y.-C. Lu, "Improved Conversion Efficiency of GaN/InGaN Thin-Film Solar Cells," *IEEE Electron Device Letters,* vol. 30, pp. 724-726, 2009.

[178] C.-L. Tsai, G.-S. Liu, G.-C. Fan, and Y.-S. Lee, "Substrate-free large gap InGaN solar cells with bottom reflector," *Solid-State Electronics,* vol. 54, pp. 541-544, 2010.

[179] Y. Kuwahara, T. Fujii, Y. Fujiyama, T. Sugiyama, M. Iwaya, T. Takeuchi, S. Kamiyama, I. Akasaki, and H. Amano, "Realization of Nitride-Based Solar Cell on Freestanding GaN Substrate," *Applied Physics Express,* vol. 3, p. 111001, 2010.

[180] R.-H. Horng, M.-T. Chu, H.-R. Chen, W.-Y. Liao, M.-H. Wu, K.-F. Chen, and D.-S. Wuu, "Improved Conversion Efficiency of Textured InGaN Solar Cells With Interdigitated Imbedded Electrodes," *IEEE Electron Device Letters,* vol. 31, pp. 585-587, 2010.

[181] J.-P. Shim, J. Seong-Ran, J. Yon-Kil, and D.-S. Lee, "Improved Efficiency by Using Transparent Contact Layers in InGaN-Based p-i-n Solar Cells," *IEEE Electron Device Letters,* vol. 31, pp. 1140-1142, 2010.

[182] H. C. Lee, Y. K. Su, W. H. Lan, J. C. Lin, K. C. Huang, W. J. Lin, Y. C. Cheng, and Y. H. Yeh, "Study of Electrical Characteristics of GaN-Based Photovoltaics With Graded $In_xGa_{1-x}N$ Absorption Layer," *IEEE Photonics Technology Letters,* vol. 23, pp. 347-349, 2011.

[183] X. Zheng, L. Tang, D. Zhang, J. Dong, and H. Yang, "Effect of contact spreading layer on photovoltaic response of InGaN-based solar cells," *Physica Status Solidi (a),* vol. 208, pp. 199-201, 2011.

[184] M.-H. Wu, S.-P. Chang, S.-J. Chang, R.-H. Horng, W.-Y. Liao, and R.-M. Lin, "Characteristics of GaN/InGaN Double-Heterostructure Photovoltaic Cells," *International Journal of Photoenergy*, 2012.

[185] M.-H. Wu, S.-P. Chang, W.-Y. Liao, M.-T. Chu, and S.-J. Chang, "Efficiency of GaN/InGaN double-heterojunction photovoltaic cells under concentrated illumination," *Surface and Coatings Technology*, vol. 231, pp. 253-256, 2013.

[186] L. Li, D.-G. Zhao, D.-S. Jiang, Z.-S. Liu, P. Chen, L.-L. Wu, L.-C. Le, H. Wang, and H. Yang, "The Effects of a Low-Temperature GaN Interlayer on the Performance of InGaN/GaN Solar Cells," *Chinese Physics Letters* vol. 30, p. 028801, 2013.

[187] X. M. Cai, Y. Wang, Z. D. Li, X. Q. Lv, J. Y. Zhang, L. Y. Ying, and B. P. Zhang, "Improved photovoltaic performance of InGaN/GaN solar cells with optimized transparent current spreading layers," *Applied Physics A*, vol. 111, pp. 483-486, 2013.

[188] R. M. Farrell, A. A. Al-Heji, C. J. Neufeld, X. Chen, M. Iza, S. C. Cruz, S. Keller, S. Nakamura, S. P. DenBaars, U. K. Mishra, and J. S. Speck, "Effect of intentional p-GaN surface roughening on the performance of InGaN/GaN solar cells," *Applied Physics Letters*, vol. 103, p. 241104, 2013.

[189] L. Li, D.-G. Zhao, D.-S. Jiang, Z.-S. Liu, P. Chen, L.-L. Wu, L.-C. Le, H. Wang, and H. Yang, "The effects of InGaN layer thickness on the performance of InGaN/GaN p-i-n solar cells," *Chinese Physics B*, vol. 22, p. 068802, 2013.

[190] Y. Zhang, M. J. Kappers, D. Zhu, F. Oehler, F. Gao, and C. J. Humphreys, "The effect of dislocations on the efficiency of InGaN/GaN solar cells," *Solar Energy Materials and Solar Cells*, vol. 117, pp. 279-284, 2013.

VITA

Chloé Fabien was born in 1987 in Paris, France. She received the Diplôme d'Ingénieur from Supélec, France, in 2011. While studying at Supélec, she entered the Georgia Institute of Technology and received the M.Sc. degree in Electrical and Computer Engineering in 2011. She is currently pursuing a Ph.D. degree at the Georgia Institute of Technology in the Advanced Semiconductor Technology Facility research group.

PUBLICATION LIST

Referred Journal Publications

1. **C. A. M. Fabien,** A. Maros, C. B. Honsberg, and W. A. Doolittle, "III-Nitride Double-Heterojunction Solar Cells with High In-content InGaN Absorbing Layers: Comparison of Large-Area and Small-Area Devices," accepted in *IEEE Journal of Photovoltaics*, 2015. **Invited**

2. **C. A. M. Fabien,** B. P. Gunning, W. Alan Doolittle, A. M. Fischer, Y. O. Wei, H. Xie, and F. A. Ponce, "Low-Temperature Growth of InGaN Films over the Entire Composition Range by MBE," *Journal of Crystal Growth*, vol. 425, pp. 115-118, 2015.

3. B. P. Gunning, **C. A. M. Fabien,** J. J. Merola, E. A. Clinton, W. A. Doolittle, S. Wang, A. M. Fischer, and F. A. Ponce, "Comprehensive study of the electronic and optical behavior of highly degenerate p-type Mg-doped GaN and AlGaN," *Journal of Applied Physics*, vol. 117, p. 045710, 2015.

4. **C. A. M. Fabien** and W. A. Doolittle, "Guidelines and Limitations for the Design of High-Efficiency InGaN Single-Junction Solar Cells," *Solar Energy Materials and Solar Cells*, vol. 130, pp. 354-363, 2014.

5. J. D. Greenlee, J. C. Shank, M. B. Tellekamp, B. P. Gunning, **C. A. M. Fabien,** and W. A. Doolittle, "Liquid Phase Electro-Epitaxy of Memristive $LiNbO_2$ Crystals," *Crystal Growth & Design*, vol. 14, pp. 2218-2222, 2014.

6. **C. A. M. Fabien,** M. Moseley, B. Gunning, W. A. Doolittle, A. M. Fischer, Y. O. Wei, and F. A. Ponce, "Simulations, Practical Limitations and Novel Growth Technology for InGaN-Based Solar Cells," *IEEE Journal of Photovoltaics*, vol. 4, pp. 601-606, 2013. **Invited**

Conference Presentations

1. W. A. Doolittle, B. Gunning, **C. A. M. Fabien**, E. Clinton, and J. Merola, "III-Nitride Growth by a New Generation Of MBE Systems," *20th American Conference on Crystal Growth and Epitaxy*, Big Sky, MT, USA, Aug. 2015.

2. B. Gunning, E. Clinton, J. Merola, **C. A. M. Fabien**, and W. A. Doolittle, "Dramatically Increased Growth Rates Exceeding 9 μm/Hour for GaN Grown by Plasma-Assisted MBE," *57th Electronic Materials Conference*, Columbus, OH, USA, June 2015.

3. **C. A. M. Fabien**, B. Gunning, J. Merola, E. Clinton, and W. A. Doolittle, "Large-Area III-Nitride Double-Heterojunction Solar Cells with Record-High In-content InGaN Absorbing Layers," *42nd Photovoltaic Specialists Conference*, New Orleans, LA, USA, June 2015.

4. B. Gunning, **C. A. M. Fabien**, J. Merola, E. Clinton, W. A. Doolittle, A. M. Fischer, S. Wang, Y. O Wei, and F. A. Ponce, "Electronic and Optical Behavior of Highly p-type GaN and AlGaN, and High Growth Rate GaN by MBE," *Workshop on Compound Semiconductor Materials and Devices*, Isle of Palms, SC, USA, Feb. 2015.

5. **C. A. M. Fabien**, B. Gunning, W. A. Doolittle, M. Moseley, A. M. Fischer, Y. O. Wei, and F. A. Ponce, "Comparison of N-rich and MME-grown InGaN Throughout the Miscibility Gap," *18th International Conference on Molecular Beam Epitaxy*, Flagstaff, AZ, USA, Sept. 2014.

6. B. Gunning, **C. A. M. Fabien**, and W. A. Doolittle, "Highly Conductive P-type III-Nitrides Using Both Bulk and 2-Dimensional Heavily Mg-doped Layers," *18th International Conference on Molecular Beam Epitaxy*, Flagstaff, AZ, USA, Sept. 2014.

7. B. Gunning, **C. A. M. Fabien**, and W. A. Doolittle, "III-Nitride Optoelectronic Devices Using Highly Mg-doped P-type Layers Grown by Metal-modulated Epitaxy," *18th International Conference on Molecular Beam Epitaxy*, Flagstaff, AZ, USA, Sept. 2014.

8. T. Smyth, H. Xia, Y. Feng, M. Dvorak, M. Tayebjee, S. Shrestha, S. Bremner, S. Huang, G. J. Conibeer, S. Yagi, **C. A. M. Fabien,** B. Gunning, W. A. Doolittle, C. Tessarek, M. Latzel, T. W. Schmidt, and M. Sugiyama, "Hot Carrier Relaxation and Phonon Dispersion in III-V Alloys," *29th European Photovoltaic Solar Energy Conference and Exhibition*, Amsterdam, the Netherlands, Sept. 2014.

9. W. A. Doolittle, B. Gunning, **C. A. M. Fabien**, A. M. Fischer, S. Wang, Y. O. Wei, and F. A. Ponce, "Extremely High Hole Concentrations in III-Nitrides," *The International Workshop on Nitride Semiconductors*, Wrocław, Poland, Aug. 2014. **Invited**

10. **C. A. M. Fabien**, B. Gunning , M. Moseley, W. A. Doolittle, A. M. Fischer, Y. O. Wei, and F. A. Ponce, "Prospects of InGaN-Based Solar Cells by Metal-Modulated Epitaxy," *5th International Symposium on Growth of III-Nitrides*, Atlanta, GA, USA, May 2014.

11. B. Gunning, **C. A. M. Fabien**, and W. A. Doolittle, "Highly Conductive P-Type GaN and AIGaN Using Both Bulk and 2-Dimensional Heavily Mg-Doped Layers," *5th International Symposium on Growth of III-Nitrides*, Atlanta, GA, USA, May 2014.

12. B. Gunning, **C. A. M. Fabien**, and W. A. Doolittle, "Breaching the Perceived Upper Bounds of p-type Doping in GaN and InGaN," *Workshop on Compound Semiconductor Materials & Devices*, San Antonio, TX, USA, Feb. 2014.

13. W. A. Doolittle, B. Gunning, **C. A. M. Fabien**, A. M. Fischer, Y. O. Wei, and F. A. Ponce, "New Advances in III-Nitride Epitaxy," *Workshop on Compound Semiconductor Materials & Devices*, San Antonio, Texas, USA, Feb. 2014.

14. W. A. Doolittle, B. Gunning, **C. A. M. Fabien**, M. Moseley, "MBE Growth Methodologies for Overcoming the Perceived Limitations of Phase Separation and P-type Doping in InGaN," *30th North American Molecular Beam Epitaxy Conference*, Banff, AB, Canada, Oct. 2013.

15. **C. A. M. Fabien**, B. Gunning, M. Moseley, W. A. Doolittle, A. M. Fischer, Y. O. Wei, and F. A. Ponce, "Advances in Nitride Growth Technology for InGaN-Based Solar Cells," *10th International Conference on Nitride Semiconductors*, Washington, D.C., USA, Aug. 2013.

16. B. Gunning, J. Lowder, M. Moseley, **C. A. M. Fabien**, G. Namkoong, W. A. Doolittle, "Optimization of Growth and Electrical Transport Properties of Highly p-type GaN and InGaN," *10th International Conference on Nitride Semiconductors*, Washington, D.C., USA, Aug. 2013.

17. W. A. Doolittle, B. Gunning, **C. A. M. Fabien**, and M. Moseley, "Growth Methodologies for Overcoming the Perceived Limitations of Phase Separation and P-type Doping in InGaN," *17th International Conference on Crystal Growth and Epitaxy*, Warsaw, Poland, Aug. 2013.

18. **C. A. M. Fabien**, M. Moseley, B. Gunning, W. A. Doolittle, A. M. Fischer, Y. O. Wei, and F. A. Ponce, "Simulations, Practical Limitations, and Novel Growth Technologies for InGaN-based Solar Cells," *39th IEEE Photovoltaic Specialists Conference*, Tampa, FL, USA, June 2013.

19. W. A. Doolittle, B. Gunning, **C. A. M. Fabien**, and M. Moseley, "Growth Methodologies for Overcoming the Challenges of Phase Separation and p-type Doping in InGaN," *Collaborative Conference on Crystal Growth*, Cancun, Mexico, June 2013.

20. **C. A. M. Fabien**, M. Moseley, B. Gunning, W. A. Doolittle, A. M. Fisher, Y. Wei, and F. A. Ponce, "Characterization of MBE-Grown, Low Threading-Dislocation Density, High-Indium InGaN without Phase Separation," *29th North American Molecular Beam Epitaxy Conference*, Stone Mountain Park, GA, USA, Oct. 2012.